

Ram pressure stripping of disk galaxies

Dissertation
zur Erlangung des Doktorgrades
der Mathematisch-Naturwissenschaftlichen Fakultät
der Christian-Albrechts-Universität zu Kiel

vorgelegt von
Elke Rödiger

Kiel
Dezember 2004

Referent: Prof. Dr. Gerhard Hensler

Koreferent: Prof. Dr. Volkmar Helbig

Tag der mündlichen Prüfung: 7. Februar 2005

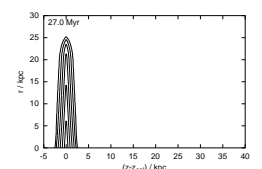
Zum Druck genehmigt: Kiel, den 1. März 2005

Der Dekan

Abstract

Galaxies divide into two main groups: elliptical and disk galaxies. In general, ellipticals are rather simple systems containing old stars and hot gas. As the name implies, in disk galaxies both stars and gas are concentrated towards the galactic disk. In contrast to ellipticals, most disk galaxies are continuously forming new stars out of the richly structured interstellar gas. Galaxies exist in various environments, ranging from isolated field galaxies over galaxy groups to clusters. Distances between field galaxies can reach about one Megaparsec, whereas in dense massive clusters there can be as many as some hundred galaxies per cubic Megaparsec. Moreover, clusters and groups are filled with a hot tenuous gas, the intracluster medium or intragroup medium (abbreviated ICM for both). The majority of all galaxies belongs to groups. About 5 to 10% can be found in clusters, but less than 1% are isolated. Comparative observations of galaxies in various environments reveal systematic differences in morphology, colour, star formation activity and gas contents. Especially disk galaxies change with environment. Theoretical work has proposed several mechanisms that can be at work in clusters and groups. On the one hand there are (gravitational) interactions among the galaxies themselves, on the other hand there is the interaction between the galaxies and the ICM. The basic idea for the latter is that a galaxy is stripped of its gas by ram pressure as it moves through the ICM. That this process can occur despite the restoring gravitational force has been estimated long ago (Gunn & Gott, 1972). The gas is the raw material for star formation, therefore such ram pressure stripping (RPS) has severe consequences for a galaxy. The aim of this work is to study the process of RPS of disk galaxies with hydrodynamical simulations.

The amount of gas a galaxy loses by RPS depends on several parameters. The strength of the ram pressure is larger for higher ICM densities and galaxy velocities. In more massive or more concentrated galaxies the gravitation provides a stronger resistance to gas removal. The stripping is expected to be strongest for galaxies moving face-on through the ICM. The simulations in this work are restricted to the face-on case, which allows us to use a 2D code. This enables us to use high resolution *and* to compile a comprehensive parameter study that varies galaxy properties as well as ICM conditions. We perform simulations for several gas disk structures, namely exponential and flared disks of various thicknesses. In addition, galaxies of two different



masses are studied. The simulations cover a large range of ICM conditions, reaching from high density environments like in cluster centres to low density environments typical for cluster outskirts or groups.

We find that RPS proceeds in three phases: firstly the instantaneous stripping phase, secondly the dynamic intermediate phase, and thirdly the quasi-stable continuous viscous stripping phase. In the first phase (time scale $2 \cdot 10^7$ to $2 \cdot 10^8$ years) the outer part of the gas disk is displaced but still largely gravitationally bound. In the second phase (10 times as long as the first phase) a part of the displaced gas falls back (about 10% of the initial gas mass) despite the constant ICM flow, but most displaced gas now becomes unbound. In the third phase the galaxy continues to lose gas at a rate of about one solar mass per year by turbulent viscous stripping. We find that the stripping efficiency depends slightly on the Mach number of the ICM flow, however, the main parameter is the ram pressure. For a fixed surface density the stripping efficiency does not depend on the vertical structure and thickness of the gas disk.

The classical analytical estimate of the stripping radius (radius of the remaining gas disk) of Gunn & Gott (1972) compares the ram pressure to the gravitational restoring force. The comparison to the numerical results shows that the analytical method overestimates the stripping radius systematically by a few kiloparsec. If one summarises all simplifications that have been assumed for the analytical estimate in a correction factor and multiplies this with the restoring force, the systematic differences can be eliminated. In addition, we adapt an alternative estimate used by Mori & Burkert (2000) for spherical galaxies, namely the comparison of the central pressure with ram pressure. We find that the latter estimate predicts the radius and mass of the gas disk remaining at the end of the second phase very well.

From our simulations we conclude that gas disks of galaxies in high density environments are heavily truncated or even completely stripped. But also the gas disks of galaxies in low density environments are disturbed by the ICM-flow and back-falling material, so that they should also be pre-processed. In addition to the simulations we compare typical ICM pressures with characteristic pressures inside gas disks of isolated galaxies. We demonstrate that ICM pressures in cluster cores can easily exceed pressures in galactic disks at radii outside ~ 7 kpc. From this comparison we conclude that the gas in disk galaxies should be affected by the ICM already by the external pressure. This effect will be subject of future research.

Zusammenfassung

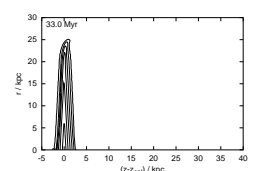
Galaxien unterteilen sich in zwei Hauptgruppen: elliptische und Scheibengalaxien. Im Allgemeinen sind elliptische Galaxien einfache Systeme. Sie enthalten alte Sterne und heißes Gas. Wie der Name sagt, bilden in Scheibengalaxien Sterne und Gas die galaktische Scheibe. Im Gegensatz zu elliptischen Galaxien ist in Scheibengalaxien das reich strukturierte interstellare Gas Schauplatz permanenter Sternentstehung. Galaxien existieren in verschiedenen Umgebungen, deren Spektrum sich von isolierten Feldgalaxien über Galaxiengruppen bis zu Galaxienhaufen erstreckt. Abstände zwischen Feldgalaxien können ungefähr einen Megaparsec erreichen, wohingegen in kompakten massiven Haufen Dichten von einigen hundert Galaxien pro Kubikmegaparsec erreicht werden. Zusätzlich zu den Galaxien enthalten Haufen und Gruppen ein heißes dünnes Gas (abgekürzt ICM¹). Die meisten Galaxien befinden sich in Gruppen, ungefähr 5 bis 10% gehören Haufen an und weniger als 1% sind isoliert. Vergleichende Beobachtungen von Galaxien in verschiedenen Umgebungen offenbaren systematische Unterschiede in Morphologie, Farbe, Sternentstehungsaktivität und Gasinhalt. Insbesondere Scheibengalaxien verändern sich mit der Umgebung. Theoretische Arbeiten haben mehrere Prozesse vorgeschlagen, die in Haufen und Gruppen ablaufen können. Einerseits gibt es (Gravitations-)Wechselwirkungen der Galaxien untereinander, andererseits die Interaktion zwischen den Galaxien und dem ICM. Die letztere Idee besagt folgendes: Während sich eine Galaxie durch das ICM bewegt, wird durch den auftretenden Staudruck ihr Gas abgestreift. Gunn & Gott (1972) haben abgeschätzt, dass dieser Effekt trotz der entgegenwirkenden Gravitation tatsächlich auftreten kann. Das Gas ist der Rohstoff für die Sternentstehung, daher hat ein solches "Staudruck-Abstreifen" (RPS²) schwerwiegende Konsequenzen für die Galaxie. Das Ziel dieser Arbeit ist es, RPS von Scheibengalaxien mit Hilfe hydrodynamischer Simulationen zu untersuchen.

Die Menge des Gases, das eine Galaxie durch RPS verliert, hängt von mehreren Parametern ab. Der Staudruck ist stärker bei höheren ICM-Dichten und Galaxiengeschwindigkeiten. In massereicheren oder kompakten Galaxien bewirkt die Gravitation einen größeren Widerstand gegen den Gasverlust. Am stärksten sollte der Gasverlust für Galaxien sein, die sich face-on³ durch das ICM bewegen. In dieser Arbeit beschränken wir uns auf diesen Fall, was die Verwendung eines 2D Codes erlaubt. Dadurch können wir eine

¹auf Englisch: IntraCluster Medium

²auf Englisch: Ram Pressure Stripping

³die Bewegungsrichtung der Galaxie steht senkrecht auf ihrer Scheibenebene



umfassende Parameterstudie mit hoher Auflösung erstellen, in der wir sowohl die ICM-Bedingungen als auch Galaxieneigenschaften variieren. Wir testen verschiedene Gasscheibenformen und -dicken. Zusätzlich werden Galaxien mit zwei unterschiedlichen Massen untersucht. Die Simulationen überdecken einen großen Bereich von ICM Bedingungen, von hohen Dichten in Haufenzentren bis zu geringen Dichten, die charakteristisch für Haufen-Randgebiete oder Galaxiengruppen sind.

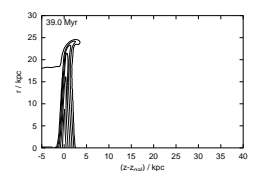
In den Simulationen läuft RPS in drei Phasen ab: instantanes Abstreifen, dann eine dynamische Zwischenphase und schließlich quasi-stabiles kontinuierliches Abstreifen. In der ersten Phase (Zeitskala $2 \cdot 10^7$ bis $2 \cdot 10^8$ Jahre) wird der äußere Teil der Gasscheibe versetzt, ist dabei aber zum größten Teil noch gravitativ gebunden. In der zweiten Phase (10mal länger als die erste Phase) fällt ein Teil des schon herausgedrückten Gases zurück (ungefähr 10% der Ausgangsgasmasse), obwohl die Simulationen eine konstante Anströmung benutzen. In dieser Phase verliert fast alles herausgedrückte Gas seine Bindung an das Gravitationspotential der Galaxie. In der dritten Phase verliert die Galaxie weiter Gas durch turbulent-viskoses Abstreifen mit einer Rate von ungefähr einer Sonnenmasse pro Jahr. Der Gesamt-Massenverlust hängt hauptsächlich vom Staudruck ab, und nur geringfügig von der Machzahl der Umströmung. Bei gleichbleibender Flächendichte ist der Massenverlust unabhängig von der Form und Dicke der Gasscheibe.

Die klassische Abschätzung (Gunn & Gott 1972) des Stripping-Radius (Radius der übriggebliebenen Gasscheibe) vergleicht den Staudruck mit der rückstellenden Gravitationskraft. Der Vergleich mit den numerischen Ergebnissen zeigt jedoch, dass die Abschätzung den Stripping-Radius systematisch um ein paar Kiloparsec überschätzt. Fasst man alle Vereinfachungen, die die Abschätzung macht, in einen Korrekturfaktor zusammen und multipliziert diesen mit der berechneten Rückstellkraft, dann kann der systematische Unterschied behoben werden. Für sphärische Galaxien verwendeten Mori & Burkert (2000) eine alternative Abschätzung, die den zentralen thermischen Druck mit dem Staudruck vergleicht. Wir adaptieren diese hier für Scheibengalaxien. Radius und Masse der übriggebliebenen Gasscheibe am Ende der zweiten Phase werden sehr gut durch diese zweite Methode der analytischen Abschätzung vorhergesagt.

Aus den Simulationen schlussfolgern wir, dass in Gebieten mit hoher ICM-Dichte die Gasscheiben deutlich abgeschnitten oder sogar vollständig abgestreift werden. In Regionen mit niedriger ICM-Dichte verlieren die Galaxien nur wenig Gas, aber die Gasscheiben werden trotzdem durch die Umströmung und zurückfallendes Material gestört. Zusätzlich zu den Simulationen vergleichen wir charakteristische Drücke im ICM und in Gasscheiben isolierter Galaxien. Wir zeigen, dass in Galaxien bei Radien $\gtrsim 7$ kpc der Druck deutlich kleiner als der ICM-Druck in Haufenzentren ist. Das lässt darauf schließen, dass Scheibengalaxien schon durch den externen ICM-Druck beeinflusst werden können. Dieser Effekt wird Thema weiterführender Untersuchungen sein.

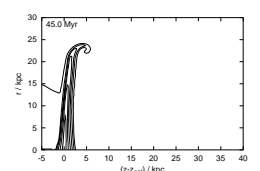
Contents

Abstract	iii
Zusammenfassung	v
List of symbols	xvi
List of frequently used abbreviations	xvi
1 Galaxies	1
1.1 Classification of galaxies	2
1.1.1 Elliptical galaxies	2
1.1.2 Spiral galaxies	3
1.1.3 S0 galaxies	4
1.2 The interstellar medium	4
1.2.1 Components	5
1.2.2 Distribution	6
1.2.3 A crude physical model	7
1.3 Clusters and groups of galaxies	13
1.3.1 Classification	13
1.3.2 The intracluster medium	14
1.4 Environmental effects	18
1.4.1 Gravitational interactions	19
1.4.2 Gas interactions	20
1.5 Galaxies in different environments	23
1.5.1 Colours, morphology and star formation rates	23
1.5.2 Gas contents of late-type galaxies	26
1.5.3 Galaxies “caught in the act”	28
1.5.4 Relevance of environmental effects	30
1.6 Aim of this work	32
2 Numerical Methods	35
2.1 Hydrodynamical equations	35
2.2 The staggered grid	37
2.3 Operator splitting	37
2.3.1 Source step	39



2.3.2	Transport step - advection	40
2.4	Time step criterion	42
2.5	Boundary conditions	42
2.5.1	Boundary at $r = 0$	42
2.5.2	Boundary at $z = 0$	43
2.5.3	Boundary at $z = z_{\max}$	44
2.5.4	Boundary at $r = r_{\max}$	44
2.6	Computation of the potential	45
2.7	Code testing and calibration	45
2.8	Colouring technique	46
3	Initial Model	47
3.1	Galactic components	47
3.1.1	Stellar disk	47
3.1.2	Stellar bulge	51
3.1.3	Dark matter halo	51
3.1.4	Gas disk	53
3.1.5	Summary of the components	54
3.2	Stability of the initial model	56
3.2.1	An equilibrium intergalactic medium?	56
3.2.2	Stability of the gas disk	57
3.3	Testing the initial model	63
3.3.1	Resolution	63
3.3.2	Stability	63
4	Simulations and results	67
4.1	Overview of performed simulations	67
4.1.1	Wind parameters	68
4.1.2	Influence of the galactic parameters	68
4.2	Analytical estimate	70
4.2.1	Instantaneous stripping	70
4.2.2	Continuous stripping	74
4.3	General simulation setup	76
4.3.1	Grid size and resolution	76
4.3.2	Wind initialisation	77
4.4	General behaviour of the simulations	78
4.5	Analysis techniques – gas disk mass and radius	79
4.5.1	Definitions – “disk region” and “galactic gas”	87
4.5.2	Colouring technique – tracing the galactic gas	87
4.5.3	Disk mass and radius	88
4.6	Varying the wind parameters	90
4.6.1	Wind density and velocity	90
4.6.2	Cross-comparisons between runs with different T_{ICM}	92
4.7	Vertical structure of the gas disk	97
4.8	The medium-mass galaxy	99

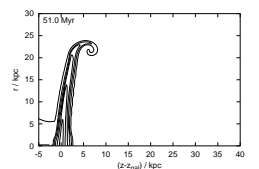
4.9	Comparison of analytical versus numerical results	99
4.9.1	Instantaneous stripping	99
4.9.2	Continuous stripping	106
5	Summary and discussion	109
6	Future work	115
	Appendices	119
A	Miscellaneous	119
A.1	Astrophysical units	119
A.1.1	Basics	119
A.1.2	Commonly used quantities	120
A.2	Useful relations	120
A.2.1	Conversion between scale lengths	120
A.2.2	Operators in cylindrical coordinates	120
A.3	Virial theorem	120
B	Kelvin-Helmholtz instability	123
C	Tests and code calibration	127
C.1	Riemann shock tube	127
C.1.1	Analytical solution	127
C.1.2	Comparison of analytical and numerical result	129
C.1.3	Courant-Friedrichs-Levy safety factor	130
C.1.4	Conservation of mass and energy	130
C.2	Sedov-Taylor blast wave	135
C.2.1	Analytical solution	135
C.2.2	Simulations	136
C.2.3	Comparison	136
C.2.4	Conservation of total mass and energy	141
C.2.5	Courant-Friedrich-Levy safety factor	142
C.3	Flow past a sphere	142
C.3.1	Analytical solution	142
C.3.2	Applicability of the analytical solution	143
C.3.3	Simulations	144
C.3.4	Comparison between analytical and numerical result	146
C.4	Potential test	153
C.4.1	Analytical solution	153
C.4.2	Simulation	153
C.4.3	Comparison	154
C.5	Implications for further simulations	156



D Tests for ram pressure stripping simulations	157
D.1 Resolution and grid size	157
D.2 Wind initialisation	158
D.3 Gravitational potential of the gas disk	160
D.4 Influence of artificial viscosity	160
Bibliography	166

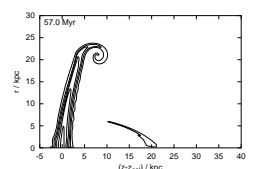
List of Figures

1.1	Hubble's tuning fork diagram	3
1.2	Degree of ionisation and mean particle mass	9
1.3	Heating and cooling rates	11
1.4	Heating and cooling time scales	12
1.5	ISM phases in T - ρ -plane	13
1.6	Coma and Virgo clusters in X-rays	15
1.7	ICM particle density profiles for Coma and Virgo cluster . . .	18
1.8	HI disks of brightest Virgo spirals, from Cayatte et al. (1990) .	27
1.9	Ram pressure stripping of the Virgo spiral NGC 4522: H α and R-band	29
1.10	Ram pressure stripping of the Virgo spiral NGC 4522: HI, R-band and H α	30
1.11	Ram pressure stripping of the Virgo spiral NGC 4402	31
2.1	Illustration of the staggered grid	38
3.1	Disk surface density profiles and cumulative masses for a Kuzmin disk and a thin exponential disk	50
3.2	Vertical potential and acceleration profiles for PK disks for various scale heights	50
3.3	DM halo density profiles and cumulative masses for a Burkert halo and a Navarro-Frenk-White halo	53
3.4	Cumulative masses for the stellar disk and the DM halo of the model galaxies	54
3.5	Rotation curve decomposition for the model galaxies	55
3.6	Contour plots (density, temperature, rotation) for the massive galaxy (exponential disk) in low-pressure ICM	59
3.7	Contour plots (density, temperature, rotation) for the massive galaxy (flared disk) in low-pressure ICM	59
3.8	Contour plots (density, temperature, rotation) for the medium- mass galaxy (exponential disk) in low-pressure ICM	60
3.9	Radial profiles for various disk models in a low-pressure ICM .	61
3.10	Dependence on ICM pressure of radial profiles (pressure, tem- perature)	62



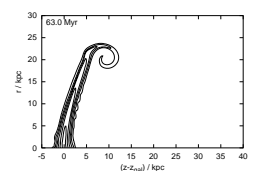
3.11	Contour plots (density, temperature, rotation) for the massive galaxy (exponential disk) in high-pressure ICM	63
3.12	Snapshots of stability test	64
3.13	Evolution of vertical profiles of stability test	65
3.14	Evolution of radial profiles of stability test	66
4.1	Overview of models in the $v_{\text{ICM}}-n_{\text{ICM}}$ plane	69
4.2	Vertical profiles of the gravitational restoring force of the galaxy	71
4.3	Analytical estimate of stripping radius r_{strip} and mass M_{strip} .	72
4.4	Analytical estimate of the mass loss rate for the continuous stripping	75
4.5	Evolution snapshots	80
4.6	Evolution snapshots	82
4.7	Evolution snapshots	84
4.8	Lost and fallen back ISM	86
4.9	Evolution of radial density and surface density profiles	86
4.10	Evolution of gas disk radius and gas disk mass, demonstration of various measurement recipes	89
4.11	Evolution of gas disk radius and mass, and bound gas mass . .	91
4.12	Evolution of mass of bound gas outside the original disk region	92
4.13	Evolution of mass of back-fallen gas	93
4.14	Evolution of gas disk radius, mass in original disk region and bound mass, for second ICM temperature	94
4.15	Evolution of mass of bound gas outside the original disk region, for second ICM temperature	95
4.16	Evolution of mass of back-fallen gas, for second ICM temperature	95
4.17	Cross-comparison of stripping radius, disk mass and bound gas mass; for different Mach numbers and velocities	96
4.18	Snapshots for different gas disk thicknesses	97
4.19	Comparison of stripping radius, gas disk mass and bound gas mass for different vertical gas disk structures and thicknesses .	98
4.20	Evolution of vertical profiles through the gas disk	100
4.21	Evolution of gas disk radius and mass, and bound gas mass; for medium-mass galaxy	101
4.22	Evolution of mass of bound gas outside the original disk region; for bound gas mass	102
4.23	Evolution of mass of back-fallen gas; for medium-mass galaxy	102
4.24	Comparison of analytical estimate and numerical result; for massive galaxy	104
4.25	Comparison of analytical estimate and numerical result; for medium-mass galaxy	104
4.26	Rankine-Hugoniot-corrected comparison of analytical estimate and numerical result; for massive galaxy	105
4.27	Rankine-Hugoniot-corrected comparison of analytical estimate and numerical result; for the medium-mass galaxy	106

4.28	Duration of the instantaneous stripping phase and intermediate phase	107
4.29	Mass loss rates of the continuous stripping phase	108
B.1	Kelvin-Helmholtz clouds at Mount Shasta	123
C.1	Schematic shock tube solution	128
C.2	Shock tube – comparison analytical-numerical result	131
C.3	Shock tube – influence of artificial viscosity	132
C.4	Shock tube – influence of spatial resolution	133
C.5	Shock tube – influence of Courant-Friedrich-Levy safety factor	134
C.6	Conservation of total mass and energy in the shock tube test.	135
C.7	Snapshot of Sedov-Test	137
C.8	Snapshot of Sedov-Test	137
C.9	Snapshot of Sedov-Test	137
C.10	Comparison of analytical and numerical result for Sedov Test	138
C.11	Comparison of analytical and numerical result for Sedov Test	139
C.12	Sedov Test – Shock front radius: influence of resolution	140
C.13	Sedov Test – Shock front radius: influence of artificial viscosity	140
C.14	Sedov Test – Shock front radius. Long time run.	141
C.15	Conservation of total mass and energy in the Sedov test.	141
C.16	Analytical solution for potential flow past a sphere	143
C.17	Snapshot of the flow around a sphere	147
C.18	Snapshot of the flow around a sphere	147
C.19	Snapshot of the flow around a sphere	147
C.20	Influence of initialisation time in the potential flow test	148
C.21	Influence of boundaries in the potential flow test	149
C.22	Detailed result for potential flow	151
C.23	Comparison of analytical and numerical potential of a homogeneous sphere	155
C.24	Error in the gravitational force for a homogeneous sphere	155
C.25	Potential test – influence of sphere position in the grid	156
D.1	Comparison of gas disk radius, mass and fallen-back mass for different grid sizes and resolutions	158
D.2	Comparison snapshots for different resolutions	159
D.3	Comparison of gas disk radius and mass for different t_{switch}	161
D.4	Influence of changing gas potential on gas disk mass and radius	162
D.5	Comparison of gas disk radius, mass and fallen-back mass for different viscosities	163
D.6	Comparison of gas disk radius, mass and fallen-back mass for different viscosities	164
D.7	Comparison of the density distribution for different viscosities	165



List of Tables

1.1	Molecular weights for instructive cases	8
1.2	Typical conditions in the ICM for galaxy clusters and groups.	18
3.1	Galaxy model parameters	55
4.1	Parameters for the simulations testing the influence of the vertical structure of the gas disk	70
4.2	Numerical parameters	77
C.1	Parameters for the simulation runs for the shock tube test . .	130
C.2	Sedov test: List of simulations	136
C.3	Constant parameters for the simulation runs for the potential flow	145
C.4	Varied parameters for the simulation runs for the potential flow	145
C.5	Parameters for the potential tests	154
D.1	List of simulations testing the influence of resolution and grid size	157
D.2	Parameters for runs testing the influence of the wind initialisation	160
D.3	List of simulations for showing the influence of the artificial viscosity	162



List of symbols

z, r, ϕ	cylindrical coordinates: z along the symmetry axis, radial coordinate r and angular coordinate ϕ
R	radius coordinate in a spherical coordinate system
z_{gal}	z -coordinate of the galactic plane (cylindrical coordinates)
ρ	mass density
n	particle number density
e	internal energy density
p	pressure
T	temperature
Φ	gravitational potential
U	velocity component parallel to symmetry (z -) axis (see Fig. 2.1)
V	velocity component in radial direction (see Fig. 2.1)
SM	linear momentum component parallel to symmetry axis (see Fig. 2.1)
TM	linear momentum component in radial direction (see Fig. 2.1)
IZ, IR	enumerate grid cells in z - and r -direction, respectively (see Fig. 2.1)
NZ, NR	total number of grid cells in z - and r -direction, respectively

List of frequently used abbreviations

1D, 2D, 3D	one-dimensional, two-dimensional, three-dimensional
DM	Dark Matter
ICM	Intra Cluster Medium (also used for the intra-group medium)
ISM	InterStellar Medium
KH	Kelvin-Helmholtz
PK	Plummer-Kuzmin
RPS	Ram Pressure Stripping
SF	Star Formation
SFR	Star Formation Rate
SN	Supernova

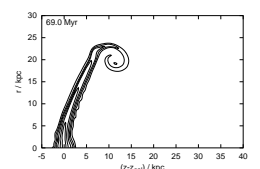
Chapter 1

Galaxies

Of all objects in the night sky visible to the naked eye there are only three that do not belong to our home galaxy, the Milky Way. These are the Large and the Small Magellanic Clouds, satellite dwarf galaxies orbiting the Milky Way, and the Andromeda galaxy, our Milky Way's sister in the local group. With the advance of large telescopes, huge numbers of other galaxies have been found in the last decades.

Today we consider galaxies as the main building blocks of the universe. They are composed of stars, interstellar medium (ISM) and dark matter (DM). Properties of the ISM are summarised in Sect. 1.2. Diameters of galaxies range from a few kpc for dwarf systems to a few 10 kpc for normal and giant ones. In normal galaxies the masses of the baryonic components (stars and ISM) range between 10^{10} and $10^{12}M_{\odot}$. Dwarf galaxies have less than $10^{10}M_{\odot}$, giants can reach a few $10^{12}M_{\odot}$. However, these masses are not sufficient to explain the observed internal dynamics in galaxies. This shortcoming led to the idea of DM to account for the missing mass. Thus the baryonic components of galaxies are thought to be embedded in DM halos of about $10^{12}M_{\odot}$. Nevertheless, the existence and nature of DM remains a matter of debate. Most normal galaxies show either an elliptical or a disk-like morphology. For dwarf galaxies morphologies range from spheroidal to irregular. The classification is described in more detail in Sect. 1.1.

The galaxies themselves are part of still larger structures. They are often found in groups or even in clusters of galaxies (see Sect. 1.3). These large structures are still growing, groups and subclusters are merging with clusters. Comparing more isolated galaxies (= "field galaxies") with galaxies inside such structures, one finds a number of differences in their properties, that are discussed in more detail in Sect. 1.5. This leads to the question to what extent the evolution of galaxies is influenced by their environment. Several possible mechanisms are explained in Sect. 1.4. It is well known that cluster or group members can interact directly via gravitation and affect each other strongly. A second possibility is the interaction between galaxies and the intergalactic or intracluster medium (ICM, see Sect. 1.3.2), the hot tenuous gas found in clusters. The basic idea here is that as the galaxy moves through



the cluster, it feels the ICM as a wind that can push out the galaxy’s gas. This process is termed ram pressure stripping (RPS). Of course the loss of the gas has severe consequences for a galaxy, as the gas is the supply of raw material for star formation (SF).

In this work we want to study the process of RPS of disk galaxies by means of hydrodynamical simulations. In this first chapter we give an overview of the necessary background knowledge and put this work into a general context. At the end of this chapter we specify the purpose and the plan of this work in more detail. Chapter 2 gives a summary of hydrodynamics and of the numerical code; Appendix C presents some tests of the code. In Chapter 3 we introduce the initial model. Chapter 4 presents the result of the simulations. Finally, in Chapter 5 we summarise and discuss these results. Chapter 6 gives an outlook on future work.

1.1 Classification of galaxies

A first step to study the “extragalactic nebulae” was done by E. P. Hubble, who classified galaxies according to their shape on blue exposures. The result was his famous “tuning fork” diagram (Fig. 1.1, Hubble 1926, 1936). The main distinction can be made between elliptical and disk galaxies. The ellipticals were characterised further by their degree of ellipticity (“ En ”, where n is calculated from the major and minor axes a and b according to $n = 10(1 - b/a)$). Disk galaxies can be divided into three subgroups: the featureless S0s and barred (SB) and unbarred spirals (S). In the latter two groups further distinctions can be made according to the prominence of the bulge and the spiral arms. Due to the assumption that the tuning fork diagram represented the evolution of the galaxies, the ellipticals were also called “early-type” galaxies and the spirals “late-type” galaxies. This assumption turned out to be wrong, however, the terms early-type and late-type are still in use. The early observations detected mainly massive bright galaxies. Among them, only a few galaxies were left outside the scheme as irregulars. More recent observations detected also many dwarf galaxies with a variety of morphologies, often irregular, elliptical or spheroidal (see e.g. Grebel 2001). Due to their low brightness, dwarf galaxies are still difficult to detect today. Later in the twentieth century the classification scheme was extended and refined, but for massive galaxies the distinction in elliptical and spiral (or disk) galaxies is still valid today.

The relative frequency of different types depends on the environment as discussed in more detail in Sects. 1.3 and 1.5.

1.1.1 Elliptical galaxies

Elliptical galaxies contain mainly old red stars, which dominate their colours and spectra. They are surrounded by extended halos of hot ($\sim 10^7\text{K}$) ionised

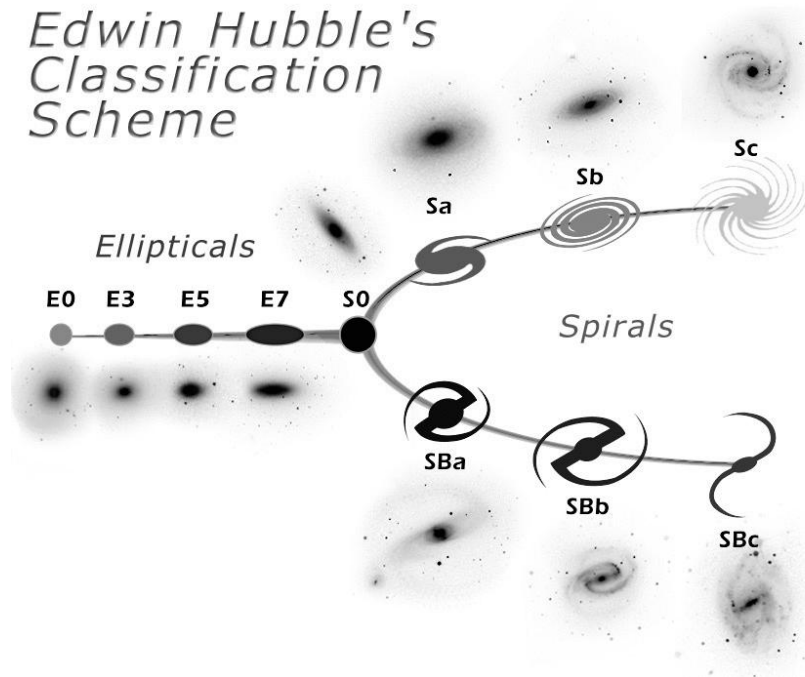


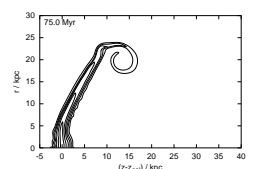
Figure 1.1: Hubble’s tuning fork diagram (according to Hubble 1926, 1936), displaying the classification of galaxies into ellipticals of different ellipticity (E0 to E7), lenticular galaxies (S0), barred spiral galaxies (SBa-c) and normal spiral galaxies (Sa-c). The irregular classes are not shown. (from <http://hubblesite.org/newscenter/newsdesk/archive/releases/1999/34/image/o>)

gas, but contain very little or no neutral or molecular gas. The lack of cool ISM as well as blue young stars shows that ellipticals do not form stars currently. In general, ellipticals are “pressure” supported systems, i.e. their dynamics are dominated by the irregular motion of the stars (in contrast to rotationally supported spirals).

1.1.2 Spiral galaxies

The appearance of a spiral galaxy is dominated by its thin disk (scale height ~ 300 pc), which contains most of the stars and the ISM. Inside this disk, blue young stars and the cold components of the ISM (dust, molecular and atomic gas; see Sect. 1.2) are concentrated towards the spiral arms. The life time of massive blue stars is short ($\sim 10^7$ yr), hence they are still near the location of their formation. This in turn means that SF takes place mainly in the spiral arms. Radial brightness profiles for the disks can be fitted well by exponential laws with scale lengths of about 3 to 4 kpc. In some galaxies, e.g. in the Milky Way, a further thick disk component (scale height ~ 1.5 kpc) can be distinguished. It is dominated by old stars.

The rotation of the disk prevents its gravitational collapse in radial direction. In vertical direction (perpendicular to the disk) the disk is “pressure”



supported. Observed rotation curves rise fast in the central region and remain flat at a constant level out to large radii. Rotation velocities range from 100 to 300 km s⁻¹ (220 km s⁻¹ for the Milky Way). The flatness of the rotation curve beyond the stellar disk cannot be explained by the visible mass alone. However, an extended spherical DM halo with a density $\propto 1/R^2$ would produce just such a rotation curve.

In addition to a disk, spiral galaxies also have a bulge and a stellar halo. The bulge is a small central elliptical component dominated by old stars. The stellar halo contains the globular cluster system of the galaxy. The globular cluster system does not show systematic rotation, it is “pressure” supported.

1.1.3 S0 galaxies

In the Hubble diagram S0 galaxies, which have smooth featureless disks, are placed between the ellipticals and the spirals. The bulges of S0s are larger than in spiral galaxies. The stars in S0s are old and red as in ellipticals. Moreover, also S0s lack substantial amounts of dust, molecular and atomic gas (see Sect. 1.2), though they are not completely free of cool ISM. E.g. molecular gas has been detected (see e.g. Welch & Sage 2003), but it is restricted to the central regions.

1.2 The interstellar medium

The ISM in our galaxy has been discovered by J. F. Hartmann 100 years ago (Hartmann 1904, see also review by Oetken & Scholz 2004). In a spectrum of the star δ Ori he found absorption lines that could originate from matter between the star and earth only, because these lines did not participate in the radial motions of the stellar spectrum. Since then the ISM has been studied extensively, but we are still far from understanding all details of how the ISM of a galaxy “works”. However, some basic knowledge has become widely accepted, so that fundamental properties of the ISM are described well in textbooks like Scheffler & Elsässer (1982), Binney & Merrifield (1998), Unsöld & Baschek (1999) and Bergmann & Schaefer (2002).

Despite the fact that ejecta from stars enrich the ISM with heavier elements, the bulk of the interstellar gas is hydrogen. Elliptical and spiral galaxies contain similar amounts of gas, but they differ in the structure of their ISM. In spiral galaxies molecular, atomic and ionised gas as well as dust can be found. Densities and temperatures cover many orders of magnitudes. In contrast, ellipticals contain mainly hot diffuse ionised gas at temperatures of a few 10⁶ K to 10⁷ K. Only few show small amounts of cooler gas and dust.

1.2.1 Components

Although the dynamic range of densities and temperatures in the ISM of spiral galaxies is enormous, the existing temperature-density combinations are not arbitrary. In fact, several thermal phases can be distinguished:

Cold molecular gas exists as molecular clouds (MCs). It cannot survive in the interstellar radiation field, where hydrogen molecules would be photo-dissociated immediately. Hence it is found in very dense regions (10^3 to 10^6 cm^{-3}) only, where the inner parts are concealed. Due to missing heating processes there the gas can cool to low temperatures (10 K to a few 10 K). Molecular hydrogen is difficult to observe, because it does not have spectral lines in the radio or infrared bands. Other lines (e.g. in the UV) are subject to strong interstellar extinction (explained below in connection with dust). Most observations of molecular gas use the CO molecule as a tracer. A further difficulty for observations arises because MCs are opaque in many wavebands, which limits the observations to the surface of the MCs.

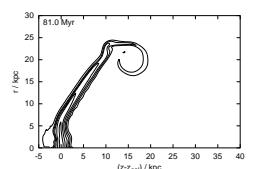
Probably molecular gas accounts for about 50% of the total ISM mass, but due to the high densities it occupies only a tiny fraction of the volume of the galaxy. The MCs are the sites of SF.

Neutral gas, or more correctly neutral hydrogen (HI^1), emits at the famous 21 cm line. This line originates from the hyperfine structure of the ground state in the H atom. The small energy difference between the two states in which proton and electron spin are either parallel or antiparallel corresponds to the radio wavelength of 21 cm. This “forbidden” transition has a low probability and therefore results in an intrinsically narrow line. This characteristic allows precise measurements of radial motions of neutral gas from Doppler-shifts and temperature measurements from line-broadening.

Neutral gas is found in a cool and a warm phase. The cool phase has a cloud-like or sheet-like structure. Typical temperatures and densities are 100 K and 30 cm^{-3} , respectively. The warm phase is more diffuse. Temperatures range from a few 1000 K to somewhat below 10^4 K. At the high temperature end of this range the gas is already partially ionised. Characteristic densities are about 1 cm^{-3} . The neutral gas has a volume filling factor of roughly 20 to 50%.

Warm ionised gas can be found in HII^1 regions and planetary nebulae. HII regions are centred around O and B stars, whose energetic radiation ionises the surrounding gas. The extent of an HII region, its Strömgen sphere, is the volume around the star that absorbs all ionising photons (energy higher 13.6 eV). Hotter stars provide a larger number of ionising

¹In the spectroscopic notation a neutral element A is referred to as “AI”, the element in its first ionisation step is denoted by “AII”, and so on.



photons and can ionise a larger volume. Radii of HII regions range from a few pc to about 100 pc. The mechanism in planetary nebulae is essentially the same, but the central object is a hot low-mass star in the final evolution phase on its way to a white dwarf. Planetary nebulae are smaller than 1 pc. Spectra of both HII regions and planetary nebulae show emission lines of hydrogen (e.g. the characteristic $H\alpha$ line) and helium as well as forbidden lines of heavier elements. These lines are an important cooling process in these regions.

Typical temperatures in this phase are somewhat below 10^4 K. Electron densities range from few 10 cm^{-3} to 10^4 cm^{-3} . The warm ionised gas fills about 20% of the disk volume.

Hot ionised gas is supplied by supernovae (SNe). The SN ejecta expand supersonically into the surrounding ISM and produce shock fronts that heat the gas to between 10^5 K and a few 10^6 K. Such high temperatures lead to thermal bremsstrahlung emission in soft X-rays and emission lines of highly ionised elements, e.g. carbon, silicon and oxygen. Observed densities in this ISM phase are about 10^{-3} cm^{-3} . Typical diameters for SN remnants are several 10 pc. The collective effect of several SNe in SF regions can produce super-bubbles with diameters of a few 100 pc. The hot ionised gas fills roughly 20% of the disk volume. In addition to that, SN also blow gas into the galactic halo, where the hot ionised gas may reach filling factors near 100%.

Dust is not exactly a thermal phase of the ISM, but it plays a crucial role. It manifests itself by absorption and reddening of the light of background objects (extinction). Extinction is observed mainly in optical and UV wavelengths, which gives a hint about the size of the dust grains. Deflection of electromagnetic waves of wavelength λ occurs on particles of the same size, so one can conclude that the typical size of dust grains is about $0.3\mu\text{m}$. The grains are mainly composed of graphite, silicate and ice. The dust is heated by the interstellar radiation field to 15-50K, but in the vicinity of hot stars the dust temperature can be a few 100K. According to its temperature dust emits in the far infrared. Around hot stars dust clouds can also be seen as blue reflection nebulae. At temperatures larger than 1800K the dust grains evaporate. In mass, the dust supplies only 1% of the ISM.

1.2.2 Distribution

The total mass of ISM ranges between a few percent up to 10 or 20% of the baryonic mass in a galaxy, where late-type spirals are more gas rich than early type ones. The ratio of total HI mass to molecular gas is also larger for late-type spirals. However, the mass of the molecular component in galaxies is still a matter of debate, as measurements rely on conversion factors between

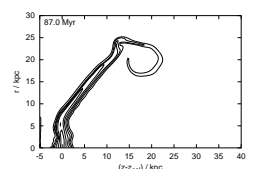
CO and H. E.g. Casoli et al. (1998) find that in most spirals the mass of the atomic gas exceeds the molecular mass. In mass, warm and hot ionised gas contribute a minor fraction to the ISM.

The distribution of the single ISM components is “not very tidy”. There are clouds, sheets, filaments, shells, supershells, bubbles (see e.g. Dickey & Lockman 1990 and references therein for a description of the HI component). Clouds or sheets of cool neutral gas are embedded in a diffuse matrix of warm and hot gas. Smoothing over large volumes leads to the following average picture: Most of the ISM (as well as the stars) is concentrated towards the disk plane. Inside the disk the radial distribution of stellar light, H α and molecular gas follow similar exponential profiles with scale radii of about 3 or 4 kpc. However, the exact distribution of molecular gas varies from galaxy to galaxy. HI extends to much larger radii than the optical disk. E.g. in the sample of Broeils & van Woerden (1994) the scale radius for the HI disks is $\gtrsim 6$ kpc, many galaxies even show nearly constant HI profiles. However, the HI profile truncates rather abruptly at a surface density of about 10^{19} cm^{-2} . This truncation is thought to be due to the fact that neutral hydrogen needs shielding from the cosmic radiation background to prevent its photoionisation. At surface densities lower than a certain limit no protective layer can be established, therefore the HI disk is truncated. Many early-type spirals show a depression in their HI profiles in the central few kpc. Inside the disk, the HI, dust and molecular gas as well as young blue stars are concentrated towards the spiral arms.

The vertical scale height depends on the component. Local fluctuations can be quite large (e.g. Dickey & Lockman 1990). Therefore only averages can be given. In our Milky Way at radii between 4-8 kpc, HI can be approximated by a composite distribution of a thick component with a scale height of 500 pc and a thin one with a scale height of about 150 pc (Dickey & Lockman 1990). In the central region the HI disk is flatter, whereas it flares and warps at larger radii. Such distortions are common features in other galaxies as well. The molecular gas and the dust are even more concentrated towards the disk plane than the HI. The warm ionised gas forms the Reynolds layer with a scale height of about 1.5 kpc (Reynolds 1989). If the galaxy has substantial SF, especially the hot ionised gas extends further into the galactic halo. However, all components known in the ISM in the disk have also been found in the galactic halo (see review by Dahlem 1997).

1.2.3 A crude physical model

Stars and the ISM form the galactic circle of life. Stars are formed out of the densest parts of the ISM. In turn, they produce important feedback on the gas by radiation and stellar mass loss, e.g. stellar winds or SNe. Even for a basic physical model such feedback mechanisms as well as cooling processes need to be taken into account.



	Hydrogen	Helium	metals	75% hydrogen, 25% helium	solar abundances
molecular	2	–	–	2.29	2.33
atomic	1	4	17	1.23	1.26
ionised	1/2	4/3	2	0.59	0.6

Table 1.1: Molecular weights μ : Mean particle mass in units of the proton mass for the different components (first three columns) and for two examples of element mixtures (last two columns). Please note that the values for metals are already approximations (see Vieser 2001).

Severing (1995) and Vieser (2001) give detailed discussions of relevant ionisation, recombination, heating and cooling processes, from which we just summarise the most important points here.

Ionisation processes: Hydrogen is ionised by photons of stellar radiation whose energy exceeds 13.6 eV. Examples are HII regions and planetary nebulae, which were discussed above. However, these regions absorb most of the ionising photons of their central stars, and therefore these ionisation mechanism can be neglected in the other parts of the ISM. Further photoionisation results from galactic and extragalactic X-rays. In addition to photoionisation also collisions with thermal electrons and cosmic particles have an ionising effect.

Recombination processes: The only relevant recombination process is radiative recombination, which is proportional to the electron density. Collisional recombination needs 3 collision partners, which is rare in low densities and can be neglected compared to radiative recombination.

If ionisation and recombination processes are assumed to be in equilibrium, for each combination of temperature and density a degree of ionisation can be calculated. If in addition the degree of dissociation of molecular gas is calculated from a temperature-dependent dissociation equilibrium (Black & Bodenheimer 1975), for all T - ρ pairs a mean particle mass (or molecular weight) μ can be calculated. The basic idea for the latter is to average over all existing particle species according to their masses and abundances. This is no trivial task as for an absolutely correct treatment all ionisation steps of all elements need to be taken into account. However, reasonable approximations can be done. Results for some instructive cases are listed in Table 1.1. The mass of the electrons can be neglected compared to the proton mass, however, electrons count as particles. Therefore e.g. for pure ionised hydrogen the mean molecular weight is 0.5. The resulting degree of ionisation and molecular weight are demonstrated in Fig. 1.2. For densities larger than 10^{-24} g cm $^{-3}$ dissociation occurs at temperatures around 10^3 K and ionisation takes place at temperatures between 10^4 K and $2 \cdot 10^4$ K.

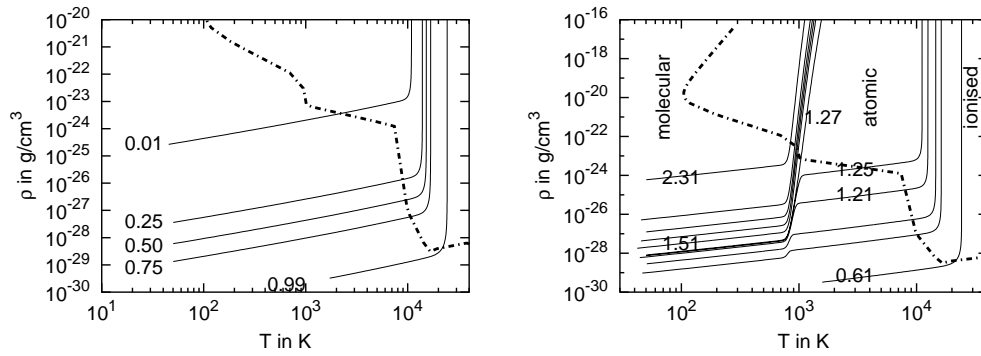


Figure 1.2: Isocontours of the degree of ionisation (**left**) and the mean particle mass μ (**right**), depending on temperature and density. The isocontours for the degree of ionisation are labelled. For μ isocontours at $\mu = 0.61, 0.81, \dots, 1.21, 1.25, 1.27, 1.51, 1.71, \dots, 2.31$ are plotted, the ones needed for orientation are labelled. The regions where the gas is molecular, atomic and ionised are marked. In both plots the thick dash-dot line shows the (T, ρ) pairs where the gas is in heating-cooling equilibrium (see Fig. 1.3).

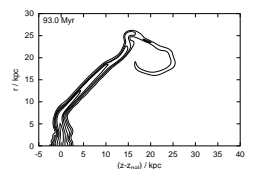
We note that the assumption of the ionisation equilibrium is an approximation only (see discussion in Vieser 2001). In the temperature range of 10^4 to 10^6 K cooling time scales are shorter than recombination time scales, which leads to a delayed recombination. The actual degree of ionisation is higher than the one calculated from the equilibrium.

Cooling: The ISM cools by emission of photons. In order to be effective, it needs to be optically thin for the emitted light. The overall cooling rate Λ is commonly written as

$$\Lambda(T, n) = n^2 \Lambda_0(T, n) \quad (1.1)$$

because the conversion of thermal energy into radiation is caused by collisional excitation and therefore Λ is proportional to n^2 . Ideally the cooling function Λ_0 depends on the temperature only. Each temperature regime is dominated by certain cooling processes.

For $T > 10^4$ K Böhringer & Hensler (1989) calculate a metallicity dependent cooling function for optically thin gas taking into account Bremsstrahlung, line emission of excited atoms and ions and continuous radiation due to recombination. Bremsstrahlung is due to acceleration of charged particles. The energy loss depends on the mass m of the accelerated particle as $\propto m^{-3/2}$. Hence electrons dominate this cooling process. The temperature dependence of the energy loss is $\propto T^{1/2}$. Bremsstrahlung dominates the cooling for $T > 10^7$ K. Radiation due to recombination of ions and electrons leads to a continuum emission and leaves excited atoms and ions behind. Due to further de-excitation these particles emit characteristic line spectra. Obviously this emission



depends on the metallicity. E.g. forbidden lines of oxygen, neon, sulphur and carbon play an important role for the cooling of HII regions. For the temperature range of $900 \text{ K} < T < 10^4 \text{ K}$ Dalgarno & McCray (1972) calculate the emission due to collisional excitation and subsequent line emission. In the low ISM densities collisional de-excitation plays a marginal role in most parts, it becomes important in dense molecular clouds only. Especially for this process metals are important, as they can be excited collisionally already at low temperatures. For temperatures below 900 K Falgarone & Puget (1985) calculate cooling rates due to emission of molecules while taking into account that dense molecular cores are not optically thin.

Collisions between dust and gas particles can exchange energy between these two components. Whether the gas is heated or cooled depends on the comparison of gas and dust temperature. However, Severing (1995) has shown that this process can be neglected in most cases.

Heating processes: There is a variety of heating processes in the ISM. One heating source is the absorption of stellar radiation. Photons with an energy $h\nu > 13.6 \text{ eV}$ ionise hydrogen. The excess energy is carried away by the free electron and thermalised by collisions. This process plays a role in HII regions only. Photons with $h\nu < 13.6 \text{ eV}$ can partially ionise metals and kick out electrons from dust particles. As explained above the excess energy of the free electrons is dispersed into the ISM by collisions. This photoelectric effect on dust particles dominates the heating at $T < 10^4 \text{ K}$.

A further effect connected with dust is the catalytic formation of H_2 at the surface of dust particles. Again the binding energy can be dispersed in surrounding ISM.

The ionisation of hydrogen by collisions with cosmic particles is accompanied by heating as the primary electrons distribute their excess energy into the ISM. This process is more effective in an ionised gas as more collisions are possible due to the higher particle density. Similarly the ionisation by X-rays is associated with heating. Both cosmic rays and X-rays together dominate the heating at $T > 10^4 \text{ K}$.

Due to viscous forces turbulence and other large-scale motions are converted into thermal energy. In addition, gas can be shock-heated. This could be treated explicitly in hydrodynamical simulations.

In Fig. 1.3 we plot isolines of heating and cooling rates \dot{e}_{heat} and \dot{e}_{cool} (where e is the internal energy density) in the T - ρ plane as they result from the processes explained above. Additionally the density-temperature pairs at which heating and cooling balance are marked with the heavy dashed-dotted line. In a similar plot (Fig. 1.4) we show isolines of heating and cooling time scales

$$\tau_{\text{cool}} = \frac{e}{\dot{e}_{\text{cool}}} \quad \text{and} \quad \tau_{\text{heat}} = \frac{e}{\dot{e}_{\text{heat}}}. \quad (1.2)$$

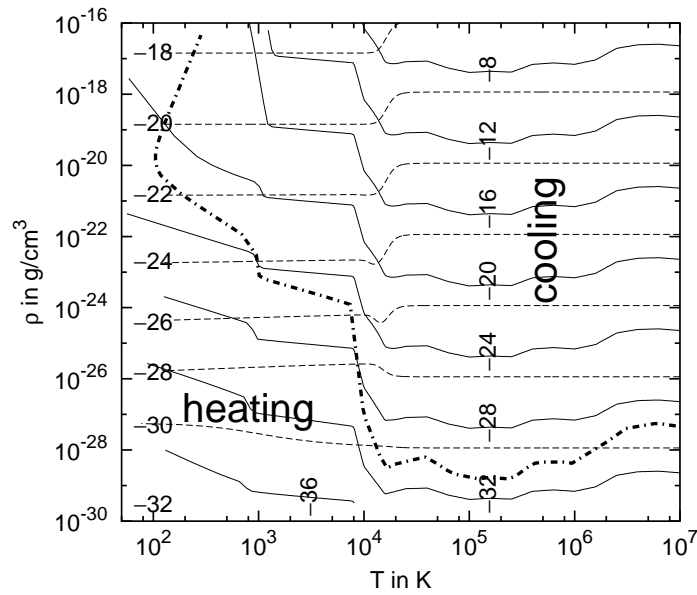
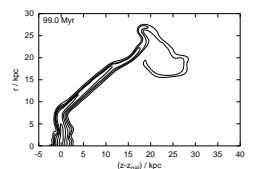


Figure 1.3: Isocontours for the heating (dashed lines) and cooling (solid lines) rates, depending on temperature and density. The isolines are labelled in units of $\log(\text{erg cm}^{-3} \text{s}^{-1})$. Upright labels are for the heating rate, rotated labels are for the cooling rate. The thick dashed-dotted line marks temperature-density pairs at which heating and cooling are in equilibrium. The regions where heating or cooling dominates are marked.

To prevent too much crowding in the figures, we show a third plot of the T - ρ plane (Fig. 1.5) where we mark the regions occupied by the ISM phases. For comparison, two isochores for $p = 10^{-13} \text{ erg cm}^{-3}$ and $p = 10^{-12} \text{ erg cm}^{-3}$ as well as the line of heating-cooling balance are given. A first thing to notice is that the cool and the warm neutral medium and the hot ionised medium are approximately in pressure equilibrium. In addition, also the magnetic energy density in the ISM is in rough equipartition with the thermal pressure. Magnetic fields can be measured from weak polarisation of light reflected on flat dust grains. In molecular clouds self-gravity plays a role, therefore their pressure is higher than the typical ISM value. The warm ionised medium (HII regions and PN) also show an overpressure due to the fact that these regions are expanding. In addition to pressure equilibrium, a basic model also expects thermal equilibrium, the gas phases should be situated along the line marking heating-cooling balance. However, for the thermal equilibrium line shown in Fig. 1.5 neither the heating process in HII regions nor the shock-heating (SN) relevant for the hot ionised medium were taken into account. Therefore in this plot these two phases must be on the cooling side of the equilibrium line. As a rough estimate, a typical SN energy of 10^{51} erg distributed over a volume of $4/3\pi(100 \text{ pc})^3$ during 10^6 yr (typical life time of a SN remnant and its final size) leads to an averaged heating rate of $2.6 \cdot 10^{-25} \text{ erg cm}^{-3} \text{ s}^{-1}$. This easily accounts for the cooling rate



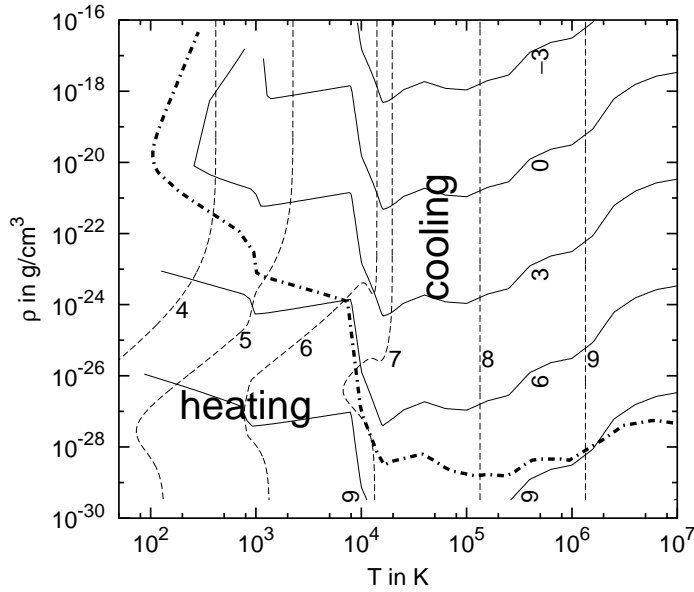


Figure 1.4: Isocontours for the heating (dashed lines) and cooling (solid lines) time scales, depending on temperature and density. The isolines are labelled in units of $\log(\tau/\text{yr})$. Upright labels are for the heating time scale, rotated labels are for the cooling time scale. The thick dashed-dotted line marks temperature-density pairs at which heating and cooling are in equilibrium. The regions where heating or cooling dominates are marked.

calculated for the hot ionised medium. More precisely, an additional heating rate of about $3 \cdot 10^{-27} \text{ erg cm}^{-3} \text{ s}^{-1}$ would put the hot ionised gas in thermal equilibrium. The heating processes calculated also did not include the fact that MCs are optically thick, which means that many heating processes are not valid inside them. This explains why MCs are situated on the heating side in Fig. 1.5. Moreover, we already noted that the assumed ionisation equilibrium does not describe the situation completely. The cooling depends strongly on the particle density, therefore also the given cooling rates are a first approximation.

The picture for the ISM arising from assuming pressure and thermal equilibrium is one of clouds of cool neutral gas embedded in a hot ionised medium, where the warm neutral medium provides a boundary layer. This is the famous 3-phase model of McKee & Ostriker (1977). Despite the success of equilibrium models, recent work, e.g. high resolution magneto-hydrodynamics simulations of Breitschwerdt (2004), stress the importance of non-equilibrium effects. Also MCs are considered a rather transient phenomenon by e.g. Ballesteros-Paredes (2004) and Monaco (2004) and are expected to be destroyed by the stars that form inside them on a time scale of a few Myr.

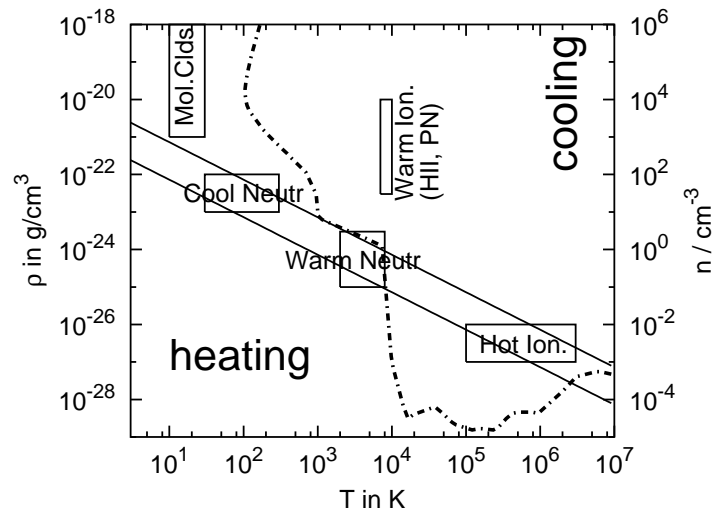


Figure 1.5: ISM phases in T - ρ -plane. Typical temperature-density regions for the ISM phases are marked by boxes and labelled. The thick dashed-dotted line marks temperature-density pairs at which heating and cooling are in equilibrium. The regions where heating or cooling dominates are marked. The diagonal solid lines are lines of constant thermal pressure ($p = 10^{-13} \text{ erg cm}^{-3}$ and $p = 10^{-12} \text{ erg cm}^{-3}$). A similar plot can be found in Turner (1989).

1.3 Clusters and groups of galaxies

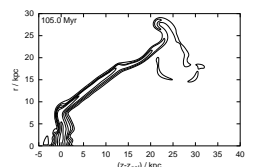
Galaxy clusters are assemblies of 50 to a few thousand galaxies. They are bound structures with radii of a few Mpc. Besides galaxies, clusters also contain intracluster medium (ICM), a hot tenuous gas of temperatures between 10^7 and 10^8 K. The observed galaxy masses and ICM mass add up to only some tenth of the virial mass (see Appendix A.3) in clusters ($\sim 10^{15} M_{\odot}$). Again DM is suggested to solve the puzzle of the missing mass.

Groups of galaxies are assemblies of a few up to some ten massive members and additional dwarf galaxies. Total group masses are about a few times $10^{13} M_{\odot}$.

1.3.1 Classification

Galaxy clusters can be classified according to their richness, concentration, regularity and galaxy contents. They divide mainly into two types (cases in between are possible) (Bergmann & Schaefer 2002; Unsöld & Baschek 1999):

Regular clusters are usually compact, spherical and concentrated. Nearby regular clusters contain about one third ellipticals, 45% S0s and 20% spirals (this changes with redshift, see Sect. 1.5.1). A giant elliptical or cD (supergiant elliptical with extended envelope) galaxy can be found in the very centre. Also the X-ray appearance of this kind of clusters



is smooth and centrally concentrated. Regular clusters are X-ray luminous. The prototype of this class is the Coma cluster with a few thousand members.

Irregular clusters do not show a clear concentration towards their centre. They are not symmetrical. Sometimes there is more than one peak in the galaxy number density. Also the X-ray appearance is patchy. The X-ray luminosity and ICM temperature are lower than that of regular clusters. Irregular clusters contain about 50% spiral galaxies, one third S0s and one sixth ellipticals. An example of this class is the Virgo cluster.

The classification becomes more difficult with increasing distance of a cluster, because due to the reduced resolution also irregular clusters can appear regular.

Mulchaey et al. (1996a,b) classify galaxy groups into S-rich (spiral-rich) and E/S0-rich (E for elliptical) according to the morphology of their giant galaxies. E/S0-rich groups tend to be more massive and to contain more galaxies than S-rich groups. As a consequence the temperature of a possible intergalactic medium and its X-ray luminosity is expected to be higher in E/S0-rich groups. The latter have indeed been detected in X-rays, whereas the observation of the group medium in S-rich groups proves difficult.

1.3.2 The intracluster medium

In recent years there has been a number of good reviews about the ICM in clusters (a classic book: Sarazin 1988; Schindler 2003, 2004; Molendi 2004; about chemical composition: Loewenstein 2004) as well as in groups of galaxies (Mulchaey 2000, 2004). In this section we summarise the relevant knowledge about the ICM briefly. For more details please refer to the reviews and references therein.

The ICM reveals itself by X-ray emission. It can be detected in nearly all clusters. Two examples are shown in Fig. 1.6, namely the Coma and the Virgo cluster. The Coma cluster is fairly regular, whereas the Virgo cluster shows significant substructure. The diffuse emission indicates that the whole cluster is filled with gas. With today's instruments the ICM can be traced out to 1-2 Mpc from the cluster centre. According to spectroscopic studies, the main part of the X-ray emission is due to continuous thermal bremsstrahlung of the highly ionised hot gas. Only a small part is line emission. Derived ICM temperatures are about a few 10^7 K to 10^8 K. Typical particle densities are about 10^{-4} cm^{-3} to 10^{-2} cm^{-3} . The density decreases towards the outer regions of the clusters. At least in the inner parts the temperature profile is approximately flat. The ICM is no primordial gas, as it has a metallicity of about 0.4 times solar (where relative abundance patterns depart from solar or galactic characteristics).

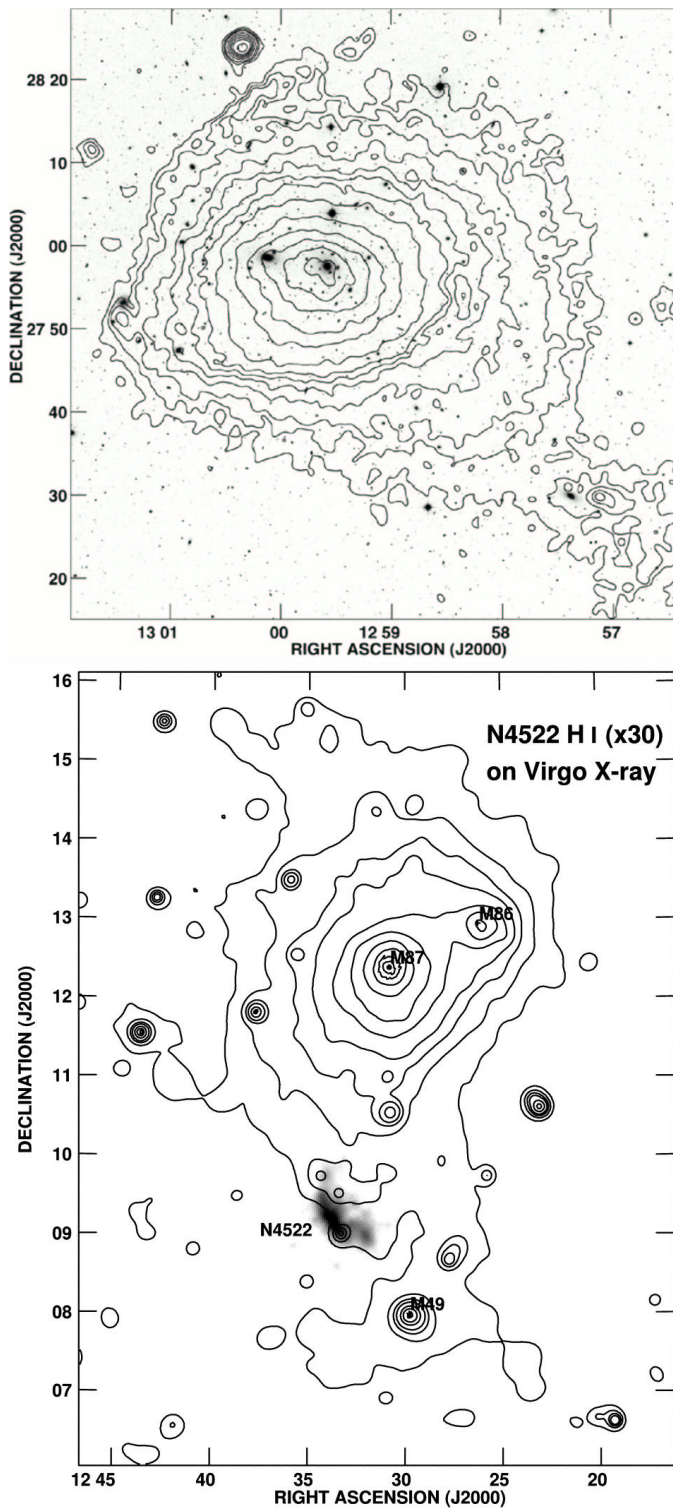
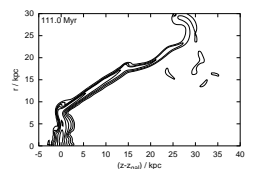


Figure 1.6: X-ray contour images of the Coma (top) and Virgo cluster (bottom), both from ROSAT. The Coma picture (taken from Burns 1998) spans about $(1^{\circ}10')^2$, which corresponds to about $(2.4 \text{ Mpc})^2$. The X-ray contours are overlaid onto an optical image of the Palomar Observatory Digital Sky Survey. The Virgo picture (taken from Kenney et al. 2004 who took the X-ray contours from Bohringer et al. 1994) spans about $7.5^{\circ} \times 10^{\circ}$, which corresponds to about $2.3 \text{ Mpc} \times 3 \text{ Mpc}$. The position of the giant ellipticals M87, M86 and M49, which are associated with subclusters, are marked. In addition, a gray-scale HI image of NGC 4522 is plotted in its position but magnified by a factor of 30 (see Sect. 1.5.3 and Figs. 1.9 and 1.10).

The galaxies as well as the ICM of a cluster both respond to the same gravitational potential. Therefore there should be a relation between their density distributions and typical velocities. This is indeed the case. The relation between the line-of-sight velocity dispersion of the cluster galaxies



σ_{gal}^2 and the typical velocity of ICM particles

$$\sigma_{\text{ICM}}^2 = 3kT_{\text{ICM}}/\mu m_{\text{H}} \quad (1.3)$$

(where μ is mean molecular weight and m_{H} is proton mass) is commonly expressed by the parameter β

$$\beta = \frac{\sigma_{\text{gal}}^2}{\sigma_{\text{ICM}}^2} = \frac{\mu m_{\text{H}} \sigma_{\text{gal}}^2}{3kT_{\text{ICM}}}. \quad (1.4)$$

In clusters, both σ_{gal} and σ_{ICM} (as well as the ICM sound speed) are of the order of 1000 km s^{-1} . Interpreting these velocities as virial velocities (see Appendix A.3) in a spherical cluster potential, the total cluster mass must be about 10^{14} to $10^{15} M_{\odot}$. Strictly speaking, this estimate can be applied to relaxed (virialised) spherical clusters only, but it yields reasonable results also for slightly elongated relaxed clusters. Most of the total mass has to be attributed to dark matter. The ICM contributes 15 to 20% to the total cluster mass. The galaxies contribute a few percent only.

As mentioned above, the ICM is highly ionised, hence we deal with a plasma. For densities and temperatures typical for the ICM, according to Spitzer (1956) the mean free path λ_{fp} for the ions as well as for the electrons is

$$\lambda_{\text{fp}} \approx 23 \text{ kpc} \frac{(T_{\text{ICM}}/10^8 \text{ K})^2}{(n_{\text{ICM}}/10^{-3} \text{ cm}^{-3})}. \quad (1.5)$$

This is much smaller than the cluster size, therefore the ICM is commonly described by fluid dynamics. The self-relaxation time scale for the electrons is (see also Spitzer 1956)

$$\tau_{\text{relax}}^{ee} \approx 3.3 \cdot 10^5 \text{ yr} \frac{(T_{\text{elec}}/10^8 \text{ K})^{3/2}}{(n/10^{-3} \text{ cm}^{-3})}, \quad (1.6)$$

the time scale for electrons and protons to reach equipartition ($T_{\text{prot}} = T_{\text{elec}}$) is longer by a factor of the ratio of proton mass to electron mass $m_{\text{prot}}/m_{\text{elec}}$

$$\tau_{\text{relax}}^{pe} \approx \frac{m_{\text{prot}}}{m_{\text{elec}}} \tau_{\text{relax}}^{ee} = 6 \cdot 10^8 \text{ yr} \frac{(T/10^8 \text{ K})^{3/2}}{(n/10^{-3} \text{ cm}^{-3})}. \quad (1.7)$$

Molendi (2004) stressed that the ICM is a magnetised plasma with typical magnetic field strengths of 0.1 to a few μG . However, the magnetic pressure associated with these fields is small compared to the thermal pressure. The magnetic fields do not drive the general dynamics of the ICM. Nevertheless they may be important for other effects. E.g. due to the small electron gyration radius of

$$\lambda_{\text{gyr}} \sim 7 \cdot 10^{-14} \text{ kpc} \left(\frac{B}{\mu\text{G}} \right)^{-1} \left(\frac{T}{10^8 \text{ K}} \right)^{1/2} \quad (1.8)$$

thermal conduction in the ICM could be suppressed.

Due to the thermal emission the ICM should cool, but its cooling time scale

$$\tau_{\text{cool}} \sim 8.5 \cdot 10^{10} \text{ yr} \left(\frac{n_{\text{prot}}}{10^{-3} \text{ cm}^{-3}} \right)^{-1} \left(\frac{T}{10^8 \text{ K}} \right)^{1/2}, \quad (1.9)$$

is longer than the age of the universe. For the typical temperatures of the ICM and the cluster size D_{cluster} a sound wave crosses the cluster on a time scale of

$$\tau_{\text{sound}} \sim 6.6 \cdot 10^8 \text{ yr} \left(\frac{D}{\text{Mpc}} \right) \left(\frac{T}{10^8 \text{ K}} \right)^2. \quad (1.10)$$

As this time scale is typically smaller than the cooling time scale, at least to first approximation the ICM is assumed to be in hydrostatic equilibrium. Number counts show that the galaxy number density $g_{\text{gal}}(r)$ in regular clusters follows the profile of a self-gravitating, isothermal sphere, which can be approximated analytically by the King-profile:

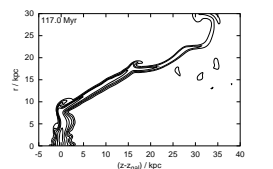
$$n_{\text{gal}}(r) = n_{\text{gal}0} \left[1 + \left(\frac{r}{r_c} \right)^2 \right]^{-3/2}, \quad (1.11)$$

where $n_{\text{gal}0}$ is the central density and r_c the core radius. Under the assumption that the cluster gas is in hydrostatic equilibrium, the ICM density profile $n_{\text{ICM}}(r)$ should be related to the galaxy density by

$$n_{\text{ICM}}(r) = n_0 \left[1 + \left(\frac{r}{r_c} \right)^2 \right]^{-3/2\beta} \propto n_{\text{gal}}^\beta. \quad (1.12)$$

This description is referred to as the “standard- β -model”. It has been applied successfully to many clusters. Results from fits to observations of 30 to 50 clusters for the central density n_0 , scale radius r_c , the parameter β and ICM temperatures are given e.g. in Mohr et al. (1999) and Matsumoto et al. (2000). A typical value for β is about $2/3$. Particle density profiles for a standard isothermal sphere and for the Coma and the Virgo cluster are given in Fig. 1.7. The Virgo cluster is irregular and still in the phase of relaxation. Therefore the fit for the Virgo cluster has to be treated with care. Hence its profile is plotted out to a radius of 1 Mpc only. There are clusters where the ICM can be described more successfully by multiple-temperature models (see e.g. Lieu 2000; Ikebe et al. 1999).

In about 50% of the galaxy groups an intra-group medium has been detected by X-ray observations. Nearly all detected groups contain a central elliptical galaxy. If smaller, spiral-only groups like our own Local group contain an intra-group medium, the expected temperature would be a few times 10^6 K, which would be hard to detect with today’s X-ray instruments. The X-ray morphology of detected groups is mostly regular, they appear relaxed.



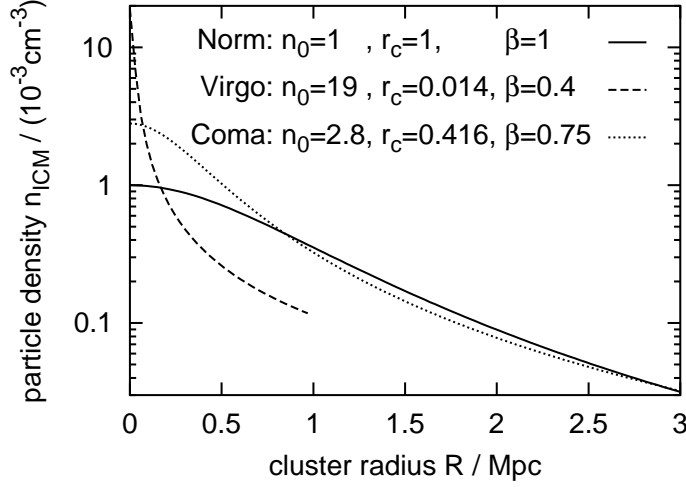


Figure 1.7: ICM particle density profiles for Coma and Virgo cluster according to Eq. 1.12. The central density n_0 is given in units of 10^{-3} cm^{-3} , the core radius r_c in Mpc. Parameters are taken from Matsumoto et al. (2000). For comparison we also show a profile with normal values $n_0 = 1 = r_c = \beta = 1$.

	clusters	groups
particle density n_{ICM}	10^{-4} to 10^{-2} cm^{-3}	
temperature T_{ICM}	3 to 10 keV	0.3-2 keV
	$3.5 \cdot 10^7 \text{ K}$ to $1 \cdot 10^8 \text{ K}$	about 10^7 K
extent D_{cluster}	few Mpc	0.1 to 1 Mpc
metallicity	about 0.4 solar	about 0.2 solar
gas mass fraction	15 to 20%	2 to 10%
galaxy mass fraction	3 to 5%	3 to 20%

Table 1.2: Typical conditions in the ICM for galaxy clusters and groups.

However, a simple isothermal model is usually not a good fit. More successfully the X-ray emission can be fitted by a combination of one isothermal model for the central galaxy plus a second more extended component. The gas temperature in groups is lower than in clusters.

Table 1.2 summarises typical ICM conditions in clusters as well as in groups. For simplicity we use the abbreviation ICM for the intra-group medium, too.

1.4 Environmental effects

Only about 1% of all galaxies are isolated (field galaxies), most galaxies are found in groups, about 5% are found in rich clusters (see e.g. Combes et al. 1995). These numbers suggest that the environment may play an important role in the evolution of galaxies. Especially in dense clusters the relative

distances between galaxies are much less than e.g. the relative distances between stars inside a galaxy. In dense clusters there can be as much as some 100 galaxies per Mpc^3 , which corresponds to a mean distance of 150 kpc to 300 kpc. Typical diameters of disk galaxies are 30 kpc, which means the average separation is just 5 to 10 times their diameter. In contrast, even in globular clusters where mean distances between stars are about 0.04 pc, this separation is still 10^5 times a typical stellar diameter.

In this section we introduce theoretical ideas how the environment can influence galaxies. We divide the processes into gravitational or tidal interactions and gas interactions, i.e. the interplay between the ICM and the ISM.

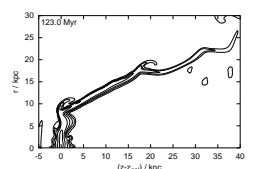
1.4.1 Gravitational interactions

Galaxies in clusters or groups can interact gravitationally with fellow cluster (or group) members as well as with the overall cluster potential. Encounters between galaxies are also known for field galaxies, however, relative velocities are much lower than in clusters. Slow encounters have rather long time scales and can result in merging. In contrast, due the short interaction time scale associated with fast encounters a single event is not expected to have strong consequences for the galaxies.

Slow encounters – mergers

During a slow encounter between two disk galaxies the mutual tidal fields disturb the stellar contents as well as the gas (see review by Mihos 2004 and references therein). The dynamically cold stellar disks are heated up. The gas is compressed and shocks are induced that in turn trigger SF. Bar instabilities can be produced, and inflowing gas can lead to (nuclear) star bursts or active galactic nuclei. A part of the material is stripped into long tails and bridges. Such structures could already be reproduced in the pioneering simulations of Toomre & Toomre (1972) despite the simplicity of their models. Most of the material in the tidal debris is not unbound, although it can be ejected to large distances. It falls back to the remnants over a long time.

The structure of the remnant galaxies after the collision depends on the orbits (impact parameter and velocity) as well as on the relative masses. In close encounters dynamical friction leads to merging of the partners. Violent relaxation after a major merger of equal mass disk galaxies destroys the dynamically cold disks and produces a kinematically hot remnant that resembles a field elliptical. The remnant of an unequal mass merging could resemble a field S0, where like in the previous case the gas has been consumed in the induced star burst. Minor mergers or the accretion of small satellite galaxies destroy the satellites but not the massive partner. However, also in the massive partner the disk heats up.



Slow encounters were considered negligible in galaxy clusters due to the high velocity dispersion of cluster galaxies. However, as stressed by Mihos (2004), cluster formation is a hierarchical process, where galaxy groups merge with clusters. Inside the groups the velocity dispersion is significantly smaller, so that slow or medium-velocity encounters play a role. Examples of directly interacting galaxies in nearby clusters are known (see review by Mihos 2004). In contrast to the long-lived tidal tails in the field, the additional cluster potential destroys such debris. These features can thus be observed for very recent cases only.

Harassment

The fast encounters in clusters were thought to have only negligible effects on galaxies due to their short time scale. However, the work of Moore et al. (1996, 1998, 1999) demonstrated that harassment, i. e. the cumulative effect of frequent close high velocity encounters and the overall tidal field of the cluster, can well transform the morphology of cluster galaxies. In this context frequent, high velocity and close encounter mean about once per Gyr, a relative velocity of $\sim 1500 \text{ km s}^{-1}$ and an impact parameter of $\sim 50 \text{ kpc}$, respectively. This process produces distorted galaxies with enhanced star formation rates (SFRs) all over the cluster. However, due to the high velocity the effects become visible some time after the interaction, so that often the second partner cannot be identified.

Harassment affects low and high surface brightness galaxies (LSB and HSB galaxies) differently. LSB galaxies have extended disks and less deep potential wells, so that they evolve dramatically. They lose up to 90% of their stars that form large diffuse tails. The remnants resemble dwarf ellipticals or dwarf spheroidals, which are the most common galaxy type in today's relaxed clusters. In HSB galaxies the disks are well inside their tidally limited DM halos. They lose only a small amount of their stars, but their disks thicken substantially and spiral features are extinguished. They could resemble S0 galaxies.

1.4.2 Gas interactions

In contrast to gravitational interactions, which affect all galaxy components, gas interactions do not influence the distribution of the stars. Only the SF activity and the stellar population can be influenced as gas is the raw material for SF.

Ram pressure stripping

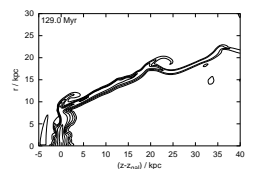
Galaxies move through the ICM with velocities similar to the ICM sound speed and experience a ram pressure $p_{\text{ram}} = \rho_{\text{ICM}} v_{\text{ICM}}^2$ (ρ_{ICM} is the ICM density and v_{ICM} the relative velocity between the galaxy and the ICM). In

order to estimate whether the ram pressure could remove gas from the disks in the face-on case, Gunn & Gott (1972) compared p_{ram} with an average gravitational restoring force per unit area $f_{\text{grav}} \sim 2\pi G \Sigma_* \Sigma_{\text{gas}}$ and found that p_{ram} could well exceed f_{grav} in inner regions of clusters. The estimate has been extended by using a radius dependent restoring force $f_{\text{grav}}(r) = \left| \frac{\partial \Phi}{\partial z} \Sigma_{\text{gas}}(r) \right|$ to infer the radius of the remaining gas disk. At a given radius r , $\frac{\partial \Phi}{\partial z}$ is the gradient of the local gravitational potential Φ in z -direction (perpendicular to the disk) and $\Sigma_{\text{gas}}(r)$ is the local gas surface density. The straightforward idea is that in the case of a face-on motion gas will be stripped at outer radii where

$$\rho_{\text{ICM}} v_{\text{ICM}}^2 = p_{\text{ram}} > f_{\text{grav}}(r) = \left| \frac{\partial \Phi}{\partial z} \Sigma_{\text{gas}}(r) \right|. \quad (1.13)$$

Due to its nature this process is referred to as ram pressure stripping (RPS) or ram pressure pushing. Commonly this process is transferred to the rest frame of the galaxy, so that the relative motion translates into an ICM wind.

First attempts to simulate RPS of disk galaxies have been made by Farouki & Shapiro (1980) and Toyama & Ikeuchi (1980), but these works were limited to low resolution and short run times due to weaker computational power. Later studies with better resolution (e.g. SPH simulations by Abadi et al. 1999, Schulz & Struck 2001 and 3D Eulerian hydro simulations by Quilis et al. 2000) performed a few simulations of massive disk galaxies in constant mostly face-on winds. The simulated winds were representative for the conditions in cluster centres, where the galaxies suffered substantial gas loss. In general, previous works found that the outer gas disks are stripped on a short time scale (few 10Myr to few 100Myr), and that the radius of the remaining gas disks agrees with the estimate derived from Eq. 1.13. Schulz & Struck (2001) used longer run times and found a long phase of turbulent viscous stripping following the rather short RPS phase. This phase was also noted by Quilis et al. (2000), although these authors used only run times of about 100 Myr. This viscous stripping works on galaxies that are oriented inclined or edge-on towards the wind as well as on face-on oriented ones. The RPS phase seems to take longer for inclined cases, but it can be suppressed completely for strict edge-on cases only (Quilis et al. 2000; Schulz & Struck 2001; Marcolini et al. 2003). Quilis et al. (2000) emphasised that gas disks are not homogeneous but porous and tried to model this feature by inserting holes in the disk. In such cases the turbulent viscous stripping was more effective. Vollmer et al. (2001b) applied a sticky particle code to simulate the passage of disk galaxies through clusters, stressing the fact that in reality the galaxies experience a rapidly changing ICM wind instead of a constant one. Consequently, the stripping is a distinct event. Moreover, during this event not all displaced gas is unbound, and up to 10% of the initial gas mass fall back to the disk. The sticky particle code does not model the ICM-ISM interaction hydrodynamically but describes the ram pressure by applying an additional force to each particle “seen” by the wind. Therefore



it misses e.g. turbulent viscous stripping. In further papers (Vollmer et al. 2000, 2001a, 1999; Vollmer 2003) this group tried to explain the features of individual galaxies by comparing simulations with observations and specifying the ram pressure, inclination angle and the moment of the stripping event. Marcolini et al. (2003) simulated RPS of disk dwarf galaxies in poor groups, where the ICM densities and hence ram pressures are weaker than in clusters. First attempts to take into account magnetic fields have been made by Otmianowska-Mazur & Vollmer (2003), who calculated magnetic fields for the gas distributions and velocity fields taken from Vollmer et al. (2001b).

In addition to RPS of disk galaxies also the ICM-ISM interaction for elliptical galaxies has been studied (Gisler 1976; Lea & Young 1976; Takeda et al. 1984; Portnoy et al. 1993; Toniazzi & Schindler 2001). Ellipticals lack cool gas, although during their life times gas replenishment by stars should accumulate a substantial amount of ISM. The idea studied was that RPS could keep ellipticals gas free despite the ongoing gas replenishment. In addition, Stevens et al. (1999) and Acreman et al. (2003) used the most simple setup of a spherical galaxy to predict observable features of bow shocks and gas tails.

Viscous stripping

Ram pressure pushing and viscous stripping cannot be separated easily as they occur simultaneously. Only in cases of strict edge-on motion the pushing contribution is small and viscous stripping may dominate. Nonetheless Nulsen (1982) estimated mass loss rates due to a turbulent viscous flow past spherical galaxies and found that under certain conditions the loss rates can be comparable to the RPS rates.

Starvation/Strangulation

A galaxy with $\sim 2 \cdot 10^9 M_{\odot}$ of gas and a SFR of $\sim 2 M_{\odot} \text{ yr}^{-1}$ would have consumed its gas within $\sim 1 \text{ Gyr}$. Even if stellar mass loss returns half of the consumed material to the ISM, the gas supply would be exhausted after some Gyr. Therefore Larson et al. (1980) suggested that galaxies are surrounded by a (hot) gas reservoir that replenishes gas in the disk. However, these reservoirs could be stripped even by low ram pressures characteristic for the outskirts of clusters. Subsequently galaxies run out of raw material, SF suffers starvation or strangulation. More recent observations by Balogh & Morris (2000) and Balogh et al. (2000) indicate that strangulation may play an important role in producing systematic differences between field and cluster galaxies concerning SF and colours (see Sect. 1.5).

Bekki et al. (2002) simulated such halo stripping using an N-body code and modelling RPS by an additional force applied to the particles. They found that even galaxies orbiting outside 3 cluster core radii lose about 80% of their halo gas in a few Gyr.

Thermal conduction

The galaxies are embedded into the hot ICM. One may ask if thermal conduction can evaporate the galactic gas disks. This depends on the interplay between energy input by thermal conduction and energy loss by radiative cooling. Cowie & McKee (1977) and McKee & Cowie (1977) studied this process for spherical clouds embedded in a hot medium and presented analytical estimates of evaporation rates and survival times. Cowie & Songaila (1977) applied these results to a disk-like system and found that under representative ICM conditions a typical spiral galaxy should evaporate in 100 Myr. Analytical estimates of Fujita (2004) yield much longer time scales. None of the analytical estimates could treat the multi-phase structure of the ISM.

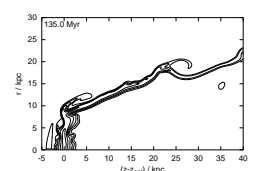
1.5 Galaxies in different environments

After having explained the theory how the environment could affect galaxies, we now give an overview of observational facts. Nearby galaxies and clusters can be studied in great detail. In addition, in recent years large surveys like the Sloan Digital Sky Survey (SDSS, York et al. 2000) and the two degree field survey (2dF, Colless et al. 2001, 2003) containing a few hundred thousand galaxies were presented. They allow comparisons between galaxies in different environments with high statistical significance. However, such large samples face the difficult task of automated classifications.

1.5.1 Colours, morphology and star formation rates

According to the picture that arose in the last years and decades, the galaxy population in the nearby universe (redshift $z < 0.1$) changes in colours, morphological mix and SFRs with environment in the sense that in dense environments blue, late-type and star forming galaxies are less common than in low-density environments. Hence these relations are termed colour-density (see Pimbblet 2003 and references therein), morphology-density (Dressler 1980) and SFR-density relation. At least for regular clusters the galaxy number density translates into a cluster-centric radius, and it is still a matter of debate if the cluster-centric radius or the local density is the more important parameter. Therefore also the colour-radius, morphology-radius and SFR-radius relations are studied.

Goto et al. (2003c) studied about 8000 galaxies at $z < 0.1$ from the SDSS and used automated morphology classifications. Galaxies were classified either by central concentration (more concentrated galaxies are classified as late-type) or by their coarseness (see Goto et al. 2003c), where late and early-type disks, early-type galaxies and intermediate types (mostly S0 galaxies) are distinguished. Gómez et al. (2003) (8600 galaxies) and Lewis et al. (2002) (11,000 galaxies) studied the SF activity of galaxies in the SDSS and



2dF catalogues, respectively. These works find three characteristic regimes in the nearby universe ($z < 0.1$):

Sparse regions: In regions with a projected galaxy number density below 1 Mpc^{-2} or outside 1 virial radius around clusters neither the morphology-density nor the SFR-density relation are distinct. Values converge towards the field population.

Intermediate regime: In regions with projected number density between 1 and 6 Mpc^{-2} or between 1 and 0.3 virial radii around clusters, the fraction of intermediate-type galaxies increases and the fraction of late-type galaxies decreases with increasing density. Along with that, the distribution of SFRs shifts towards lower values with increasing density. Especially galaxies with strong star formation vanish.

High-density regime: In the inner 0.3 virial radii of clusters or at densities above 6 Mpc^{-2} the trend in the SFR distribution continues. Concerning morphologies, here the intermediate-type fraction decreases and the early-type fraction increases.

Despite high-tech instruments such observations are still restricted to bright (massive) galaxies. Results from observations of dwarf galaxies in nearby clusters indicate that in general also dwarf galaxies change with increasing local density (transition from gas rich, star forming late-type irregulars to gas poor spheroidals, see e.g. Binggeli et al. 1990; Davies 2004).

Goto et al. (2003c) suggest that two different mechanisms are at work that change the populations in the intermediate and the high-density regime. Interestingly, Goto et al. (2003a) find passive spirals (confirmed to be passive spirals and neither misclassified S0 or dusty starburst galaxies by Yamauchi & Goto 2004) in the transition region between the low and the intermediate density regime. They suggest that the passive spirals are the link between red elliptical/S0 in low redshift clusters and blue spirals in high redshift clusters.

In addition to the dependence of the galaxy population on the environment in the nearby universe, the population also changes with redshift. The most famous example is the Butcher-Oemler effect (Butcher & Oemler 1978a,b, 1984, 1985; Butcher et al. 1983), the increase of the fraction of blue galaxies inside clusters with redshift. Despite the large scatter in this correlation, it has been confirmed in recent studies (e.g. Goto et al. 2003b; Margoniner et al. 2001; De Propris et al. 2004). However, the origin of the large scatter remains unclear. Margoniner et al. (2001) suggested that it arises due to a correlation between cluster richness and blue fraction (richer clusters having a smaller blue fraction of galaxies), but De Propris et al. (2004) could not confirm that.

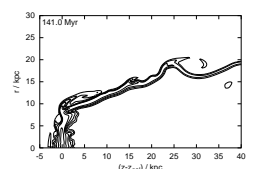
The influence of the environment on galaxies seems not to be limited to clusters but seems to work in galaxy groups as well, if the local density

exceeds the limit (Balogh et al. 2004; Martínez et al. 2002; Helsdon & Ponman 2003).

Nearby clusters can be studied in more detail. E.g. Schindler et al. (1999) find a similar distribution of galaxies (all types) and X-ray emitting ICM in the Virgo cluster. But the distribution of late-type galaxies is more extended and the early-types are concentrated to the cluster centre, which again reflects the known trend that late-type galaxies are more common in low-density regions. $H\alpha$ and R-band imaging and photometry of bright Virgo spirals allowed Koopmann & Kenney (1998, 2004a,b) and Koopmann et al. (2001) to study the spatial distribution of SF in cluster galaxies. They found that 52% of the bright Virgo spirals have sharply truncated $H\alpha$ -disks (whereas only 12% of the field sample have). Most of these $H\alpha$ -truncated spirals have relatively normal stellar disks. As $H\alpha$ is a tracer of massive SF, the authors conclude that the global reduction of SF in cluster galaxies is mainly due to a truncation of SF, i.e. SF is suppressed in the outer disk regions, but normal or even enhanced in the inner disk. These observations favour RPS as an important process. Gavazzi et al. (2002) also studied the SF in Virgo spirals and found that galaxies with quenched SF coincide with significant gas deficiency (see Sect. 1.5.2).

Aguerri et al. (2004) investigated structural parameters of 116 Coma galaxies and found that Coma spirals have smaller disks than field spirals. The disk size decreases towards the cluster centre. The bulges are not affected. The bluest spirals are located at larger distances from the cluster centre and show a larger velocity dispersion. The authors interpret these findings as results from harassment.

Poggianti (2003) summarises results of spectroscopic observations which aimed not only on the current SF, but also on the SF history of cluster galaxies. In the Coma, Fornax and Abell 2218 clusters the spectra revealed that more than 40% of the S0 galaxies have undergone SF during the last 5 Gyr (the percentage is even higher among the low luminosity S0), whereas ellipticals have not. The reason that studies on other clusters could not find this behaviour could be that only the luminous galaxies were observed, whereas the effect is found strongest in fainter galaxies. In addition to these observations of nearby clusters, observations of clusters at $z \sim 0.4$ show a large fraction of “post-starburst” galaxies (also “E+A” galaxies, as the spectra seem composed of one of a passive elliptical galaxy superimposed with an A-star like spectrum). These are galaxies with suppressed star formation, but they have undergone a star burst before the ceasing of the SFR. From images most of these galaxies were classified as spirals. Such post-starburst galaxies are not found among the luminous Coma galaxies, but among the faint ones. One explanation suggests is that galaxies, when they are accreted to a cluster, undergo some process which first causes a star burst and then a decline in star formation, and that fainter galaxies are accreted later. So the differences between high and low luminosity galaxies trace the accretion



history. However, the origin and relevance of E+A galaxies is still a matter of debate. E.g. Goto et al. (2004) found E+As in all environments, which questions the model that they result from the influence of a dense environment.

1.5.2 Gas contents of late-type galaxies

HI deficiency

The HI deficiency of cluster galaxies has been known for some decades (see e.g. review by van Gorkom 1996 and references therein). At first nearby clusters were studied. In a classic paper Cayatte et al. (1990) presented HI maps of the 25 brightest spiral galaxies in the Virgo cluster. The summary of their results is shown in Fig. 1.8, where the HI maps (magnified by a factor of 5) are plotted at their proper positions in the cluster. The galaxies closer to the cluster centre have smaller HI disks. Cayatte et al. (1994) analysed the same sample further and distinguished cases of global deficiency and truncated disks (with normal central surface densities). They suggest that the former characteristic is caused by turbulent viscous stripping or by thermal conduction. Truncated disks are thought to be due to RPS. Similar results to the one in Fig. 1.8 have been obtained e.g. for the Coma cluster (Bravo-Alfaro et al. 2000), ACO 3627 (Vollmer et al. 2001c), Fornax cluster (Schröder et al. 2001), and Hercules cluster (Dickey 1997). A counter-example is the volume-limited HI survey of the Hydra I cluster (see van Gorkom 1996 and references therein), which did not find a correlation between HI disk size or deficiency with cluster-centric radius. However, this cluster has a low X-ray luminosity.

Giovanelli & Haynes (1985) compiled a catalogue of 9 clusters and studied HI properties of their galaxies. In six of the clusters the galaxies showed substantial HI deficiency. In them the degree of HI depletion is higher closer to the cluster centre and the fraction of deficient galaxies is correlated with the X-ray luminosity of the cluster. The three non-deficient clusters are loose systems with weak X-ray luminosity (not detected in 1985). From a subset of the sample of Giovanelli & Haynes, Valluri & Jog (1991) concluded that, surprisingly, large galaxies are more deficient than small ones. In a further subsample Magri et al. (1988) could not find any correlation between HI deficiency and radial velocity. Both findings do not agree with the RPS model. However, these results are contradicted by the large study of Solanes et al. (2001) who compiled a catalogue of 1900 spirals in clusters in 18 nearby clusters. In two thirds of the clusters the galaxies show HI deficiency. Significantly gas poor galaxies were found out to 2 Abell radii (≈ 3 Mpc). Inside this radius the fraction of gas-poor spirals increases towards the centre. Moreover, in agreement with the analysis of Dressler (1986), gas-poor galaxies tend to be on more radial orbits that lead them deeper into the cluster core than normal galaxies. No correlation between deficiency and galaxy size was found, but early-type spirals seem to be more deficient than late-type

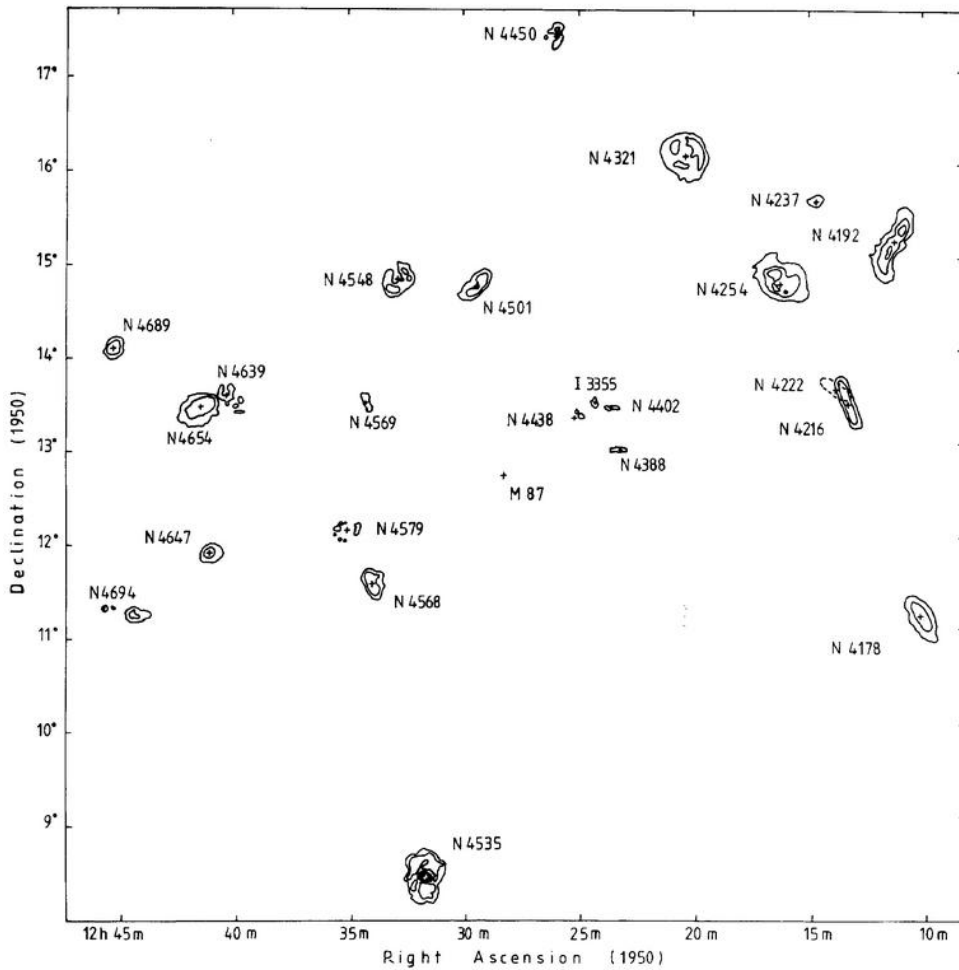
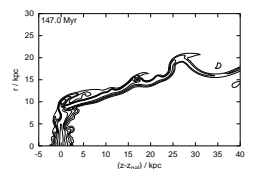


Figure 1.8: Integrated HI maps of the 25 brightest Virgo spirals, plotted at their projected position in the cluster, magnified by factor 5. From Cayatte et al. (1990). The first contour corresponds to about 10^{20}cm^{-2} . The size of the plot corresponds approximately to $3\text{Mpc} \times 3\text{Mpc}$. The position of the central elliptical galaxy in the Virgo-cluster (M87) is marked. For comparison with Fig. 1.6: M86 is located between N4438, N4388 and N4402.

ones, which has also been found in a smaller sample by Dressler (1986). The authors speculate that the reason might be that the central depression in the HI disk common in early-type spirals makes them more vulnerable to the process responsible for the deficiency. Dressler (1986) argues that if preferably late-type spirals are transformed into S0s, S0s should have mostly large bulges, as is observed. These characteristics found by Solanes et al. (2001) match the predictions of the RPS model. However, no correlations between HI deficiency and the X-ray emission of the ICM could be found. The authors point out that this may be a selection effect, as completely stripped galaxies



would be (mis)classified as S0s and left out of the sample. Also Koopmann & Kenney (2004b) give a warning that the correlation between Hubble type and HI deficiency may be due to the misclassification of stripped cluster spirals. Even a part of the morphology-density relation might be due to such misclassifications (Koopmann & Kenney 1998). In a series of papers Sanchis et al. (2002), Mamon et al. (2004), and Sanchis et al. (2004) investigate the origin of the deficient spirals in the outskirts of the Virgo cluster which are not explained easily by RPS. They exclude that these galaxies have lost their gas during a core passage and bounced out of the cluster to the large distances they are found in. Therefore they propose that the determined cluster-centric distances of these galaxies have large errors, or the deficiency is overestimated due to a misclassification or their gas is heated by recent tidal interactions or minor mergers.

Little is known about HI deficiency in galaxy groups. E.g. Kilborn et al. (2004) find no global deficiency in the NGC 1566 group, whereas Omar (2004) detects a mild deficiency in the Eridanus group. However, he suggests that this is due to tidal interactions.

Molecular gas and dust

The general impression from observations is that the molecular gas is not affected by the environment, as the masses of molecular gas derived from CO observations are comparable for cluster and field galaxies (Stark et al. 1986; Casoli et al. 1996, 1998; Boselli et al. 1997, 2002; Kenney & Young 1988, 1989). However, most CO observations are restricted to the inner 5 to 15 kpc of the galaxies. On the other hand the truncation of SF to the inner disks is difficult to understand if the molecular gas is not affected in the outer parts, as molecular clouds are the sites of SF.

Systematic studies of dust in clusters are very rare. According to a survey in the Virgo cluster (Doyon & Joseph 1989) galaxies lacking HI are also mildly deficient in dust.

1.5.3 Galaxies “caught in the act”

Galaxies with truncated gas disks, one-sided off-plane gas (a tail) and perhaps a bow shock on the opposite side are suspected to suffer RPS. Tidal interactions can cause similar features, but are expected to distort the stellar component as well, whereas RPS is thought to affect solely the gas component. Also combinations of both processes have been found. We do not attempt to give a complete list of possible candidates here but describe only a few.

One of the best candidates is NGC 4522, a low to medium mass Virgo spiral (rotation velocity of 100 to 130 km s⁻¹, see Kenney & Koopmann 1999 and Vollmer et al. 2000 and references therein). Its stellar disk is undisturbed, but the H α distribution is truncated to a radius of about 3 kpc (see

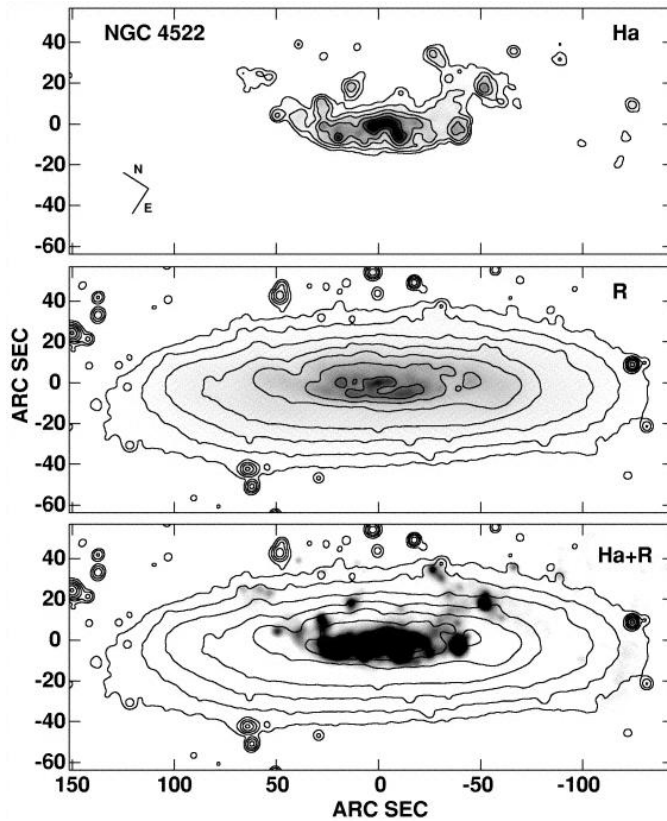
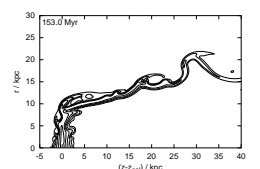


Figure 1.9: Ram pressure stripping of the Virgo spiral NGC 4522 (Fig. 3 from Kenney & Koopmann 1999). a: H α contours, tracing the star forming disk. b: R-band contours, showing the unperturbed stellar disk. c: H α gray-scale on top of R-band contours, comparing the truncated H α disk to the undisturbed stellar disk. 50 arcsec correspond to about 4 kpc.

Fig. 1.9, which is taken from Kenney & Koopmann 1999). At the edges of the truncated H α disk gas extends up to 3 kpc out of the plane to one side. The lack of SF in the outer disk could suggest that even molecular gas is stripped there. The HI distribution is very similar to the H α , as shown in Fig. 1.10 (taken from Kenney et al. 2004). Radio-continuum observations (Vollmer et al. 2004b) indicate a large-scale shock at the side of the galaxy opposite to the extraplanar gas. Given the fact that this galaxy is located at a distance of about 1 Mpc to the cluster centre (see also bottom panel of Fig. 1.6), the clear RPS signature provides a puzzle. NGC 4522 has a high line-of-sight velocity ($\sim 1300 \text{ km s}^{-1}$ with respect to the cluster), but at its position the ICM density is expected to be too low to provide a ram pressure capable to cause the observed stripping. Kenney et al. (2004) discuss the possibilities of bulk motions and density enhancements due to subcluster merging in the ICM of the Virgo cluster. Sticky-particle simulations of RPS with a peak ram pressure of $\rho_{\text{ICM}} v_{\text{ICM}}^2 = 28 \cdot 10^{-4} \text{ cm}^{-3} (1000 \text{ km s}^{-1})^2$ of Vollmer et al. (2000) could reproduce the main characteristics of the gas distribution and the velocity field. The authors interpret the extraplanar gas as resettling to the disk after the peak stripping.

Another candidate is the large Virgo spiral NGC 4569 (see Vollmer et al. 2004a and references in the introduction; see also Fig. 1.8). It is highly HI deficient as a result of a heavily truncated gas disk. However, it shows a central starburst. Soft X-ray emission (Tschöke et al. 2001) is limited to one



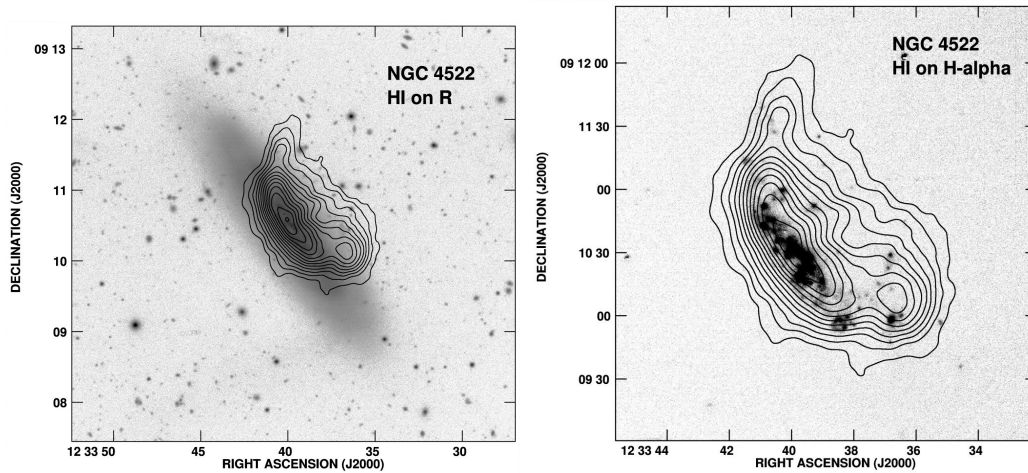


Figure 1.10: Ram pressure stripping of the Virgo spiral NGC 4522 (Figs. 3 and 13 from Kenney et al. 2004). Left: HI (neutral gas) contours on top of unperturbed stellar disk in gray-scale. Right: HI contours on top of $H\alpha$ (tracing SF) in gray-scale.

side (the downstream side). In both X-rays and in $H\alpha$ (Bomans et al. 2004) an outflow to the downstream side has been detected. Vollmer et al. (2004a) find a low surface brightness HI arm extending to the same side. With a line-of sight velocity of $\sim 1100 \text{ km s}^{-1}$ with respect to the cluster mean and a distance of only $\sim 500 \text{ kpc}$ to the cluster centre RPS is a likely scenario. Comparing with sticky-particle simulations, Vollmer et al. (2004a) conclude that the major stripping event took place $\approx 300 \text{ Myr}$ ago.

NGC 4402 is a nearly edge-on Virgo spiral with truncated gas disk (HI as well as $H\alpha$) and extraplanar gas on one side (Crowl et al. 2004). The dust lane, a typical feature for edge-on spirals, curves corresponding to the HI distribution, suggesting that also the dust is stripped. Small filaments of dust emerge to the upstream side of the disk. The authors interpret them as dense molecular clouds first left behind by the ICM wind, which are now ablated nonetheless (see Fig. 1.11).

CGCG 97073 and 97079 are two irregular galaxies in the A1367 cluster. Both have extremely long tails of ionised gas on the one side and HII regions aligned in a bow-shock-like structure on the opposite side, where SF may be induced by compression due to ram pressure (Gavazzi et al. 1995, 2001).

Phookun & Mundy (1995) regarded the morphology of NGC 4654 as a signature of RPS, but according to Vollmer (2003) this galaxy is an example of combined RPS and tidal interaction.

1.5.4 Relevance of environmental effects

In the light of the observations summarised in the last sections, the relevance of environmental influences on the evolution of galaxies is without doubt.

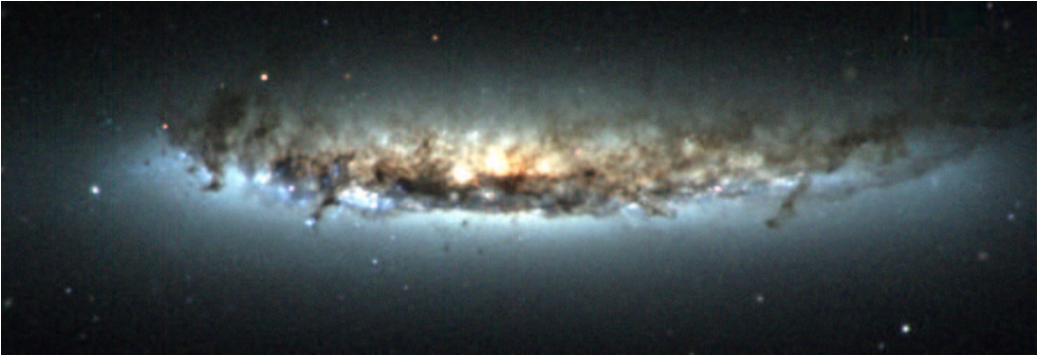
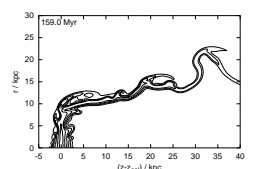


Figure 1.11: Ram pressure stripping of the Virgo spiral NGC 4402 (Press release NOAO 04-06 of the National Optical Astronomy Observatory). The dust can be seen as dark lanes.

Theoretical work has to explain the reduction of SF, the decrease of the blue fraction and the decrease of the spiral fraction in dense environments as well as the HI deficiency in clusters. All these properties are linked by the interplay between gas and stars inside the galaxy. A galaxy bereft of its gas ceases to form stars. Blue stars have a short lifetime, so if no new stars are formed, the colour of the galaxy will change from blue to red. Then it may be classified as an S0. The gas interactions explained in Sect. 1.4.2 deplete the gas in cluster galaxies on different time scales. The gravitational interactions (Sect. 1.4.1) can cause an accelerated gas consumption and even change the morphologies in a more dramatic way. However, the relative importance of the individual processes is still a matter of debate.

In a series of papers Fujita (1998, 2001) and Fujita & Nagashima (1999) estimate the influence of environmental effects on SFRs and colours of galaxies. They construct an analytical model of SF efficiency based on the mass and pressure of molecular clouds. They report that RPS enhances the SFR in the inner disk regions by about a factor of 2, but conclude that this is not sufficient to change a galaxy's colour. From a semi-analytic study of RPS and minor mergers also Okamoto & Nagashima (2003) conclude that RPS alone cannot reproduce the observed morphology-radius relation. They consider strangulation and minor mergers more important than RPS. Especially for cluster outskirts and groups RPS has been assumed to have negligible effects due to the low ICM densities. However, Fujita (2004) considers the effect of RPS, strangulation and thermal conduction in subgroups in a hierarchical cluster formation scenario. The effects of RPS and thermal conduction are again modelled by simple analytical estimates. The main result is that galaxies could be pre-processed in the subgroups, which could explain e.g. the reduced SFR and the HI deficiency in the outer cluster regions. Also the examples of truncated gas disks with normal inner gas densities and normal or enhanced SFRs strongly favour RPS, especially if these characteristics are accompanied by undisturbed stellar disks.



1.6 Aim of this work

In this work we want to study RPS by means of numerical simulations. Most previous works performed a few simulation runs with massive galaxies in winds representative for cluster centres and found that for these cases the gas loss can be predicted by Eq. 1.13 (at least for face-on winds). Massive galaxies in weak winds corresponding to conditions in cluster outskirts were not simulated, as in general it is assumed that weak winds do not have important effects. We want to compile a comprehensive parameter study with ICM winds which are representative for the whole range from cluster centres to cluster outskirts and groups. We want to check if we can confirm the analytical estimate for this large range of ram pressures. Moreover, the analytical estimate incorporates just p_{ram} and does not distinguish with which combination of ρ_{ICM} and v_{ICM} this p_{ram} was achieved. We want to test systematically if the analytical estimate misses some dependence on Mach number, especially as v_{ICM} is expected to be similar to the sound speed. As a second point, we want to investigate the dependence of RPS on galactic parameters. Concerning the dependence on overall galaxy mass, we perform simulations for a massive and a medium size disk galaxy. In addition, we pay special attention to the vertical structure and thickness of the gas disk, as the analytical estimate (Eq. 1.13) does not distinguish such cases, either.

Section 1.2 made clear that the ISM of spiral galaxies is a highly complex system. So far no complete model for the ISM has been found. An overview about recent work is given in de Avillez & Breitschwerdt (2004). Moreover, for the simulation of RPS a large volume of ICM around the galaxy needs to be included, which would be beyond computational power. Therefore we need to use certain approximations. In agreement with other authors we assume that mainly the diffuse components of the ISM react to the ICM wind. E.g. molecular clouds are too small to “feel” the flow of the ICM. In addition, they are a transient phenomenon. The feedback of stars formed inside them transforms them back to a diffuse medium on a time scale of a few Myr. Therefore we approximate the ISM by a single diffuse component. We note that this includes implicitly a thermal equilibrium.

We describe the interaction between the ICM and the ISM hydrodynamically. Despite the single-phase approximation the temperatures and densities in the ISM and ICM still differ by several orders of magnitudes. Thus it is advisable to consider the validity of the hydrodynamical treatment, which is that relaxation (or collision) time scales are shorter than the dynamic time scale of the problem; and that mean free paths are small compared to macroscopic scales of interest. We aim to resolve length scales of ~ 100 pc. The dynamical time scale for RPS is $\sim 1 \text{ kpc}/(1000 \text{ km s}^{-1}) \approx 1 \text{ Myr}$. These scales do not pose any problems for the ISM. But for the ICM in Sect. 1.3.2 we calculated a typical mean free path and equipartition time scale of 23 kpc and 600 Myr, respectively. However, these numbers are valid for interactions inside the ICM. The mean free path and the collision time scale of hot ICM

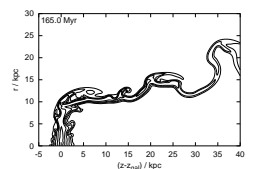
particles inside the dense ISM are small enough as well. In addition, according to its mean free path and relaxation time scale, on cluster scales the ICM can be treated hydrodynamically, and it can be considered to be relaxed. So the galaxy meets a relaxed ICM when it enters the cluster. However, the effects of the galaxy on the ICM as produced with a hydrodynamical code (like vortices) should not be overinterpreted.

The simulations in this work are restricted to galaxies moving face-on through the ICM. This allows to use a 2D code, which is computationally less expensive and significantly faster. Thus it is possible to perform a large set of simulations.

Furthermore, we expose the model galaxies to constant ram pressures, i.e. they move with constant velocity through a homogeneous ISM. This allows us to isolate the influence of the ram pressure from the effect of its variability.

For convenience we transform the interaction between the ICM and the galaxy into the rest frame of the galaxy, where the relative motion translates into an ICM wind.

In Chapter 2 we give a summary of hydrodynamics and of the numerical code. Chapter 3 introduces the initial model. Chapter 4 presents the result of the simulations, which are discussed in Chapter 5. Chapter 6 gives an outlook on future work.



Chapter 2

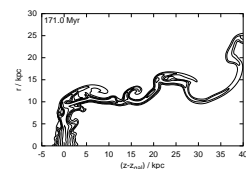
Numerical Methods

Hydrodynamics can be described either in the Eulerian or in the Lagrangian form. The Eulerian approach follows the evolution of *local* continuum quantities like density, pressure and velocity. In contrast, the Lagrangian description follows the fate of certain fluid elements. Both methods have their counterparts in numerical codes. Grid codes take the Eulerian approach, whereas smoothed particle hydrodynamics (SPH) codes follow the Lagrangian description.

We choose a 2D Eulerian code in cylindrical coordinates z and r for the RPS simulations, where the grid is fixed in the rest frame of the galaxy. The restriction to two dimensions makes the code less time and memory consuming and therefore allows us to aim at higher resolution, longer runtimes or larger sets of simulations. In addition, the code can be vectorised very well and runs efficiently on e.g. the vector machine in the computer centre of the University of Kiel. The code is developed from an original implementation of Różyczka (1985). The numerical techniques are essentially the same as in the ZEUS code (Stone & Norman 1992), and the one presented by Norman & Winkler (1986). Also Storm (1993), Severing (1995), Lohmann (2000) and Vieser (2001) have used this code and give detailed descriptions. Therefore here we summarise the most important points. For further details please refer to the aforementioned papers and theses. Before we explain the numerics, we introduce the hydrodynamical equations.

2.1 Hydrodynamical equations

In the Eulerian approach the state of a fluid at each position \vec{x} and time t is characterised by the *local* mass density ρ , particle number density n , internal energy density e , pressure p , temperature T , and velocity \vec{v} . We list all hydrodynamical equations summarised in the end of this section (Eqs. 2.2 to 2.8). They are derived from conservation laws for the mass, momentum and energy. In addition, ρ , p , e and T are linked through the equation of state for an ideal gas (Eq. 2.8). Assuming a source and sink free fluid, the mass



conservation leads to the well known continuity equation (Eq. 2.2), which expresses that the change of mass inside a volume element is due to the flux through the surface of the element.

For the conservation of momentum one has to consider the change of momentum in a fluid element, which is due to the flux of momentum through its surface. In addition, pressure and viscosity are external forces working on the surface of the fluid element. Furthermore, the gravitational force works on all mass in the volume. This is expressed in the extended Eulerian equations (Eqs. 2.3 and 2.4) (the original Eulerian equation did not contain viscosity).

The change of internal energy in a fluid element (see Eq. 2.6) is again due to the flux of energy through the element's surface. In addition to that, the energy can change due to compressional heat and due to viscous forces. If heating and cooling should be taken into account, the appropriate rates would have to be added as sources and sinks. However, as discussed above, the single-phase approximation of the ISM includes heating and cooling implicitly. Finally, the gravitational potential is determined by the total mass density ϱ_{total} via the Poisson equation (Eq. 2.7).

The sound speed in a gas

$$c_s = \sqrt{\frac{\gamma k T}{\mu m_H}} = 118 \text{ km s}^{-1} \sqrt{\frac{T/(10^6 \text{ K})}{\mu}}, \quad (2.1)$$

is independent of ϱ .

We assume cylindrical (rotational) symmetry from now on. Therefore we summarise the hydrodynamical equations in 2D cylindrical coordinates z and r (Eqs. 2.2 to 2.8). Dependencies on the third cylindrical coordinate ϕ vanish due to the assumed symmetry (i.e. $\frac{d}{d\phi} = 0$). For a disk galaxy we need to include rotation. In cylindrical symmetry, rotation manifests itself by angular momentum density $L = \varrho v_{\text{rot}} r$ and the centrifugal force per unit volume $\varrho v_{\text{rot}}^2 / r = L^2 / (\varrho r^3)$. Due to conservation of angular momentum, the angular momentum density needs to obey a continuum equation as well (Eq. 2.5). In other words, Eq. 2.5 originates from the momentum equation for the third coordinate ϕ assuming the cylindrical symmetry. The velocity components parallel and perpendicular to the symmetry axis are U and V , respectively. With that the complete set of equations reads:

$$\frac{\partial}{\partial t} \varrho = -\nabla \cdot (\varrho \vec{v}) \quad (\text{continuity equation}) \quad (2.2)$$

$$\frac{\partial}{\partial t} (U \varrho) = -\nabla \cdot (U \varrho \vec{v}) - \frac{\partial p}{\partial z} - \varrho \frac{\partial \Phi}{\partial z} - \nabla \cdot \vec{Q}_z \quad (\text{momentum eqs}) \quad (2.3)$$

$$\frac{\partial}{\partial t} (V \varrho) = -\nabla \cdot (V \varrho \vec{v}) - \frac{\partial p}{\partial r} - \varrho \frac{\partial \Phi}{\partial r} - \nabla \cdot \vec{Q}_r + \frac{L^2}{\varrho r^3} \quad (2.4)$$

$$\frac{\partial}{\partial t} L = -\nabla \cdot (L\vec{v}) \quad (\text{continuity equation for angular momentum density}) \quad (2.5)$$

$$\frac{\partial}{\partial t} e = -\nabla \cdot (e\vec{v}) - p\nabla\vec{v} - \sum_{ik} Q_{ik} \frac{\partial v_i}{\partial x_k} \quad (\text{energy equation}) \quad (2.6)$$

$$\Delta\Phi = 4\pi G \varrho_{\text{total}} \quad (\text{Poisson equation}) \quad (2.7)$$

$$p = (\gamma - 1)e = \frac{\varrho}{\mu m_H} kT = nkT \quad (\text{equation of state}) \quad (2.8)$$

For the adiabatic index γ in this work we assume the value for a monoatomic gas $\gamma = 5/3$. The mean molecular weight μ multiplied by the proton mass m_H is the mean particle mass. The elements of the viscosity tensor \mathbf{Q} are Q_{ik} . In the momentum equations \vec{Q}_z and \vec{Q}_r are the appropriate columns of \mathbf{Q} .

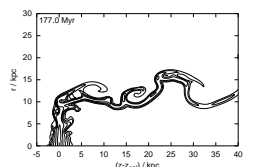
2.2 The staggered grid

The grid of our code runs from $r = 0$ to $r = r_{\text{max}}$ in radial direction and from $z = 0$ to $z = z_{\text{max}}$ in z -direction. The number of cells in z -direction is NZ , in r -direction NR . ICM winds are set to flow in the direction from $z = 0$ to $z = z_{\text{max}}$. A grid code divides the computational region into spatially fixed cells. Throughout one cell all hydrodynamical quantities are constant. Our code uses a “staggered” grid (see Fig. 2.1), which means that scalar quantities (density ϱ , internal energy density e , pressure p , temperature T , potential Φ) are defined at cell centres, whereas vector quantities (linear velocity components U and V , linear momentum components $SM \equiv U\varrho$, $TM \equiv V\varrho$) are defined on the cell walls. For the conversion between the momentum components and the velocity components the averaged value of the density at the cell wall is used. In the 2D cylindrical code also the angular momentum density L and the rotation velocity v_{rot} are defined in the cell centres. The counters IZ and IR enumerate grid cells in z - and r -direction, respectively. Fig. 2.1 illustrates where quantities are defined in the grid and how they are referred to. In most plots to come the grid will be oriented like in Fig. 2.1, where the symmetry axis (the z -axis) is in horizontal direction.

In this code the grid is evenly spaced.

2.3 Operator splitting

The hydrodynamical differential equations are transformed to finite difference equations. Formally these can be derived by expanding the differential equations into Taylor series up to a certain order. Our code takes terms up to first order into account. However, it improves accuracy to formally second order by the technique of operator splitting.



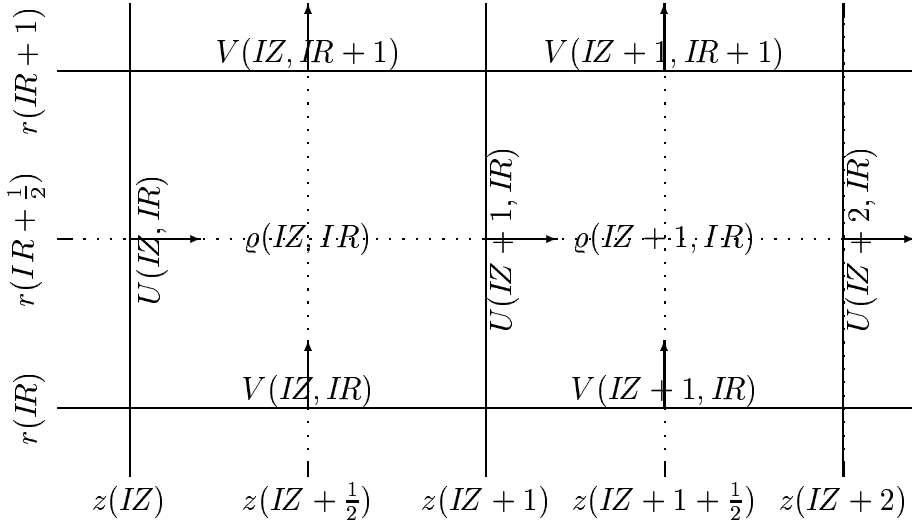


Figure 2.1: Illustration of the staggered grid: The cell walls of two adjacent cells are shown by solid lines. The coordinates z and r of the cell walls and cell centres are labelled. As a representative of scalar quantities, the density ρ of the two cells is written into their centres. As representatives of vector quantities the components of the velocity V and U are labelled and marked by arrows at the appropriate cell walls.

The idea of this method is the following: Consider a differential equation

$$\frac{\partial}{\partial t} X = L_1(X) + L_2(X) \quad (2.9)$$

for a quantity X , where the current change in X is the sum of the expressions L_1 and L_2 . These in turn can depend on X . In the standard first order discretisation the value of X at time step $n + 1$ is derived from the value at time step n according to

$$X^{n+1} = X^n + \Delta t [L_1(X) + L_2(X)]. \quad (2.10)$$

The length of the time step is Δt . Operator splitting divides this into two substeps:

$$X' = X^n + \Delta t \cdot L_1(X) \quad (2.11)$$

$$X^{n+1} = X' + \Delta t \cdot L_2(X'), \quad (2.12)$$

where the second substep uses the result of the first one. This method also improves numerical stability (see Press et al. 1992).

In our hydro-code each time step is separated into several substeps that are subsumed into a source step and a advection step. Advection describes the transport of gas from one cell to its neighbours, i.e. the flux through the

cell walls. The corresponding parts in the hydro-equations are the $\nabla(X\vec{v})$ terms (for quantity X) in Eqs. 2.2 to 2.5. All other terms belong to the source step.

2.3.1 Source step

Substep 1 - gravity, pressure, centrifugal forces

The first substep updates the components of the linear momentum density SM and TM with changes due to gravitation, pressure and centrifugal forces. In differential equations this reads:

$$\frac{\partial}{\partial t}(SM) = -\frac{\partial p}{\partial z} - \varrho \frac{\partial \Phi}{\partial z} \quad (2.13)$$

$$\frac{\partial}{\partial t}(TM) = -\frac{\partial p}{\partial r} - \varrho \frac{\partial \Phi}{\partial r} + \frac{L^2}{\varrho r^3} \quad (2.14)$$

For this substep we explicitly give the discretisation. During a time step of length Δt the new value of SM is found from the old value according to:

$$SM^{\text{new}}(IZ) = SM^{\text{old}}(IZ) + \Delta t \left[-\bar{\varrho}(IZ) \frac{\Delta \Phi(IZ)}{\Delta z} - \frac{\Delta p(IZ)}{\Delta z} \right] \quad (2.15)$$

$$\text{with } \Delta X(IZ) = X(IZ) - X(IZ - 1)$$

$$\text{and } \bar{X}(IZ) = \frac{1}{2}[X(IZ) + X(IZ - 1)]$$

for each quantity X (except for Δt).

The analogue in r -direction is

$$TM^{\text{new}}(IR) = TM^{\text{old}}(IR) + \Delta t \left[-\bar{\varrho}(IR) \frac{\Delta \Phi(IR)}{\Delta r} - \frac{\Delta p(IR)}{\Delta r} + \frac{\bar{L}^2}{\bar{\varrho} r^3(IR)} \right] \quad (2.16)$$

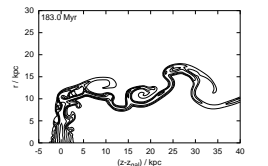
$$\text{with } \Delta X(IR) = X(IR) - X(IR - 1)$$

$$\text{and } \bar{X}(IR) = \frac{1}{2}[X(IR) + X(IR - 1)]$$

for each quantity X (except for Δt).

One needs to take care if the values at cell centres or cell walls are needed. The components of the momenta are defined at the cell walls, therefore also all other values here need to be given at the cell walls. This means that the gradients $\Delta X/\Delta z$ and $\Delta X/\Delta r$ must be centred at the appropriate cell wall. Moreover, also the values used for the scalar quantities ϱ , L and r must be the values at the appropriate cell *wall*. The radius r of the cell wall is known directly. For the other quantities the appropriate value is found by averaging.

The momentum densities are converted to velocities by dividing by the averaged values of ϱ at the associated cell walls.



Substep 2 - artificial viscosity

In a similar way, the next substep updates the momentum densities as well as the internal energy density e with changes due to viscosity. While calculating the changes the velocities as they result from the first substep are used.

The natural viscosity is neglected in this code. In a description without viscosity, however, shock fronts would be infinitely thin. Rankine-Hugoniot jump conditions and the propagation velocity of the shock could not be reproduced correctly. Therefore an artificial viscosity is introduced following Norman & Winkler (1986) and Stone & Norman (1992). The goal is a viscosity that is non-zero in compressed regions to give the correct behaviour at shock fronts, but is negligible in all other regions. Therefore only the diagonal elements of the viscosity tensor \mathbf{Q} are non-zero. Due to the cylindrical symmetry also the component $Q^{\phi\phi}$ is zero. The two remaining components take the form

$$Q^{ZZ}(IZ, IR) = \varrho(IZ, IR) \cdot [U(IZ + 1, IR) - U(IZ, IR)] \cdot [-C_1 c_s + C_2 \cdot \min\{U(IZ + 1, IR) - U(IZ, IR), 0\}], \quad (2.17)$$

$$Q^{RR}(IZ, IR) = \varrho(IZ, IR) \cdot [V(IZ, IR + 1) - V(IZ, IR)] \cdot [-C_1 c_s + C_2 \cdot \min\{V(IZ, IR + 1) - V(IZ, IR), 0\}], \quad (2.18)$$

where c_s is the adiabatic sound speed. The constant C_1 sets a linear term, which is, according to Norman & Winkler (1986), used rarely “and then only sparingly to damp oscillations in stagnant regions”. The constant C_2 sets the quadratic term, it gives roughly the number of cells over which a shock front is spread. It is usually set to values between 1 and 4. Here we use $C_1 = 0$, $C_2 = 2$ in agreement to previous work and in agreement with results from numerical tests (see Appendix C). A concern may be that hydrodynamical instabilities like the Kelvin-Helmholtz(KH)-instability are not modelled correctly due to the artificial viscosity. We test its influence in Appendix D.4 and find that it does not bias our results.

The new temperature and pressure are calculated from the equation of state. For this purpose the mean molecular weight has to be calculated as summarised in Sect. 1.2.3.

Substep 3 - sources and sinks

Finally the internal energy density is updated with changes due to compressional heat. Along with that the new temperature and pressure are calculated with the equation of state.

2.3.2 Transport step - advection

In a spatially fixed grid matter moves from one grid cell to the next. This process is called transport or advection. Along with the matter itself also

properties like the internal energy and linear and angular momenta are transported.

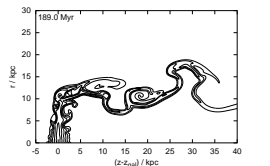
The advection scheme can be explained best for the case of the mass density. The strategy is to calculate how much mass moves through a cell surface during the current time step – these are the mass fluxes through the cell walls – and to update the mass inside each cell according to the fluxes. The fluxes can be either positive or negative, that means matter can enter or leave the cell. The difficult part is to calculate the fluxes. Consider a one-dimensional strip of cells in z -direction. To simplify matters, the flow shall be in positive direction, i.e. gas enters the cell IZ through the cell wall at $z(IZ)$ and leaves it at the wall $z(IZ + 1)$ (see Fig. 2.1). The velocities at these cell walls are $U(IZ)$ and $U(IZ + 1)$. How much gas does cross the cell wall at $z(IZ + 1)$ during a time step of length Δt ? During Δt a particle with velocity $U(IZ + 1)$ can move the distance $U(IZ + 1)\Delta t$. So all gas between cell wall $z(IZ + 1)$ and $z(IZ + 1) - U(IZ + 1)\Delta t$ can cross this wall. The time step criterion (see Sect. 2.4) ensures that $U(IZ + 1)\Delta t$ is smaller than the cell size, so that only a fraction of the gas in the cell can leave it. An alternative point of view would be to average over regions left and right of the cell wall. However, this incorporates information from both the upwind and the downwind side of this cell wall. The point of view taken above uses information from the upwind side only, which turned out to be preferable. Now we are left with calculating the mass of the advected gas, then we would know the flux through the cell wall. The idea is to calculate the volume $\tau(IZ + 1, IR + \frac{1}{2})$ of the advected gas (i.e. gas that can cross the cell wall during Δt , see some lines above) and multiply it with a mean density inside this volume. For advection in z -direction τ is simply

$$\begin{aligned} \tau(IZ + 1, IR + \frac{1}{2}) &= U(IZ + 1, IR)\Delta t \cdot \pi [r^2(IR + 1) - r^2(IR)] \\ &= U(IZ + 1, IR)\Delta t \cdot 2\pi r(IR + \frac{1}{2})\Delta r \end{aligned} \quad (2.19)$$

with $\Delta r = r(IR + 1) - r(IR)$ (which is constant throughout the grid). Similarly for advection in r -direction we have

$$\begin{aligned} \tau(IZ + \frac{1}{2}, IR + 1) &= \pi \Delta z [r^2(IR + 1) - \{r(IR + 1) - V(IZ, IR + 1)\Delta t\}^2] \\ &= V(IZ, IR + 1)\Delta t \\ &\quad \times 2\pi \Delta z \left[r(IR + 1) - \frac{1}{2}V(IZ, IR + 1)\Delta t \right], \end{aligned} \quad (2.20)$$

where we again assumed that the flow direction is in positive direction. Now we need to calculate an average value for the density in the advected volume. These averages must ensure that discontinuities are not smeared out and that the numerics do not generate local extrema out of monotonic profiles. Therefore very simple ideas for the averages do not work. A more sophisticated



way that meets these criteria is the monotonic interpolation scheme of van Leer (1977). Detailed descriptions can also be found in the works mentioned in the beginning of this chapter.

For the internal energy and angular momentum the method of “consistent advection” is applied, i.e. the quantity is advected along with the mass. Technically this means that one stores the information about the advected volumes and mass fluxes. In addition, one calculates the specific internal energy e/ϱ and angular momentum L/ϱ (internal energy and angular momentum per unit mass). The interpolated specific quantity times the mass flux returns the amount of advected internal energy or angular momentum that is used to update e and L , respectively.

The advection of the linear momenta is done in analogy to the advection of mass, though one needs to take care to use the appropriate cells. Due to the fact that U and V are defined on the cell walls of the basic grid, for the advection of U and V one has to think in terms of two additional shifted grids which have either U or V cell centred.

2.4 Time step criterion

The time step length is limited by the demand that information can travel only a fraction $1/S_{\text{CFL}}$ of the cell size in each time step. This is expressed in the Courant-Friedrichs-Lewy (CFL) condition

$$(|\vec{v}|_{\text{max}} + c_s)\Delta t \cdot S_{\text{CFL}} \leq \Delta x \quad S_{\text{CFL}} > 1, \quad (2.21)$$

where $|\vec{v}|_{\text{max}}$ is the maximal current velocity, c_s the local adiabatic sound speed, Δx the cell size and S_{CFL} the CFL safety factor. The inequality must hold for each grid cell. Numerical tests showed that $S_{\text{CFL}} = 5$ to 10 is sufficient (see Appendix C). In the simulations we use $S_{\text{CFL}} = 10$.

2.5 Boundary conditions

A grid code cuts a finite region of interest out of the real space. Therefore the solution of the inner part of the grid has to be extrapolated over the boundaries. Boundary conditions have to be specified at $r = 0$, $r = r_{\text{max}}$, $z = 0$ and $z = z_{\text{max}}$. The outmost cells of the grid, where the boundary conditions need to be specified, are called ghost cells. Here we explain only those boundary conditions that are relevant for this work.

2.5.1 Boundary at $r = 0$

The boundary at $r = 0$ is the axis of symmetry. The exact position of $r = 0$ is set on the second cell wall in r -direction, i.e. $r(\text{IR} = 2) = 0$. This means the strip of cells at $r(\text{IR} = 1 + \frac{1}{2}) = -\frac{1}{2}\Delta r$ are ghost cells. The first cell wall

in r -direction is placed at $r(IR = 1) = -\Delta r$. All quantities are reflected at $r = 0$, i.e.

- $V(IZ, 2) = 0$,
- $V(IZ, 1) = -V(IZ, 3)$,
- $U(IZ, 1) = U(IZ, 2)$,
- $X(IZ, 1) = X(IZ, 2)$ for all scalar quantities X .

Due to $r(IR = 1) < 0$ for the rotation velocity v_{rot} (which is also a scalar and defined in the cell centres) the boundary condition is $v_{\text{rot}}(IZ, 1) = -v_{\text{rot}}(IZ, 2)$, which is consistent with the condition for the angular momentum density $L(IZ, 1) = L(IZ, 2)$.

Advection in r -direction faces the problem that the cell volumina depend on r . This is particularly obvious near the symmetry axis, where the ratio of cell volumina of neighbouring cells is not close to one any more. Especially in connection with rotation boundary problems arose in the sense that the rotating gas disk developed a small central hole during the simulations. Numerical inaccuracies led to an enhancement of angular momentum near the symmetry axis which in turn increased the centrifugal force and caused an outflow out of the innermost cells. We solved this problem by enforcing the additional boundary condition

- $V(IZ, 3) = 0$.

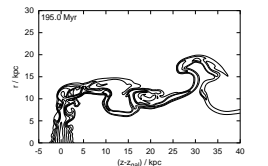
Essentially this prohibits any exchange across these cell walls and decouples the cells next to the symmetry axis from the rest of the grid. When setting an inflow at $z = 0$ (see next Sect.), no inflow should be set for these decoupled cells.

2.5.2 Boundary at $z = 0$

In cases with ICM wind this is the inflow boundary. The first cell wall is placed at $z(IZ = 1) = 0$. An inflow is achieved by setting ICM conditions at this boundary:

- $U(1, IR) = U(2, IR) = v_{\text{ICM}}$,
- $V(1, IR) = 0$,
- $\varrho(1, IR) = \varrho_{\text{ICM}}$,
- $e(1, IR) = e_{\text{ICM}}$.

For cases without ICM winds here the open boundary condition is used (see Sect. 2.5.3).



2.5.3 Boundary at $z = z_{\max}$

In cases with ICM wind this is the outflow boundary. In cases without wind this boundary is equivalent to the one at $z = 0$. In any case this boundary can be open. As an alternative for cases with ICM wind here an active outflow can be set. Both versions are described below.

Open Boundary

The term “open” boundary is used when the flow is extrapolated across the boundary. However, only outflow can be extrapolated, no inflow is allowed across an open boundary. This is simply due to the fact that the code has no information about regions outside the grid and thus cannot know how to set an appropriate inflow. Therefore, for the open boundary the values of ρ , e , L , U and V are copied from cell (wall) $IZ_{\max} - 3$ into the last cells, if the velocity of the cell wall $IZ_{\max} - 3$ is positive. If it is negative, all scalar quantities are copied nonetheless, but the velocities are set to zero in the ghost cells.

An open boundary is very difficult to handle, because spurious reflections of waves occur (Stone & Norman 1992). Such reflections also happen at the inflow boundary, because the numerical boundaries are not perfectly transparent for wave energy.

Active Outflow

To set an active outflow, ρ and e are extrapolated like for the open boundary. However, the velocity in the ghost cells is fixed to $U = v_{\text{ICM}}$ and $V = 0$ to balance the inflow. Therefore this version can be used in cases with inflow only.

As long as no strong density enhancements (e.g. clumps of gas stripped from the galaxy disk) cross this boundary, the active outflow performs very well. Unfortunately clumps that have to cross the boundary lead to strange reflections. Therefore we use an open boundary for the RPS simulations.

2.5.4 Boundary at $r = r_{\max}$

Also at $r = r_{\max}$ an open boundary can be used in all cases considered in this work. However, for simulations of the flow past a body we figured out the following problem: A general feature of the flow past a body is that the velocities on the upstream side of the body have a component in positive radial direction, whereas the velocities on the downstream side have a negative radial component (viewed in cylindrical coordinates). This is also true at the r_{\max} boundary, even if it is far away from the body. The open boundary condition can handle the upstream part where it extrapolates the slight outflow out of the grid. However, it cannot handle the corresponding slight inflow at the downstream side that should occur through the r_{\max}

boundary. This flaw leads to a slight but continuous gas loss through that boundary, so that the true wind density decreases with time. The effect is not strong, but for long runtimes it is not negligible.

As an alternative we implemented a “solid wall” at this boundary, which is achieved easily by enforcing $V(r_{\max}) = TM(r_{\max}) = 0$. Again this just means that nothing can cross this boundary. With this setup, simulations with wind correspond to the flow through a tube, however, the creeping mass loss out of the grid is prevented. This boundary condition is used for the RPS simulations.

2.6 Computation of the potential

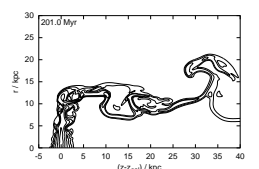
Our code uses the alternating direction implicit (ADI) method, a modified form of operator splitting (see Press et al. 1992), for the calculation of the potential. It involves an extension of the Poisson equation by an artificial time derivative. Thus one has to solve a diffusion equation whose stability solution corresponds to the solution of the Poisson equation.

For solving the Poisson equation boundary values need to be known. At the symmetry axis the derivatives perpendicular to the boundary are $\partial\Phi/\partial r = 0$. At the other boundaries the values of Φ are calculated directly from an expansion into spherical harmonics.

2.7 Code testing and calibration

The code has been developed for many years and changes and extensions have been made by several people. Thus we considered some tests necessary to be sure that the code works correctly. Concerning the hydrodynamics we performed basic tests like the Riemann shock tube and the Sedov blast wave. In addition we tested the potential flow past a sphere as an example related closely to the actual application. The functionality of the potential solver was tested for the example of a homogeneous sphere.

The tests are presented in Appendix C. All tests were passed. Results concerning the choices of boundaries and parameters for the artificial viscosity and the CFL safety factor have already been explained above in the appropriate sections. A further important finding from the potential flow tests is that the initialisation of the ICM wind should be done as slowly as possible. Furthermore, the computational region must be large enough so that the boundaries do not disturb the flow. The potential flow tests suggest the following: $r_{\max} \geq 2r_{\text{gal}}$, $z_{\max} \geq 4r_{\text{gal}}$, $z_{\text{gal}} \geq r_{\text{gal}}$, $z_{\max} - z_{\text{gal}} \geq 2r_{\text{gal}}$, where z_{gal} is the z coordinate of the galaxy and r_{gal} the galaxy’s radius.



2.8 Colouring technique

In the introduction of this chapter we explained that Eulerian codes evolve local properties of a fluid, but they cannot trace certain fluid elements. Nevertheless we aim at tracing the whereabouts of the galactic gas after it is stripped from the disk. The trick how this can be done with an Eulerian code is to “dye” the gas, advect the colour density along with the mass density, and examine the intensity of the colour throughout the grid. Further details are explained in Sect. 4.5.2.

Chapter 3

Initial Model

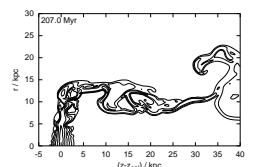
Simulations are performed for two galaxy models, one representing a massive spiral with a flat rotation curve at the level of 200 km s^{-1} , a second depicting a medium-mass galaxy with a rotation velocity of about 150 km s^{-1} .

3.1 Galactic components

The model galaxy consists of a stellar disk, a stellar bulge, a DM halo and a gas disk. Neither the stellar components nor the DM halo are influenced by an ICM wind, hence they are kept static. They affect the gas disk by gravitation. The gas disk's contribution to the gravitational potential is small compared to the contributions of the other components, thus it is neglected for the potential calculation. This allows us to use a static potential. The degree of vectorisation for the potential routine is not as high as for the rest of the code, therefore the use of a static potential makes the simulations significantly faster. We verified that this simplification does not bias the results (see Appendix D.3).

3.1.1 Stellar disk

In the literature there are different models how the density distribution or the potential of stellar disks can be described analytically. We summarise the most important ones below. All models assume rotational symmetry, so that the density distributions and potentials depend only on the cylindrical coordinates z and r . As stellar disks are generally flat, some models describe them as infinitely thin disks. In these cases naturally only a surface density $\Sigma(r)$ can be given, but the potentials depend on both r and z . For the parametrisation of the extent and mass of the disks we follow the commonly used convention where a is the radial scale length and b the vertical scale height (“vertical” means in z -direction). The fraction b/a governs the flatness of the disk, smaller b/a lead to thinner disks. The mass in the disk is ruled by the parameter M_0 . In most cases this is identical to the total



mass M_{total} . For each model we give the volume (surface) density $\varrho(z, r)$ ($\Sigma(r)$), the cumulative mass $M(R)$ (mass inside spherical radius R) and the gravitational potential $\Phi(z, r)$.

- A **Kuzmin disk** describes an infinitely thin disk (see Miyamoto & Nagai 1975 or Binney & Tremaine 1987 and references therein).

$$\begin{aligned}\Sigma(r) &= \frac{aM_0}{2\pi} (r^2 + a^2)^{-3/2}, \text{ here } M_0 = M_{\text{total}} & (3.1) \\ &= \frac{M_0}{2\pi a^2} (r^2/a^2 + 1)^{-3/2},\end{aligned}$$

$$M(r) = M_0 \left[1 - \frac{1}{\sqrt{r^2/a^2 + 1}} \right] \quad (3.2)$$

$$\begin{aligned}\Phi(z, r) &= -\frac{GM_0}{\sqrt{r^2 + (a + |z|)^2}} & (3.3) \\ &= -\frac{GM_0}{a} \frac{1}{\sqrt{r^2/a^2 + (1 + |z|/a)^2}}\end{aligned}$$

- A **Plummer-Kuzmin disk** (PK, or Miyamoto-Nagai disk) is a generalisation of the Kuzmin disk and the Plummer sphere (see Binney & Tremaine 1987 and references therein). It was introduced by Miyamoto & Nagai (1975). For $b = 0$ or $a = 0$ this model reduces to the Kuzmin disk or the Plummer sphere, respectively. Contour plots of the density distribution for several flatness parameters b/a are given in Miyamoto & Nagai (1975).

$$\varrho(r, z) = \frac{M_0 b^2}{4\pi} \cdot \frac{ar^2 + (a + 3\sqrt{z^2 + b^2})(a + \sqrt{z^2 + b^2})^2}{(r^2 + [a + \sqrt{z^2 + b^2}]^2)^{5/2} (\sqrt{z^2 + b^2})^3} \quad (3.4)$$

$$= \frac{M_0 (\frac{b}{a})^2}{4\pi a^3} \cdot \frac{(\frac{r}{a})^2 + \left(1 + 3\sqrt{(\frac{z}{a})^2 + (\frac{b}{a})^2}\right) \left(1 + \sqrt{(\frac{z}{a})^2 + (\frac{b}{a})^2}\right)^2}{\left(\left(\frac{r}{a}\right)^2 + \left[1 + \sqrt{(\frac{z}{a})^2 + (\frac{b}{a})^2}\right]^2\right)^{5/2} \left(\sqrt{(\frac{z}{a})^2 + (\frac{b}{a})^2}\right)^3},$$

here $M_0 = M_{\text{total}}$

$$\begin{aligned}\Phi(z, r) &= -\frac{GM_0}{\sqrt{r^2 + (a + \sqrt{z^2 + b^2})^2}} & (3.5) \\ &= -\frac{GM_0}{a} \frac{1}{\sqrt{\left(\frac{r}{a}\right)^2 + \left(1 + \sqrt{\left(\frac{z}{a}\right)^2 + \left(\frac{b}{a}\right)^2}\right)^2}}\end{aligned}$$

- An **exponential disk** has a very simple density distribution:

$$\varrho(z, r) = \frac{M_0}{4\pi b a^2} \exp\left(-\frac{r}{a}\right) \exp\left(-\frac{|z|}{b}\right), \quad M_0 = M_{\text{total}}. \quad (3.6)$$

The surface density follows from integration over z :

$$\Sigma(r) = \frac{M_0}{2\pi a^2} \exp\left(-\frac{r}{a}\right). \quad (3.7)$$

The potential needs to be computed numerically.

- A **thin exponential disk** is the infinitely thin analogue of the normal exponential disk with a surface density according to Eq. 3.7. The cumulative mass is

$$M(r) = M_0 [1 - \exp(-r/a) (r/a + 1)] \quad (3.8)$$

For this model the potential can be calculated semi-analytically (see Binney & Tremaine 1987).

- In “**softened**” **exponential disks** the exponential function is replaced by 0.5 times secans hyperbolicus. This prevents the cusp at $r = 0$ or $z = 0$ while converging towards the usual exponential profile for larger r or z . E.g. a softened thin exponential disk would be

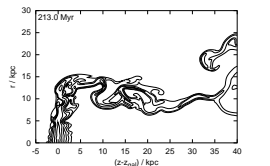
$$\Sigma(r) = \frac{M_0}{2\pi a^2} 0.5 \operatorname{sech}\left(\frac{r}{a}\right). \quad (3.9)$$

Here the total mass is somewhat smaller than M_0 .

The surface density profiles for a Kuzmin disk, a thin exponential disk and a softened thin exponential disk with $a = 4 \text{ kpc}$ and $M_0 = 8 \cdot 10^{10} M_\odot$ are displayed in the left panel of Fig. 3.1. The right panel compares the cumulative masses of the thin exponential and the Kuzmin model. For the Kuzmin model the cumulative mass converges slower towards the total mass than for the exponential model. In Fig. 3.2 profiles of the gravitational potential and the acceleration in z -direction $\frac{\partial\Phi}{\partial z}$ ¹ due to PK disks are compared. The figure demonstrates that the introduction of the finite thickness smoothes the

¹The acceleration in z -direction due to a PK disk is

$$\begin{aligned} \frac{\partial\Phi}{\partial z} &= GM_0 \frac{z (a + \sqrt{z^2 + b^2})}{\left[r^2 + (a + \sqrt{z^2 + b^2})^2\right]^{3/2} \sqrt{z^2 + b^2}} \\ &= \frac{GM_0}{a^2} \frac{\frac{z}{a} \left(1 + \sqrt{\left(\frac{z}{a}\right)^2 + \left(\frac{b}{a}\right)^2}\right)}{\left[\frac{r^2}{a^2} + \left(1 + \sqrt{\left(\frac{z}{a}\right)^2 + \left(\frac{b}{a}\right)^2}\right)^2\right]^{3/2} \sqrt{\left(\frac{z}{a}\right)^2 + \left(\frac{b}{a}\right)^2}} \end{aligned} \quad (3.10)$$



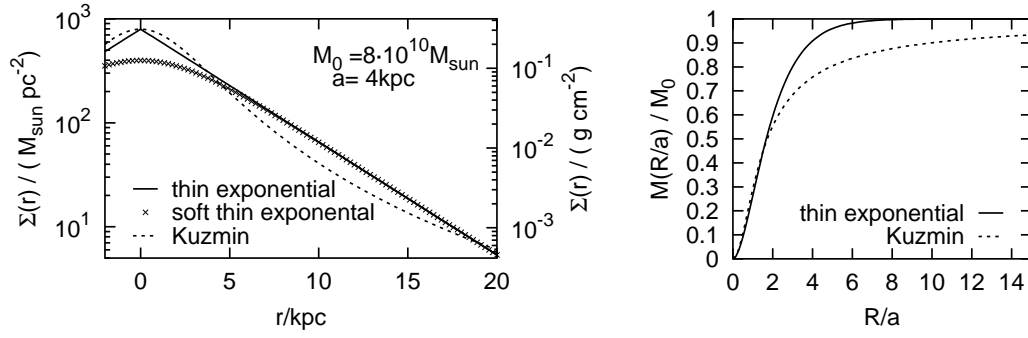


Figure 3.1: **Left:** Surface density profiles for a Kuzmin disk (Eq. 3.1), a thin exponential disk (Eq. 3.7) and a softened thin exponential disk (Eq. 3.9) with identical mass M_0 and scale radius a as given in the plot. **Right:** Comparison of cumulative mass $M(r)$ (mass inside radius r) for a thin exponential and a Kuzmin disk.

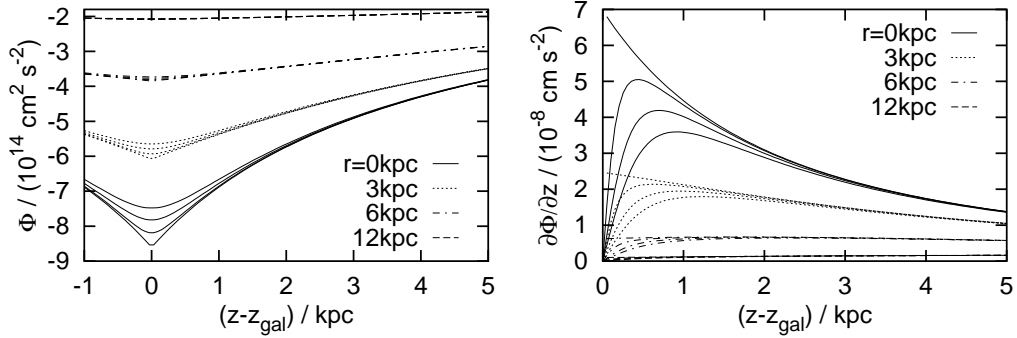


Figure 3.2: **Left:** Potential profiles perpendicular to the disk for PK disks with different scale heights b , at different radii (as given in the plot). The scale radius and mass are the same as in Fig. 3.1. For each radius four profiles are shown, which correspond to $b = 0, 0.2, 0.4, 0.6$ kpc from bottom to top. **Right:** Acceleration in z -direction ($\partial\Phi/\partial z$) for the same potentials as in the left panel, as functions of distance to galactic plane ($z = z_{\text{gal}}$), at different radii. The four lines shown for each radius correspond to $b = 0, 0.2, 0.4, 0.6$ kpc from top to bottom.

Please note that for $b = 0$ (Kuzmin disk) the potential is cusped and that the acceleration profiles are not continuous at $z = 0$. Allowing $b > 0$ softens this behaviour and gives continuous acceleration profiles.

cusps of the potential, and the acceleration profiles are made continuous for all z . The discontinuity at $z = 0$ for the infinitely thin Kuzmin disk (or PK disk with $b = 0$) is a feature that is not desired in numerical simulations. Moreover, it does not provide a good model for the gravitational potential near the disk plane ($z = z_{\text{gal}}$). The same is true for all infinitely thin disks. These models are used best if the potential is needed at larger distances from the disk plane only, where the infinitely thin disk and its finite

analogue converge, as is shown in Fig. 3.2 for the case of a Kuzmin and a PK disk. (We used a PK and a Kuzmin disk for this demonstration as for them the gravitational potential is known analytically.)

For the simulations the stellar disk is described by an exponential model with finite thickness (Eq. 3.6). This model agrees best with observations. For PK disks the density does not decrease fast enough at large r to produce a realistic rotation curve. In addition, for exponential disks the parameters a and b translate very clearly into the disk structure. The scale radius, scale height and total mass for the stellar disk are denoted by a_* , b_* and M_* , respectively.

3.1.2 Stellar bulge

The bulge is modelled following the suggestion of Hernquist (1993). We assume a spherical bulge, which is described by

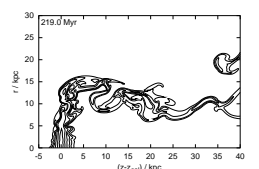
$$\varrho_{\text{bulge}}(R) = \frac{M_{\text{bulge}}}{2\pi} \frac{R_{\text{bulge}}}{R(R + R_{\text{bulge}})^3}, \quad (3.11)$$

where ϱ_{bulge} is the mass density, R_{bulge} is the scale radius of the density distribution and M_{bulge} the total bulge mass.

3.1.3 Dark matter halo

The mass distribution for DM halos can be derived indirectly only. One way is to measure rotation curves, infer the underlying potential and decompose the potential into contributions from the galactic components. Even if a rotation curve is known very accurately, assumptions about the contribution of the baryonic components to the overall potential have to be made, the “rest” of the potential then is ascribed to the DM halo. Usually, either one tries to find the baryon distribution directly from observations, or one uses the “maximum disk” approach, which seeks the solution with the most dominant disk contribution. Another approach to infer the structure of DM halos are cosmological simulations. Below we introduce one model of each kind. DM halos can be triaxial systems, however, as a good approximation the models assume spherical symmetry. The given density distributions $\varrho(R)$, cumulative masses $M(R)$ and potentials $\Phi(R)$ depend on the distance to the halo centre R only. The extent and mass are parametrised by the scale length $R_{0\text{DM}}$ and a central density $\varrho_{0\text{DM}}$, respectively.

- The model of **Burkert** (1995) is based on observed rotation curves of dwarf spiral galaxies. Further work of Persic et al. (1996), Salucci & Burkert (2000) and Borriello & Salucci (2001) using large samples of rotation curves could also confirm this model for massive spirals. (For equations for the potential and cumulative mass see also Mori &



Burkert 2000.)

$$\varrho(R) = \frac{\varrho_{0\text{DM}} R_{0\text{DM}}^3}{(R + R_{0\text{DM}})(R^2 + R_{0\text{DM}}^2)}, \quad (3.12)$$

$$\begin{aligned} \Phi(z, R) = & -\pi G \varrho_{0\text{DM}} R_{0\text{DM}}^2 \times \\ & \left[\pi - 2 \left(1 + \frac{R_{0\text{DM}}}{R} \right) \arctan \left(\frac{R}{R_{0\text{DM}}} \right) \right. \\ & + 2 \left(1 + \frac{R_{0\text{DM}}}{R} \right) \ln \left(1 + \frac{R}{R_{0\text{DM}}} \right) \\ & \left. - \left(1 - \frac{R_{0\text{DM}}}{R} \right) \ln \left(1 + \frac{R^2}{R_{0\text{DM}}^2} \right) \right] \end{aligned} \quad (3.13)$$

$$\begin{aligned} M(R) = & \pi \varrho_{0\text{DM}} R_{0\text{DM}}^3 \times \left[-2 \arctan \left(\frac{R}{R_{0\text{DM}}} \right) \right. \\ & \left. + 2 \ln \left(1 + \frac{R}{R_{0\text{DM}}} \right) + \ln \left(1 + \frac{R^2}{R_{0\text{DM}}^2} \right) \right] \end{aligned} \quad (3.14)$$

According to observations, the core radius $R_{0\text{DM}}$, core mass $M_{0\text{DM}} = M(R_{0\text{DM}})$ and central density $\varrho_{0\text{DM}}$ follow scaling relations, so that Burkert-halos are essentially a one-parameter family.

$$\begin{aligned} \varrho_{0\text{DM}} &= 4.5 \cdot 10^{-2} \frac{M_{\odot}}{\text{pc}^3} \left(\frac{R_{0\text{DM}}}{\text{kpc}} \right)^{-2/3} \\ &= 3 \cdot 10^{-24} \text{ g cm}^{-3} \left(\frac{R_{0\text{DM}}}{\text{kpc}} \right)^{-2/3} \end{aligned} \quad (3.15)$$

$$= 1.46 \cdot 10^{-24} \text{ g cm}^{-3} \left(\frac{M_{0\text{DM}}}{10^9 M_{\odot}} \right)^{-2/7} \quad (3.16)$$

$$M_{0\text{DM}} = 1.6 \varrho_{0\text{DM}} R_{0\text{DM}}^3 = 7.2 \cdot 10^7 M_{\odot} \left(\frac{R_{0\text{DM}}}{\text{kpc}} \right)^{7/3} \quad (3.17)$$

$$R_{0\text{DM}} = 3.07 \text{ kpc} \left(\frac{M_{0\text{DM}}}{10^9 M_{\odot}} \right)^{3/7} \quad (3.18)$$

- **Navarro-Frenk-White (NFW):** An alternative halo form comes from Cold Dark Matter (CDM) simulations performed by Navarro et al. (1996). In contrast to the Burkert-halo, this model shows a central cusp, but at large radii the Burkert-halo and the NFW halo have the same dependence on R .

$$\varrho(R) = \frac{\varrho_{0\text{DM}}}{(R/R_{0\text{DM}})(1 + R/R_{0\text{DM}})^2} \quad (3.19)$$

$$\begin{aligned} M(R) = & 4\pi \varrho_{0\text{DM}} R_{0\text{DM}}^3 \left[(R/R_{0\text{DM}} + 1)^{-1} \right. \\ & \left. + \ln(R/R_{0\text{DM}} + 1) - 1 \right] \end{aligned} \quad (3.20)$$

$$\Rightarrow M(R_{0\text{DM}}) = 2.426 \varrho_{0\text{DM}} R_{0\text{DM}}^3 \quad (3.21)$$

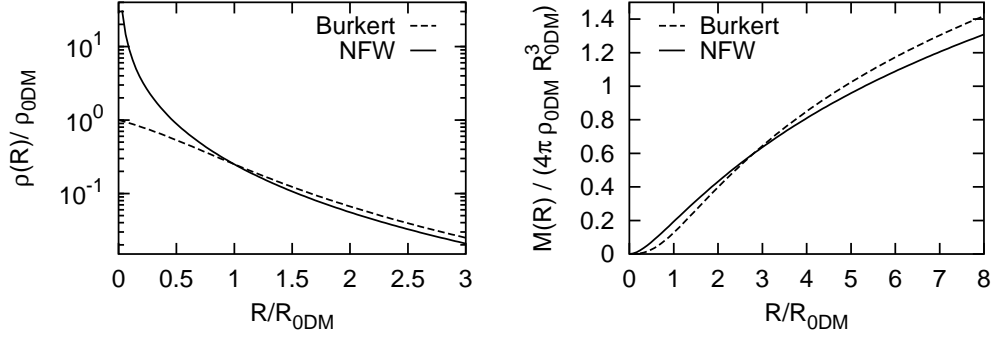


Figure 3.3: Comparison of DM halo models of Burkert (1995) and Navarro et al. (1996) (NFW). **Left:** Density profiles. **Right:** Cumulative masses.

In Fig. 3.3 the density profiles and cumulative mass profiles for both models with identical parameters ρ_{0DM} and R_{0DM} are compared.

A Burkert halo will be used for the simulations, as the potential is known analytically and it is confirmed observationally.

3.1.4 Gas disk

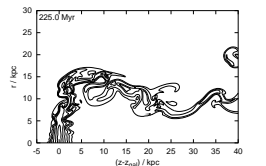
The simulations concentrate on the diffuse component of the ISM (see Sects. 1.2, 1.6), mainly on the HI. According to observations, HI disks show exponential surface density profiles with scale radii of about 5 to 8 kpc. We adopt such a surface density law for the simulations. The most straightforward way to describe the vertical structure is to use an exponential law as well. If the scale height is fixed for the whole disk, this is just the normal exponential disk described by Eq. 3.6. However, HI disks often show a flare, which means that the scale height increases with increasing radius. Therefore we use two gas disk models. In general, for both versions the density and surface density distribution can be written as

$$\varrho(z, r) = \frac{\tilde{M}_{\text{gas}}}{4\pi b_0 a_\Sigma^2} \exp\left(-\frac{r}{a_{\text{gas}}}\right) \exp\left(-\frac{|z|}{b_{\text{gas}}(r)}\right), \quad (3.22)$$

$$\Sigma_{\text{gas}}(r) = \frac{\tilde{M}_{\text{gas}}}{2\pi a_\Sigma^2} \exp\left(-\frac{r}{a_\Sigma}\right), \quad (3.23)$$

where the parameters have the usual meaning (\tilde{M}_{gas} is the total mass of such a density distribution; the reason for the \sim will become clear in a moment). Now there are two options:

1. For a **normal exponential disk** the scale height $b(r)$ is constant, leading to the same model as in Eqs. 3.6 and 3.7. In this case both the density distribution and the surface density have the same scale radius, $a_{\text{gas}} = a_\Sigma$.



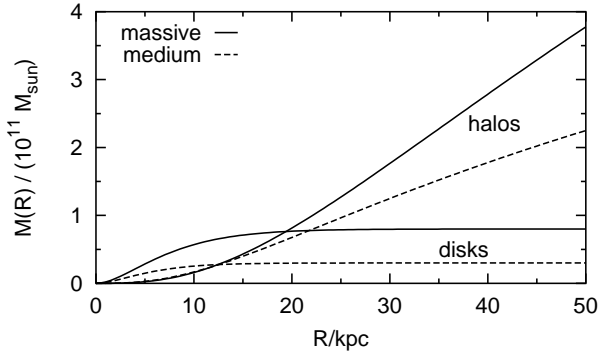


Figure 3.4: Cumulative masses for the stellar disk and the DM halo for the massive and the medium-size galaxy.

2. For a **flared disk**, the scale height b is a function of radius:

$$b(r) = b_0 \exp\left(\frac{r}{r_b}\right). \quad (3.24)$$

In this case a_{gas} and a_{Σ} are not identical but relate to the parameter r_b according to

$$\frac{1}{r_b} = \frac{1}{a} - \frac{1}{a_{\Sigma}} \quad \Leftrightarrow \quad r_b = \frac{a_{\Sigma} a}{a_{\Sigma} - a}. \quad (3.25)$$

To have an unperturbed flow past the galaxy there must be enough space between the outer edge of the gas disk and the r_{max} -boundary of the computational grid (see Sect. 4.3.1). Due to the large a_{Σ} the gas disk would extend to large r , leaving not enough space between the disk edge and the grid boundary, although the grid is already sizable (100 kpc \times 100 kpc, see Sect. 4.3.1). To prevent such problems, we cut the gas disk gradually to a finite radius of 26 kpc. If the disk gets stripped at radii smaller than this, also the parts outside 26 kpc would be stripped, so this does not bias the results. Due to this cut the true mass of the gas disk M_{gas} is a bit lower than what is set by the parameter \tilde{M}_{gas} in Eq. 3.22.

The density distribution of a normal exponential gas disk and a flared one are shown in the left panels of Figs. 3.6 and 3.7, respectively.

3.1.5 Summary of the components

The model type, scale lengths and masses for the individual components of both the massive and the medium mass galaxy are summarised in Table 3.1. The mass given for the gas disk is the mass after truncation (see Sect. 3.1.4). Fig. 3.4 shows cumulative masses for the DM halo and the stellar disk for both the small and the medium size galaxy. In Fig. 3.5 rotation curves for the massive and the medium size galaxy are decomposed into the contributions of the stellar disk, the bulge and the DM halo. The calculation of the rotation velocity is explained in Sect. 3.2.2.

galaxy:		massive	medium
stellar disk (Sect. 3.1.1)		exponential	
	M_*	$8 \cdot 10^{10} M_\odot$	$3 \cdot 10^{10} M_\odot$
	a_*	4 kpc	3 kpc
	b_*	0.25 kpc	0.25 kpc
bulge (Sect. 3.1.2)		Hernquist	
	M_{bulge}	$2 \cdot 10^{10} M_\odot$	$0.8 \cdot 10^{10} M_\odot$
	R_{bulge}	0.4 kpc	0.15 kpc
DM halo (Sect. 3.1.3)		Burkert	
	$R_{0\text{DM}}$	23 kpc	15 kpc
	$\rho_{0\text{DM}}$	$5.56 \cdot 10^{-3} M_\odot \text{pc}^{-3}$	$7.4 \cdot 10^{-3} M_\odot \text{pc}^{-3}$
	$M_{0\text{DM}}$	$1.1 \cdot 10^{11} M_\odot$	$4 \cdot 10^{10} M_\odot$
gas disk (Sect. 3.1.4)		exponential or flared	
	M_{gas}	$0.8 \cdot 10^{10} M_\odot$	$0.3 \cdot 10^{10} M_\odot$
	a_Σ	7 kpc	7 kpc
	(b_{gas})	(0.4 kpc)	(0.4 kpc)
	v_{rot}	200 km s ⁻¹	150 km s ⁻¹

Table 3.1: Model parameters for the massive and the medium mass galaxy. The first line for each component names the model type, subsequent lines list masses, scale radii, scale heights and additional information. See also text (Sects. 3.1.1 to 3.1.5) for further explanations. The value given for b_{gas} is the standard value for the exponential disk. It is varied in the parameter study (see Table 4.1). The value for M_{gas} is the mass of the gas disk after cutting it to the finite radius of 26 kpc.

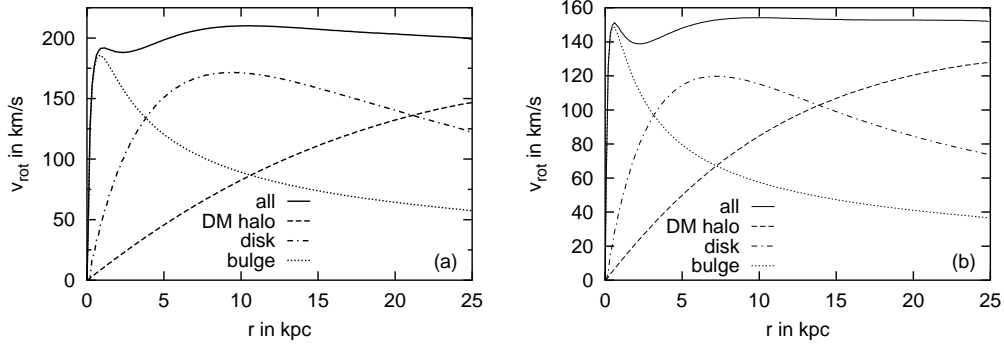
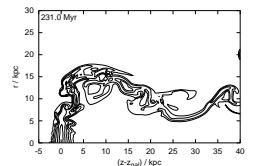


Figure 3.5: Rotation curves and contributions of the single components for the massive (a) and the medium size galaxy (b).

The galaxy models are set symmetrically with respect to the disk plane. The disk plane is placed on the cell wall with $z = z_{\text{gal}}$ (the second option would be to put the disk plane on a cell centre, see Fig. 2.1).

In the course of this work other model options than the ones listed in Table 3.1 have been implemented and tested for feasibility. The densities of the PK disk (for both the stellar and the gas component) and the Burkert



halo had been coded by Lohmann (2000). Now all models introduced in Sects. 3.1.1 to 3.1.4 are available. Also the complete galaxy model of Hernquist (1993) has been implemented for the sake of comparative simulations with B. Vollmer's sticky particle code (see Sect. 6). In addition to the density distributions, analytical potentials have been implemented as far as they exist. For each component with analytical potential an individual choice can be made whether the analytical potential will be used or whether the potential is calculated from the density distribution.

3.2 Stability of the initial model

This work investigates the (destructive) effect of the ICM wind on the gas disk. Therefore it is necessary to start with a model galaxy that is reasonably stable in the absence of a wind. If gravity was the only force affecting the gas it would collapse into the potential. The general idea is to achieve stability by balancing gravitation with rotation in radial direction and gravitation with pressure in vertical direction.

3.2.1 An equilibrium intergalactic medium?

How shall the ICM be set initially? For simulations with constant ICM wind, at least at the inflow boundary the ICM must be set to the nominal density and temperature of the wind. The most straightforward way is to set a homogeneous ICM everywhere outside the galactic gas disk. However, a homogeneous ICM is not in equilibrium with the galactic potential and will collapse into the potential well. This could be prevented by setting the ICM in hydrostatic equilibrium with the galactic potential, but this would be purely for numerical stability reasons. Moreover, a hydrostatic equilibrium configuration would be close to the homogeneous case: At a distance of 5 kpc above the galactic centre a typical amplitude of the vertical potential gradient is about $\Delta\Phi/\Delta R \approx 10^{14} \text{ cm}^2 \text{ s}^{-2}/\text{kpc}$. In case of a hydrostatic equilibrium for a characteristic ICM temperature of 10^7 K this leads to a relative pressure difference of

$$\frac{\Delta p}{p}(z - z_{\text{gal}} = 5 \text{ kpc}) \approx \frac{\Delta\Phi}{kT_{\text{ICM}}/(\mu m_{\text{H}})} = 0.07 \frac{1}{T_{\text{ICM}}/10^7 \text{ K}} \quad (3.26)$$

on a length scale of 1 kpc. At a distance of about 15 kpc from the galactic centre the potential gradient already decreased to $\approx 2.5 \cdot 10^{13} \text{ cm}^2 \text{ s}^{-2}/\text{kpc}$, which reduces the relative pressure change to a factor of about 1.02 on a length scale of 1 kpc. In addition, the thermal energy density of the ICM exceeds the gravitational energy density. The ICM is not bound to the galactic potential. Therefore we choose to set a homogeneous ICM initially, accepting that this configuration is not perfectly stable. The influence of this flaw on the stability is tested in Sect. 3.3.2 and found negligible.

3.2.2 Stability of the gas disk

Stability equations and their numerical solution

The conditions for a stable gas disk can be derived easily from the hydrodynamical equations (Eqs. 2.2 to 2.8). For stability, all time derivatives have to be zero. Initially, all gas shall be at rest ($U = V = 0$). Due to its construction the viscosity tensor (see Sect. 2.3.1) vanishes for zero velocities. With that Eqs. 2.2 to 2.8 reduce to

$$0 = \frac{\partial p}{\partial z} + \varrho \frac{\partial \Phi}{\partial z}, \quad (3.27)$$

$$0 = \frac{\partial p}{\partial r} + \varrho \frac{\partial \Phi}{\partial r} - \varrho \frac{v_{\text{rot}}^2}{r}, \quad (3.28)$$

plus the Poisson-equation (Eq. 2.7) and the equation of state (Eq. 2.8). In Eq. 3.28 the centrifugal force term $-\varrho \frac{v_{\text{rot}}^2}{r}$ would have to be dropped for non-rotating material. What remains are the well known hydrostatic equation (Eq. 3.27) balancing the pressure force and gravitation in vertical direction (perpendicular to the disk); and a similar equation (Eq. 3.28) balancing the pressure force, gravitation and the centrifugal force (if $|v_{\text{rot}}| > 0$) in radial direction. The gravitational potential is given by the Poisson equation (Eq. 2.7).

When the equations are solved numerically, one should use the same discretisation as will be used in the further integration of the hydrodynamical equations (see Chapter 2). First the pressure distribution is computed from the hydrostatic equilibrium (Eq. 3.27). The consistent discretisation is

$$p(IZ) = p(IZ - 1) - \frac{\varrho(IZ) + \varrho(IZ - 1)}{2} \cdot (\Phi(IZ) - \Phi(IZ - 1)). \quad (3.29)$$

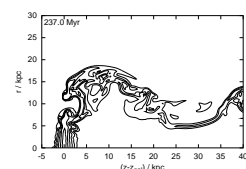
The variable IZ enumerates the cells in z -direction. This kind of discretisation ensures that the pressure force and gravitational force cancel *at the cell wall* (see Sect. 2.2 and Fig. 2.1).

The hydrostatic equilibrium alone demands a certain pressure gradient only. To fix the level of the pressure profile, a boundary value is needed. For an isolated galaxy this is $p(z = \infty) = 0$, leading to the lowest-possible non-negative pressure and temperature distribution. The temperature distribution is calculated from the equation of state (Eq. 2.8).

Finally, for the ISM (identified by $\varrho > \varrho_{\text{ICM}}$) stability in r -direction is ensured by setting the correct rotation velocity. Equation 3.28 leads to

$$v_{\text{rot}} = \sqrt{r \left(\frac{1}{\varrho} \frac{\partial p}{\partial r} + \frac{\partial \Phi}{\partial r} \right)} \quad \text{or} \quad (3.30)$$

$$L = \varrho r \sqrt{r \left(\frac{1}{\varrho} \frac{\partial p}{\partial r} + \frac{\partial \Phi}{\partial r} \right)} \quad (3.31)$$



for angular momentum density $L = \varrho v_{\text{rot}} r$. The contribution of the pressure gradient to the rotation velocity is very small, the rotation velocity is determined mainly by the gradient in Φ . The consistent discretisation of Eq. 3.31 (ensuring force balance at the *cell wall*) is

$$L(IR) = 2\bar{\varrho} \sqrt{r^3(IR) \left(\frac{1}{\bar{\varrho}} \frac{\Delta p}{\Delta r} + \frac{\Delta \Phi}{\Delta r} \right)} - L(IR - 1) \quad (3.32)$$

with $\bar{X} = \frac{X(IR) + X(IR - 1)}{2}$ and $\Delta X = X(IR) - X(IR - 1)$,

where IR enumerates the grid cells in r -direction and the barred values are the averages at the *cell walls*. The radius $r(IR)$ is the radius at a *cell wall*, see Fig. 2.1. In analogy to Eq. 3.29 this is a successive solution. The obvious choice for the boundary value is $v_{\text{rot}}(r = 0) = 0$. This procedure can be applied straightforwardly to exponential disks, but there is a problem for flared disks. E.g. consider a radial cut through the disk at $z = 2$ kpc in Fig. 3.7. The innermost part ($r \lesssim 3$ kpc) belongs to the ICM, where $v_{\text{rot}} = 0$. Therefore the boundary value in such cases cannot be given at $r = 0$, but at the smallest r that is inside the ISM. This starting value can be calculated from a direct discretisation of Eq. 3.31:

$$L(IR) = \varrho(IR) \sqrt{r^3(IR + 1/2) \left[\frac{1}{\varrho(IR)} \frac{\Delta p}{\Delta r} + \frac{\Delta \Phi}{\Delta r} \right]} \quad (3.33)$$

with² $\Delta X = 0.5 [X(IR + 1) - X(IR - 1)]$,

where $r(IR + 0.5)$ is the radius of a *cell centre*, see Fig. 2.1. Using the direct discretisation for all r is not consistent with the discretisation of the Eulerian equations in the code (see Chapter 2). Therefore we use the consistent discretisation (Eq. 3.32) as far as possible.

Equilibrium between the ICM and the gas disk

The simulations do not deal with isolated galaxies but with galaxies embedded in the hot ICM. To be stable, the gas disk needs to be in pressure equilibrium with the surrounding ICM. Therefore the boundary value for Eq. 3.29 is not $p(z = \infty) = 0$ like for isolated galaxies, but at the boundary between the ICM and the gas disk the pressure must be p_{ICM} . We show the density distribution and the resulting temperature distribution and rotation field for the massive galaxy with a normal exponential disk in Fig. 3.6. For this case the ICM particle density and temperature are $n_{\text{ICM}} = 1.56 \cdot 10^{-5} \text{ cm}^{-3}$ and $T_{\text{ICM}} = 4.4 \cdot 10^7 \text{ K}$, respectively. The same is shown for a flared disk in Fig. 3.7 and for the medium-mass galaxy with a normal exponential disk in Fig. 3.8.

Profiles of the density, surface density, pressure, temperature and rotation

²Here the ΔX are centred at *cell centres* and not at *cell walls* as in Eq. 3.32. However, for Δr this distinction is irrelevant, because the grid has a constant spacing.

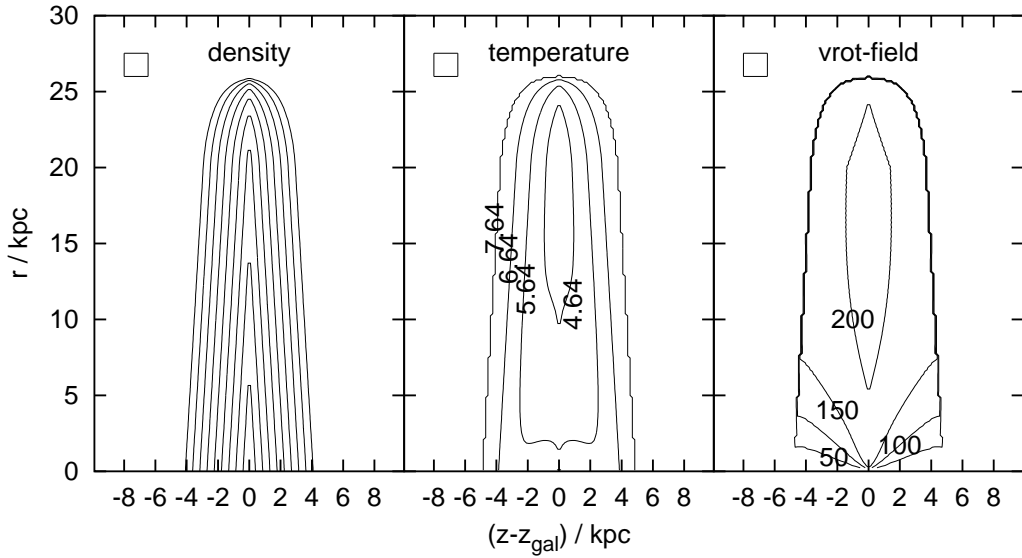


Figure 3.6: Contour plots for the density (left), temperature (middle) and rotation field (right) for the massive galaxy with a simple exponential disk (see left column of Table 3.1). The ICM particle density and temperature are $n_{\text{ICM}} = 1.56 \cdot 10^{-5} \text{ cm}^{-3}$ and $T_{\text{ICM}} = 4.4 \cdot 10^7 \text{ K}$, respectively. Both the density and the temperature contours have a logarithmic spacing. For the density plot there is one contour line every half order of magnitude, with the innermost contour at $10^{-24} \text{ g cm}^{-3}$. For the temperature the spacing of the contour lines is one order of magnitude; the contours are labelled in units of $\log_{10}(T/\text{K})$. In the velocity field the contours are labelled in km s^{-1} . The gas disk is set symmetrically with respect to the disk plane ($z = z_{\text{gal}}$). The box in the top left corner demonstrates the size of 10×10 grid cells (resolution 153 pc). Corresponding radial profiles can be found in Fig. 3.9.

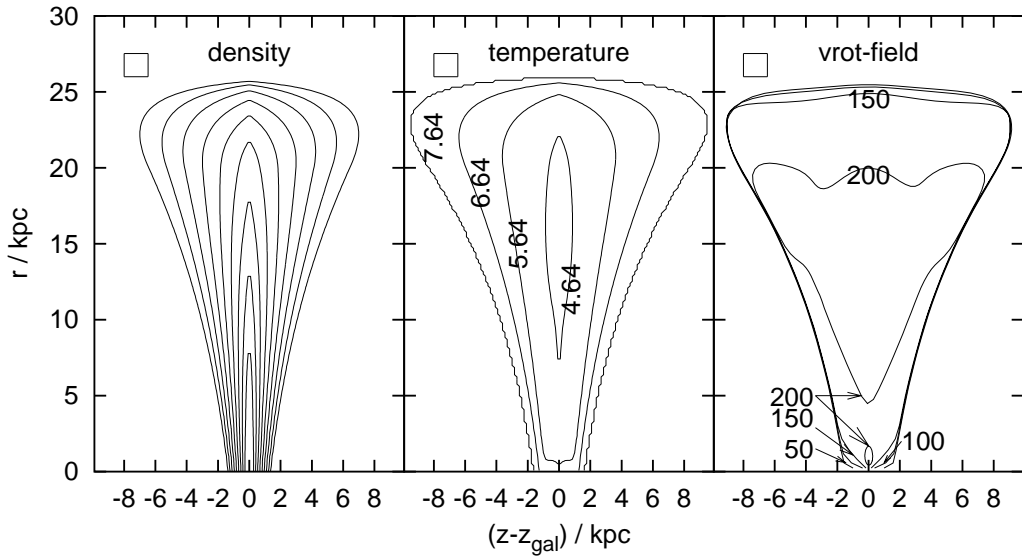
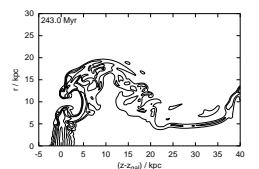


Figure 3.7: Same as Fig. 3.6 for the massive galaxy with a flared disk.



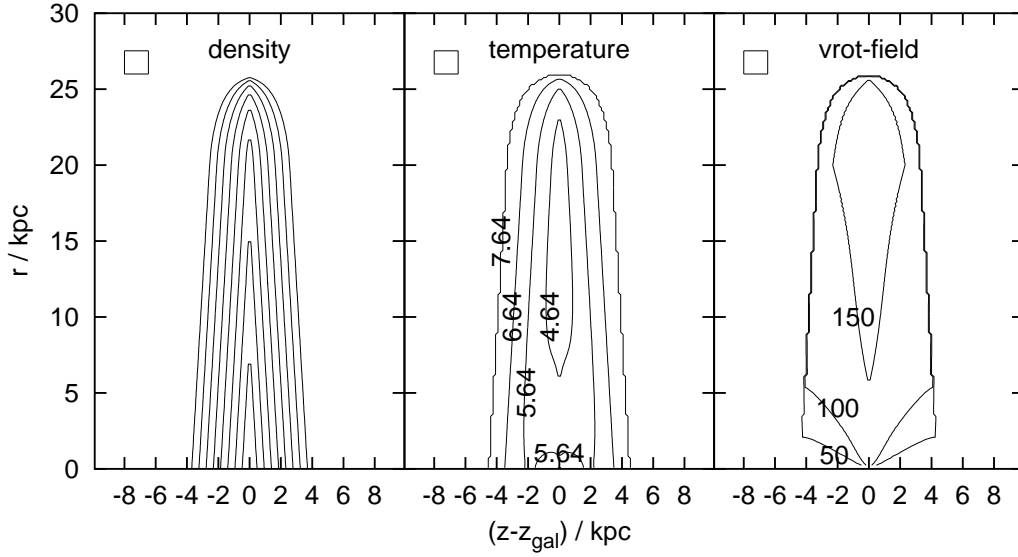


Figure 3.8: Same as Fig. 3.6 for the medium-mass galaxy.

velocity along the galactic plane for various disk models are summarised in Fig. 3.9.

The ICM pressure p_{ICM} in the cases shown in Figs. 3.6 to 3.9 is relatively low. What happens if the p_{ICM} increases? To stay in equilibrium, the pressure in the gas disk must increase. There are two options how the disk can achieve this: Either, if the temperature distribution is fixed (e.g. by heating-cooling balance), the disk is compressed. The density increases and the disk becomes thinner. Or, if the density distribution is fixed, the disk temperature must increase. This behaviour is demonstrated in Fig. 3.10, which shows pressure and temperature profiles along the galactic plane for several p_{ICM} . The profiles for the case with the lowest p_{ICM} (solid lines in Fig. 3.10) are representative for the solution in case of an isolated galaxy. With increasing p_{ICM} , the pressure and temperature in most parts of the gas disk have to increase up to one or two orders of magnitude above the level typical for isolated galaxies. Only the inner 2 to 3 kpc remain unaffected. In Fig. 3.11 we repeat density, temperature and rotation velocity contours for the massive galaxy, but for an ICM pressure a factor of 100 higher than in Fig. 3.6 (now $n_{\text{ICM}} = 1.56 \cdot 10^{-3} \text{ cm}^{-3}$ and $T_{\text{ICM}} = 4.4 \cdot 10^7 \text{ K}$).

There is an important point to learn here: The ICM pressure in clusters can easily reach values of $10^{-11} \text{ erg cm}^{-3}$, which is higher than the pressure in the disk of an isolated galaxy at radii larger than 7 kpc. Simply from comparing typical pressures in gas disks of normal (isolated) galaxies and in the ICM we can conclude that normal gas disks cannot exist in a dense cluster environment, because they could not be in pressure equilibrium.

This conclusion raises a problem for RPS simulations with constant winds. In cases where dense, hot winds shall be simulated, initially the galaxy needs to be set into a high pressure ICM. However, we have just deduced that

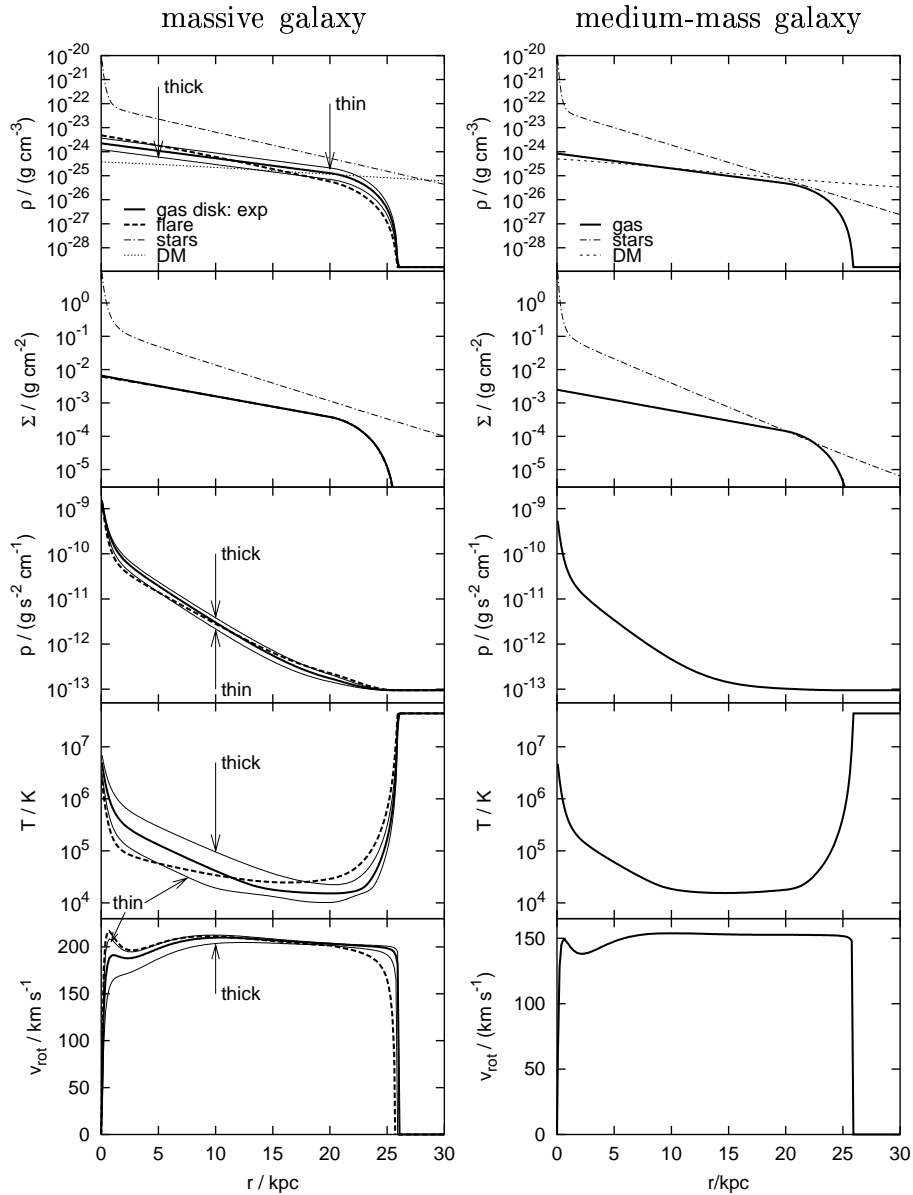
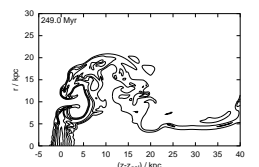


Figure 3.9: Profiles along the galactic plane. From top to bottom: First panels: densities of the gas disk, the stellar components (disk+bulge), and the DM halo. Second panels: surface density for the gas disk and the stellar components. The subsequent panels show the pressure p , temperature T and rotation velocity v_{rot} for the gas disk.

In the **left** column all quantities are shown for the massive galaxy for the case of a normal exponential disk (heavy solid lines), thick and thin exponential disk (thin solid lines, see Sect. 4.1.2) and a flared disk (heavy dashed lines). The surface density is the same for all cases. The heavy lines correspond to the cases shown in Figs. 3.6 and 3.7. The **right** column is for the medium-mass galaxy; the profiles correspond to Fig. 3.8.



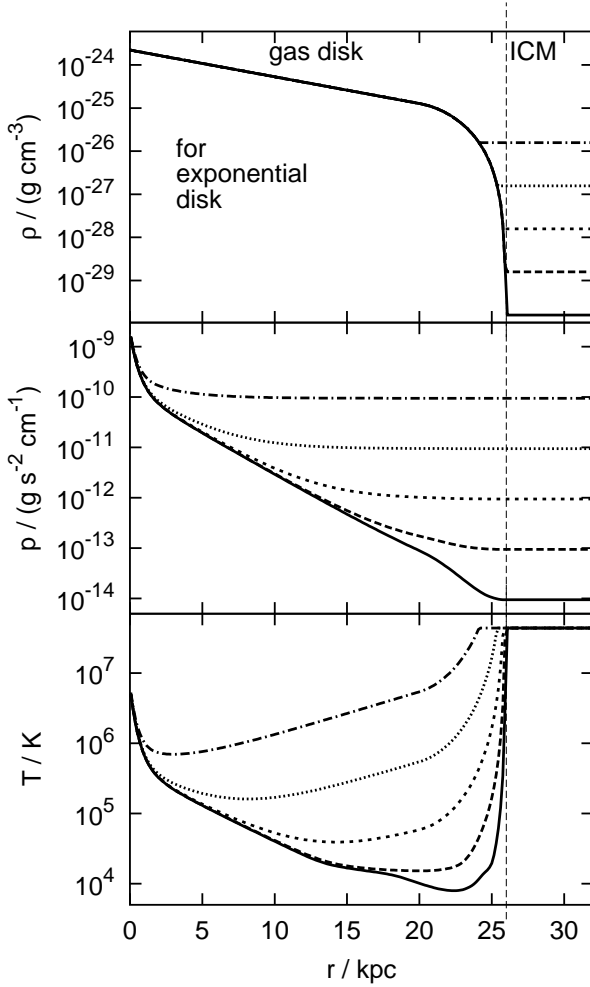


Figure 3.10: Profiles of the density ρ , pressure p and temperature T along the galactic plane, as they result from the hydrostatic equilibrium for different ICM densities (shown by different line styles). The profiles are shown for the case of an exponential gas disk. The density profile was fixed, so it does not change with changing ICM density. The ICM densities, pressures and temperature can be read from the plot on the rhs of the dashed vertical line (the ICM temperature was the same in all cases). This plot demonstrates how everywhere except in the very centre the pressure in the gas disk adapts to the ICM pressure. See text for discussion (Sect. 3.2.2).

a normal galaxy cannot be in equilibrium with a high pressure ICM, or vice versa, an equilibrium model does not resemble a normal spiral. Either it is too thin or too hot. The more correct way would be to simulate a whole cluster passage, i.e. starting in a low pressure ICM and varying the wind density, pressure and velocity. Nonetheless we stick to constant wind simulations in order to keep the parameter space as clear as possible. The simulation of a cluster passage is one of the next steps for the future. So for the simulations with constant wind we proceed as follows: To allow a systematic parameter scan we specify the density distribution and accept the varying disk temperatures. Keeping in mind that the disks are presumably compressed when they enter a cluster, we study disks of various thicknesses. In how far the unrealistically high pressure and temperature profiles influence the results is discussed in Chapter 5.

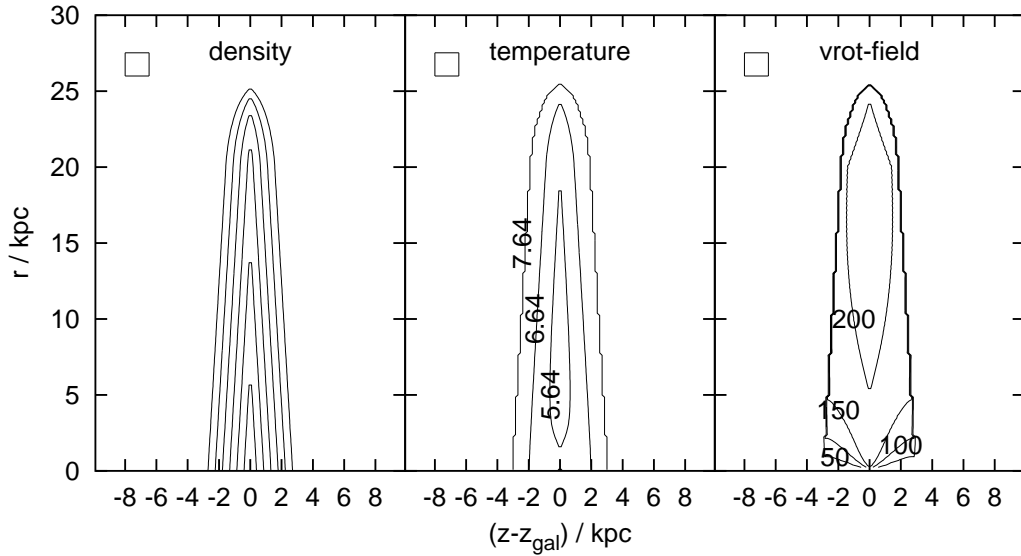


Figure 3.11: Same as Fig. 3.6 but different ICM ($n_{\text{ICM}} = 1.56 \cdot 10^{-3} \text{ cm}^{-3}$, $T_{\text{ICM}} = 4.4 \cdot 10^7 \text{ K}$). These contours correspond to dotted profiles in Fig. 3.10). The number of contour lines is smaller here than in Fig. 3.6, as here ρ_{ICM} is higher than in the case shown in Fig. 3.6.

3.3 Testing the initial model

3.3.1 Resolution

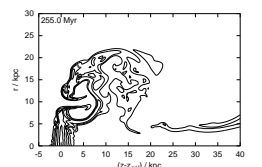
The solution of the equilibrium initial model that is described and shown in the previous sections depends only slightly on resolution. We tested resolutions from 600 pc to 100 pc. Further resolution tests for simulations with winds are described in Appendix D.1.

3.3.2 Stability

In order to test the stability of the initial model we perform test runs with the ICM at rest. As discussed in Sect. 3.2.1, the surrounding ICM was *not* set in equilibrium with the galactic potential and therefore it must collapse into the potential well. The stability tests are also used to check how much the collapse flow in the ICM influences the gas disk. The setup for the case shown here is:

- massive galaxy with standard exponential gas disk,
- ICM: $n_{\text{ICM}} = 1.56 \cdot 10^{-4} \text{ cm}^{-3}$, $T_{\text{ICM}} = 4.4 \cdot 10^7 \text{ K}$,
- resolution 150 pc, grid size 30 kpc \times 30 kpc.

Snapshots of the temporal evolution of the gas density distribution are displayed in Fig. 3.12. The evolution of vertical and radial profiles is shown in



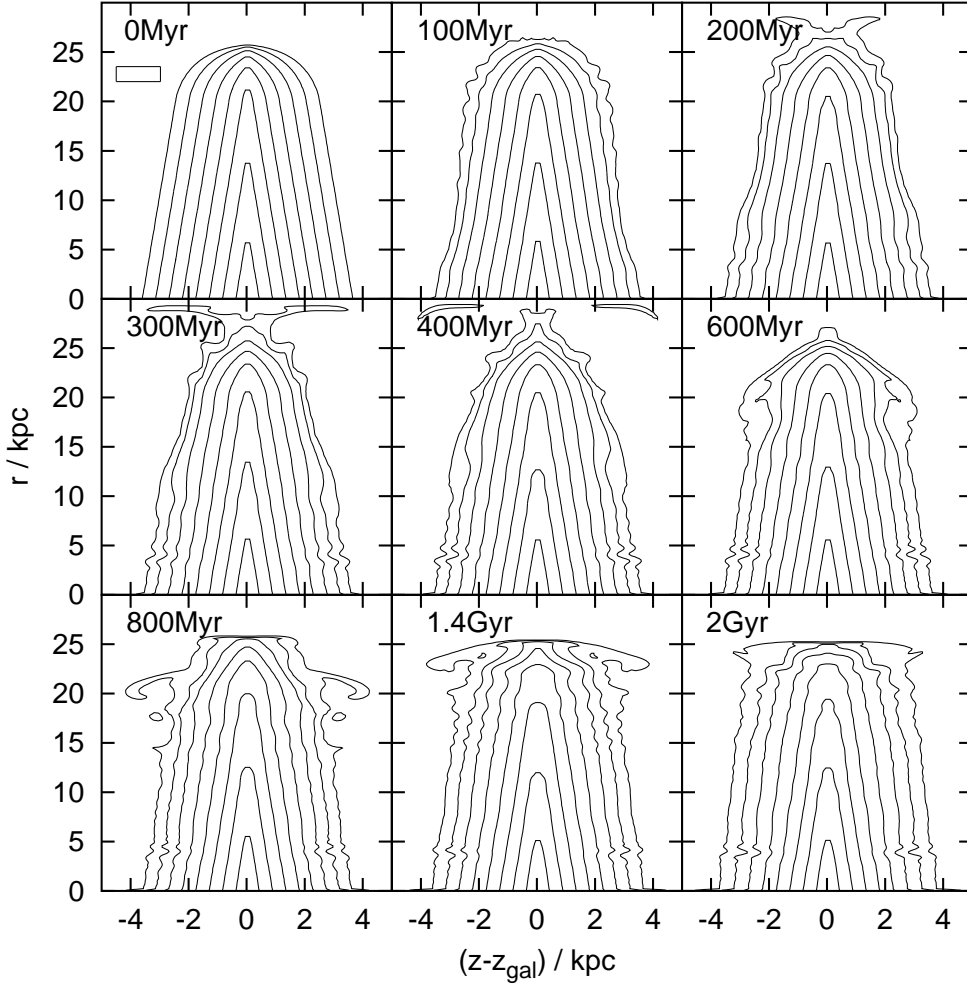


Figure 3.12: Snapshots of the stability test. The density distribution is shown in logarithmic contours like in Fig. 3.6. ICM parameters are $n_{\text{ICM}} = 1.56 \cdot 10^{-4} \text{ cm}^{-3}$ and $T_{\text{ICM}} = 4.4 \cdot 10^7 \text{ K}$. The box in the top left corner of the first panel shows the size of 10×10 cells (resolution 150 pc). Please note that the axes have different scales.

Figs. 3.13 and 3.14, respectively. Velocities in the ICM reach a few percent of the ICM sound speed. Due to the collapsing ICM first the outer layers of the gas disk are slightly compressed, as can be seen in the snapshot of 100 Myr and the corresponding profiles. The ICM oscillates slowly between contraction and expansion. When the expansion flow reaches the grid boundaries, gas is lost from the grid, which results in a slow decrease of the ICM density and pressure. Therefore, towards the end of the simulation, the gas disk thickens slightly as the ICM pressure decreases. While the resulting ICM flow is parallel to the disk surface, small Kelvin-Helmholtz instabilities (see Appendix B) are produced in the outmost layers of the gas disk. In the turn of the simulation the inner disk regions are hardly affected at all, but

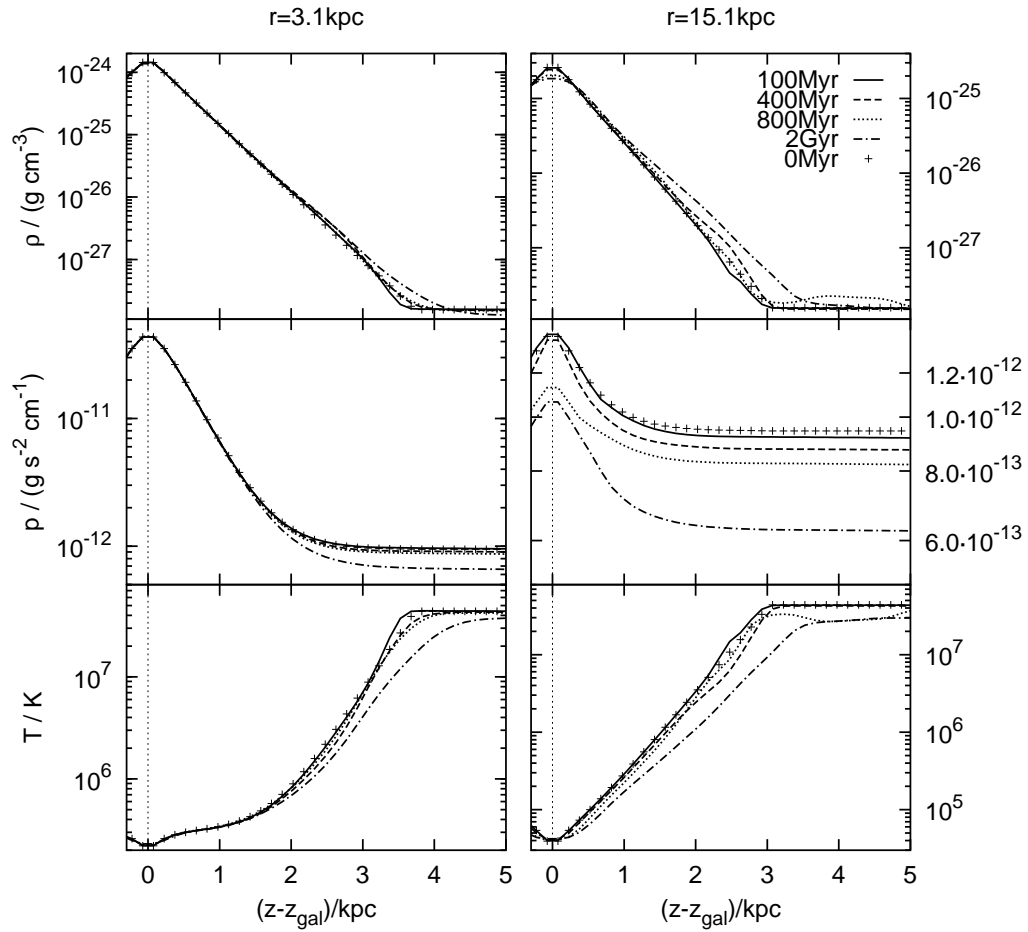
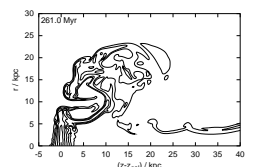


Figure 3.13: Evolution of vertical profiles of density ρ , pressure p and temperature T at two radii (as indicated above the columns) for the stability test. Only one half of the profiles is shown as they are symmetric with respect to the disk plane ($z = z_{\text{gal}}$, indicated by the dotted vertical line). The profiles correspond to Fig. 3.12.

the outermost edge of the gas disk is perturbed and truncated slightly. After a runtime of 2 Gyr the disk radius is reduced from 26 kpc to 25 kpc.

Despite the fact that the model galaxy is not perfectly stable, it has passed the stability test. Compared to the time scales involved in RPS events (see Sects. 4.2 and 4.4), the evolution during the stability test is very slow. The destruction of the gas disk produced during simulations with ICM winds can be assigned to the wind and is not caused by an unstable setup.



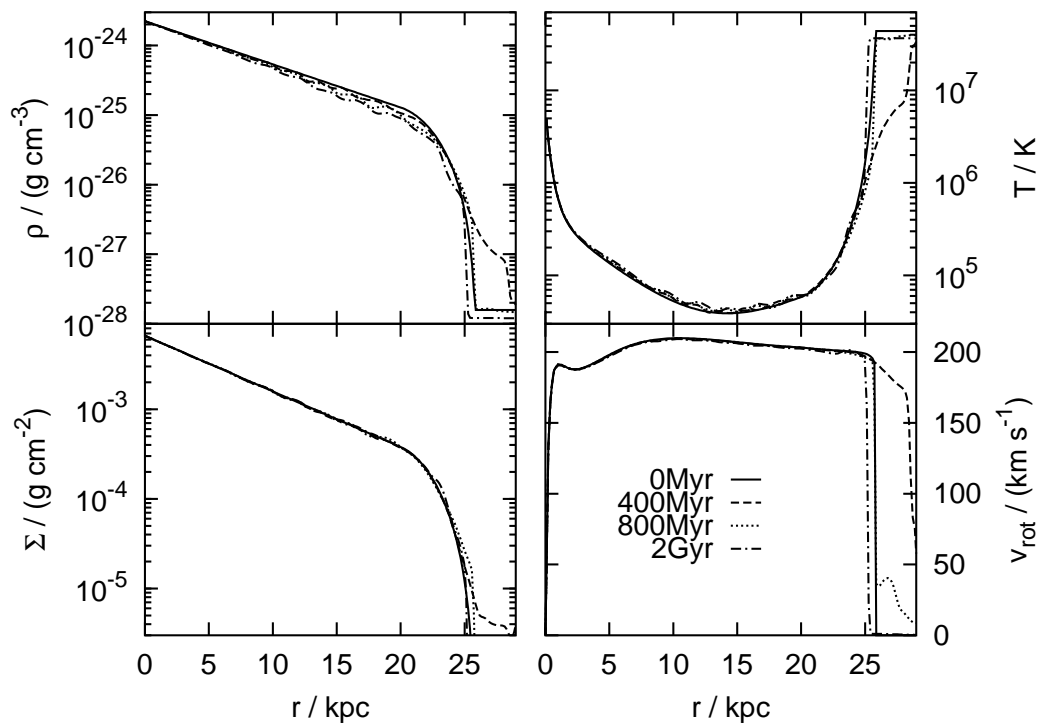


Figure 3.14: Evolution of radial profiles of density ρ , surface density Σ , temperature T and rotation velocity v_{rot} in the stability test. The profiles correspond to Fig. 3.12.

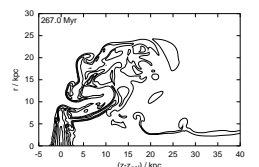
Chapter 4

Simulations and results

Performing simulations is not a linear process. Numerical parameters like grid size and resolution need to be chosen. Test runs have to be performed for a first impression of what is going on at all. The planned range of reasonable physical parameters needs to be scanned coarsely to make sure that everything works. Then the numerical parameters need to be reconsidered and possibly rechosen. One has to verify that they are chosen appropriately. A detailed plan of all simulations to be done needs to be drawn up. Probably on the way one hits on some bug in the code, fixes that, and has to redo at least some runs. So doing simulations is a rather iterative business. Hopefully at some point all bugs are fixed, the optimal numerical parameters are set, the plan for the simulation runs is revised and accepted, and the data production can begin. It is not the aim of a thesis to document all the steps just mentioned. For the presentation of the results we choose the following order: In Sect. 4.1 we give an overview of the performed simulations and explain the strategy how the physical parameter space is scanned. In Sect. 4.2 we make some analytical estimates. Section 4.3 describes the general setup for the simulations. The appropriate choice of the numerical parameters is verified in Appendix D. In Sect. 4.4 we describe the general behaviour of the simulations. Section 4.5 introduces some analysis techniques. The results of varying both ICM wind parameters and galactic parameters are presented in Sects. 4.6 to 4.8. In Sect. 4.9 the analytical estimate and the numerical results are compared. Finally, Sect. 5 gives a brief summary.

4.1 Overview of performed simulations

The main purpose of this work is to investigate how the mass loss from the gas disk due to RPS depends on the strength of the ICM wind and on the galaxy itself. Therefore one needs to vary ICM parameters and/or galaxy properties. For the wind, different densities, velocities and temperatures are considered. Concerning the galaxy, the vertical structure of the gas disk is modified with respect to disk shape (normal exponential and flared, see



Sect. 3.1.4) and scale height. In addition, some runs are repeated for a less massive galaxy.

4.1.1 Wind parameters

To investigate the influence of the wind strength we expose the massive galaxy with a standard gas disk (exponential, $b_{\text{gas}} = 0.4 \text{ kpc}$) to different ICM winds. These winds resemble conditions reaching from the centres to the outskirts of galaxy clusters.

Typical velocities of cluster galaxies (and hence the wind velocities) are of the same order as the sound speed of the ICM. The ICM temperatures in clusters range between 10^7 K and 10^8 K . As the standard ICM temperature we choose $T_{\text{ICM1}} = 4.385 \cdot 10^7 \text{ K}$. With a mean molecular weight of $\mu = 0.6$ for the ionised ICM this temperature corresponds to a sound speed of 1000 km s^{-1} . For some simulations a lower ICM temperature of $T_{\text{ICM2}} = T_{\text{ICM1}}/\sqrt{10} = 1.39 \cdot 10^7 \text{ K}$ corresponding to a sound speed of $1000 \text{ km s}^{-1}/\sqrt[4]{10} = 562 \text{ km s}^{-1}$ is used. ICM particle densities n_{ICM} range from 10^{-5} to a few 10^{-3} cm^{-3} . We additionally include extreme cases for the density to be able to scan the ICM parameter space systematically.

For the sake of suitable numbers we use the specific ram pressure

$$\tilde{p}_{\text{ram}} = n_{\text{ICM}} v_{\text{ICM}}^2 \quad (4.1)$$

in units of $\text{cm}^{-3} \text{ km}^2 \text{ s}^{-2}$. It relates to the ram pressure p_{ram} through

$$\begin{aligned} p_{\text{ram}} &= \mu \cdot \text{amu} \cdot \tilde{p}_{\text{ram}} \quad (\text{amu} = \text{atomic mass unit}) \\ &= 1.002 \cdot 10^{-14} \text{ erg cm}^{-3} \frac{\tilde{p}_{\text{ram}}}{\text{cm}^{-3} \text{ km}^2 \text{ s}^{-2}}. \end{aligned} \quad (4.2)$$

In Fig. 4.1 we show isolines of \tilde{p}_{ram} in the $(v_{\text{ICM}}, n_{\text{ICM}})$ plane. The simulations cover a range from 10 to 10 000 $\text{cm}^{-3} \text{ km}^2 \text{ s}^{-2}$ in \tilde{p}_{ram} (10^{-13} to $10^{-10} \text{ erg cm}^{-3}$ in p_{ram}).

The pairs of $(v_{\text{ICM}}, n_{\text{ICM}})$ used for the simulations are marked in Fig. 4.1. For both T_{ICM} every \tilde{p}_{ram} is covered by four different combinations of v_{ICM} and n_{ICM} , two in the subsonic and two in the supersonic regime. Moreover, we combined T_{ICM} , v_{ICM} and n_{ICM} so that the velocities $v_{\text{ICM}} = 253, 450, 800, 1423, 2530 \text{ km s}^{-1}$ correspond to Mach numbers 0.253, 0.45, 0.8, 1.423, 2.53 for T_{ICM1} , and to Mach numbers 0.8, 1.423, 2.53, 4.5 for T_{ICM2} , respectively. This enables us to distinguish whether the Mach number plays a role or whether the effect of RPS depends on p_{ram} alone. E.g. a wind with a velocity of 800 km s^{-1} can be studied once for the case this velocity corresponds to Mach 0.8 and once to Mach 1.423.

4.1.2 Influence of the galactic parameters

In this work we focus on two aspects of the galaxy. First we address the question whether the stripping efficiency is determined solely by the gas

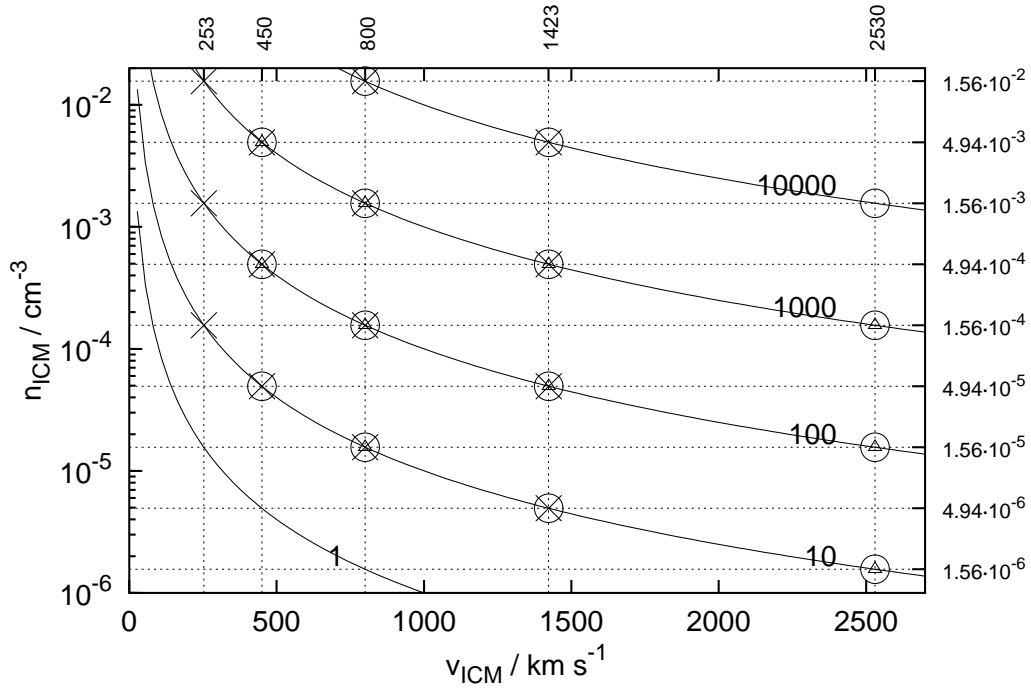
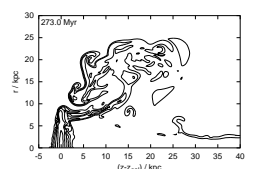


Figure 4.1: Models in the $v_{\text{ICM}}-n_{\text{ICM}}$ plane. Contours of constant specific ram pressure \tilde{p}_{ram} are plotted with a spacing of one order of magnitude. The lines are labelled with \tilde{p}_{ram} in units of $\text{cm}^{-3} \text{km}^2 \text{s}^{-2}$. The open circles mark the $(v_{\text{ICM}}, n_{\text{ICM}})$ pairs used for the simulations with the massive galaxy and $T_{\text{ICM}1}$. The triangles mark the winds used for simulations of the medium mass galaxy and the same T_{ICM} . The crosses mark the winds used for the massive galaxy and $T_{\text{ICM}2}$. See also Sects. 4.1.1 and 4.1.2.

surface density as suggested by the Gunn & Gott criterion (Eq. 1.13), or if the vertical structure of the gas disk plays a role. The second point of interest is the influence of the total mass of the galaxy.

Influence of the vertical structure of the gas disk

To study the influence of the shape and thickness of the gas disk on the RPS efficiency we expose exponential and flared gas disks with different scale heights b_{gas} to some representative ICM winds. The simulations done for this point of interest are listed in Table 4.1. We refer to exponential disks with $b_{\text{gas}} = 0.2, 0.4, 0.8$ kpc as “thin”, “standard” and “thick”, respectively. Radial profiles for (surface) density, pressure, temperature and rotation velocity for gas disks of various thicknesses and shapes are compared in Fig. 3.9.



$\tilde{p}_{\text{ram}}/$ ($\text{cm}^{-3} \text{ km}^2 \text{ s}^{-2}$)	$v_{\text{ICM}}/$ (km s^{-1})	$n_{\text{ICM}}/$ (cm^{-3})	gas disk model	$b_{\text{gas}}/$ kpc
1000	800	$1.56 \cdot 10^{-3}$	exp	0.2, 0.4, 0.8
.	.	.	flared	0.2, 0.4
1000	2530	$1.56 \cdot 10^{-4}$	exp	0.2, 0.4, 0.8
.	.	.	flared	0.2
100	800	$1.56 \cdot 10^{-4}$	exp	0.2, 0.4, 0.8
.	.	.	flared	0.2
100	2530	$1.56 \cdot 10^{-5}$	exp	0.2, 0.4, 0.8
.	.	.	flared	0.2

Table 4.1: Parameters for the simulations testing the influence of the vertical structure of the gas disk (see Sect. 4.1.2). Common to all these runs are the massive galaxy, T_{ICM1} , $t_{\text{switch}} = 20 \text{ Myr}$ (see Sect. 4.3.2). The “.” means the same value as in the previous line. The value given for b is $b(r = 5 \text{ kpc})$. For the simple exponential disk this value is valid for all r ; for the flared disk $b(r)$ changes according to Eq. 3.24.

Influence of galaxy mass

In order to check the results for a smaller galaxy we rerun a subset of simulations with a medium-mass galaxy (see right column of Table 3.1). The wind velocities and particle densities used here are marked in Fig. 4.1 by small open triangles, the ICM temperature used for the medium-mass galaxy is T_{ICM1} .

4.2 Analytical estimate

As discussed by previous authors (e.g. Mori & Burkert 2000; Marcolini et al. 2003), the ICM-ISM interaction can be divided into two sub-processes: instantaneous stripping and continuous stripping. The first process is determined by the force balance between the ram pressure and the gravitational resistance. Depending on the strength of the ram pressure, the outer gas disk down to a radius r_{strip} should be pushed away in a relatively short time (see Sect. 4.2.1). In contrast, continuous (turbulent viscous) stripping has a rather long time scale (see Sect. 4.2.2). Due to the different time scales of the two subprocesses the overall process should appear to proceed in two phases, first the instantaneous stripping, followed by the continuous stripping phase.

4.2.1 Instantaneous stripping

As mentioned in the introduction, for face-on cases Gunn & Gott (1972) suggested to compare the ram pressure p_{ram} and the gravitational restoring force per unit area in z -direction $f_{\text{grav}}(r)$ to estimate which part of the gas

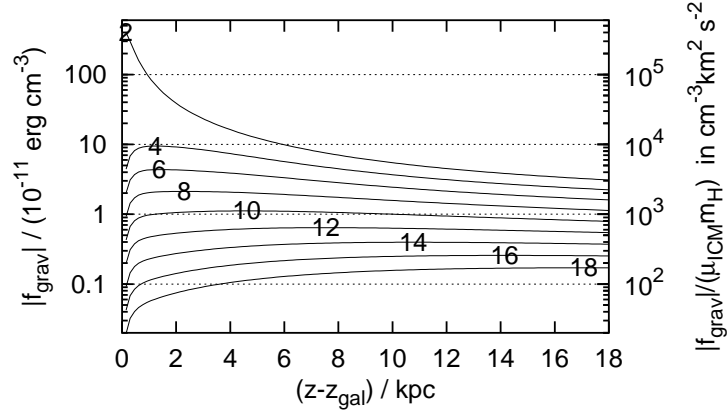


Figure 4.2: Profiles of the gravitational restoring force per unit area in z -direction $f_{\text{grav}}(z, r)$ behind the disk, at different radii r . Each profile is labelled with its cutting radius in kpc. The label is placed at the maximum of the particular profile. Please note that for larger r the strongest gravitational resistance is far behind the disk. For comparison, the right y-axis is labelled in units of $\text{cm}^{-3} \text{km}^2 \text{s}^{-2}$ (unit of \tilde{p}_{ram}).

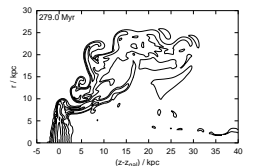
disk will be pushed out by the ICM wind: at radii r where

$$p_{\text{ram}} = \rho_{\text{ICM}} v_{\text{ICM}}^2 > |f_{\text{grav}}(r)| = \left| \Sigma_{\text{gas}}(r) \frac{\partial \Phi}{\partial z} \right|, \quad (4.3)$$

the gas should be stripped. We consider this estimate a bit closer here. A crucial point is the assumption that the gas disk is thin enough so its mass distribution can be represented solely by its surface density $\Sigma_{\text{gas}}(r)$. Secondly, the gravitational acceleration in z -direction at any position is $\frac{\partial \Phi}{\partial z}(z, r)$. So, strictly speaking,

$$|f_{\text{grav}}(z, r)| = \left| \frac{\partial \Phi}{\partial z}(z, r) \Sigma_{\text{gas}}(r) \right|, \quad (4.4)$$

is the gravitational force per unit area in z -direction that works on the gas disk at radius r if this gas disk is shifted to position z in the galactic potential. We point this out in such detail, because for a given r , $f_{\text{grav}}(z, r)$ changes with z . E.g. in the most simple case, in the disk plane ($z = z_{\text{gal}}$) the acceleration due to the gravitational potential is $\frac{\partial \Phi}{\partial z} = 0$ and so is the restoring force. In Fig. 4.2 we plot profiles of $f_{\text{grav}}(z, r)$ perpendicular to the galactic plane (in z -direction), on the downstream side of the galaxy, for different radii. As expected, for small radii the restoring force is strongest. Interestingly, with increasing r the maximum of $f_{\text{grav}}(z)$ is located at increasingly large distances from the galactic plane. So for radii > 10 kpc the maximum of $f_{\text{grav}}(z)$ is *outside* (in z -direction, i.e. above/below the disk) the initial gas disk (this feature was already mentioned briefly by Schulz & Struck 2001). Which $f_{\text{grav}}(z)$ should be used for the estimation of r_{strip} ? Two plausible choices are possible: either to use the maximal $f_{\text{grav}}(z)$ *inside* the original



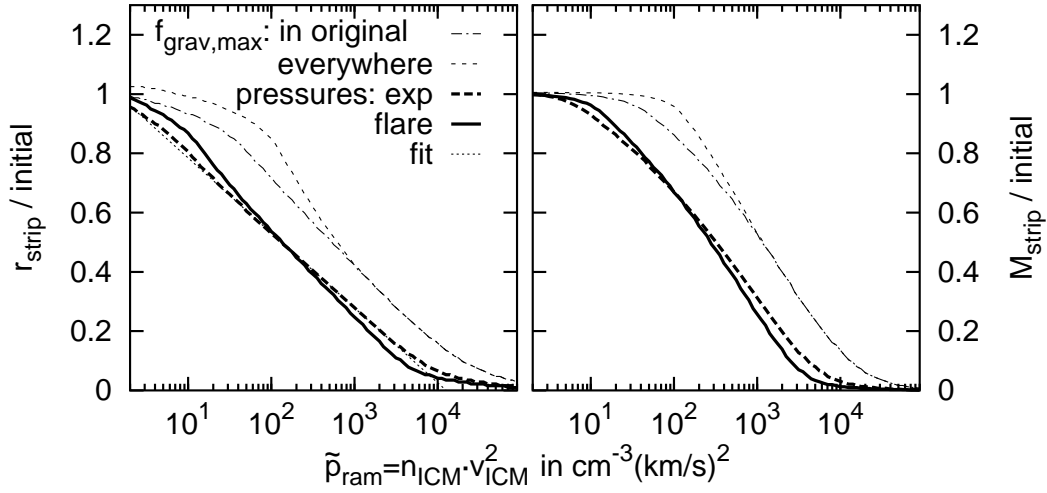


Figure 4.3: Analytical estimate of stripping radius r_{strip} and mass M_{strip} of the remaining gas disk after the instantaneous stripping as a function of \tilde{p}_{ram} . The thin dash-dotted and short-dashed lines are derived from comparing the gravitational restoring force f_{grav} with the ram pressure. The dash-dotted line uses the maximum of $f_{\text{grav}}(z)$ inside the original gas disk, the short-dashed line is the estimate using $f_{\text{grav}}(z)$ at any z . The solid and long-dashed thick lines are derived from comparing the thermal pressure in the galactic plane with the ram pressure for the flared and the exponential disk, respectively. See also Sect. 4.2. The dotted line is the fit to the result of the pressure comparison for the exponential disk according to Eq. 4.14.

gas disk, or to use the maximal $f_{\text{grav}}(z)$ at any z . For the comparison of p_{ram} and $f_{\text{grav}}(r)$ the two versions can lead to different results at radii $\gtrsim 10$ kpc.

At the stripping radius r_{strip} , p_{ram} and $f_{\text{grav}}(r)$ are equal. For smaller r the gas is retained in the galaxy as $p_{\text{ram}} < f_{\text{grav}}(r)$, for larger r the gas will be lost because $p_{\text{ram}} > f_{\text{grav}}(r)$. The resulting r_{strip} as a function of \tilde{p}_{ram} is shown in the left panel of Fig. 4.3 for the standard massive galaxy for both versions of $f_{\text{grav}}(z)$ (thin short-dashed and dashed-dotted lines). The right panel shows the mass of the gas disk remaining after the instantaneous stripping M_{strip} , i.e. all gas at radii smaller than r_{strip} . The estimates according to the two versions differ only for lower \tilde{p}_{ram} , and the difference is small.

We note that for gas disks with larger scale heights the assumption that the mass distribution is represented well enough by the surface density alone may be wrong. In this case the gravitational restoring force per unit area on a gas package of volume ΔV is

$$\begin{aligned}
 |f_{\text{grav}}(z, r)| &= \left| \frac{\partial \Phi}{\partial z}(z, r) \frac{\rho_{\text{gas}}(r) \Delta V}{\Delta A} \right| \\
 &= \left| \frac{\partial \Phi}{\partial z}(z, r) \rho_{\text{gas}}(r) \Delta z \right|, \quad (4.5)
 \end{aligned}$$

where ΔA is the surface of the gas package perpendicular to the wind direction and Δz is the length of this package in wind direction. To obtain an upper limit, for $\varrho_{\text{gas}}(r)$ the density in the galactic plane is used. It is not obvious which value should be used for Δz , so that this is rather a free parameter (which should be somewhere between the grid resolution and the overall thickness of the disk). If the scale height b_{gas} is the same for all radii r , the expression in Eq. 4.5 is proportional to the one in Eq. 4.4, but smaller; Eq. 4.4 would overestimate the restoring force. With f_{grav} from Eq. 4.5, the predicted $r_{\text{strip}}(\tilde{p}_{\text{ram}})$ has the same shape as before (using Eq. 4.4), but is shifted in horizontal direction towards lower \tilde{p}_{ram} . If however the gas disk is flared, the expressions in Eqs. 4.4 and 4.5 are not proportional and the analytical estimates of $r_{\text{strip}}(\tilde{p}_{\text{ram}})$ would have different shapes.

Mori & Burkert (2000) suggest an alternative criterion for the stripping efficiency for spherical galaxies, namely a spherical galaxy will be stripped completely if the ram pressure exceeds the thermal pressure in the galactic centre. we modify this estimate for the application to disk galaxies. Given the radial thermal pressure profile $p_0(r)$ in the galactic plane of an *isolated* galaxy (as shown in Fig. 3.10), the gas will be stripped from radii r where

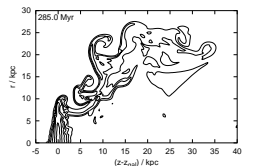
$$p_{\text{ram}} > p_0(r). \quad (4.6)$$

Again, r_{strip} is the radius where $p_{\text{ram}} = p(r)$. The result from this estimate is also shown in Fig. 4.3 for both the exponential and the flared disk (heavy dashed and solid lines, respectively). As the pressure profiles for both cases are similar, also the functions $r_{\text{strip}}(\tilde{p}_{\text{ram}})$ are similar. The difference between the pressure profiles for the different disk scale heights (thick and thin disks) is not larger than the difference between the pressure profiles for the flared and the exponential disk (see Fig. 3.9). Hence the profile for the medium scale height is representative for all thicknesses. Interestingly, the shape of the function $r_{\text{strip}}(\tilde{p}_{\text{ram}})$ is very similar to the shape of the estimate from the Gunn & Gott criterion, but the result from the pressure comparison is offset towards smaller ram pressures, indicating that $p_0(r) < f_{\text{grav,max}}(r)$. This can be understood analytically. The pressure in the galactic plane at a certain radius $p_0(r)$ derived from hydrostatics (for an isolated galaxy, i.e. $p(\pm\infty) = 0$) is

$$p_0(r) = \int_{-\infty}^{z_{\text{gal}}} -\frac{\partial\Phi}{\partial z}(z) \varrho(z) dz. \quad (4.7)$$

The calculation of $|f_{\text{grav}}|$ uses the steepest potential gradient $|\frac{\partial\Phi}{\partial z}(r)|_{\text{max}}$ and the surface density (the gas disk is symmetrical with respect to the disk plane)

$$\Sigma(r) = \int_{-\infty}^{\infty} \varrho(z) dz = 2 \int_{-\infty}^{z_{\text{gal}}} \varrho(z) dz. \quad (4.8)$$



Herewith $|f_{\text{grav}}(r)|$ from Eq. 4.4 reads

$$|f_{\text{grav}}(r)| = \int_{-\infty}^{z_{\text{gal}}} 2 \left| \frac{\partial \Phi}{\partial z}(r) \right|_{\text{max}} \varrho(z) dz. \quad (4.9)$$

As in Eqs. 4.7 and 4.9 all functions are positive in the integral range and as $\left| \frac{\partial \Phi}{\partial z} \right|_{\text{max}} \geq -\frac{\partial \Phi}{\partial z}$ in this range, it follows that

$$|f_{\text{grav}}(r)| \geq 2p_0(r). \quad (4.10)$$

For the galaxy model here both quantities relate as $f_{\text{grav}}(r) \approx 4p_0(r)$.

The time scale for the instantaneous stripping t_{strip} can be estimated from the simple uniformly accelerated motion. With a constant acceleration $a \approx p_{\text{ram}}/\Sigma_{\text{gas}}$ a body that starts with zero velocity moves the distance s during the time

$$t_{\text{strip}} = \sqrt{\frac{2s}{a}} = \sqrt{\frac{2s\Sigma_{\text{gas}}}{p_{\text{ram}}}} \quad (4.11)$$

$$\begin{aligned} &= 56 \text{ Myr} \left(\frac{s}{5 \text{ kpc}} \right)^{1/2} \left(\frac{\Sigma_{\text{gas}}}{10^{-3} \text{ g cm}^{-2}} \right)^{1/2} \\ &\quad \times \left(\frac{\tilde{p}_{\text{ram}}}{1000 \text{ cm}^{-3} \text{ km}^2 \text{ s}^{-2}} \right)^{-1/2}. \end{aligned} \quad (4.12)$$

We assume here that a gas package is stripped when it has reached a distance of 5kpc from the disk plane. Stripping time scales range from a few 10 Myr for stronger ram pressures to a few 100 Myr for very weak ones. In the medium galaxy the surface density is about a factor of 0.38 lower, hence the corresponding stripping time scale for the medium galaxy should be about a factor of $\sqrt{0.38} \approx 0.6$ shorter. This estimate only holds where the gravitational deceleration is small compared to the ram pressure acceleration, i.e. for large ram pressures or at large radii.

4.2.2 Continuous stripping

During the continuous stripping phase the Kelvin-Helmholtz (KH) instability works on the surface of the gas disk. Some estimates concerning stability criteria for the KH-instability are summarised in Appendix B. For the simple perturbation theory applied in Appendix B all fluids are assumed to be incompressible, which is clearly not a valid assumption for flows with Mach numbers around 1, as pointed out by Nulsen (1982). Taking the compressibility of the gas and the finite width of the boundary layer into account, Nulsen (1982) estimated the maximal mass loss rate of a spherical cloud of radius R in an ICM wind to

$$\dot{M} \approx 20 M_{\odot} \text{ yr}^{-1} \left(\frac{R}{20 \text{ kpc}} \right)^2 \left(\frac{n_{\text{ICM}}}{10^{-3} \text{ cm}^{-3}} \right) \left(\frac{v_{\text{ICM}}}{1000 \text{ km s}^{-1}} \right). \quad (4.13)$$

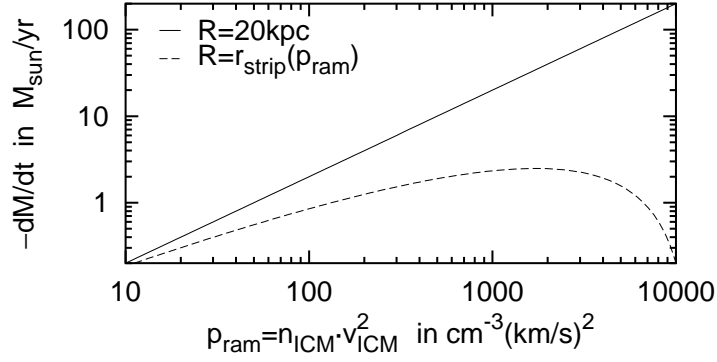


Figure 4.4: Analytical estimate of the mass loss rate for the continuous stripping. The solid line shows the result if a constant radius for the gas disk is assumed, the dashed line shows the reduced mass loss rate if r_{strip} as a function of \tilde{p}_{ram} is used (Eq. 4.14). Both functions are shown for $v_{\text{ICM}} = 1000 \text{ km s}^{-1}$. One has to keep in mind that this estimate is only rough, as it is derived for a spherical and not a disk galaxy.

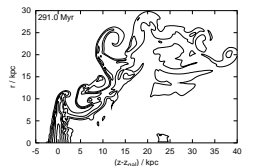
Although this estimate was derived for spheres, also a rough estimate for disks can be deduced. Apart from the geometry, for the face-on wind flowing past a disk galaxy, the radius of the remaining gas disk depends on the strength of the wind, as the gas disk is truncated quickly by the instantaneous stripping. Over a wide range of ram pressures the stripping radius can be fitted by

$$\begin{aligned} \frac{r_{\text{strip}}}{r_0} &= 1.037 - 0.253 \log_{10} \left(\frac{\tilde{p}_{\text{ram}}}{\text{cm}^{-3} \text{ km}^2 \text{ s}^{-2}} \right) \quad \text{or} \\ \frac{r_{\text{strip}}}{\text{kpc}} &= 25.44 - 6.2 \log_{10} \left(\frac{\tilde{p}_{\text{ram}}}{\text{cm}^{-3} \text{ km}^2 \text{ s}^{-2}} \right), \end{aligned} \quad (4.14)$$

as is shown in Fig. 4.3. One can rearrange Eq. 4.13 to

$$\begin{aligned} \dot{M} &\approx 20 M_{\odot} \text{ yr}^{-1} \left(\frac{R}{20 \text{ kpc}} \right)^2 \times \\ &\quad \left(\frac{\tilde{p}_{\text{ram}}}{10^3 \text{ cm}^{-3} \text{ km}^2 \text{ s}^{-2}} \right) \left(\frac{v_{\text{ICM}}}{10^3 \text{ km s}^{-1}} \right)^{-1} \end{aligned} \quad (4.15)$$

and replace R by $r_{\text{strip}}(\tilde{p}_{\text{ram}})$, thus deriving a rough estimate for the mass loss rate for a disk. Fig. 4.4 compares the predicted mass loss rates of the continuous stripping as a function of \tilde{p}_{ram} for $v_{\text{ICM}} = 1000 \text{ km s}^{-1}$ for a constant R on the one hand, and for $R = r_{\text{strip}} = r_{\text{strip}}(\tilde{p}_{\text{ram}})$ on the other hand. If we take into account that the radius is truncated by the instantaneous stripping, the mass loss rate is reduced significantly. However, this estimate can only be rough as it was derived for spherical bodies instead of disks. Beyond that the dependence on v_{ICM} (see Eq. 4.15) introduces a further factor. So we can only estimate that the mass loss rate due to the continuous stripping is of the



order of one $M_{\odot} \text{ yr}^{-1}$. With this number the time scale for the continuous stripping

$$t_{\text{visc}} = \frac{M_{\text{gas}}(t=0)}{\dot{M}} \quad (4.16)$$

is of the order of several Gyr.

4.3 General simulation setup

4.3.1 Grid size and resolution

The choice of the grid size and resolution is governed by contradicting demands. First of all, the numerical grid must be large enough so that the boundaries do not disturb the flow. Some experience concerning this point can be gained from the test of a potential flow past a sphere (see Appendix C.3). With the aid of a few more test runs of the actual RPS, we decided to use a grid size of $100 \text{ kpc} \times 100 \text{ kpc}$ and place the galaxy at a distance of 40 kpc from the inflow boundary ($z_{\text{gal}} = 40 \text{ kpc}$). With a galaxy radius of $r_{\text{gal}} = 26 \text{ kpc}$, in radial direction the distance between the grid boundary and the galaxy is about $3r_{\text{gal}}$. The distance from the galaxy to the inflow and outflow boundaries is about $2r_{\text{gal}}$.

The resolution must be good enough to resolve all important processes. However, higher resolution increases the working memory as well as the runtime. Resolution tests showed that 650^2 grid cells, corresponding to a resolution of 153 pc are sufficient. In this configuration the code uses about 360 MB working memory. The runtime to simulate an evolution of 2 Gyr with the standard wind ($\tilde{p}_{\text{ram}} = 1000 \text{ cm}^{-3} \text{ km}^2 \text{ s}^{-2}$, Mach number 0.8 , T_{ICM1}) is about 15 h on the vector machine NEC SX-5. The machine as a theoretical peak performance of 4 GFLOPS (FLOPS=floating point operations per second) per processor. Due to a high degree of vectorisation the code reaches 1.7 GFLOPS .

The simulations evolve the gas disk in the ICM wind for 2 Gyr . The gravitational potential is fixed during the simulations. The grid parameters are summarised in Table 4.2. We demonstrate in Appendix D.1 that this choice of grid size and resolution is appropriate. Appendix D.3 shows that the assumption of a static potential does not bias the results.

Given the fact that a large part of the grid is occupied by the more or less structure-poor ICM, a resolution of 150 pc is not needed in most parts of the computational area, it is needed solely to resolve the galactic gas. For such problems Adaptive Mesh Refinement (AMR) codes were developed, which use a coarse resolution in general but a high resolution where required. However, making the grid-refinement self-adaptive and passing information between grid levels is not an easy task. Using a conventional available hydro-code had the advantage that it was ready to apply, so this work could concentrate on the astrophysical aspect instead of on code development. Due to

physical grid size	$z_{\max} \times r_{\max}$	100 kpc \times 100 kpc
number of grid cells	$NZ \times NR$	650 \times 650
distance of galaxy from inflow boundary	z_{gal}	40 kpc
resolution	$\Delta z = \Delta r$	153 pc
runtime		2 Gyr
boundary at r_{\max} :		solid
boundary at $z = 0$:		inflow
boundary at $z = z_{\max}$:		open (see also Sect. 4.3.2)

Table 4.2: Numerical parameters: Grid size and resolution, simulation runtime, boundary conditions (for further explanations see Sect. 2.5).

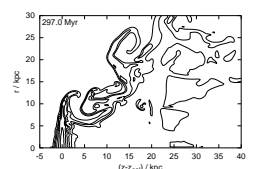
the simplifying assumption of rotational symmetry which allows to perform the simulations in 2D, and due to the high degree of vectorisation reached with this code, the simulations can still be done with very reasonable computational effort. However, for 3D simulations it would be highly advisable to use an AMR code.

4.3.2 Wind initialisation

Usually for simulations of e.g. spherical clouds in a wind a potential flow around this cloud is used as the initial condition. For the simulations here this is not possible because the simulations shall be done for Mach numbers 0.45 to 2.53, and the potential flow is only a solution for small Mach numbers. At least for the supersonic runs it just makes no sense to start with a “potential” flow. To keep the simulations comparable, we want to start all cases in the same way. The easiest way is to start with a galaxy at rest and then increase the inflow velocity.

So initially all gas is set to be at rest. To start the simulation we increase the ICM velocity at the inflow boundary and the outflow boundary linearly over the time interval t_{switch} from zero to the final value v_{ICM} . Afterwards the inflow conditions are kept at the inflow boundary, and the downstream side boundary switches to the usual open boundary condition (if v_{ICM} is supersonic, the outflow velocity at the downstream side boundary was only increased up to Mach 0.9 and then this boundary switched to the open condition).¹ So t_{switch} is the time during which the simulation is “switched on”.

¹In contrast to the expectation from the potential flow test (Appendix. C.3), this method did not lead to a satisfactory flow for small Mach numbers. Here, in contrast to a flow past a solid sphere, the obstacle to the flow is not solid but reacts to the flow. Smaller Mach numbers also mean a lower ram pressure, and hence the size of the obstacle for the flow (namely the gas disk) remains considerable throughout the simulation. The problem that arises is that the true wind velocity comes out a bit smaller than what is set, whereas the wind density is a bit larger. However, the momentum flux ρv is correct. Hence also the true ram pressure ρv^2 is reduced by the same factor as v . To achieve the nominal flow,



Two contradicting demands make it difficult to choose this parameter. On behalf of a smooth flow t_{switch} should be as long as possible, at best a few grid crossing times (see Appendix C.3). On the other hand, we expect that the galaxy responds to the ram pressure on short time scales (a few 10 Myr, see Sect. 4.2.1). Therefore t_{switch} should be rather short in order to resolve this time scale. As this choice is not straightforward, we ran some representative cases with different t_{switch} and found that the influence of this parameter is negligible (see Appendix D.2). For the simulations $t_{\text{switch}} = 20$ Myr was used.

4.4 General behaviour of the simulations

For an impression of the temporal evolution of the stripping process you can find snapshots of the gas disk in 6 Myr time steps in the bottom right corners of the odd pages. The density distribution is displayed in logarithmic contours like in Fig. 3.6. In addition, Figs. 4.5, 4.6 and 4.7 show colour-coded snapshots for a strong subsonic, a strong supersonic and a weak subsonic wind, respectively. The flip book corresponds to the case of Fig. 4.5.

The ICM-ISM stripping proceeds in three phases:

Instantaneous stripping: First the outer gas disk, down to a certain radius, is bent towards the downstream side of the galaxy. The appearance of the gas disk in this phase is very similar to the state shown in the first panels with $t > 0$ Myr in Figs. 4.5 to 4.7. The time scale on which the bending takes place is determined by the ram pressure. It reaches from a few 10 Myr for high to about 200 Myr for low ram pressures. Also the radius down to which the disk is bent depends on the strength of the ram pressure. Reasonably, for higher ram pressures only a small inner part is retained, and for low ram pressures only the outer edge is bent, but the disk is affected even for very small ram pressures. In all cases a large part of the matter that is pushed out of its original position is still bound.

Intermediate phase: The first phase is followed by a quite dynamical intermediate phase, during which the bent-out part of the disk breaks up. A fraction of the material that is pushed out is now stripped completely and a part falls back to the original disk region. This back-fall always happens in the lee of the galaxy, where the displaced gas is protected against the wind, but near the disk edge. Figure 4.8 demonstrates this situation by showing only galactic gas that had left the disk region at some time (see Sect. 4.5). Gas that is now seen inside the original disk region has fallen back. In this dynamic phase substantial amounts of bound ISM can be found behind the original disk. This feature was

for the runs with Mach number 0.45 the following recipe was used: No active outflow is set at the outflow boundary. For the initial ICM and at the inflow boundary wind parameters slightly off the nominal values are set so that the true wind is close to the nominal one.

already noticed by Schulz & Struck (2001). The duration of this phase depends on the ram pressure. For high ram pressures it is short (a few 100 Myr), for low ram pressures this phase continues for the rest of the simulation (up to 2 Gyr).

Continuous stripping: Actually the continuous stripping – the peeling off of the outer disk layers of the upstream side of the gas disk by the Kelvin-Helmholtz (KH) instability – works on the gas disk from the beginning on. However, the effect of this process is quite small, so that it is not distinct before the first two phases are finished. During the simulations the state of pure continuous stripping is only reached for stronger ram pressures, as for weaker ones the intermediate phase is as long as the runtime. Even though the effect of the continuous stripping is small, it slowly decreases the mass and the radius of the remaining gas disk.

Typical for the supersonic runs is a stagnant region in the wake of the galaxy, where gas with low density, that is still bound to the galaxy, tends to linger (see final stage in Fig. 4.6).

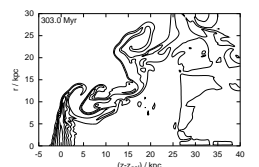
In all runs bound gas can be found at quite large distances (10 to 15 kpc) behind the galaxy during the instantaneous stripping phase and the intermediate dynamic phase. For lower ram pressures some gas packages are still bound at distances of 20 kpc behind the galaxy. Bound gas is enclosed in the heavy black contour in Figs. 4.5 to 4.7.

Another feature that appears in all simulations is the fluttering of the outer edge of the galaxy. The KH-instability pulls low density tongues along the upstream side of the remaining gas disk from the centre towards the edge. There these pieces of gas are exposed to the full wind and blown away (see e.g. last panel in Fig. 4.5). This procedure repeats continuously and leads to an oscillation in the radius of the gas disk $r_{\text{disk}}(t)$ (see e.g. Fig. 4.10 in Sect. 4.5.3).

The evolution of the density in the galactic plane and the surface density profile are shown in Fig. 4.9 for a stronger and for a weak subsonic wind. As long as a substantial part of the gas disk remains, neither the density profile nor the surface density in the inner part change much. However, we observe a compression of the outer layers on the upstream side of the gas disk (see Sect. 4.7). For low ram pressures only the very outer layers are compressed, for stronger winds the compression goes deeper towards the galactic plane.

4.5 Analysis techniques – gas disk mass and radius

For all simulations we need to calculate the mass and radius of the remaining gas disk. Concerning the fate of the stripped gas, the code can trace



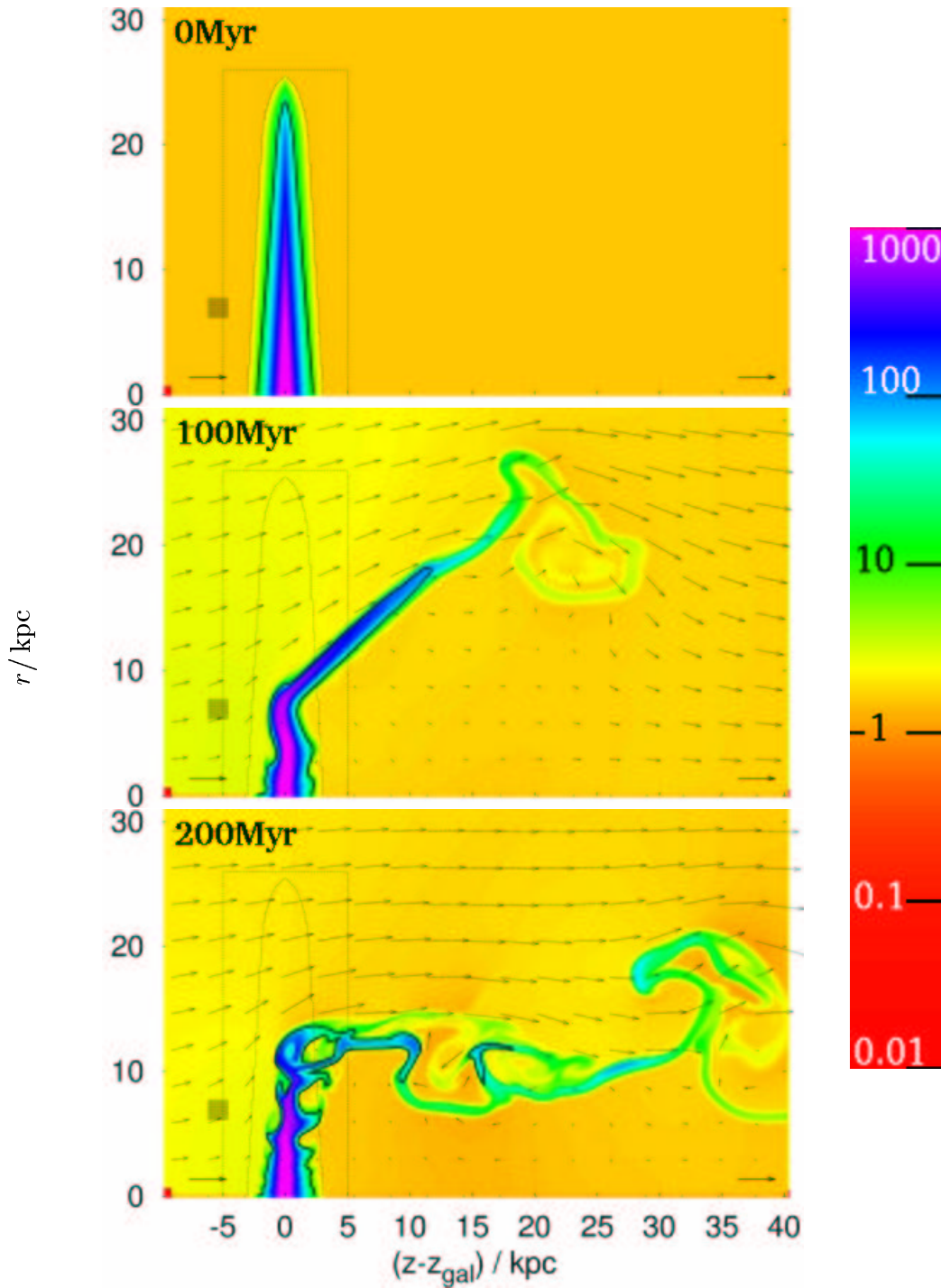


Figure 4.5: Evolution of gas density distribution for the massive galaxy in a wind with $T_{\text{ICM}1}$, $\tilde{p}_{\text{ram}} = 1000 \text{ cm}^{-3} \text{ km}^2 \text{ s}^{-2}$, Mach 0.8. The density distribution is shown colour-coded, the logarithmic colour scale on the right is in units of $10^{-27} \text{ g cm}^{-3}$. The arrows show the local flow velocity, the two bold arrows in the lower corners are standards indicating the nominal flow. The time is given in the panels. The gas enclosed by the heavy black line is gravitationally bound. Also the original disk region and a cylindrical region are indicated by thin black lines (see Sect. 4.5.3). The size of the small gray rectangle in the bottom left corner corresponds to 10×10 grid cells.

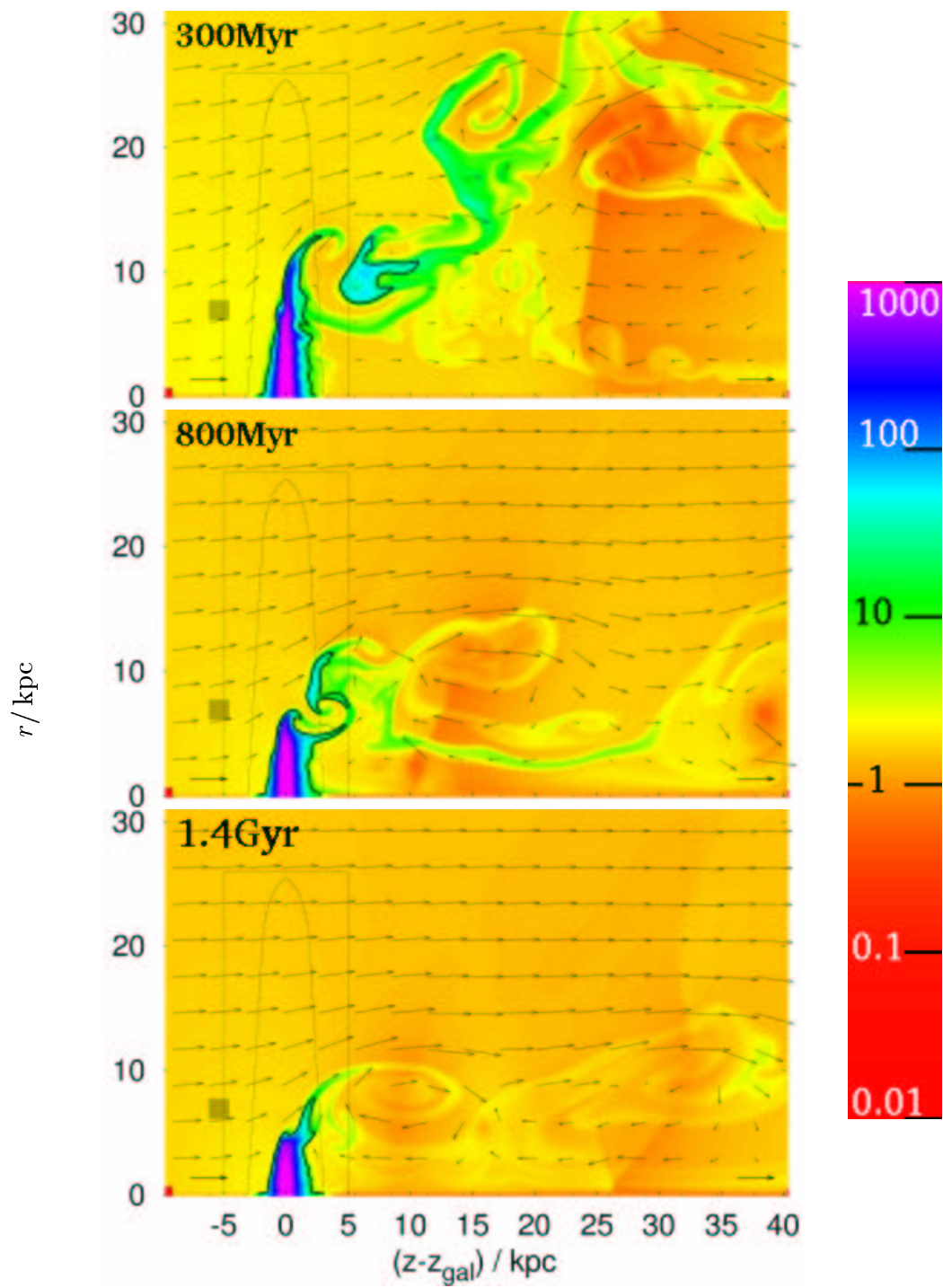
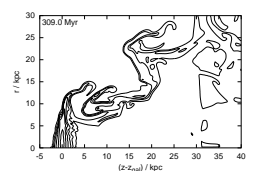


Fig. 4.5 continued



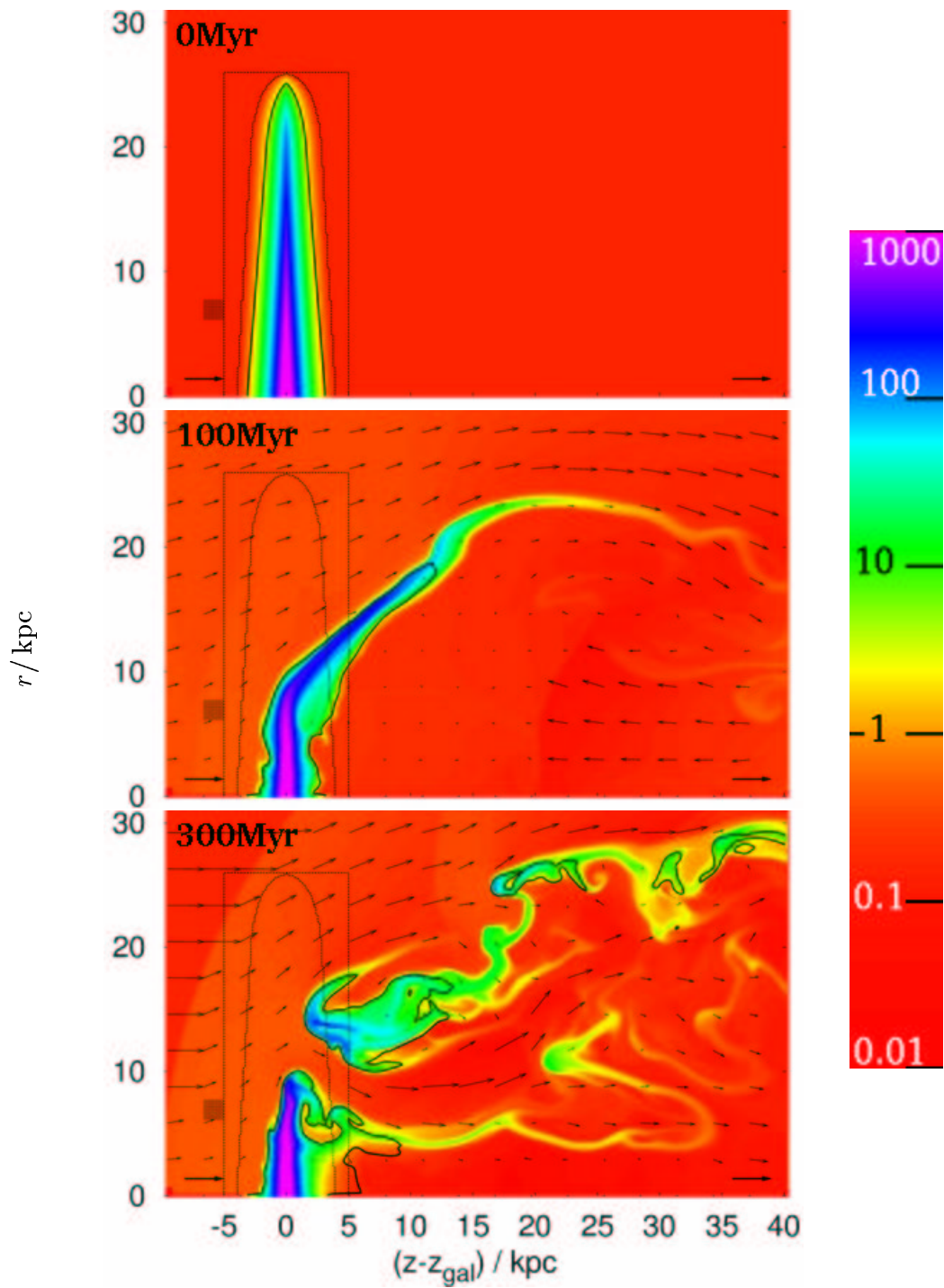


Figure 4.6: Same as Fig. 4.5, but for a wind with $T_{\text{ICM}1}$, $\tilde{p}_{\text{ram}} = 1000 \text{ cm}^{-3} \text{ km}^2 \text{ s}^{-2}$, Mach 2.53.

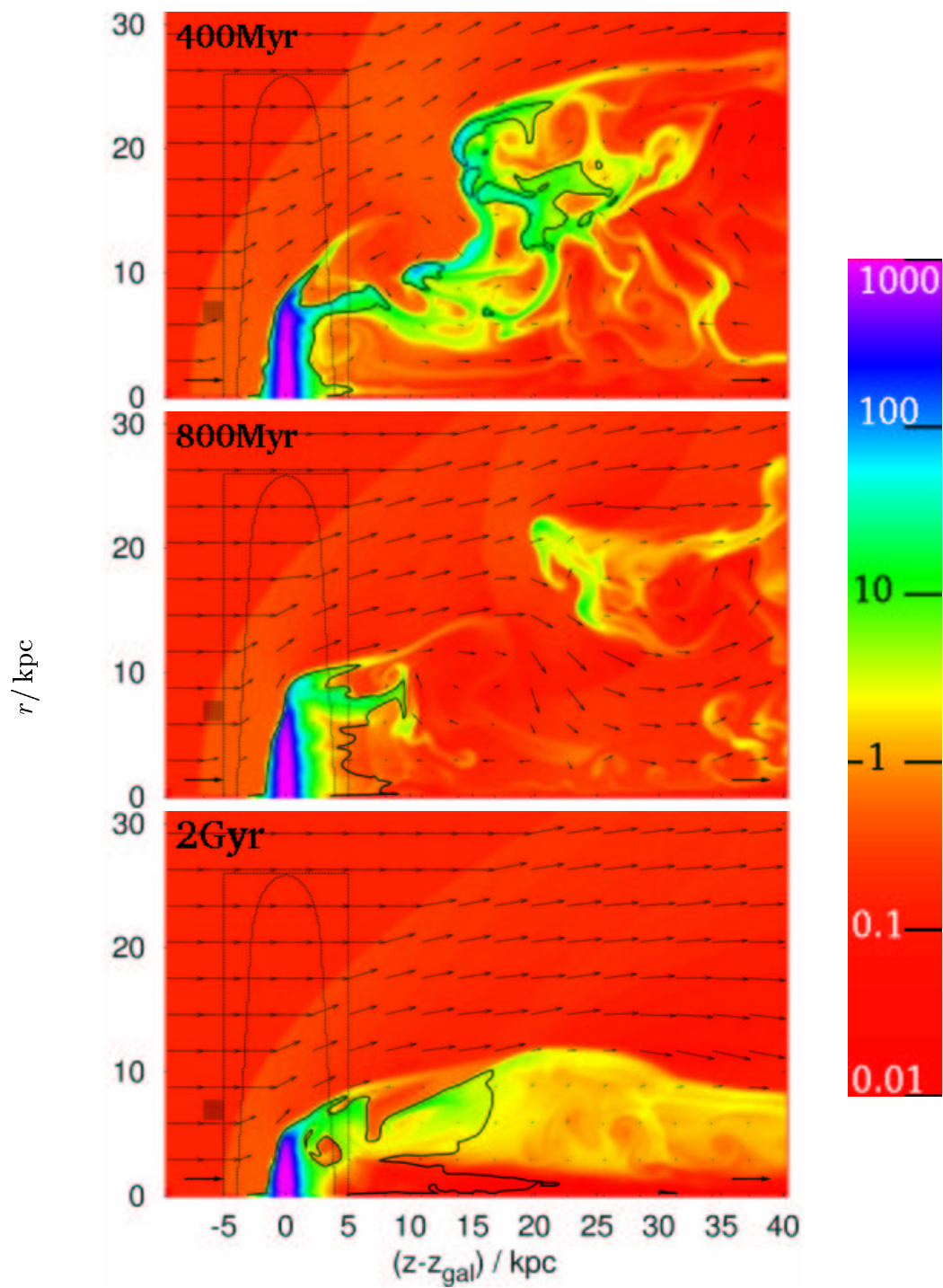
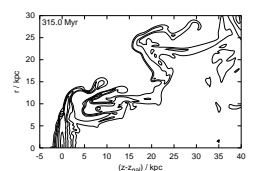


Fig. 4.6 continued



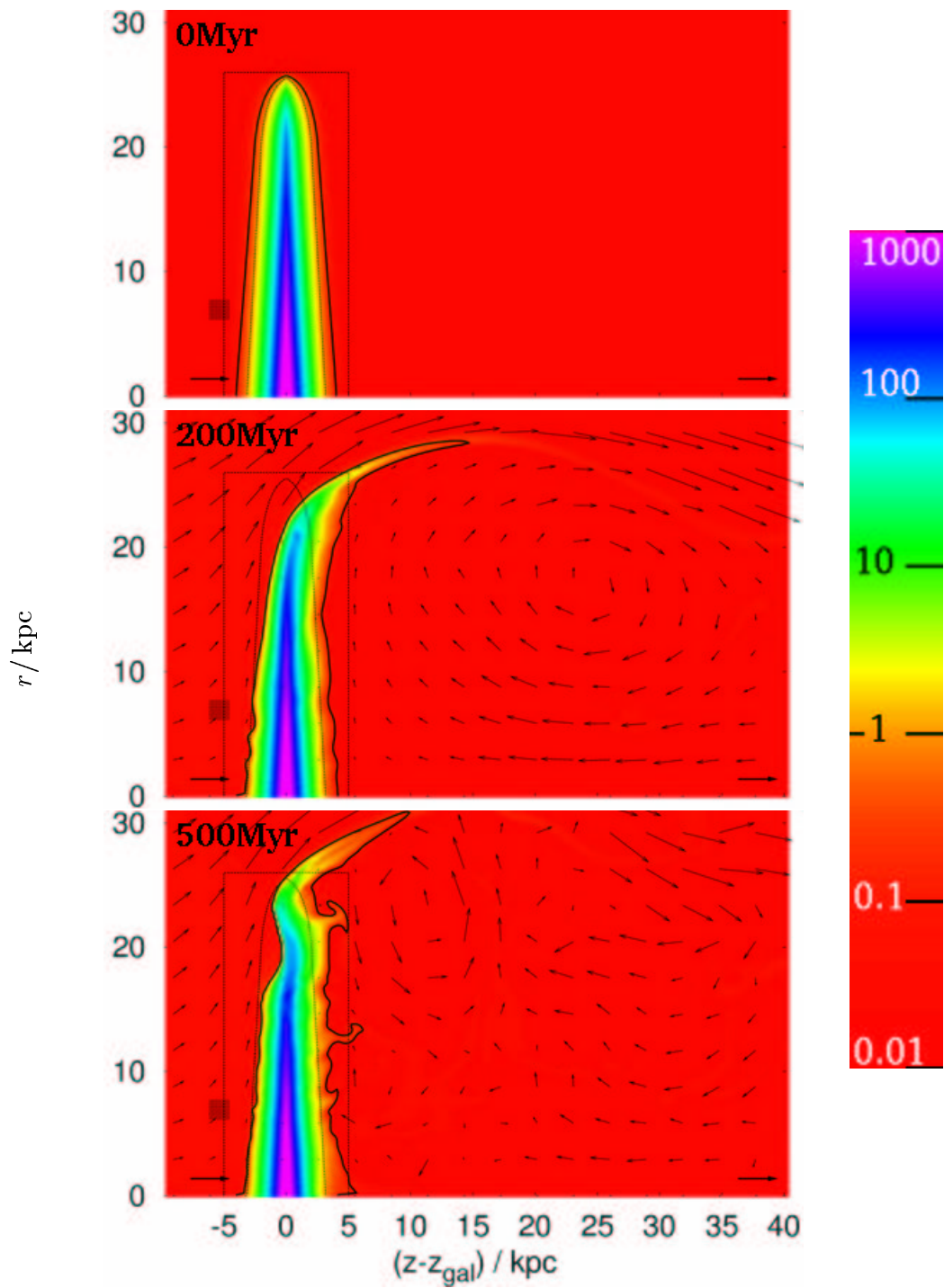


Figure 4.7: Same as Fig. 4.5, but for a wind with $T_{\text{ICM}1}$, $\tilde{p}_{\text{ram}} = 10 \text{ cm}^{-3} \text{ km}^2 \text{ s}^{-2}$, Mach 0.8.

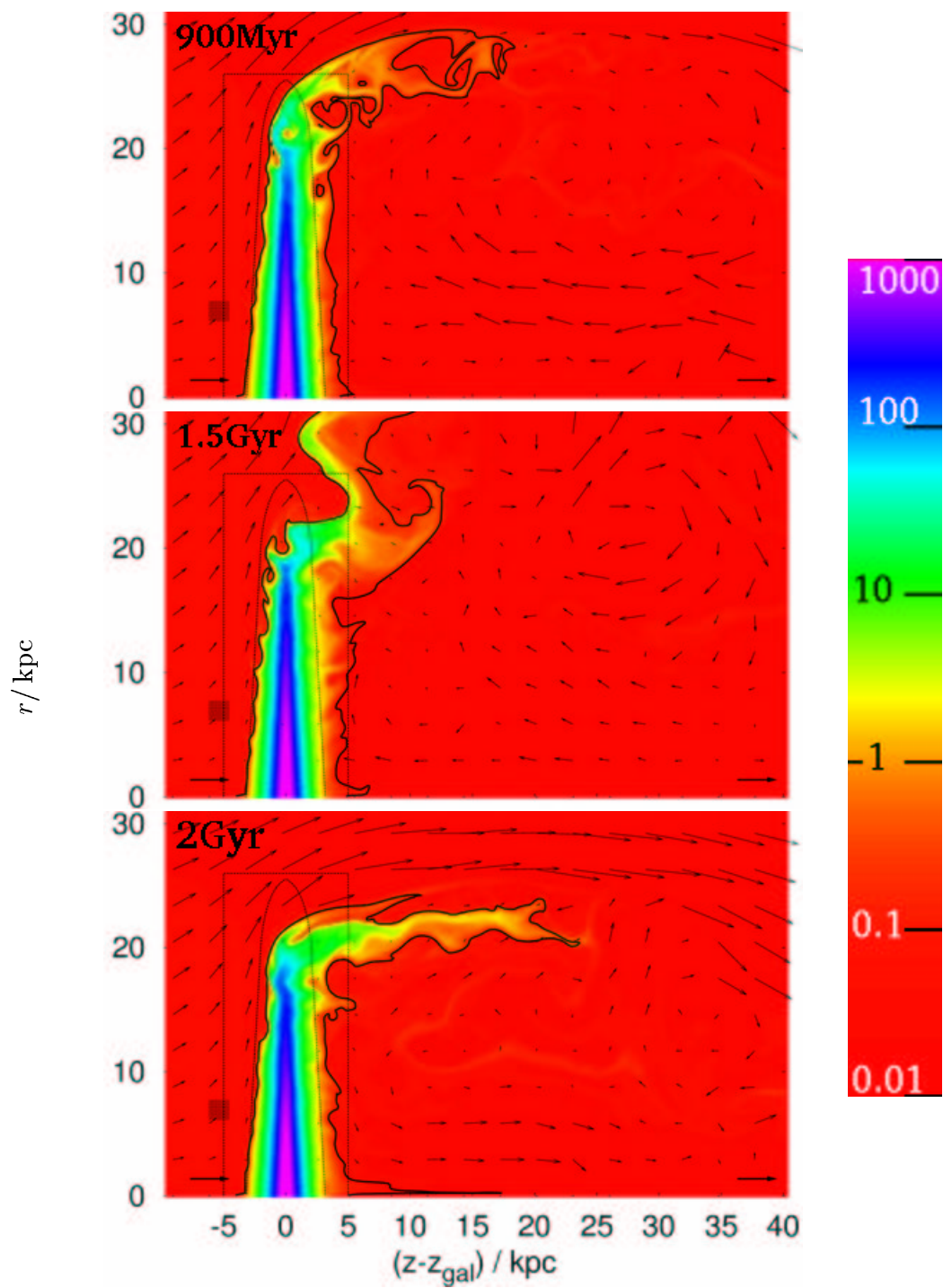
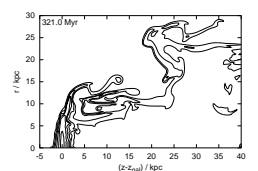


Fig. 4.7 continued



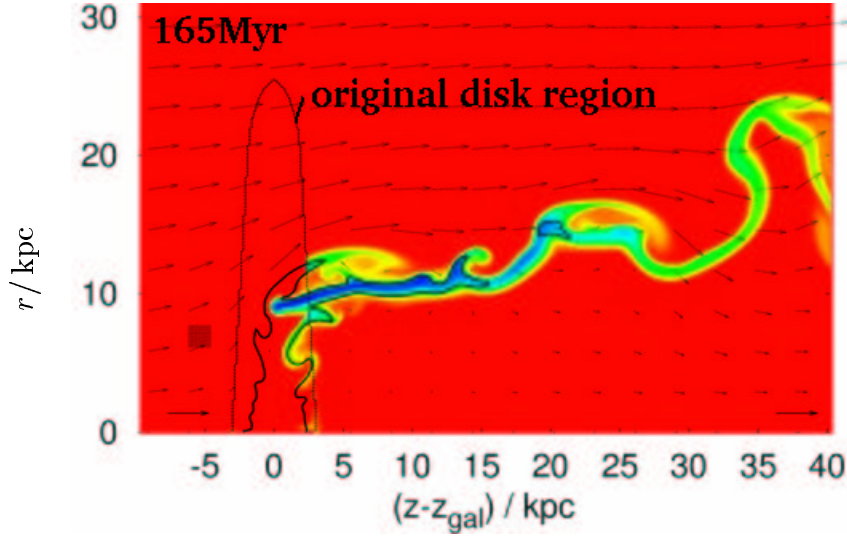


Figure 4.8: Same as in Fig. 4.5, but only galactic gas that had left the original disk region at some time is shown (see Sect. 4.5). This means gas that is seen inside the original disk region now has been outside and has fallen back. The colour scale is the same as in Fig. 4.5.

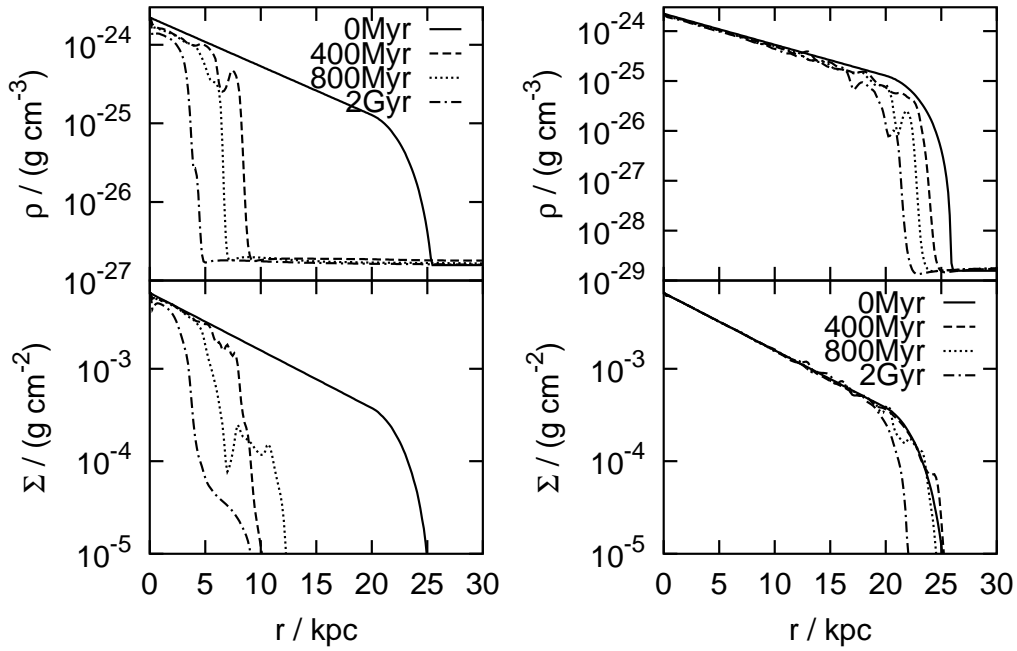


Figure 4.9: Evolution of density ρ and surface density Σ profiles along the galactic plane for the runs shown in Figs. 4.5 (left) and 4.7 (right). For the calculation of Σ we integrate over interval $(z_{\text{gal}} - 5\text{kpc}, z_{\text{gal}} + 5\text{kpc})$ to avoid that stripped material at larger distances to the galaxy appears in Σ .

how much of the stripped gas falls back into the disk and how much is lost permanently.

4.5.1 Definitions – “disk region” and “galactic gas”

To disambiguate the discussion, we want to define the following terms:

The original disk region is defined as the region where $\rho > \rho_{\text{ICM}}$ at the start of the simulation.

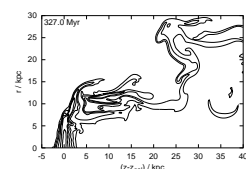
Galactic gas – version I: Galactic gas is gas that has been inside the original disk region initially. The method used to trace this gas is described in Sect. 4.5.2. This version will be used if not stated otherwise.

Galactic gas – version II: To distinguish between galactic gas (ISM) and ICM, a temperature threshold can be used. All gas with $T < 5 \cdot 10^6$ K (about virial temperature of the massive galaxy) is defined to belong to the ISM.

4.5.2 Colouring technique – tracing the galactic gas

To follow the fate of the galactic gas (version I) we use the technique of “colouring”. The basic idea is to “dye” the galactic gas. Then, as it moves through the grid, it takes its “colour” along. Thus, if gas at some position has an “intense colour”, it must originate from the galactic disk. For its basic version (Severing 1995; Lohmann 2000) one has to do the following: Define an additional array COLOUR1. At the start of the simulation, copy the density of the galactic gas (i.e. gas in the disk region with $\rho > \rho_{\text{ICM}}$) to this array. During the simulation advect this array in the same way as the usual density. Thus the value of COLOUR1 in a certain cell tells the density of galactic gas at this position. Of course this method can be used to trace the whereabouts of any part of the initial setup.

We extended this method to determine how much of the stripped galactic gas falls back to the original disk region. Therefore gas of colour 1 (galactic gas) that leaves the original disk region “changes its colour” to colour 2. This is done with the help of a second array COLOUR2, which is set to zero initially. Then at each time step the procedure is as follows: for each grid cell outside the original disk region add the value of COLOUR1 to the value of COLOUR2 in the same cell, then set COLOUR1 to zero in this cell. This causes the stripped gas to change its colour. Stripped gas with colour 2 that comes back to the disk region does not change its colour again, but keeps colour 2. Hence integrating over the array COLOUR2 inside the original disk region gives the amount of galactic gas that has been outside at some time – which is the amount of galactic gas that has been stripped and fallen back M_{fb} . Integrating over COLOUR1 gives the amount of galactic gas that has never left the original disk region M_{stay} , and $M_{\text{fb}} + M_{\text{stay}} = M_{\text{orig}}$ is the total



amount of galactic gas inside the original disk region, no matter if it has been outside this region in the meantime or not.

4.5.3 Disk mass and radius

Concerning the disk mass, we measure at each time t :

- (a) mass $M_{\text{orig}}(t)$ of galactic gas inside the original disk region,
- (b) mass $M_{\text{cyl}}(t)$ of galactic gas inside a fixed cylinder centred on the galactic plane with $r < 26$ kpc and $|z - z_{\text{gal}}| < 5$ kpc,
- (c) mass $M_{\text{bnd}}(t)$ of galactic gas bound to the galaxy potential. Bound gas is identified by a negative total energy density $e_{\text{tot}} = e_{\text{pot}} + e_{\text{therm}} + e_{\text{rot}} + e_{\text{kin}}$ (potential, thermal, rotational and kinetic energy density).
- (d) mass $M_{\text{fb}}(t)$ of galactic gas that has left the original disk region at some moment but is now back in the original disk region – that is the amount of fallen back gas (see Sect. 4.5.2).

For points (a) to (c) either identification of galactic gas (either by colour or by temperature) can be used.

There are several versions to determine the disk radius, too:

- (A) The outmost cell (largest distance to the symmetry axis) with a temperature lower than $5 \cdot 10^6$ K inside the original gas disk region sets the gas disk radius.
- (B) Scan along the galactic plane, starting at $r = 0$. The radius where $\varrho < 10^{-26} \text{ g cm}^{-3}$ for the first time sets the gas disk radius.
- (C) Same as before, but the condition is $\varrho < 10\varrho_{\text{ICM}}$.

A typical result for $r_{\text{disk}}(t)$ and $M_{\text{disk}}(t)$ is demonstrated in Fig. 4.10. The top panel shows the evolution of the gas disk radius, measured according to the three explained versions. As the edge of the gas disk “flaps” in the ICM wind, all three versions give an oscillation of $r_{\text{disk}}(t)$ (see Sect. 4.4). Please note that this is *not* due to a radial oscillation of the whole gas disk. To avoid too much crowding in plots comparing several $r_{\text{disk}}(t)$, these functions are smoothed over a p_{ram} dependent time scale (which is specified later). However, this smoothing is not applied to the first phase of the evolution. The smoothed $r_{\text{disk}}(t)$ are shown in the top panel of Fig. 4.10 by thin lines of the same colour. Due to its nature $r_{\text{disk}}(t)$ resulting from recipe (A) is slightly larger than the result of the two other recipes. For consistency between runs with different winds and gas disk models recipe (B) proved best and is used if not stated otherwise.

The bottom panel shows the results of the different recipes to measure the gas disk mass. The difference between the two definitions of which gas is

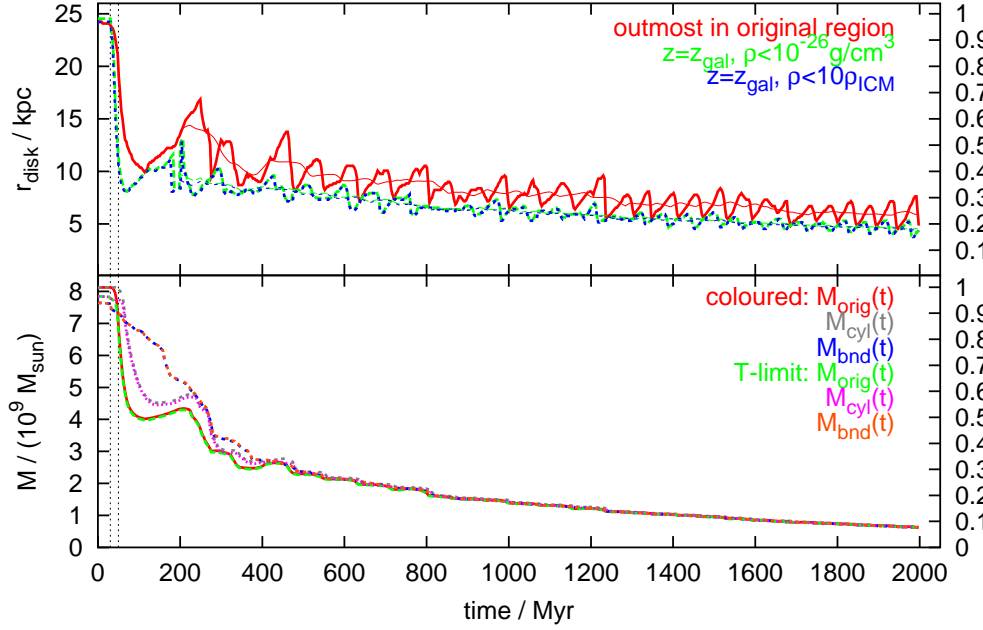
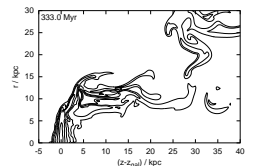


Figure 4.10: Demonstration of various measurement recipes for the gas disk radius r_{disk} (top panel) and disk mass M_{disk} (bottom panel). Results for the time evolution of these quantities are shown for the standard galaxy in an ICM wind with $p_{\text{ram}} = 1000 \text{ cm}^{-3} \text{ km}^2 \text{ s}^{-2}$, $T_{\text{ICM}1}$ and Mach 0.8. For further explanation see text.

considered as “galactic gas” (either dyed gas or gas identified by the temperature limit) is negligible. Only the initial values for M_{cyl} and M_{orig} change slightly between using the colour or the temperature to identify galactic gas. In the versions that use the temperature limit slightly less gas is recognised as belonging to the gas disk as (depending on the external pressure). A bit of the gas at the surface between the ICM and ISM may exceed the temperature limit. For M_{bnd} no difference between using the colour and the temperature can be found. Therefore, for further analysis we use the colouring method to identify galactic gas (definition of galactic gas – version I, see Sect. 4.5.1). The exact moment and the shape of the slope during the initial decrease in $M_{\text{disk}}(t)$ depends on the disk region used. Of course for the larger cylindrical region the decrease starts a moment later than for the smaller initial disk region. However, during the KH phase all versions of measurement give the same result. If not stated otherwise, for the further analysis M_{orig} is used as the disk mass M_{disk} . Details of the interpretation of $r_{\text{disk}}(t)$ and $M_{\text{disk}}(t)$ are discussed in the next sections.

For subsonic cases, any change of the inflow conditions reaches the galaxy with a delay of $z_{\text{gal}}/c_{\text{ICM}}$ (where c_{ICM} is the sound speed in the ICM). This is also true for the wind initialisation (see Sect. 4.3.2). Therefore, at the position of the galaxy, the wind does not increase between $t = 0$ and $t =$



t_{switch} (like at the inflow boundary), but delayed between $t = z_{\text{gal}}/c_{\text{ICM}}$ and $t = z_{\text{gal}}/c_{\text{ICM}} + t_{\text{switch}}$. Before $t = z_{\text{gal}}/c_{\text{ICM}}$ the galaxy does not feel any flow. In Fig. 4.10 and similar figures we mark the moments $t = z_{\text{gal}}/c_{\text{ICM}}$ and $t = z_{\text{gal}}/c_{\text{ICM}} + t_{\text{switch}}$ with thin vertical lines.

4.6 Varying the wind parameters

4.6.1 Wind density and velocity

In this section we demonstrate how the results for the gas disk radius $r_{\text{disk}}(t)$, the gas mass inside the original disk region $M_{\text{orig}}(t)$ and the bound gas mass $M_{\text{bnd}}(t)$ depend on the wind density ρ_{ICM} and velocity v_{ICM} . We also show in separate plots (in order to maintain clarity) how much bound gas can be found outside the original disk region (that is $M_{\text{bnd}}(t) - M_{\text{orig}}(t)$) and how much fallen-back gas is contained inside the original disk region (this is $M_{\text{fb}}(t)$, see Sect. 4.5.3). The results in this section are for the following setup:

- massive galaxy,
- exponential gas disk with scale height $b_{\text{gas}} = 0.4$ kpc,
- $T_{\text{ICM}1}$ (corresponding to an ICM sound speed of 1000 km s^{-1}).

The results are shown in Figs. 4.11, 4.12 and 4.13.

For clarification we apply a time-averaging to most $r_{\text{disk}}(t)$ curves, smoothing the oscillations that are due to the flittering edge of the galaxy. We average $r_{\text{disk}}(t)$ over 100 Myr for the cases with $\tilde{p}_{\text{ram}} \geq 1000 \text{ cm}^{-3} \text{ km}^2 \text{ s}^{-2}$ and over 200 Myr for the lower ram pressure cases. The smoothing is applied neither to the initial 250 Myr (500 Myr) for the stronger ram pressures (for the weaker ram pressures), nor to the curves for $\tilde{p}_{\text{ram}} = 10 \text{ cm}^{-3} \text{ km}^2 \text{ s}^{-2}$. Also in each group of constant ram pressure we leave one curve oscillating. The amplitude and the frequency of the oscillations are similar within a group.

The first thing to notice is that the mass and radius of the remaining gas disk depend mainly on the ram pressure, with higher ram pressures resulting in smaller disks. For the strongest ram pressures even the complete gas disk is stripped. At second glance one can see that for a given ram pressure the gas loss is stronger for subsonic winds than for supersonic ones.

The phases of the stripping process as explained in Sect. 4.4 are clearly visible in the $r_{\text{disk}}(t)$, $M_{\text{orig}}(t)$ and $M_{\text{bnd}}(t)$ curves. The bending of the outer gas disk during the instantaneous stripping phase results in a first strong decrease of $r_{\text{disk}}(t)$ and $M_{\text{orig}}(t)$. We define the duration of this phase τ_{push} to last from the moment when the flow reaches the galaxy to the first local minimum in $r_{\text{disk}}(t)$. Fig. 4.28 shows the dependence of τ_{push} on ram pressure, this point is discussed in Sect. 4.9.1. After the instantaneous stripping phase, the intermediate dynamical phase follows with the fall-back of some gas. This

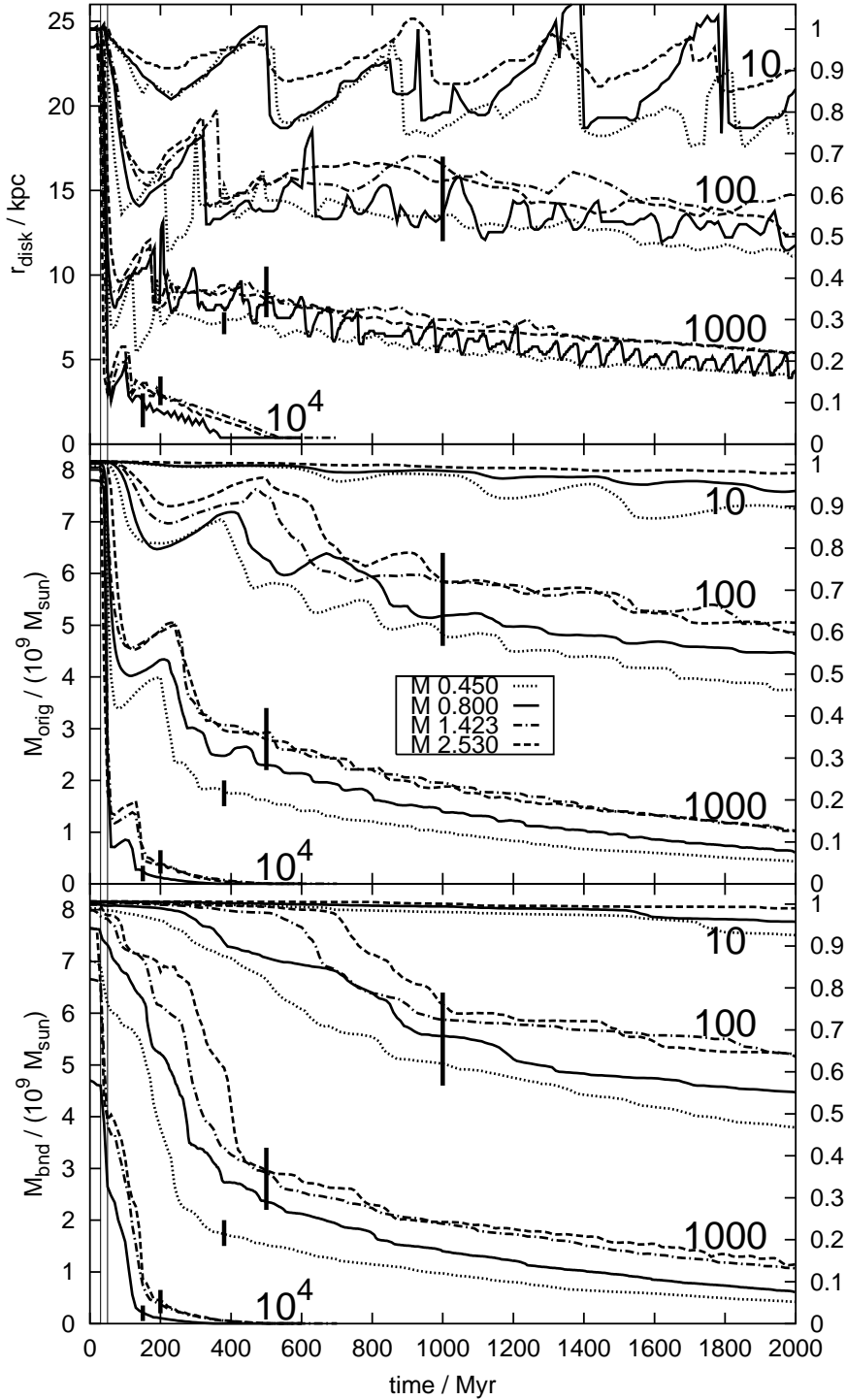
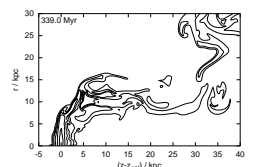


Figure 4.11: Gas disk radius $r_{\text{disk}}(t)$ (top panel), mass $M_{\text{orig}}(t)$ in the original disk region (middle panel) and bound gas mass $M_{\text{bnd}}(t)$ (bottom panel) of the massive galaxy in ICM winds with T_{ICM1} for different ram pressures \tilde{p}_{ram} and Mach numbers. Curves for the same \tilde{p}_{ram} group together. Each group is labelled accordingly with its \tilde{p}_{ram} in units of $\text{cm}^{-3} \text{km}^2 \text{s}^{-2}$. The Mach number for each curve is coded by the line style (see key in the middle panel). The right axes are labelled in units of the initial radius or mass.

In the top panel all curves except the ones for Mach number 0.8 are shown in the smoothed version for clarity (see text for explanation). The frequency and amplitude in $r_{\text{disk}}(t)$ are comparable for all runs with the same \tilde{p}_{ram} . The vertical bars show where we consider the intermediate phase to be finished. The two thin vertical lines mark the moment when the flow reaches the galaxy ($t_0 = 40$ Myr) and $t_0 + t_{\text{switch}} = 60$ Myr.

can be seen in the slight increase of $M_{\text{orig}}(t)$ just after the initial decrease, and in the plots showing $M_{\text{fb}}(t)$ directly (Fig. 4.13). Although the gas disk always reacts to the wind in the initial instantaneous stripping phase, only for stronger winds this also results in unbinding a substantial amount of gas from the galactic potential. The duration of the intermediate phase, this is until



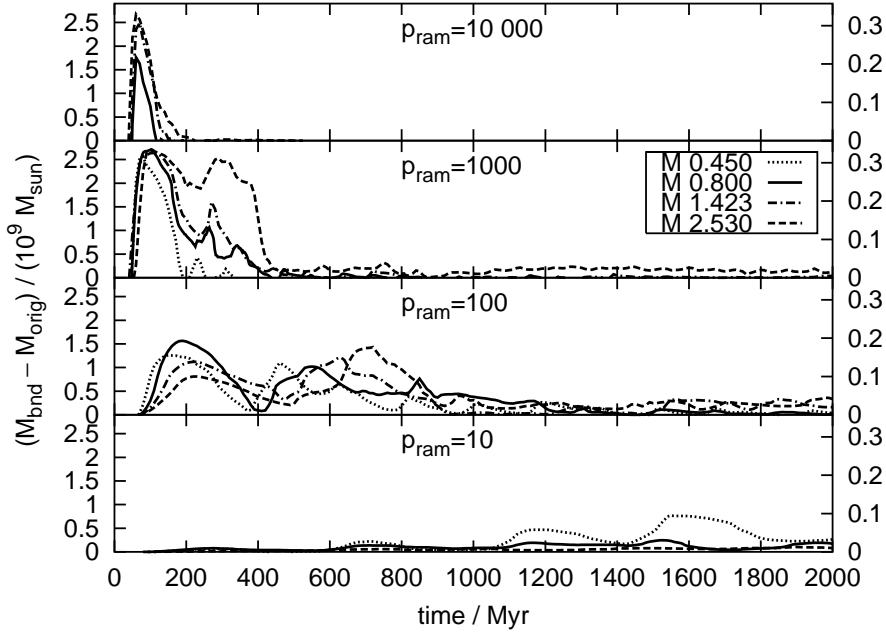


Figure 4.12: Mass of bound gas outside the original disk region as a function of time; for the massive galaxy in different ICM winds with $T_{\text{ICM}1}$. There is one labelled panel for each ram pressure. Inside the panels the Mach number of the wind is coded by the line style (see key). The right axes are labelled in units of the initial mass.

most of the bound gas outside the disk region has vanished, takes much longer for weak winds than for strong ones. For ram pressures of $10 \text{ cm}^{-3} \text{ km}^2 \text{ s}^{-2}$ this phase is not finished at the end of the simulations. For all but the very weakest ram pressure, during the first few 100 Myr between 20 and 40% of the original gas disk mass linger outside the original disk region but are still bound. The amount of gas that falls back to the original disk region is of the order of 5 to 10% of the original gas disk mass.

For the weakest ram pressure ($\tilde{p}_{\text{ram}} = 10 \text{ cm}^{-3} \text{ km}^2 \text{ s}^{-2}$) the galaxy loses only a few percent of its gas, although also in this case the radius of the gas disk is truncated.

4.6.2 Cross-comparisons between runs with different T_{ICM}

The results from Sect. 4.6.1 suggest that the effect of the stripping does not depend on the ram pressure alone but also slightly on the Mach number. To investigate this point in more detail we repeat some of the simulations from Sect. 4.6.1 with the second ICM temperature $T_{\text{ICM}2}$ (corresponding to an ICM sound speed of 562 km s^{-1} ; see Sect. 4.1.1 and Fig. 4.1). The resulting disk masses and radii are shown in Figs. 4.14, 4.15 and 4.16. They are very

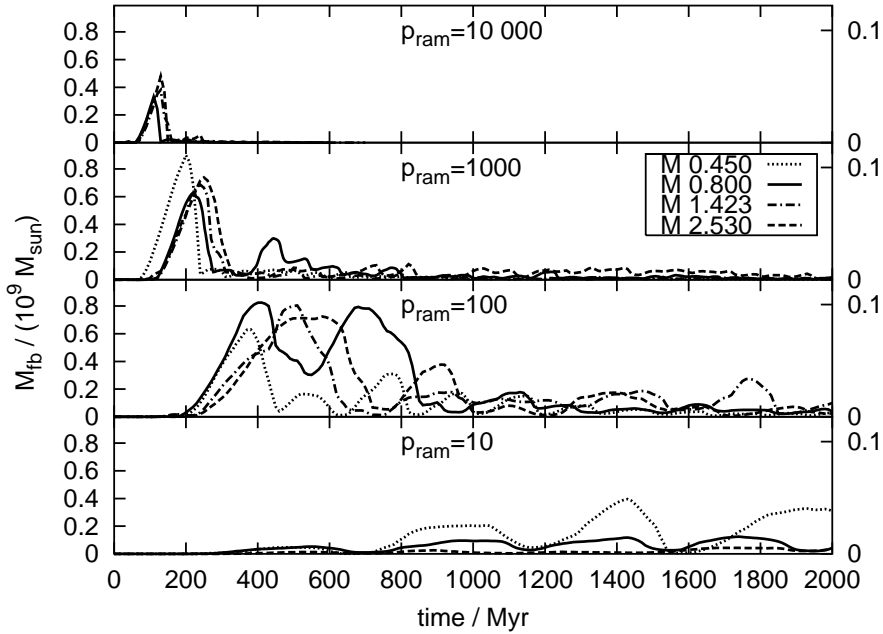
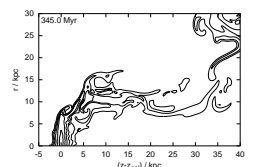


Figure 4.13: Mass of fallen back gas $M_{\text{fb}}(t)$ (= galactic gas that has left the original disk region and fell back to that region) as function of time; for the massive galaxy in different ICM winds ($T_{\text{ICM}1}$). There is one labelled panel for each ram pressure. Inside the panels the Mach number of the wind is coded by the line style (see key). The right axes are labelled in units of the initial mass.

similar to the results in Sect. 4.6.1.

We cross-compare runs with different ICM temperatures. E.g. for $T_{\text{ICM}1}$ the velocity of 800 km s^{-1} is equivalent to Mach number 0.8, whereas for $T_{\text{ICM}2}$ the same velocity corresponds to Mach number 1.423. The velocity that belongs to Mach number 0.8 for $T_{\text{ICM}2}$ is 450 km s^{-1} . If indeed the Mach number is the determining parameter, then for this example the result of the run with $(T_{\text{ICM}1}, 800 \text{ km s}^{-1}, \text{Mach number } 0.8)$ should be the same as the result of the case $(T_{\text{ICM}2}, 450 \text{ km s}^{-1}, \text{Mach number } 0.8)$ rather than $(T_{\text{ICM}2}, 800 \text{ km s}^{-1}, \text{Mach number } 1.423)$. We show this comparison for $r_{\text{disk}}(t)$, $M_{\text{orig}}(t)$ and $M_{\text{bnd}}(t)$ in Fig. 4.17 for some cases. In the middle panel, where the velocity is subsonic for $T_{\text{ICM}1}$ and supersonic for $T_{\text{ICM}2}$, indeed runs with the same Mach number rather than with the same velocity correspond to each other. The same seems to hold for the left panels, in the pure subsonic range, although not as clear as in the transition from the subsonic to the supersonic regime. In the supersonic range (right panels) no systematic difference is seen. As qualitative issues we conclude that (i) for a given wind density and velocity, RPS is slightly more effective if this wind is subsonic (compared to supersonic winds); and (ii) that in the subsonic regime winds with smaller Mach numbers are a bit more effective than winds with



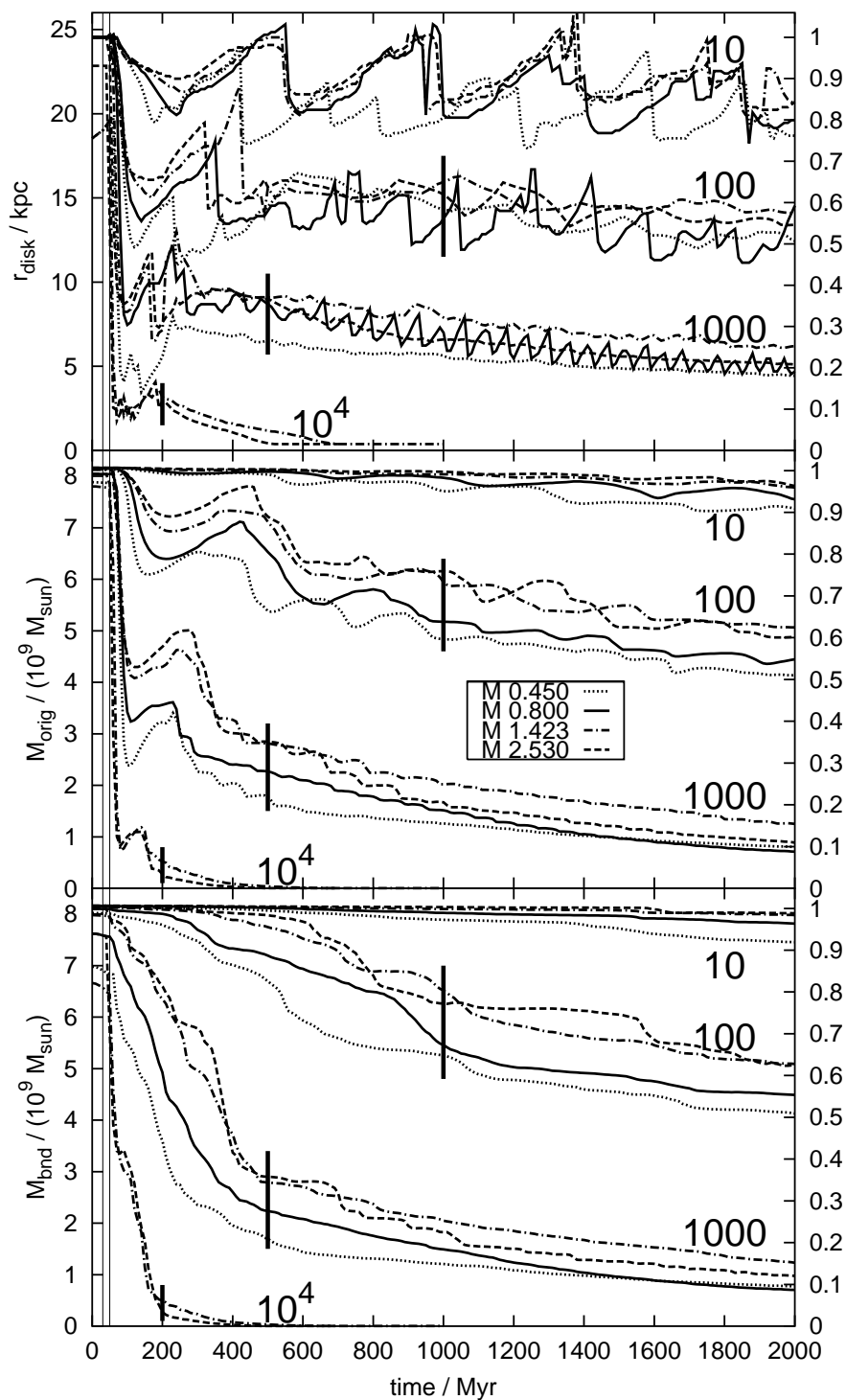


Figure 4.14: Same as Fig. 4.11, but for the massive galaxy in ICM winds with $T_{\text{ICM}2}$.

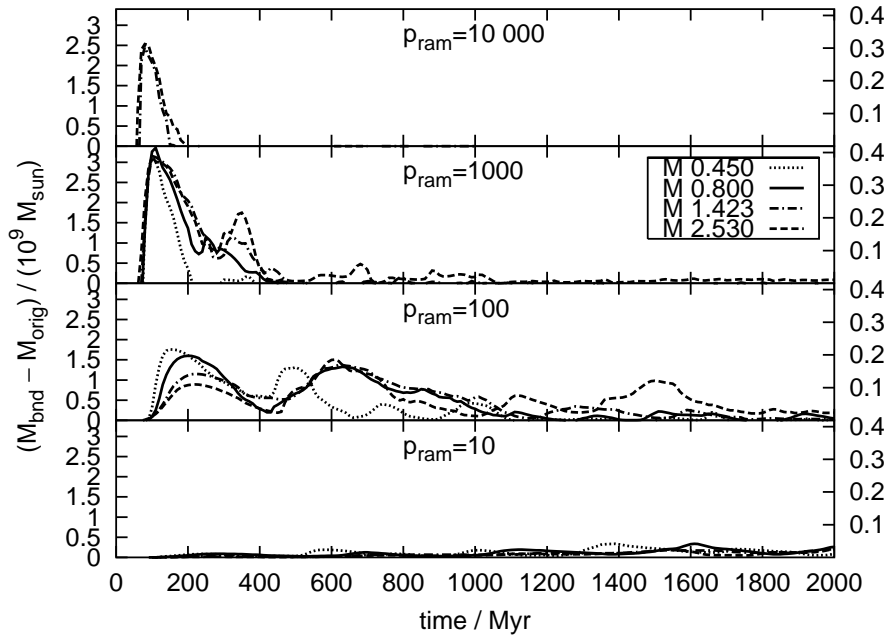


Figure 4.15: Same as Fig. 4.12, but for the massive galaxy in ICM winds with $T_{\text{ICM}2}$.

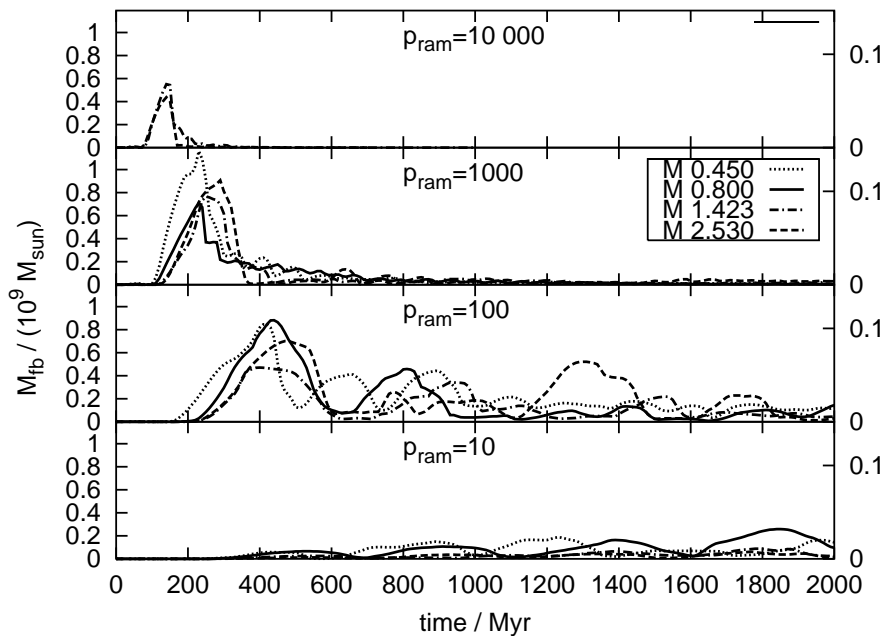
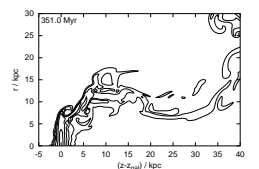


Figure 4.16: Same as Fig. 4.13, but for the massive galaxy in ICM winds with $T_{\text{ICM}2}$.



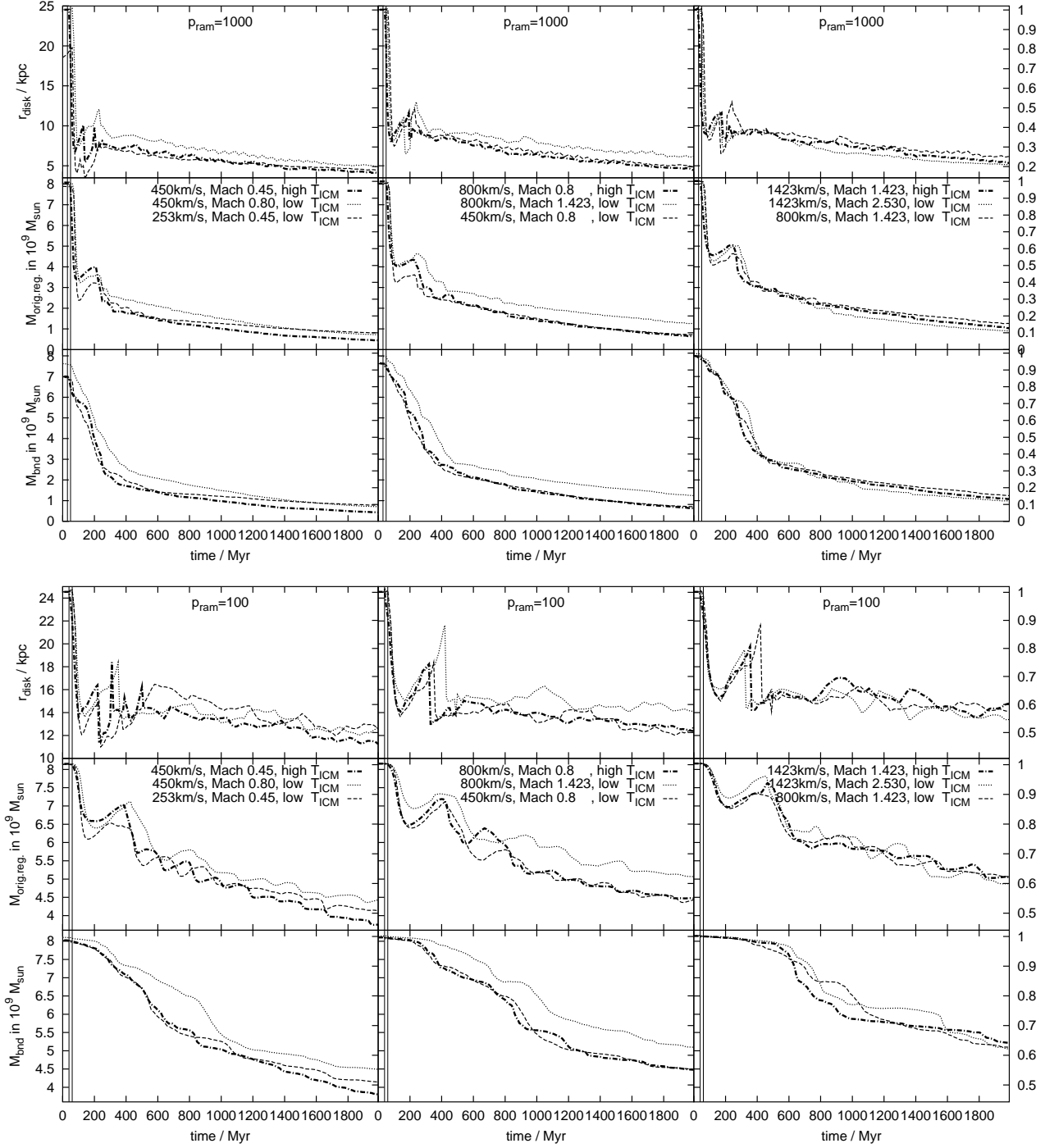


Figure 4.17: Comparison of stripping radius $r_{\text{disk}}(t)$, mass in the original disk region $M_{\text{orig}}(t)$ and bound mass $M_{\text{bnd}}(t)$ for selected runs with $\tilde{p}_{\text{ram}} = 1000 \text{ cm}^{-3} \text{ km}^2 \text{ s}^{-2}$ (upper panel) and $\tilde{p}_{\text{ram}} = 100 \text{ cm}^{-3} \text{ km}^2 \text{ s}^{-2}$ (lower panel). For further explanations see Fig. 4.11 and text of Sect. 4.6.2.

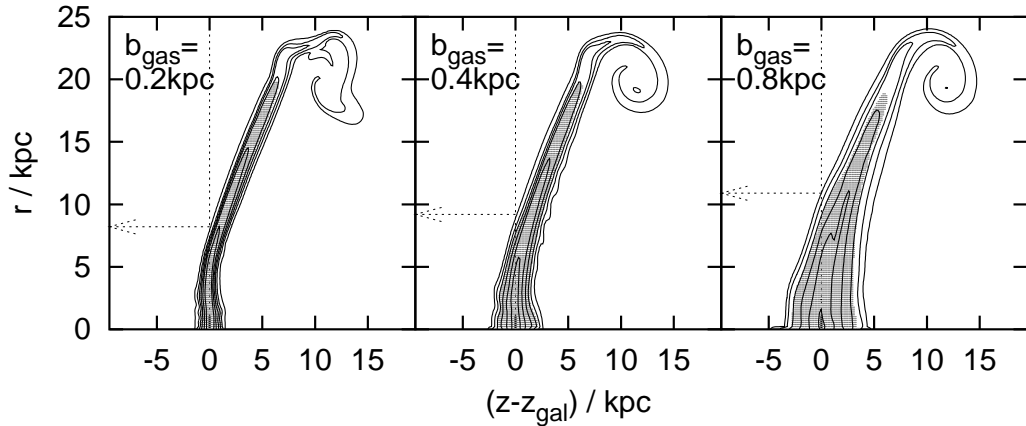


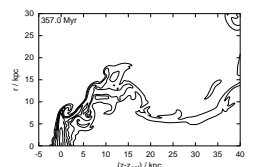
Figure 4.18: Density contours at 70 Myr for three different gas disk thicknesses ($b_{\text{gas}} = 0.2, 0.4, 0.8$ kpc). The gas in the shaded area is bound. The wind was the same in all cases ($\tilde{p}_{\text{ram}} = 1000 \text{ cm}^{-3} \text{ km}^2 \text{ s}^{-2}$, T_{ICM1} , Mach 0.8). The method of radius measurement illustrated (see Sect. 4.5.3).

higher Mach numbers. Nevertheless, the Mach number is only a secondary parameter, the main parameter is the ram pressure.

Moreover, we do not want to over-interpret the differences between the subsonic and supersonic cases, as we used a single-fluid description. In contrast, the ICM is highly ionised, it actually consists of a proton and an electron fluid. With respect to the proton fluid, the galaxy's velocities are transonic, but with respect to the electron fluid they still move subsonically. Portnoy et al. (1993) studied the difference between the single-fluid and a two-fluid description for a spherical galaxy (with gas replenishment) and found no difference for the amount of gas remaining inside the galaxy.

4.7 Vertical structure of the gas disk

In order to study the influence of the vertical structure of the gas disk we perform some simulation runs with exponential and flared disks of varying scale heights in representative wind cases. Fig. 4.18 shows snapshots at the same moment during the instantaneous stripping phase for three exponential disks with different scale heights. Despite their different thicknesses, all three cases look very similar. The resulting radius and mass curves are compared in Fig. 4.19. It does not make sense to use M_{orig} for this comparison, as for gas disks with different thicknesses and shapes also the original disk regions differ strongly. Hence we use M_{cyl} here, the mass inside the cylinder with $r < 26$ kpc and $|z - z_{\text{gal}}| < 5$ kpc. The different starting points of the curves for the bound mass are due to the different disk thicknesses and external pressures (see Sect. 3.2.2 and Fig. 3.10); for thicker disks the outer layers become unbound. The radius curves are again smoothed as explained in



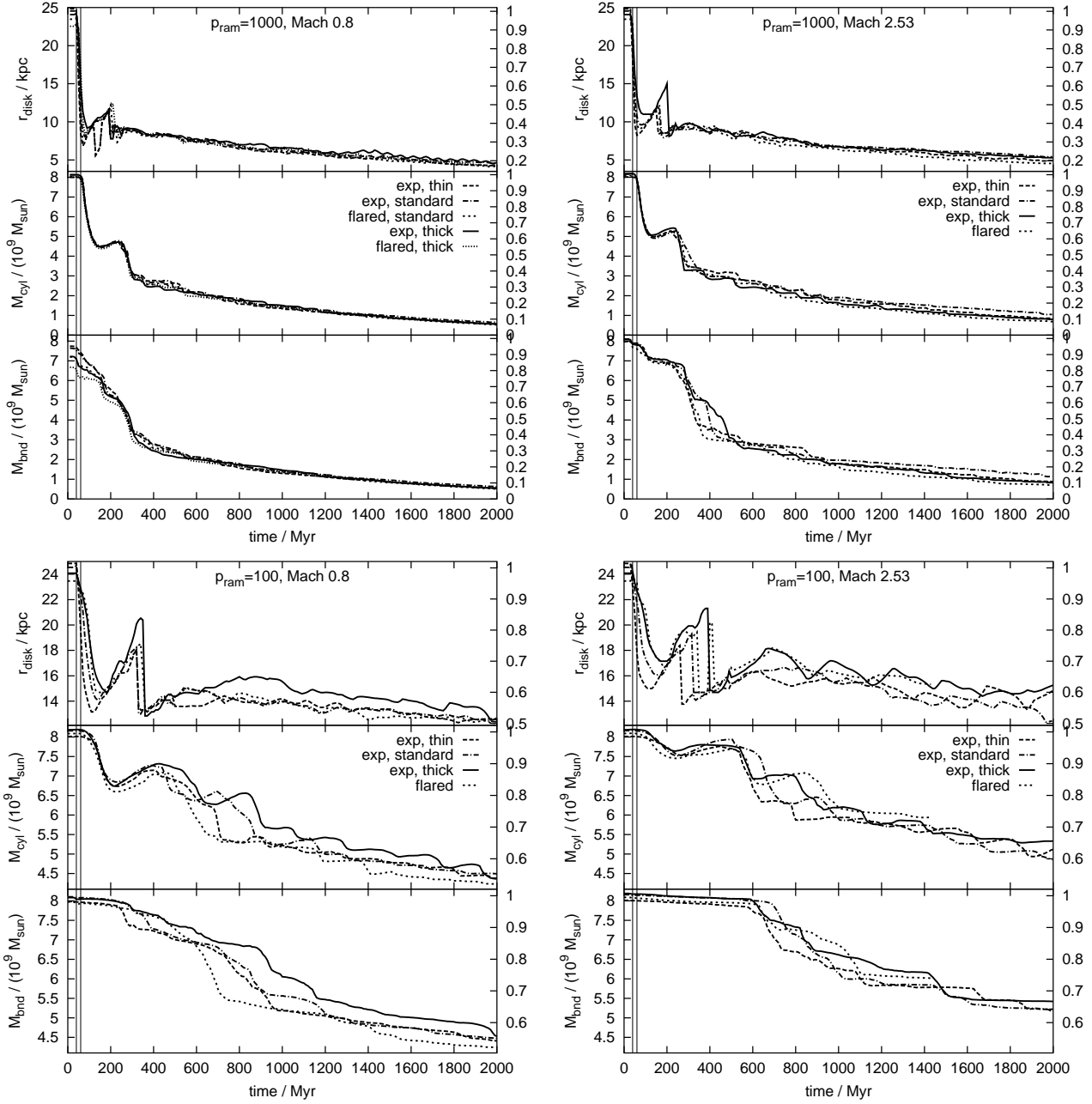


Figure 4.19: Comparison of stripping radius $r_{\text{disk}}(t)$, mass in the original disk region $M_{\text{orig}}(t)$ and bound mass $M_{\text{bnd}}(t)$ for different vertical structures, for four representative winds. For further explanations see Fig. 4.11. All radius curves are smoothed as explained in Sect. 4.6.

Sect. 4.5.3.

The r_{disk} as well as M_{cyl} and M_{bnd} are nearly independent of the vertical structure of the gas disk. For the higher ram pressure of $1000 \text{ cm}^{-3} \text{ km}^2 \text{ s}^{-2}$ the results for the different gas disks agree excellently. For the lower ram pressure ($100 \text{ cm}^{-3} \text{ km}^2 \text{ s}^{-2}$) the scatter is a bit larger as the galaxies stay

longer in the dynamic (chaotic) intermediate phase. The difference in the radius curves during the initial instantaneous stripping phase are due to the method of measurement, as is demonstrated in Fig. 4.18. We conclude from this test that the success of RPS is independent of the vertical structure of the gas disk.

We compare the compression of the upstream side of the gas disk for different scale heights and winds by showing the evolution of the vertical density profile through the gas disk at $r = 0.23$ kpc in Fig. 4.20. The compression of the upstream side of the gas disk results in a steepening of the density profile of the outer layers. In the compressed region the density profile can be fitted with an exponential function of a smaller scale height than the original b_{gas} . The scale height in the compressed layers is about 0.12 kpc independently of the wind and the original b_{gas} , but for stronger ram pressures the compressed layer reaches deeper towards the galactic plane. The dependence of the scale height of the compressed layer on resolution is demonstrated in the bottom line in Fig. 4.20, it is only a weak dependence. These panels shows vertical profiles at $t = 100$ Myr and in the time intervals 300-400 Myr and 700-800 Myr. We chose to show time intervals to allow averaging over the intrinsic oscillations in the profiles. In any way, if the scale height of the compressed layer was set by the resolution, it should vary from thick to thin disks. For the medium galaxy the profile of the outer layers is steepened to a scale height of about 0.09 kpc.

4.8 The medium-mass galaxy

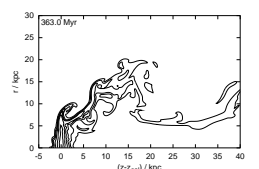
In order to check the results for another galaxy, most simulations from Sect. 4.6.1 are repeated with a medium-mass galaxy (see Table 3.1). The detailed wind parameters are given in Sect. 4.1.2 and Fig. 4.1. The resulting gas disk radii and masses are summarised in Figs. 4.21, 4.22 and 4.23. We smooth $r_{\text{disk}}(t)$ over 100 Myr for the cases with $\tilde{p}_{\text{ram}} \geq 100 \text{ cm}^{-3} \text{ km}^2 \text{ s}^{-2}$ and with a smoothing length of 200 Myr for the lower ram pressure cases (see also Sect. 4.5.3).

Again, the results are very similar to the ones in Sect. 4.6.1, except that the smaller galaxy is stripped stronger because of its weaker gravitation.

4.9 Comparison of analytical versus numerical results

4.9.1 Instantaneous stripping

The models show that during the instantaneous stripping phase the outer part of the gas disk is displaced, but not immediately unbound. It takes a while until the displaced gas is also unbound. As the analytical estimate in



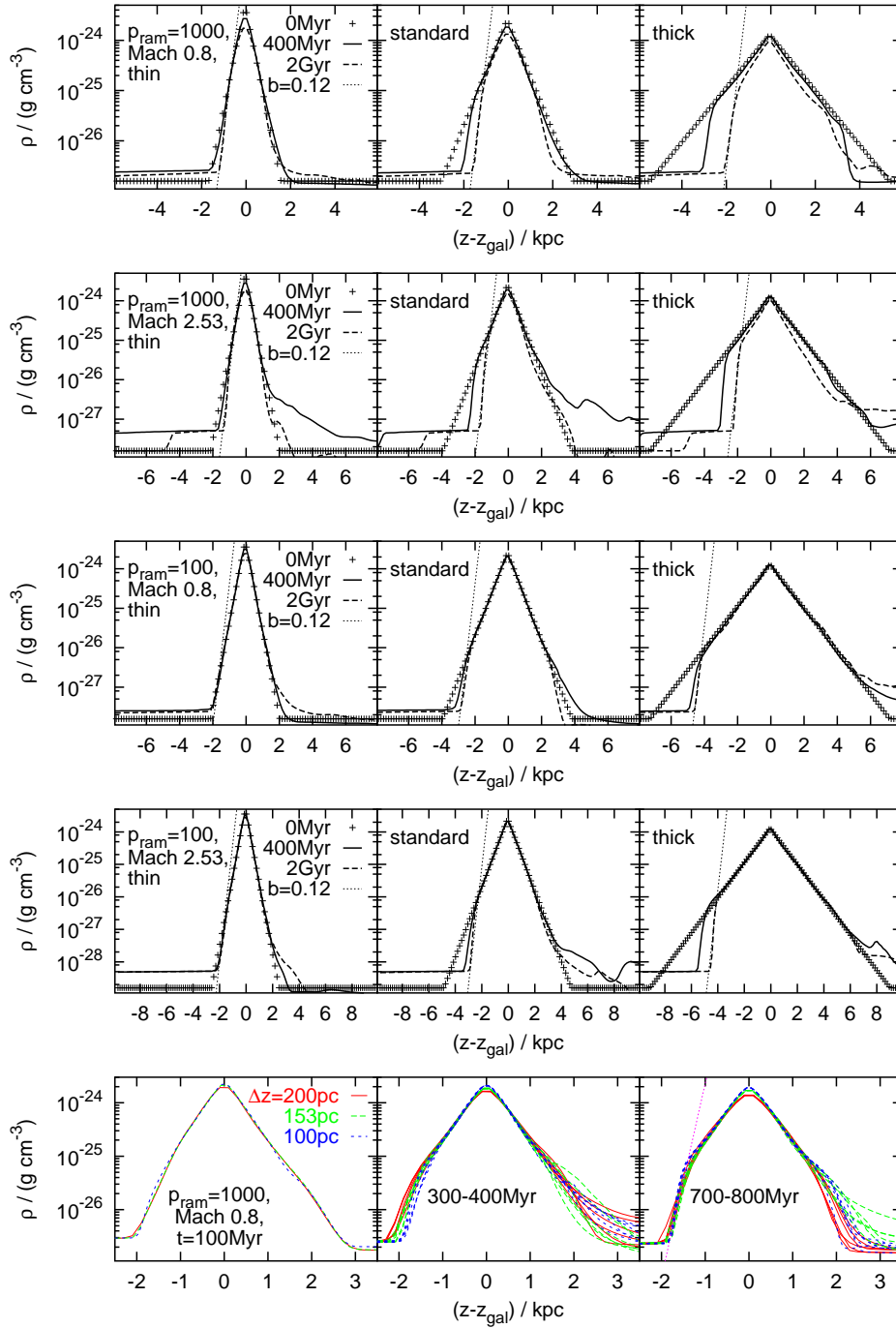


Figure 4.20: Evolution of vertical profiles at $r = 0.23$ kpc for different winds and gas disk thickness. We use an exponential disk for all cases, the scale heights are $b_{\text{gas}} = 0.2$ kpc (thin), $b_{\text{gas}} = 0.4$ kpc (standard) and $b_{\text{gas}} = 0.8$ kpc (thick). We fit an exponential function to the steepened part of the profile, the scale height for this fit is approximately 0.12 kpc for all cases. In the bottom line the variation of the vertical profiles with resolution for three different time steps/time intervals is demonstrated.

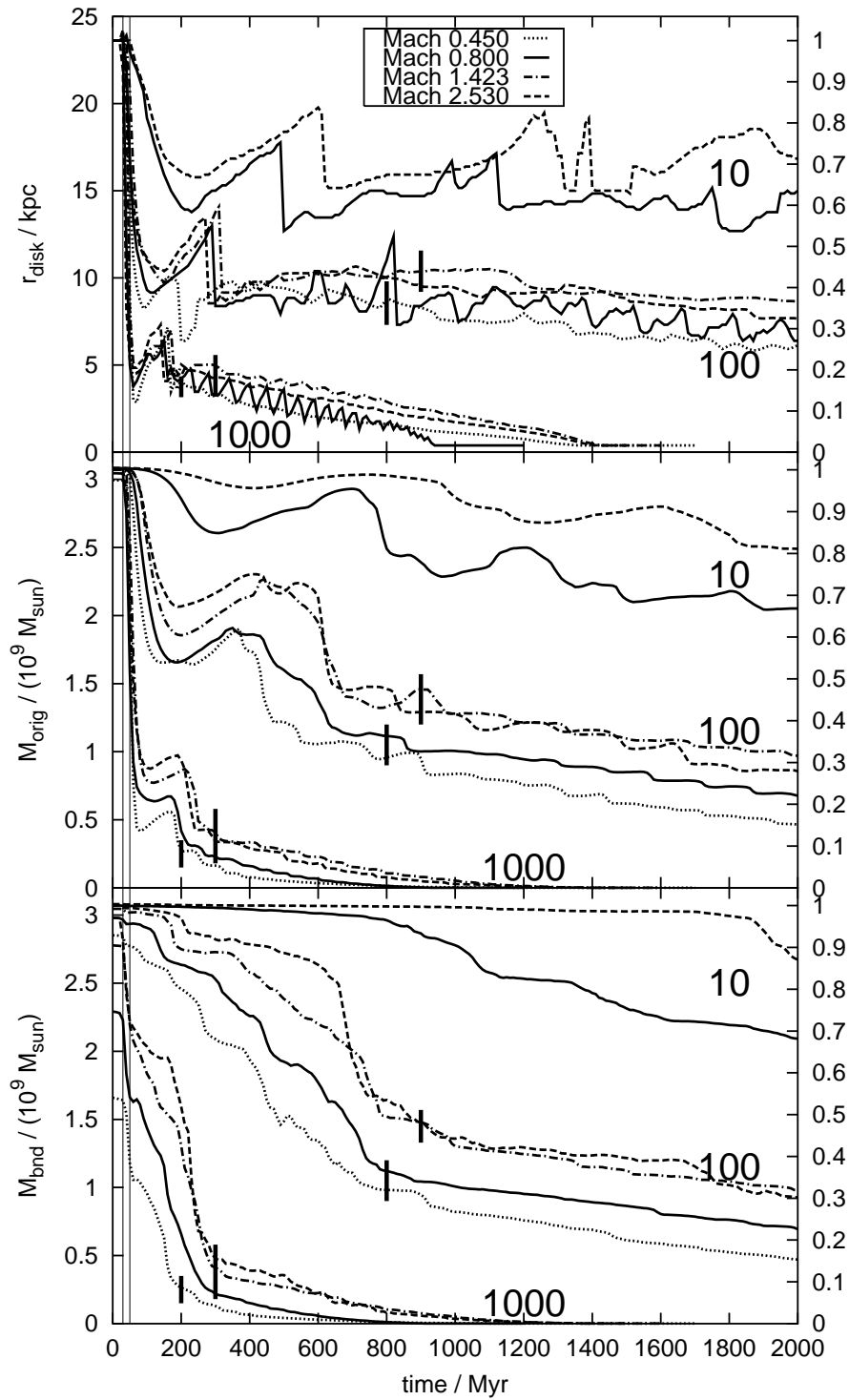
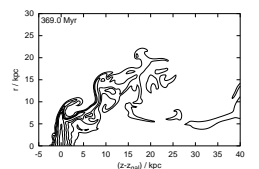


Figure 4.21: Same as Fig. 4.11, but for the medium galaxy in ICM winds with $T_{\text{ICM}1}$.



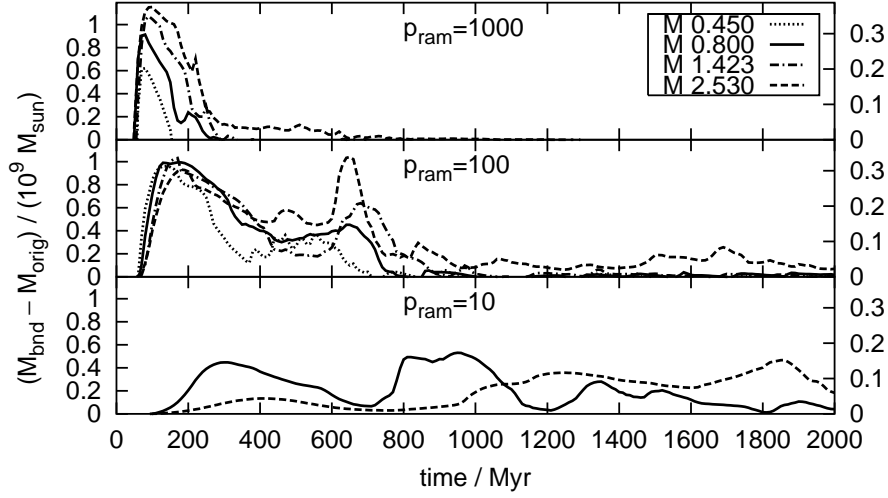


Figure 4.22: Same as Fig. 4.12, but for the medium galaxy in ICM winds with $T_{\text{ICM}1}$.

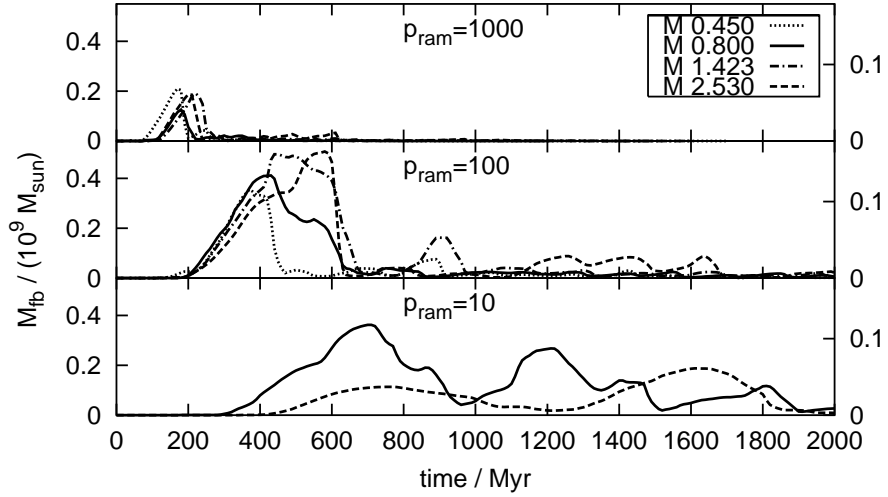


Figure 4.23: Same as Fig. 4.13, but for the medium galaxy in ICM winds with $T_{\text{ICM}1}$.

Eq. 4.3 just compares the forces working on the gas disk, it tells how much gas will be unbound, but it cannot quantify how long this process may take. As the analytical estimate states how much gas will be unbound from the galaxy, we also need to extract this quantity from the simulations. Hence we measure the radius and the mass of the remaining gas disk at the end of the dynamic intermediate phase, i.e. when no substantial amount of bound gas outside the disk region is left. We have marked this moment in Figs. 4.11, 4.14 and 4.21 by vertical bars. For the lowest ram pressure ($\tilde{p}_{\text{ram}} = 10 \text{ cm}^{-3} \text{ km}^2 \text{ s}^{-2}$) the intermediate phase is not completed during the simulation run time, here we use the final values for the comparison.

As pointed out in Sect. 4.2.1, there are several versions how the analytical estimate can be done, therefore we discuss the following recipes (see Figs. 4.24 and 4.25):

- (a) Use Eq. 4.4 to compute the restoring force while using the maximal potential gradient inside the original disk region (marked by “ Σ /in disk”).
- (b) Use Eq. 4.5 with $\Delta z = 150$ pc and use the maximal potential gradient inside the original disk region (marked by “ ρ /in disk”).
- (c) Use Eq. 4.5 with $\Delta z = 150$ pc and use the maximal potential gradient found for any z (marked by “ ρ /all z ”).
- (d) Compare the thermal pressure in the galactic plane and the ram pressure (Eq. 4.6, marked by “pressures”).

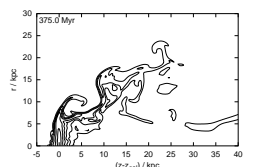
Version (c) lies between (a) and (b); for higher ram pressures it is indistinguishable from version (b), as there smaller radii are concerned where the steepest potential gradient is found inside the disk region. Also the result from the pressure comparison (d) has a very similar shape to (a) and (b) and is between those two. As already mentioned in Sect. 4.2.1, the estimates according to versions (a) and (b) are identical despite a shift in horizontal direction for exponential disks. These two versions represent the two extremes in the uncertainty how the gravitational restoring force f_{grav} shall be computed – either simplifying to a thin disk (a) or computing f_{grav} for a single cell only (b). This uncertainty can be parametrised by a factor of α in the calculation of f_{grav} , modifying Eq. 4.4 to

$$|f_{\text{grav}}(z, r)| = \alpha \left| \frac{\partial \Phi}{\partial z}(z, r) \Sigma_{\text{gas}}(r) \right|. \quad (4.17)$$

Choosing $\alpha = 1$ corresponds to version (a), choosing $\alpha = 0.16$ recovers version (b), but α can be adjusted to fit the numerical results. A further approximation whose uncertainty manifests itself in this parameter is the use of $\frac{\partial \Phi}{\partial z}$, because the wind does not accelerate stripped material exactly in z -direction.

Before we do any fitting, we show the pure analytical estimates (versions (a) to (d)) and the numerical results in Fig. 4.24 for the massive galaxy and in Fig. 4.25 for the medium galaxy. The numerical results are indeed in the range suggested by the analytical estimates.

We also want to consider the Mach number dependence of the numerical results again. So far we calculated the ram pressure according to $\tilde{p}_{\text{ram}} = n_{\text{ICM}} v_{\text{ICM}}^2$ for the supersonic cases as well. However, the velocity and density behind the formed bow shock differ from the values on its upstream side. It may be more appropriate to calculate the ram pressure for supersonic winds with the values of ρ and v at the downstream side of the shock. The



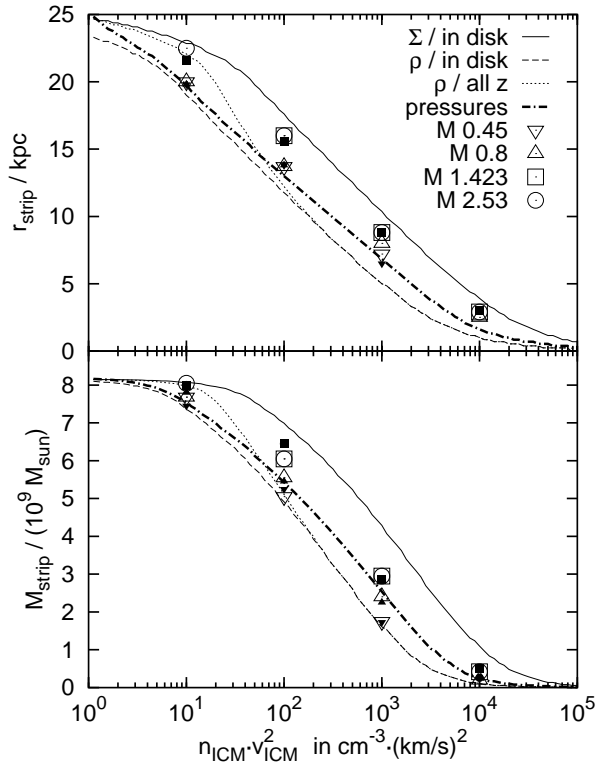


Figure 4.24: Comparison of analytical estimate (lines) and numerical result (symbols) for the stripping radius and the remaining gas mass as a function of ram pressure, for the massive galaxy. We show four versions of the analytical estimate, see Sect. 4.9.1. The Mach numbers for the numerical result are coded with different symbol shapes. Open symbols are for cases with $T_{\text{ICM}1}$, solid symbols of the same shape for cases with $T_{\text{ICM}2}$.

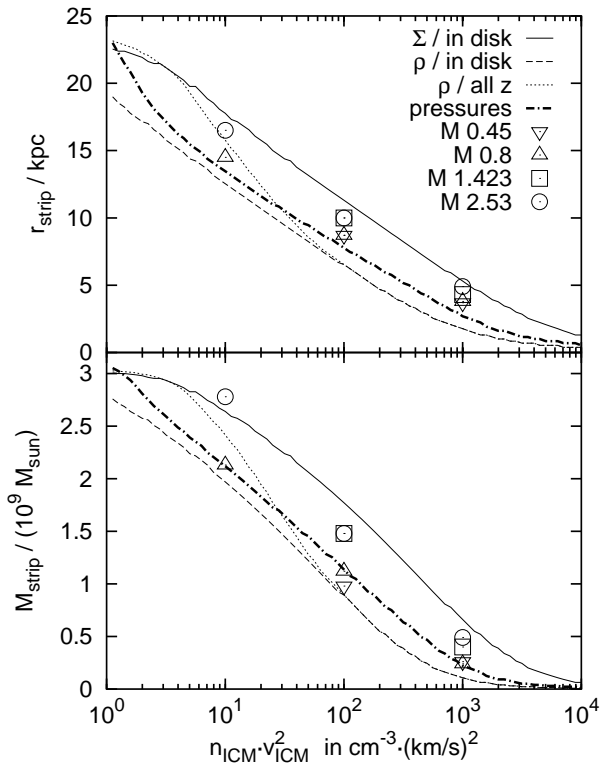


Figure 4.25: Same as Fig. 4.24, but for the medium galaxy.

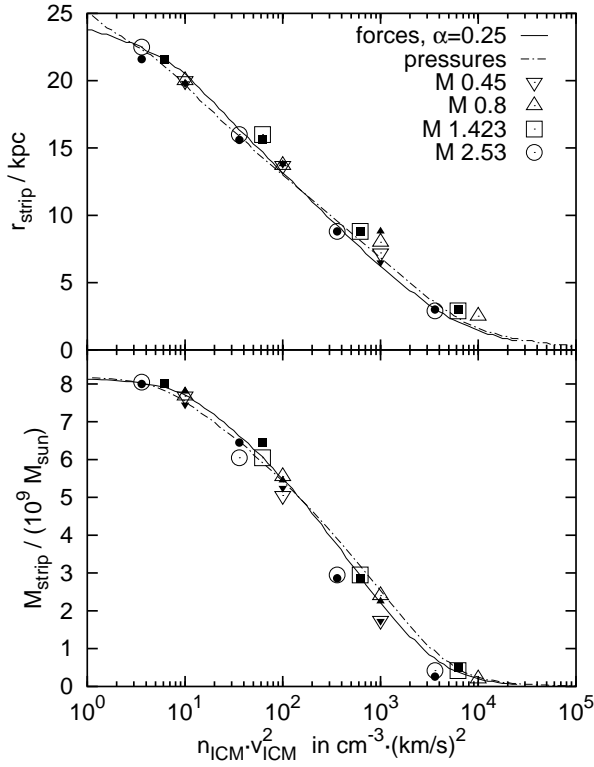
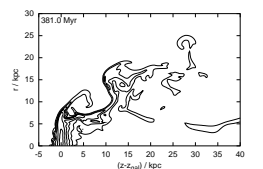


Figure 4.26: Comparison between the analytical estimates and the numerical result for the massive galaxy with Rankine-Hugoniot-corrected ram pressures for the supersonic cases (see text). Open and solid symbols are for cases with T_{ICM1} and T_{ICM2} , respectively. The symbol shape codes the Mach number. The analytical estimate for the force comparison (solid line) is fitted to the numerical results via the parameter α (see also text). The estimate from the pressure comparison is repeated unmodified.

component of the momentum density $\rho_{\text{ICM}} v_{\text{ICM}}$ perpendicular to the shock front is conserved across such a shock, whereas the velocity at the downstream side is reduced (and the density increased) by a certain factor according to the Rankine-Hugoniot conditions. Then also the true ram pressure would be diminished by the same factor as v . In case of a straight shock, for Mach numbers of 1.423 and 2.53 (at the upstream side) the velocity at the downstream side is reduced by factors of 0.62 and 0.36, respectively. We calculate these corrections for the straight shock, because the exact shape of the bow shock depends on the object causing it (here the galaxy). Only at large distances to the object the bow shock angle approaches the well-known Mach angle, and – strictly speaking – then it is no shock any more but degenerates to a small amplitude acoustic wave (see e.g. Shu 1992). In Figs. 4.26 and 4.27 we replot the numerical results with this correction, that is shifting the points for the supersonic results down to the corrected ram pressures. In addition, we repeat the analytical estimate from the pressure comparison (version (d), marked with “pressures” in Figs. 4.26 and 4.27) and plot the estimate from the force comparison with an adjusted α (see Eq. 4.17, marked with “forces, $\alpha = 0.25$ ” in Figs. 4.26 and 4.27). For $\alpha = 0.25$ the numerical result and the analytical estimate agree well. In contrast to the uncertainty expressed by α in the force comparison, there is no uncertainty in the pressure comparison. And indeed the (Rankine-Hugoniot-corrected) numerical result and the estimate from the pressure comparison are in good agreement. With $\alpha = 0.25$, the estimate from the force comparison was



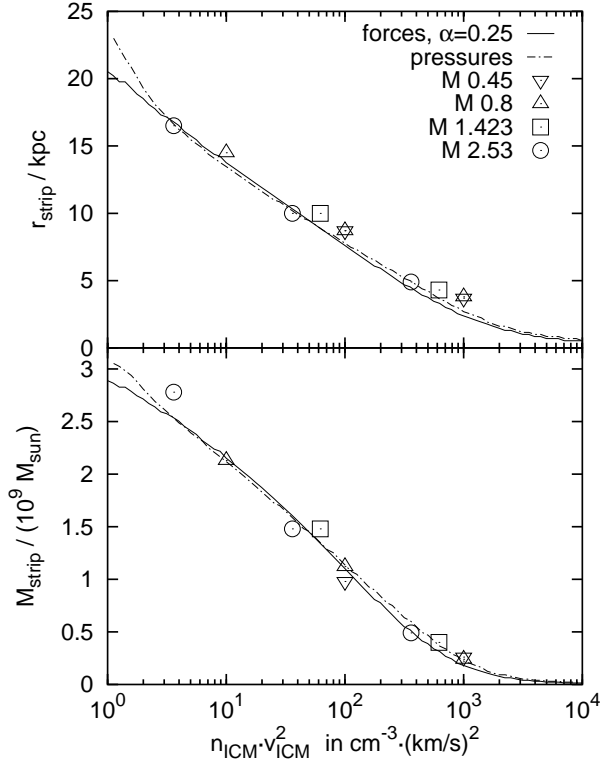


Figure 4.27: Same as Fig. 4.26, but for the medium galaxy.

shifted to match the result from the pressure comparison. The point for the lowest ram pressure and Mach 2.53 in Fig. 4.27 that lies above the analytical estimate is explained easily because the dynamic intermediate phase for this run is not finished at the end of the simulation. We note that the correction of the ram pressures for the supersonic cases according to the Rankine-Hugoniot conditions cannot describe the situation completely, because it would mean that also in the supersonic range the results should depend slightly on the Mach number. This is not found in the simulations (see Sect. 4.6.2).

We can also compare the predicted duration for the instantaneous stripping with the numerical result. The prediction drawn from Eq. 4.12 refers only to the replacement of the outer gas disk. The numerical result for the replacement is given by the time of the first local minimum in the r_{disk} curves in Figs. 4.11, 4.14 and 4.21 (τ_{push}). The trends in the numerical result and the analytical estimate shown in Fig. 4.28 agree well, also the absolute values agree roughly. We also show the duration of the intermediate phase, that is the time until all gas that is not bound tightly enough is truly unbound. We find that this time is approximately 10 times as long as the instantaneous stripping phase.

4.9.2 Continuous stripping

The estimate of the mass loss rate during the continuous stripping phase (see Sect. 4.2.2) is only a rough one. The mass-loss rates are expected to

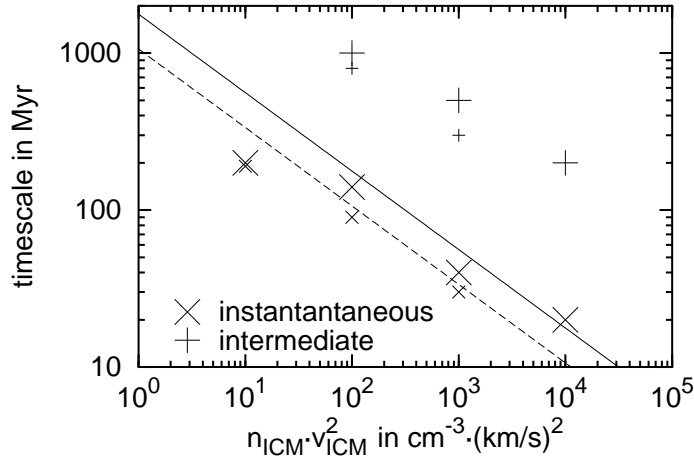
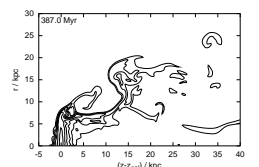


Figure 4.28: Duration of the instantaneous stripping phase τ_{push} and intermediate phase as a function of ram pressure. Large symbols are for the massive galaxy, small symbols for medium galaxy. Also the analytical estimate for the instantaneous phase according to Eq. 4.12 is shown, the solid line is for the massive galaxy, the dashed one for the medium galaxy.

be of the order of one $M_{\odot} \text{ yr}^{-1}$. Fig. 4.29 demonstrates the mass-loss rates derived from the simulations by fitting a linear function to $M_{\text{bnd}}(t)$ during the continuous stripping phase. Because the runs with $\tilde{p}_{\text{ram}} = 10 \text{ cm}^{-3} \text{ km}^2 \text{ s}^{-2}$ do not reach the continuous phase during the runtime, for those runs we fit the time range between 1 and 2 Gyr. From the simulations we can derive mass-loss rates between 0.1 and $2 M_{\odot} \text{ yr}^{-1}$. Except that the highest ram pressures produced the highest mass-loss rates, we cannot find any further trends. The analytical estimate could give a rough impression only.



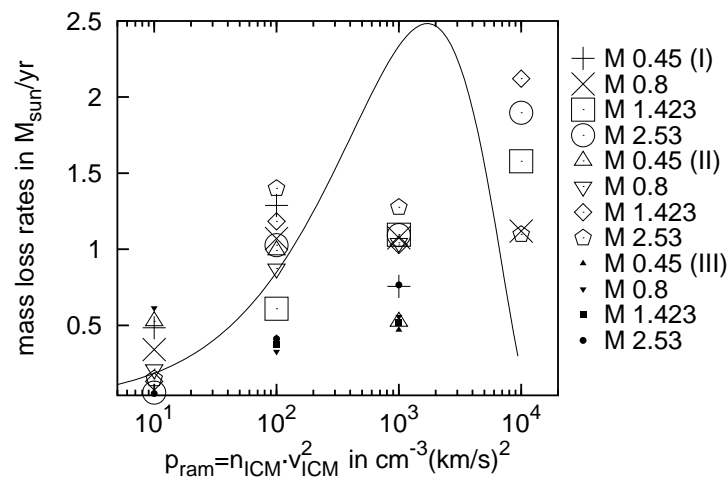


Figure 4.29: Mass loss rates of the continuous stripping phase as a function of ram pressure. The Mach numbers are coded by different symbols. The upmost four symbols (group (I)) are for the massive galaxy in winds with $T_{\text{ICM}1}$, the symbols of group (II) for the massive galaxy in winds with $T_{\text{ICM}2}$, and the lower four symbols (group (III)) for the medium galaxy in winds with $T_{\text{ICM}1}$. The solid line shows the rough analytical estimate (see Sect. 4.2.2).

Chapter 5

Summary and discussion

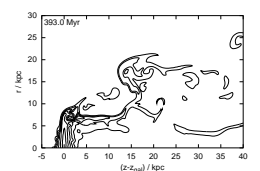
Summary

We have used a Eulerian hydrodynamics code to simulate RPS of disk galaxies in various environments. We restricted the simulations to the face-on case, which can be addressed with a 2D code assuming cylindrical symmetry. This enabled us to use high resolution and compile a comprehensive parameter study. Concerning the ICM winds, we covered conditions ranging from strong winds like expected near cluster centres to weak winds like in cluster outskirts or groups. For lucidity we use constant ICM winds. Concerning the galaxy, we concentrated on the influence of the vertical structure of the gas disk by testing the behaviour of exponential and flared disks of various thicknesses. Additionally we studied galaxies of two different masses.

We find that the stripping process proceeds in three phases:

- **Instantaneous stripping:** The outer disk is bent towards the downstream side, but it is only partially unbound. This phase is short (20 to 200 Myr), its duration is a function of ram pressure. The main reduction of the gas disk radius takes place in this phase.
- The **intermediate phase** is rather dynamic. A part of the displaced gas falls back to the disk (about 10% of the original gas mass), but most displaced gas is stripped completely now. This phase lasts about 10 times as long as the instantaneous stripping phase.
- Finally the galaxy enters the **quasi-stable continuous stripping** phase. It continues to lose gas at a rate of about $1M_{\odot} \text{ yr}^{-1}$. Also the disk radius decreases slowly.

In order to predict the stripping radius and stripping mass (i.e. the radius and mass of the remaining gas disk), the classic estimate of Gunn & Gott (1972) compares the ram pressure with the local gravitational restoring force. However, this method does neither distinguish between ICM flows with the same ram pressure but different Mach numbers, nor between gas disks of



different vertical structure. Our simulations confirm that the stripping process is independent of the vertical structure of the gas disk (exponential or flared shape, various thicknesses). However, we find a slight dependence of the stripping efficiency on the Mach number of the flow in the sense that the galaxy loses somewhat less gas in supersonic winds. Nevertheless, the main parameter governing the gas loss is the ram pressure. The dependence on Mach number also needs to be confirmed with a two-fluid model of the ICM.

We extract the stripping radius and stripping mass as functions of the ram pressure from our simulations. Comparing them to the classical analytical estimate, we find that the analytical result is offset with respect to the numerical one; the analytical estimate somewhat underestimates the stripping efficiency. If one summarises all simplifications that have been assumed for the analytical estimate in a correction factor and multiplies this with the restoring force, the systematic difference can be eliminated. Mori & Burkert (2000) have proposed an alternative estimate for spherical galaxies, namely comparing the central thermal pressure with the ram pressure. We adapt this for disk galaxies: We calculate the thermal pressure in the disk plane assuming zero external pressure (corresponding to an isolated galaxy). At radii where the ram pressure exceeds this thermal pressure, the gas will be stripped. We find that this estimate agrees very well with the numerical results.

In a careful contemplation of the initial conditions used for the simulations we have shown that normal gas disks cannot exist in the high pressure environment near cluster centres. The impact of this conclusion on our simulation has been tested and is discussed below along with further implications (and limitations) of our results.

Galaxies in clusters

We find that even massive galaxies can lose a substantial part of their gas disks, and can be stripped completely in cluster centres. This confirms results of previous works. For the high ram pressures in the central cluster regions the compression of the remaining gas disks may lead to an enhanced SFR. However, our simulations cannot resolve this process. Moreover, the fact that we do not observe an enhancement in the gas surface density of the remaining disk may be due to the cylindrical symmetry. In the three-dimensional reality the disturbed gas disk could develop radial or non-symmetrical instabilities that increase the surface density at least locally.

Cluster outskirts and galaxy groups

In our simulations we found that even mild ram pressures of about $100 \text{ cm}^{-3} \text{ km}^2 \text{ s}^{-2}$ and less already truncate the gas disk of massive galaxies to about 15kpc. Even if low ram pressures do not unbind much gas, they still displace the outer parts of the gas disk. The wind itself and back-falling

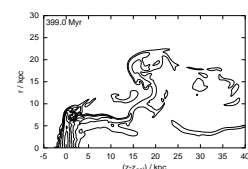
gas disturb the disk and send shock waves through it which could trigger SF (e.g. Fujita & Nagashima 1999). We therefore expect that even at larger distances from the cluster centre or in groups the gas disks of most galaxies should be “pre-processed” (see also Fujita 2004). This pre-processing of galaxies in cluster outskirts and groups could explain the HI deficient galaxies at large distances to the cluster centre found by Solanes et al. (2001). The ICM-ISM interaction in low density environments may be more important than thought so far.

Morphological features of stripped galaxies

In agreement with previous work, our simulations suggest that disk galaxies suffering (approximately) face-on RPS should have truncated disks, where the radius of the disk is set by the ram pressure and the galactic potential. Moreover, if they are in the instantaneous stripping phase or the dynamic intermediate phase, stripped gas could be found behind the disk. How long such tails exist depends at least on p_{ram} . In how far this stripped gas actually remains visible, is dispersed or cools, forms stars or is affected by heat conduction, our simulations cannot predict as they do not include such processes. Due to the homogeneous gas disk used in our simulations, filaments emerging from the disk are found mainly at the disk edge. This resembles NGC 4522 very closely (see Sect. 1.5.3). The filaments found in NGC 4569 do not seem to emerge from the edge but more from the centre of the disk. This may be due to activity in the galactic nucleus or due to RPS of an inhomogeneous gas disk.

Time dependent winds

During its passage through a cluster a galaxy does not experience a constant wind. Galaxies on more radial orbits go through the high density cluster core. With a typical velocity of 1000 km s^{-1} a galaxy needs 1 Gyr to cross the inner Mpc of the cluster. Vollmer et al. (2001b) calculated the time dependent ram pressure for a galaxy falling into the Virgo cluster (their Fig. 3) and found that typically the ram pressure exceeds $1000 \text{ cm}^{-3} \text{ km}^2 \text{ s}^{-2}$ for about 100 Myr before and after the core passage, and still exceeds $300 \text{ cm}^{-3} \text{ km}^2 \text{ s}^{-2}$ about 250 Myr before and after the core passage. According to our simulations these times are definitely long enough to truncate the radius of the gas disks. However, the duration of the high ram pressure may be too short to unbind all displaced gas. Even in our simulations with constant winds several $10^8 M_{\odot}$ fall back to the disk region, and for quite a while about $10^9 M_{\odot}$ of gas that is still bound lingers behind the galaxy. If the ram pressure abates too early after the core passage all this gas should fall back to the disk. From our simulations we cannot infer in how far and how fast the gas disk resettles after the core passage.



Inclination

We have studied only cases where galaxies move face-on. What can we learn for inclined cases? Marcolini et al. (2003) found that the inclination angle matters only for medium ram pressures. This can be understood also in the context of our simulations. For very weak winds hardly any gas is unbound from the galaxy by the pushing effect, the main mechanism is the continuous stripping. For this mechanism the inclination angle is not important, it works on the whole surface. For very strong winds the complete disk is lost independently of inclination. Only for the intermediate winds the inclination decides how much mass can be pushed out in the beginning, hence for heavily inclined cases less gas is lost in this phase. After that the continuous stripping continues at the stage where the previous phase has ended. Also Quilis et al. (2000) agreed that only strict edge-on galaxies can retain more gas, intermediately inclined galaxies are stripped similarly to face-on ones. This is also in agreement with the results of Vollmer et al. (2001b), who constructed a generalised formula relating the remaining gas mass with the ram pressure and the inclination angle. However, their sticky-particle simulations cannot model the turbulent viscous stripping. Schulz & Struck (2001) found that for inclined galaxies less gas lingers in the lee of the disk, hence our results concerning back-falling gas may change in such situations. However, the unbinding of the gas after it has left the disk region should take some time also for inclined cases.

Mixing with the intracluster medium

We tried to infer to what extent ICM gets mixed into the remaining gas disk. Such mixing would change the angular momentum and metallicity of the gas disk. To investigate this point we compared the two alternatives for defining galactic gas (see Sect. 4.5.1). In our standard way to calculate the gas mass inside the disk region we identified galactic gas by its “colour” (see Sect. 4.5.2). The alternative is to identify all gas with a temperature below $5 \cdot 10^6$ K (about the virial temperature of the massive galaxy) as galactic gas. This prevents that we include the ICM that is streaming freely through the already swept disk region, but it would include all ICM that has already mixed with the gas disk. Concerning the mass of the bound gas, we compared summing over all gas in the region of the bound gas and summing over the “coloured” gas only. The first version includes the ICM there, the second does not. We find, however, no differences between the versions that should include or exclude the ICM, so we conclude that no ICM is accreted by the galaxy.

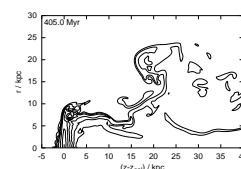
Influence of the external pressure

What happens to the gas disk of a spiral galaxy in a high pressure external medium? Already from the comparison of typical pressures in the disks of

isolated galaxies (10^{-13} to 10^{-11} erg cm $^{-3}$) and typical ICM pressures (e.g. $\sim 10^{-12}$ erg cm $^{-3}$ for $n_{\text{ICM}} \approx 3 \cdot 10^{-4}$ cm $^{-3}$ and $T_{\text{ICM}} \approx 3 \cdot 10^7$ K) it is obvious that normal disk galaxies cannot exist in cluster environments, no matter if they move or not. We have already discussed in Sect. 3.2.2 that a field galaxy entering a cluster has to increase its internal pressure either by being compressed or by heating up, depending on whether the temperature or the density distribution shall remain unchanged.

To allow a systematic study of galactic parameters we chose to fix the ISM density distribution and accepted the varying temperature. A concern about this point is that due to the high temperature (and hence higher thermal energy) our gas disks are not bound as strongly as cooler disks in isolated galaxies and hence are stripped easier. In this case we would overestimate the stripping efficiency. However, in varying the gas disk thickness and shape we have already checked if such thin (and cooler) disks are harder to strip, but we did not find them to be more resistant to RPS. We also performed test runs that started with a galaxy resembling an isolated one (concerning disk pressure and temperature), but put into a high-pressure ICM. As this galaxy was not in hydrostatic equilibrium with the ICM, it was compressed immediately and then stripped like its equilibrium analogue. Hence we conclude that our results are not biased significantly by the initial pressure and temperature distribution.

The fate of a more realistic multi-phase disk in a high pressure external medium may be rather complex. A first reaction to an increased external pressure could be an enhanced star formation due to the compression of molecular clouds. In how far the formation of molecular clouds would be prevented or nurtured by a continuing external pressure is difficult to judge. It would be worth to study this question in a separate work.



Chapter 6

Future work

Some of the ideas proposed here for future projects result from the limitations of the code discussed in the previous chapter. The most important step will be to go from 2D to 3D. But before that, some more points can be studied with the 2D code.

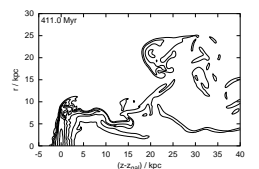
Can a gas halo protect the disk?

Some galaxies have an extended hot gas halo. The idea is that it might be able to protect the gas disk from being stripped to some degree. However, closer considerations suggest that this is rather unlikely. Firstly, the particle density in such halos is about 10^{-3} cm^{-3} . This value is reached easily in the ICM near cluster centres. Like the gas disks, also the halos should be either compressed or heated by the external pressure. For a fixed density distribution, under the assumption of hydrostatic equilibrium with the ICM, the gas halo can become unbound easily. For $p_{\text{ICM}} \gtrsim 10^{-12} \text{ erg cm}^{-3}$ the thermal energy in the gas halo reaches values that exceed the gravitational energy. This suggests that the halo can play a role in the cluster outskirts only. There, however, only the outer parts of the disk are stripped in any way. The gas halo density decreases with increasing distance to the galactic centre, so it is unlikely that the halo can protect the outer edge of the disk. These suppositions seem to be confirmed by first test runs. We could use the colouring technique (see Sect. 4.5.2) to trace the whereabouts of disk gas and halo gas separately. This allows to study mixing processes. The extension of the code by one more “colour” should be straightforward. We could also try to study in how far the halo can buffer the compression of the disk by the external medium.

This point can be studied with the 2D code.

Do (central) holes enhance the stripping efficiency?

Especially early-type galaxies show central depressions in their radial HI profiles. Some scientists suppose that these holes could make the disks more



vulnerable to RPS (see introduction). Also the simulations of Quilis et al. (2000), who cut a real hole in the gas disk, suggest that this enhances the stripping efficiency. However, we would like to point out that generally the HI disks do not show a central hole but a depression of the density profile, the density is only reduced by a factor of 3 to 10. Moreover, the missing cooler HI gas could be replaced by hot gas. Whether the ram pressure can push out the central part should depend on the local pressure or gravitational restoring force. We already performed test runs with a central hole of 2.5 kpc radius (using a real hole to test the extreme case). The instantaneous stripping phase and the beginning of the intermediate phase appear nearly identical with and without the hole. It seems that the mass loss rate in the continuous stripping phase is enhanced only in cases of stronger ram pressures. E.g. for $\tilde{p}_{\text{ram}} = 1000 \text{ cm}^{-3} \text{ km}^2 \text{ s}^{-2}$ all the gas was stripped completely after 1.5 Gyr.

On the basis of their simulations Quilis et al. (2000) concluded that especially small holes scattered over the disk (mimicking an inhomogeneous ISM) enhance the stripping efficiency. However, they did not quantify their results in detail. Introducing small non-central holes in the 2D code proved difficult, as here the holes always represent rings. So far, with a simple ansatz, we could not achieve radial stability in the initial model. Due to the deep depressions in the density profile the rotation curve is deformed. The holes do not persist but are filled from neighbouring cells. They are not filled completely to produce a smooth radial density profile, but dips remain. However, these depressions are not always “deep” enough for the wind to flow through them. Nevertheless we can learn from these tests (and we could have guessed before) that the surface density inside the “holes” must be below a certain limit if the gas in the holes shall be blown away by the ICM wind.

Comparison with other codes

Every numerical code has its limitations. Therefore it would be of great interest to compare the results of different codes applied to the same problem. Such comparative simulations are planned with B. Vollmer, who uses a sticky particle code. Basically this code describes the effect of RPS by an additional force on each particle exposed to the wind (see Vollmer et al. 2001b for more detailed description). Also comparisons with SPH (smoothed particle hydrodynamics) are planned with D. Michielsen.

Such comparisons should be made using our 2D code as well as a 3D grid code.

Cluster crossing

To simulate a cluster crossing the ICM velocity and density need to be varied simultaneously. Unfortunately this cannot be done by simply varying both values at the inflow boundary. This works for the velocity. Increasing ϱ_{ICM} and keeping T_{ICM} constant also increases the ICM pressure at the inflow

boundary, resulting in conditions very similar to the Riemann shock tube (see Appendix C.1). This leads to a supersonic flow independently of the value set for v_{ICM} . One idea might be to keep p_{ICM} constant by decreasing T_{ICM} according to the increase of ϱ_{ICM} . However, ϱ_{ICM} has to be increased over about two orders of magnitudes, and T_{ICM} does not vary that much in clusters. The solution is to take the cluster potential into account and provide a large-scale potential gradient that cancels the pressure gradient introduced by increasing ϱ_{ICM} .

Although this seems to be a straightforward task, usually the devil is in the details. We need to consider carefully whether we want to implement this feature into the 2D code or whether it would be more economical to delay this until we have a working 3D code.

Other inclinations

A 3D code is a must for modelling various inclinations between the galaxy and the wind. The necessary compromise between computational expense and resolution favours adaptive-mesh-refinement codes.

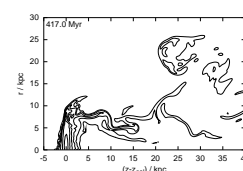
The attempts of B. Vollmer to infer the stripping history of individual galaxies by detailed comparison between observations and simulations (see Sect. 1.5.3) are promising. They show clearly that besides the density distribution of the (stripped) gas also kinematic information is necessary. This can be derived from 3D simulations only. It would be interesting to compare the kinematics predicted by the sticky-particle code and by a hydrodynamical one.

When choosing the code we should take its feasibility for long-term aims into account.

Influence of the hot high-pressure environment on a multi-phase ISM

What we would need in order to study this question is a code that could model a multi-phase ISM including effects like cooling, SF, feedback by stars due to radiation, winds and SNe; evaporation and condensation between the gas phases, thermal conduction, magnetic fields; all in a self-consistent description. We then could add a high-pressure, hot external medium and could study the effect of thermal conduction from the ICM into the ISM and the result of the compression. Unfortunately – such a code does not exist yet. We do not understand the dynamics of the ISM well enough. Making progress in ISM modelling, especially including magnetic fields, is a very interesting topic in itself.

Nonetheless this is a very important question, as most galaxies are members of galaxy groups or clusters. Nearly all clusters are filled with an ICM, and also most groups are thought to contain an intra-group medium (Burstein & Blumenthal 2002). Therefore the influence of an external pressure and



thermal conduction between the external gas and the ISM could play an essential role.

We need to consider carefully how we can make reasonable simplifications to derive answers to this questions.

What happens to the stripped gas?

Are stars formed in the stripped clumps? Are clumps evaporated? These are questions for both modelling and observations. E.g. the $H\alpha$ observations of NGC 4522 (see Fig. 1.9) show filaments emerging above the disk plane. However, the ionisation of this gas is not necessarily due to the radiation of young massive stars formed inside this gas. Other ionisation processes like extragalactic radiation or radiation from the galactic centre are possible. To distinguish between them spectra need to be taken.

Is molecular gas stripped?

The fate of molecular clouds (MCs) in a ram pressure stripped galaxy is subject to ongoing discussion. The first idea is that MCs are much too small and too dense to be affected by the tenuous ICM wind. On the other hand, according to multi-phase ISM models they are a transient phenomenon. Soon after a MC started to form stars it is disrupted and transferred to the diffuse gas phase by the stellar feedback. This gas then could be stripped and MCs cannot be re-formed. This scenario matches the observation that no $H\alpha$ emission is observed in the outer parts of NGC 4522. If MCs would not be lost, why do they not form stars? Observations of molecular gas so far are restricted mainly to the central parts of galaxies. Deep CO observations of the outer parts of HI-stripped galaxies could be undertaken to check if MCs can be found there or not.

Generalisation for statistical studies

One aim of the simulations should be to deduce generalisations, e.g. a relation that describes the dependence of the mass loss on orbit parameters, galaxy mass and other parameters. Such results can be used as input models by large-scale simulations of e.g. the evolution of the ICM of the galaxy populations.

Appendix A

Miscellaneous

A.1 Astrophysical units

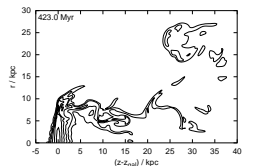
A.1.1 Basics

$$\begin{aligned}1 \text{ pc} &= 3.086 \cdot 10^{16} \text{ m} = 3.086 \cdot 10^{18} \text{ cm} \\1 \text{ yr} &= 3.156 \cdot 10^7 \text{ s} \\1000 \text{ km s}^{-1} &= 1.02 \text{ kpc Myr}^{-1} = 1.02 \text{ pc (1000 yr)}^{-1}\end{aligned}$$

$$\begin{aligned}1 M_{\odot} &= 1.989 \cdot 10^{30} \text{ kg} \\1 \text{ amu} &= 1.66053873 \cdot 10^{-27} \text{ kg} \\m_{\text{proton}} &= 1.673 \cdot 10^{-27} \text{ kg} \\m_{\text{electron}} &= 9.109 \cdot 10^{-31} \text{ kg}\end{aligned}$$

$$\begin{aligned}\text{redshift}^1 z &= 2 \cdot 10^{-4} \frac{r}{\text{Mpc}} && \text{for small distances } r \\ \text{distance}^1 r &= 5 \cdot 10^3 \text{ Mpc} \cdot z && \text{for small redshifts } z \\ \text{diameter}^1 \text{ of an object } D &= 0.3 \text{ kpc} \cdot \frac{r}{\text{Mpc}} \cdot \frac{b}{\text{arcmin}} \\ D &= 1.5 \text{ Mpc} \cdot z \cdot \frac{b}{\text{arcmin}} && \text{for small distances}\end{aligned}$$

¹for Hubble constant $H_0 = 60 \text{ km s}^{-1} \text{ Mpc}^{-1}$



A.1.2 Commonly used quantities

$$\begin{aligned}
\text{mass density: } 0.6033 \text{ amu} \cdot 10^{-3} \text{ cm}^{-3} &= 1.002 \cdot 10^{-27} \text{ g cm}^{-3} \\
&= 1.47 \cdot 10^{-5} M_{\odot} \text{ pc}^{-3} \\
1 \text{ amu} \cdot 10^{-3} \text{ cm}^{-3} &= 1.66 \cdot 10^{-27} \text{ g cm}^{-3} \\
&= 2.45 \cdot 10^{-5} M_{\odot} \text{ pc}^{-3} \\
\text{surface density: } 1 \text{ amu} \cdot 10^{21} \text{ cm}^{-2} &= 1.66 \cdot 10^{-3} \text{ g cm}^{-2} \\
&= 7.95 M_{\odot} \text{ pc}^{-2} \\
(\text{ram}) \text{ pressure: } 1.002 \cdot 10^{-11} \text{ erg cm}^{-3} &= 0.6033 \text{ amu} \cdot 1000 \text{ cm}^{-3} \text{ km}^2 \text{ s}^{-2} \\
\text{temperature: } 1 \text{ keV} &\hat{=} 1.16 \cdot 10^7 \text{ K} \\
10^7 \text{ K} &\hat{=} 0.86 \text{ keV}
\end{aligned}$$

A.2 Useful relations

A.2.1 Conversion between scale lengths

$$e^{-x/x_0} = 10^{-x/(2.3 x_0)} = 2^{-x/(0.69 x_0)} \quad (\text{A.1})$$

A.2.2 Operators in cylindrical coordinates

The nabla operator (gradient) in cylindrical coordinates (z, r, ϕ) :

$$\vec{\nabla} f = \frac{\partial f}{\partial z} \vec{e}_z + \frac{\partial f}{\partial r} \vec{e}_r + \frac{1}{r} \frac{\partial f}{\partial \phi} \vec{e}_{\phi} \quad (\text{A.2})$$

Divergence of a vector field $\vec{A} = (A_z, A_r, A_{\phi})$ in cylindrical coordinates:

$$\vec{\nabla} \cdot \vec{A} = \frac{\partial A_z}{\partial z} + \frac{1}{r} \frac{\partial (r A_r)}{\partial z} + \frac{1}{r} \frac{\partial A_{\phi}}{\partial \phi} \quad (\text{A.3})$$

The Laplace operator in cylindrical coordinates:

$$\Delta f = \frac{\partial^2 f}{\partial z^2} + \frac{1}{r} \frac{\partial}{\partial r} \left(r \frac{\partial f}{\partial r} \right) + \frac{1}{r^2} \frac{\partial^2 f}{\partial \phi^2} \quad (\text{A.4})$$

A.3 Virial theorem

The Virial theorem states that in a closed system, the temporal mean values for the kinetic energy and potential energy relate as

$$\bar{E}_{\text{kin}} = -\frac{1}{2} \bar{E}_{\text{pot}}. \quad (\text{A.5})$$

An especially interesting application is to calculate the typical velocity σ of particles in a spherically symmetric mass distribution of mass M and radius R . For such a system the potential energy as well as its mean is

$$\bar{E}_{\text{pot}} = -a G \frac{M^2}{R}; \quad (\text{A.6})$$

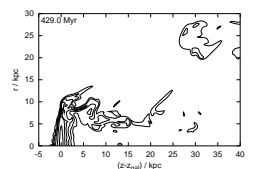
(for a homogeneous sphere $a = 3/5$). The mean of the total kinetic energy of course is

$$\bar{E}_{\text{kin}} = \frac{1}{2} M \sigma^2. \quad (\text{A.7})$$

Because of the Virial theorem M , R and σ relate as

$$\begin{aligned} \sigma^2 \sim G \frac{M}{R} &\approx (200 \text{ km s}^{-1})^2 \frac{M/(2 \cdot 10^{11} M_{\odot})}{R/(20 \text{ kpc})} \\ &\approx (1000 \text{ km s}^{-1})^2 \frac{M/(2.3 \cdot 10^{14} M_{\odot})}{R/(1 \text{ Mpc})} \end{aligned} \quad (\text{A.8})$$

(approximating $a \sim 1$). σ^2 can be translated to a temperature. Given an observed temperature or velocity dispersion and the spatial extent of a system, its mass can be estimated with the above relation.



Appendix B

Kelvin-Helmholtz instability

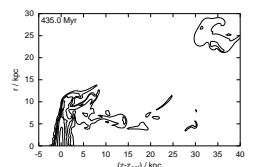
The Kelvin-Helmholtz (KH) instability is an interface instability due to a shear motion between two fluids. A daily-life example is wind blowing over water causing whitecaps. Under rare atmospheric conditions also clouds can trace KH instabilities between moving layers of air. Such an example is shown in Fig. B.1.

A detailed derivation of stability conditions and growth rates is given in Chandrasekhar (1961) for the case of a sharp discontinuity between the two fluids as well as for a finite boundary layer. Here we summarise the most important points for the case of a discontinuity between the fluids.

The derivation assumes two incompressible, inviscid fluids of densities ρ_1 (lower fluid) and ρ_2 (upper fluid) in a homogeneous gravitational field (like on earth the gravity shall work downwards), separated by a horizontal interface. If $\rho_1 > \rho_2$, in the absence of streaming this configuration is stable. Now assume the lower and the upper fluid stream horizontally in (anti)parallel direction with U_1 and U_2 , respectively. The perturbation theory is applied to this setup as usual: write down the hydrodynamical equations, replace each hydrodynamical quantity a with $a + \delta a$ (where δa is a small perturbation),



Figure B.1: Kelvin-Helmholtz clouds at Mount Shasta, northern California, USA (photo by Shannon 1999).



simplify the equations using the relations of the initial state and keep terms of first order in δa only. Then decompose the perturbations into Fourier modes and consider a single mode

$$\delta a = A \exp i(kx + \omega t). \quad (\text{B.1})$$

For real wave numbers k , depending on ω the perturbations are just oscillations (ω real) or grow in time (ω negative imaginary) or decay (ω positive imaginary). From the perturbation theory one can derive a dispersion relation $\omega(k)$ for the KH modes:

$$\omega(k) = -\frac{\varrho_1 U_1 + \varrho_2 U_2}{\varrho_1 + \varrho_2} k \pm k \sqrt{\frac{g}{k} \left(\frac{\varrho_1 - \varrho_2}{\varrho_1 + \varrho_2} + \frac{k^2 T_S}{g(\varrho_1 + \varrho_2)} \right) - \frac{\varrho_1 \varrho_2}{(\varrho_1 + \varrho_2)^2} (U_1 - U_2)^2}, \quad (\text{B.2})$$

where g is the gravitational acceleration and T_S is the surface tension. In the presence of surface tension and gravity the interface between the two fluids can only be stable if the square root in the dispersion relation is real, which means for the relative velocity $U = U_1 - U_2$ between the layers

$$(U_1 - U_2)^2 = U^2 < \frac{\varrho_1 + \varrho_2}{\varrho_1 \varrho_2} \left(\frac{g}{k} (\varrho_1 - \varrho_2) + k T_S \right). \quad (\text{B.3})$$

The right hand side of this inequality has a minimum for the wave number $k_* = \sqrt{g(\varrho_1 - \varrho_2)/T_S}$. Introducing k_* in Eq. B.3 leads to a critical velocity U_{crit} in the sense that the interface between the fluids can only be stable if

$$U^2 < U_{\text{crit}}^2 = \frac{\varrho_1 + \varrho_2}{\varrho_1 \varrho_2} 2 \sqrt{g T_S (\varrho_1 - \varrho_2)}. \quad (\text{B.4})$$

This means that as soon as the relative velocity between the fluids exceeds U_{crit} , the interface becomes unstable at wave numbers k_* . Applying this to the example of wind blowing over water, this estimate predicts a critical velocity of about $6.5 \text{ m s}^{-1} = 24 \text{ km h}^{-1}$ and critical wavelength of 1.7 cm. In reality, ripples appear at the water surface at much lower wind speeds, but they are no interface instability yet. But indeed, at the predicted velocity (wind force 4 on Beaufort scale) on the surface of the seas the number of whitecaps, real surface instabilities, increases suddenly.

In the absence of surface tension, one finds that instabilities grow if

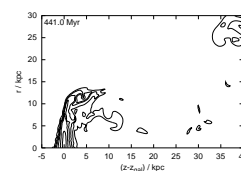
$$k > \frac{(\varrho_1^2 - \varrho_2^2)g}{\varrho_1 \varrho_2 U^2} \approx \frac{\varrho_1}{\varrho_2} \frac{g}{U^2} \quad \text{for } \varrho_1 \gg \varrho_2. \quad (\text{B.5})$$

Even if the relative velocity is very small, the instability will grow at small wave lengths. In the absence of gravity, the instability will grow for all wave numbers.

For cases where the interface becomes KH unstable, the growth rate of the stability can be calculated from Eq. B.2. In the case with gravity but without surface tension the growth rate is

$$\Im[\omega(k)] = k \sqrt{\frac{\varrho_2}{\varrho_1} U^2 - \frac{g}{k}} \approx \sqrt{\frac{\varrho_2}{\varrho_1}} U k = 2\pi \sqrt{\frac{\varrho_2}{\varrho_1}} U \lambda^{-1} \quad \text{for } \varrho_1 \gg \varrho_2, \quad (\text{B.6})$$

where $\lambda = 2\pi/k$ is the wave length of this mode.



Appendix C

Tests and code calibration

The code has been developed for many years and changes and extensions have been made by several people (e.g. Storm 1993; Severing 1995; Lohmann 2000; Vieser 2001). Thus we considered some tests necessary to be sure that the code works correctly. Concerning the hydrodynamics we performed basic tests like the Riemann shock-tube (Sect. C.1) and the Sedov blast wave (Sect. C.2). In addition we tested the potential flow past a sphere (Sect. C.3) as an example related closely to the actual application. The functionality of the potential solver was tested for the example of a homogeneous sphere (Sect. C.4).

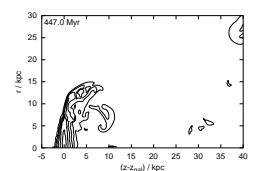
The tests and their results are summarised briefly in this Appendix. General conclusions from the tests are collected in Sect. C.5.

C.1 Riemann shock tube

A quintessential test for hydrodynamic codes is the Riemann shock tube problem (Sod 1978; Hawley et al. 1984; Stone & Norman 1992). The analytical solution can be found in the literature (e.g. Toro 1999), here we summarise the main points. In the simulations the influence of the resolution and the artificial viscosity was studied.

C.1.1 Analytical solution

The test deals with gas in a tube set up in two different states: a hot dense gas on the left, and a cool tenuous gas on the right. Initially these states can be imagined to be separated by a membrane, which is removed at $t = 0$. Then the two gases start to interact. The discontinuity in pressure leads to a shock wave travelling into the tenuous gas towards the right, and a rarefaction wave, travelling into the dense gas towards the left. Figure C.1 shows schematically the profiles for the density, pressure and velocity (in laboratory rest system) along the tube (z -axis). Regions 1 and 5 still show the initial conditions on the left and on the right. Region 2 is the rarefaction



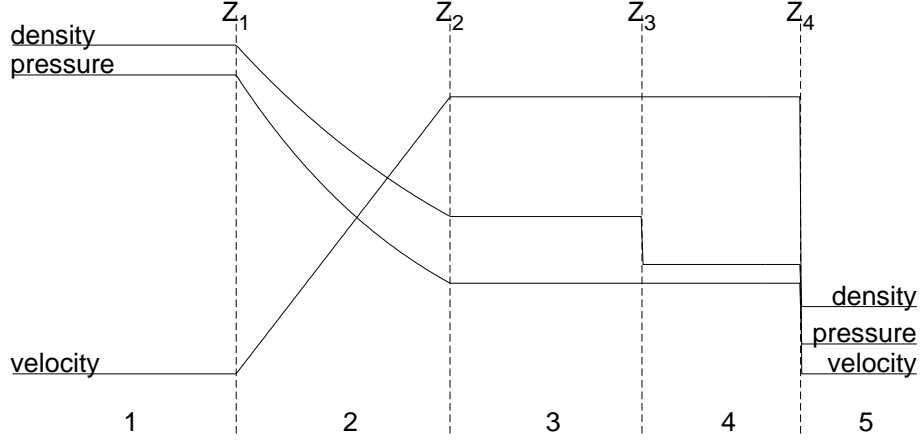


Figure C.1: Schematic shock tube solution for density, pressure and velocity. Characteristic features are: initial conditions on the left (region 1), initial condition on the right (region 5), rarefaction fan (region 2), shock front (Z_4), post-shock region (region 4), contact discontinuity (Z_3)

fan. The shock front is located at Z_4 , and region 4 is the post shock region. Region 3 connects the rarefaction fan and the post-shock region. In order to meet all conservation laws, there must be a contact discontinuity in density and temperature at Z_3 .

The variables ϱ_i , p_i , T_i and U_i name the density, pressure, temperature and velocity in z -direction. The index $i = 1, \dots, 5$ labels the different regions explained above and in Fig. C.1. Consequently $i = 1$ and $i = 5$ label the initial conditions on the left and right side, respectively. The initial conditions used here (and in Sod 1978) are:

$$\begin{aligned} u_1 = u_5 &= 0, \\ p_5 &= 0.1 p_1, \\ \varrho_5 &= 0.125 \varrho_1, \end{aligned} \tag{C.1}$$

where ϱ_1 and p_1 can be chosen arbitrarily. The solution for regions $i = 2, 3, 4$ is given in normalised units. Lengths are normalised to the length of the tube (the computational area) z_{\max} ; the density, pressure and temperature are normalised to the initial values on the left ϱ_1 , p_1 and T_1 ; velocities are scaled to a standard velocity of

$$v_{\text{stand}} = \sqrt{\frac{kT_1}{\mu m_{\text{H}}}} = \frac{c_1}{\sqrt{\gamma}} = \frac{c_1}{1.183} \quad \text{for } \gamma = 1.4, \tag{C.2}$$

where c_1 is the sound speed in the initial state on the left. The time is normalised to $t_{\text{stand}} = z_{\max}/v_{\text{stand}}$, that is the time to cross the computational

area with the standard velocity. The solutions for regions 2, 3 and 4 are

$$\begin{aligned}
 c_2 &= \frac{1}{\gamma + 1} \left(2c_1 - [\gamma - 1] \frac{z}{t} \right) \\
 u_2 &= \frac{2}{\gamma + 1} \left(c_1 + \frac{z}{t} \right) \\
 \rho_2 &= \rho_1 \left(\frac{c_1}{c_2} \right)^{\frac{2}{1-\gamma}} \\
 p_2 &= p_1 \left(\frac{c_1}{c_2} \right)^{\frac{2\gamma}{1-\gamma}}
 \end{aligned} \tag{C.3}$$

$$\begin{aligned}
 u_3 = u_4 &= 0.927 v_{\text{stand}} \\
 p_3 = p_4 &= 0.303 p_1 \\
 \rho_3 &= 0.426 \rho_1 \\
 \rho_4 &= 0.266 \rho_1
 \end{aligned} \tag{C.4}$$

Knowing the density and pressure, the temperature can be computed in the usual way:

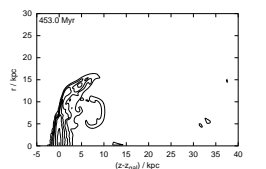
$$\frac{T}{T_1} = \frac{p/p_1}{\rho/\rho_1} \tag{C.5}$$

The positions of the borders between the regions depend on time according to:

$$\begin{aligned}
 Z_1/z_{\text{max}} &= -1.183 v_{\text{stand}} t \\
 Z_2/z_{\text{max}} &= -0.071 v_{\text{stand}} t \\
 Z_3/z_{\text{max}} &= 0.927 v_{\text{stand}} t \\
 Z_4/z_{\text{max}} &= 1.752 v_{\text{stand}} t
 \end{aligned} \tag{C.6}$$

C.1.2 Comparison of analytical and numerical result

Simulations with different spatial resolutions and artificial viscosity parameters were performed. An overview is given in Table C.1. Figure C.2 displays a direct comparison between the analytical and numerical result for the standard model (ST) and the model with pure linear viscosity (LV). For the standard case the numerical result agrees well with the analytical solution except at the contact discontinuity and shock front. Due to the artificial viscosity both discontinuities are spread over a few grid cells. Small overshoots can be seen where functions go from nonzero slope to zero slope discontinuously. According to Winkler & Norman (1986) this is the correct solution for a finite difference code including viscosity as $\Delta x \rightarrow 0$. Therefore these overshoots are a sign of low diffusivity. For the case with pure linear viscosity (LV) the agreement between the analytical and the numerical result is not so good, the discontinuities in slopes are softened significantly. The test case that uses the linear and the quadratic viscosity term (LQV) produces



Model	physical grid size (in pc)	number of cells	C_1, C_2
ST (standard)	10×0.5	200×10	0,2
HR (high resolution)	10×0.25	400×10	.
LR (low resolution)	10×1	100×10	.
NV (no viscosity)	10×0.5	200×10	0,0
HV (high viscosity)	.	.	0,4
LV (linear viscosity)	.	.	1,0
LQV (linear+quadr.visc.)	.	.	1,2

Table C.1: Parameters for the simulation runs for the shock tube test: physical grid size $z_{\max} \times r_{\max}$, number of cells $NZ \times NR$, artificial viscosity parameters C_1 and C_2 . Parameters common to all runs are the lhs particle density $n_1 = 1 \text{ cm}^{-3}$, lhs temperature $T_1 = 100 \text{ K}$, and the Courant-Friedrichs-Levy safety parameter $S_{\text{CFL}} = 5$. The \cdot means the same value as in the previous line. For an explanation of the numerical parameters see Chapter 2.

a similar result as the LV run. For the shock tube problem the use of the linear viscosity term ($C_1 > 0$) cannot be recommended. This is no wonder as the linear viscosity was designed for cases with strong shocks and stagnant regions, which are not present in the shock tube problem.

The results of varying the quadratic viscosity parameter or the resolution are displayed in Figs. C.3 and C.4, respectively. Both figures show normalised errors of the different quantities in the rarefaction fan and in the connection and post shock region (please compare to Fig. C.2). Due to its design the artificial viscosity has nearly no effect in the rarefaction fan, but improves accuracy in the connection and post shock region. Vice versa, the spatial resolution reduces the errors in the rarefaction fan. Also the result at the boundaries between the regions improves with higher resolution.

C.1.3 Courant-Friedrichs-Levy safety factor

The standard test case (ST) was rerun twice varying the Courant-Friedrichs-Levy safety factor (see Sect. 2.4) to $S_{\text{CFL}} = 2$ and $S_{\text{CFL}} = 10$. The influence is demonstrated in Fig. C.5. The largest differences appear at the zone borders, and for the temperature in the post shock region, but all differences are small.

C.1.4 Conservation of mass and energy

Fig. C.6 demonstrates the conservation of total mass and energy (thermal plus kinetic energy) in the computational area for the different models. The mass is conserved to a very high degree, no systematic difference between the different models is evident. The total energy is conserved to a few promille. The conservation is better for higher spatial resolution and higher viscosity.

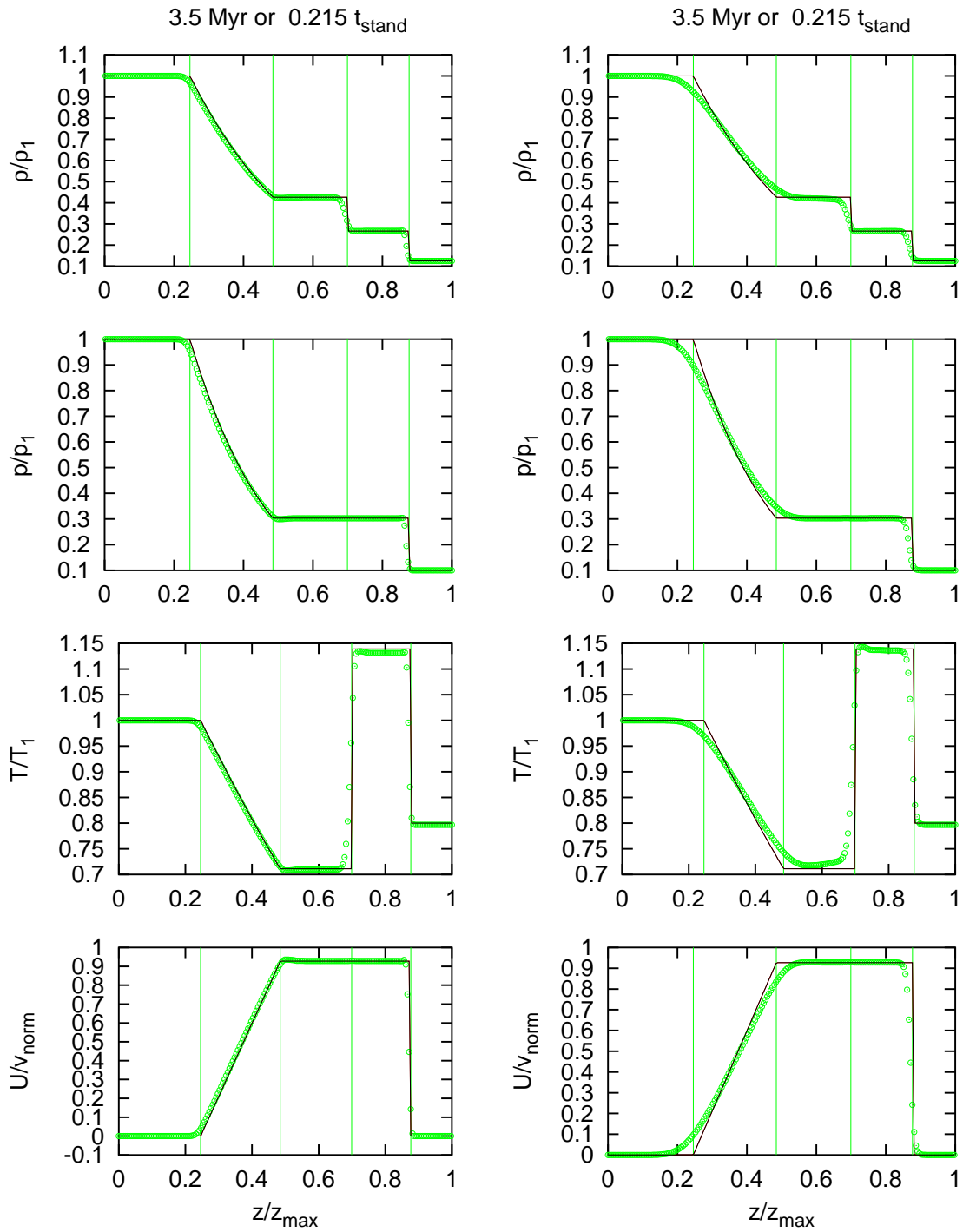
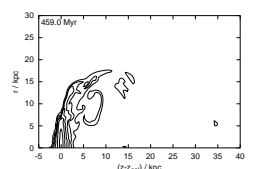


Figure C.2: Riemann Shock tube – comparison of analytical (black line) and numerical (circles, one for each cell) result. Normalised profiles for density ρ , pressure p , temperature T and axial velocity U for two models. The time is given in real and normalised units on top of each column. The zone borders are marked with vertical lines. **Left column:** standard run (ST). **Right column:** run with linear viscosity only (LV).



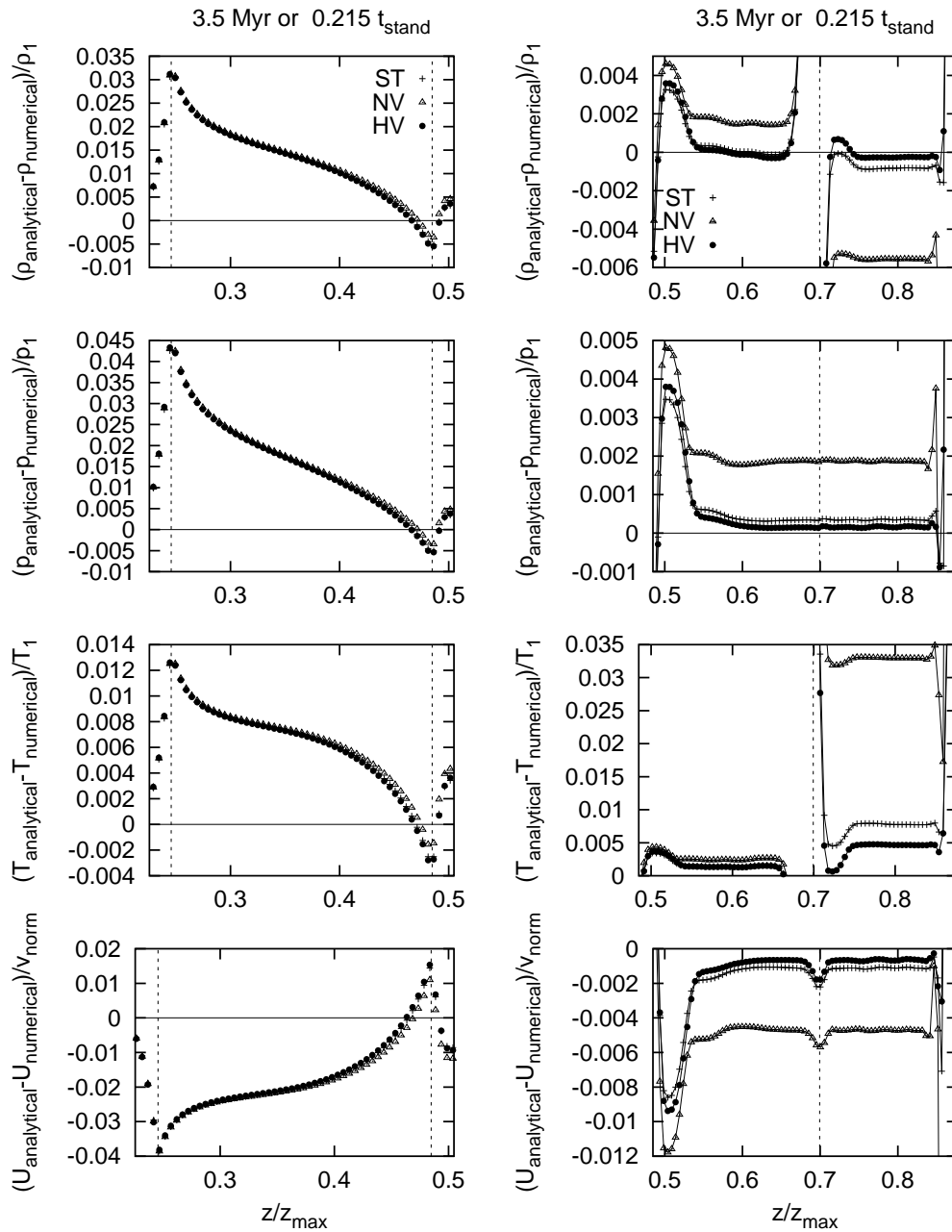


Figure C.3: Riemann Shock tube – influence of artificial viscosity (see key in density plot). Normalised differences between analytical and numerical result for density, pressure, temperature and velocity. The **left column** shows the region of the rarefaction fan, the **right column** shows the connection and post shock region. The zone borders are marked with dashed vertical lines. For orientation please compare with Fig. C.2.

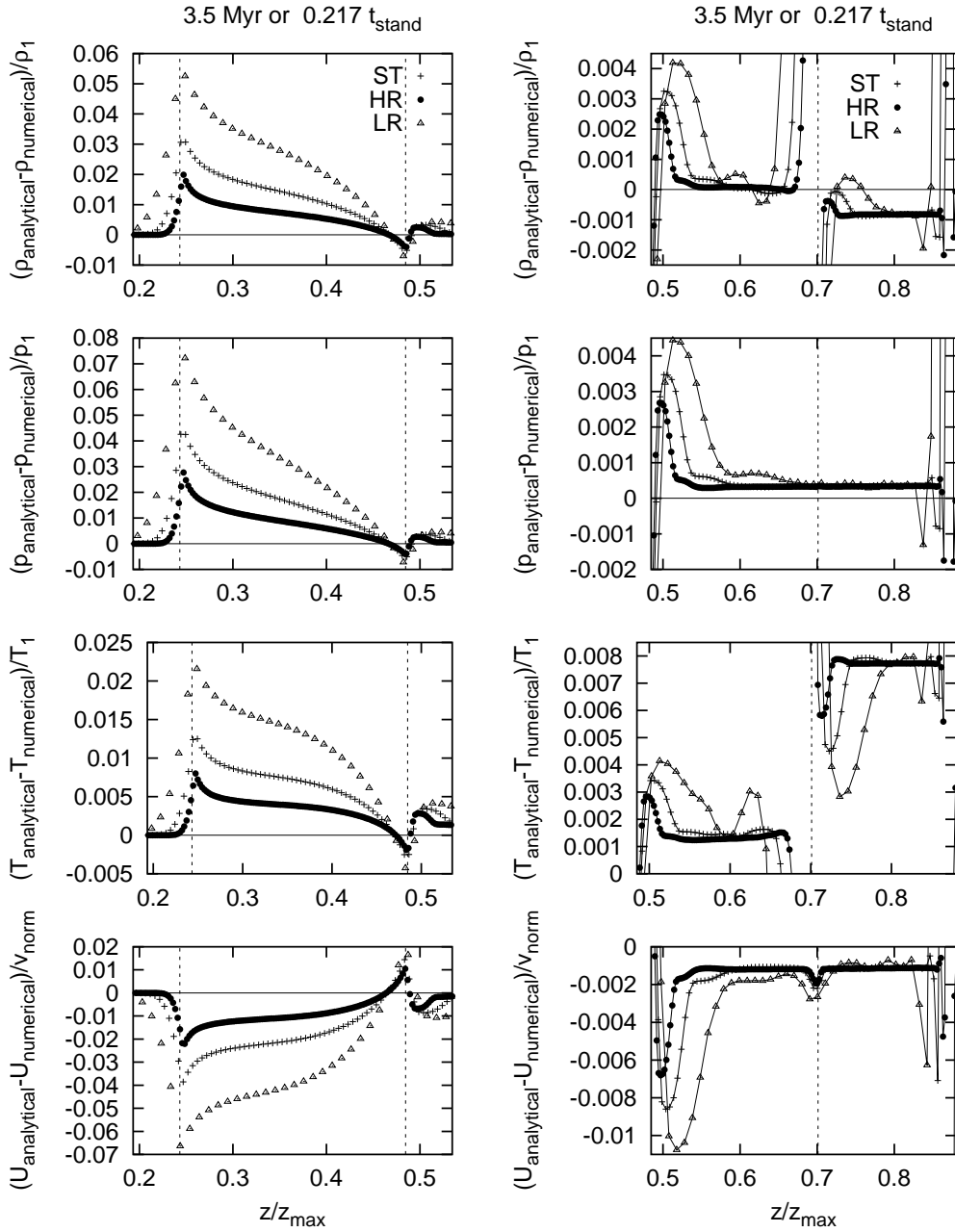
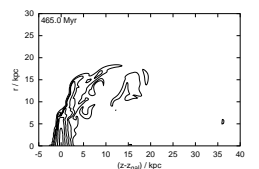


Figure C.4: Riemann Shock tube – influence of spatial resolution (see key in density plot). Normalised differences between analytical and numerical result for density, pressure, temperature and velocity. The **left column** shows the region of the rarefaction fan, the **right column** shows the connection and post shock region. The zone borders are marked with dashed vertical lines.



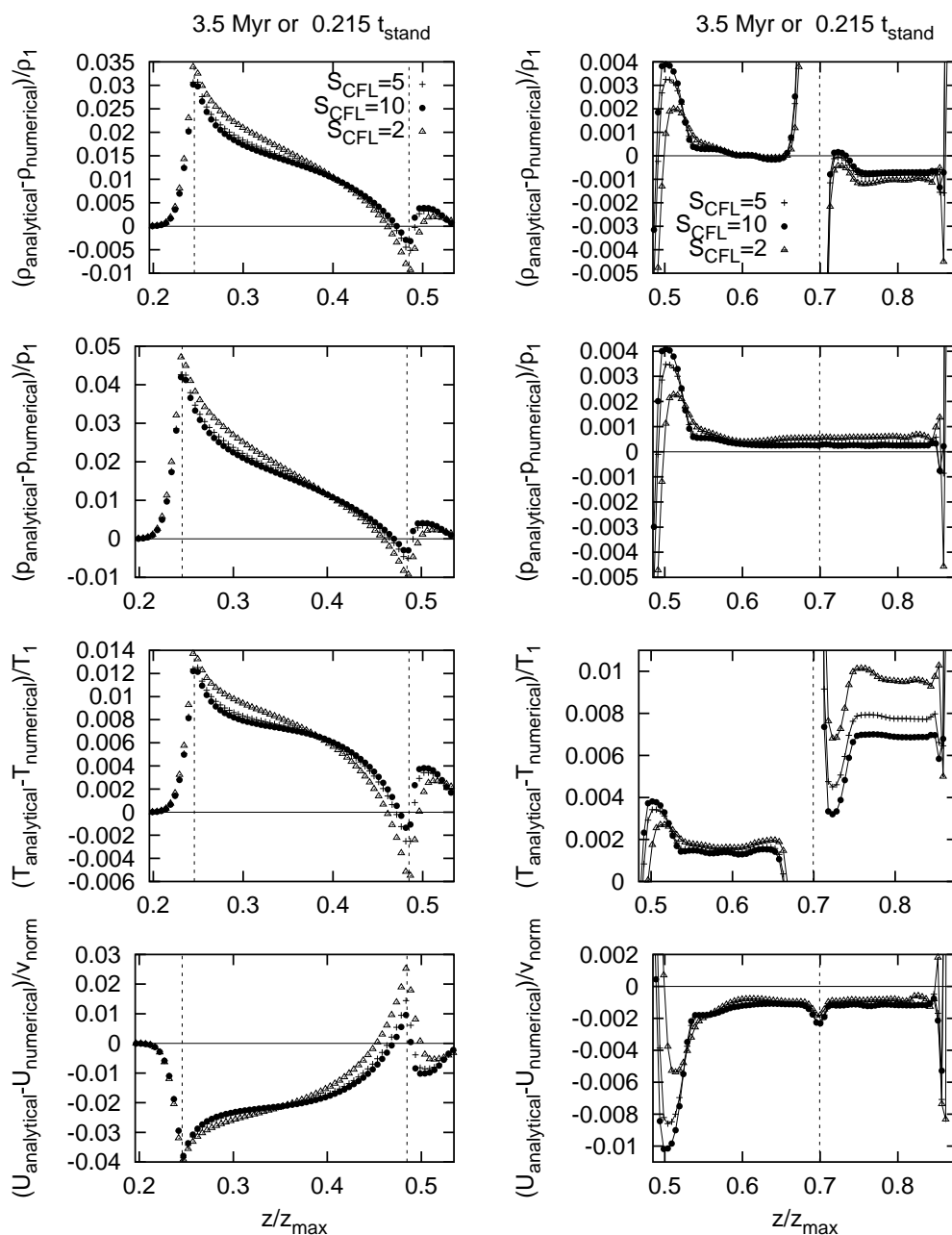


Figure C.5: Sod Shock tube – influence of Courant-Friedrich-Levy safety factor (see key in density plot). Normalised differences between analytical and numerical result for density, pressure, temperature and velocity. The **left column** shows the region of the rarefaction fan, the **right column** shows the connection and post shock region. The zone borders are marked with dashed vertical lines.

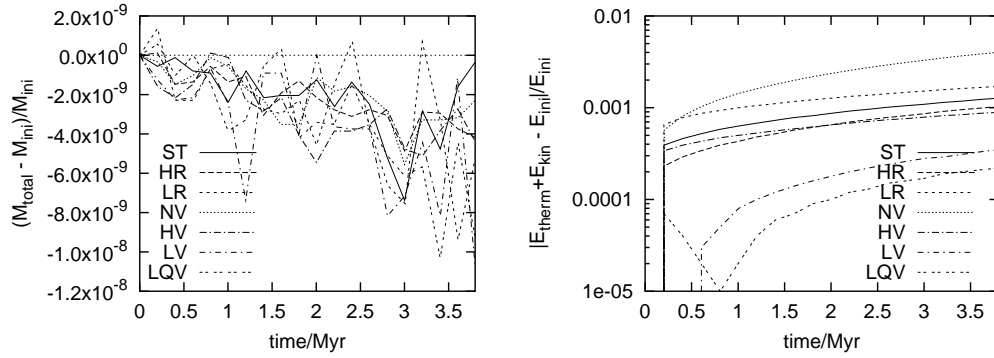


Figure C.6: Conservation of total mass and energy in the shock tube test. **Left:** relative change in total mass for different models. **Right:** relative change in total energy for different models.

The best conservation is achieved if the linear viscosity term is used, but, as seen before, these models cannot reproduce the discontinuities.

C.2 Sedov-Taylor blast wave

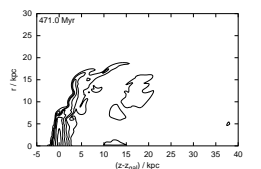
In cylindrical coordinates the shock tube test (Sect. C.1) can be used for the z -direction only. To check both r - and z -direction we perform the Sedov-Taylor blast wave test, which describes an intense explosion. A large amount of thermal energy E_0 is injected into a small volume in a homogeneous background gas of density ϱ_0 , temperature T_0 and pressure p_0 . This leads to a rapid expansion of a spherical shock front.

C.2.1 Analytical solution

The analytical solution was found independently by Sedov and Taylor in the 1950's (see e.g. Sedov 1959 and Landau & Lifschitz 1991). The main assumption made is that the explosion is intense, i.e. the external pressure is negligible compared to the pressure at shock front. The radius of the shock front R_{sh} and its velocity u_{sh} can be derived from dimensional considerations. The density, pressure and local velocity directly at the shock front (ϱ_{sh} , v_{sh} , p_{sh}) are calculated from the jump conditions. The result for these quantities is:

$$R_{\text{sh}} = \xi \left(\frac{E_0 t^2}{\varrho_0} \right)^{1/5}, \quad \xi = 1.033 \text{ for } \gamma = 1.4 \quad (\text{C.7})$$

$$u_{\text{sh}} = \frac{2}{5} \frac{R_{\text{sh}}}{t} \quad (\text{C.8})$$



Model	physical grid size (in kpc)	number of cells	C_1 , C_2	runtime
ST (standard)	1×0.5	300×150	0,2	60Myr
HR (high resolution)	.	450×225	.	.
LR (low resolution)	.	200×100	.	.
NV (no viscosity)	.	300×150	0,0	.
HV (high viscosity)	.	.	0,4	.
LV (linear viscosity)	.	.	1,0	.
LQV (linear+quadr.visc.)	.	.	1,2	.
LT (long time run)	2×1	300×150	0,2	300Myr

Table C.2: Sedov test: List of simulations. Physical grid size $z_{\max} \times r_{\max}$, number of cells $NZ \times NR$, artificial viscosity parameters C_1 and C_2 and runtime. The \cdot means the same value as in the previous line. Parameters common to all runs are external particle density $n_0 = 1 \text{ cm}^{-3}$, external temperature $T_0 = 100 \text{ K}$, injected energy $E_0 = 10^{51} \text{ erg}$, injection sphere radius $r_{E_0} = 0.05 \text{ kpc}$.

$$\rho_{\text{sh}} = \frac{\gamma + 1}{\gamma - 1} \rho_0 \quad (\text{C.9})$$

$$v_{\text{sh}} = \frac{2}{\gamma + 1} u_{\text{sh}} \quad (\text{C.10})$$

$$p_{\text{sh}} = \frac{2}{\gamma + 1} \rho_0 v_{\text{sh}}^2 \quad (\text{C.11})$$

Radial profiles for the density, pressure and radial velocity are self-similar and can be scaled to R_{sh} and $\rho_{\text{sh}}, v_{\text{sh}}, p_{\text{sh}}$. For $\gamma = 1.4$ a tabular result can be found in Sedov (1959).

C.2.2 Simulations

The initial energy is injected into a small sphere of radius r_{E_0} in the centre of the grid in order to minimise non-symmetry effects due to the cell geometry.

The list of the simulation runs and their parameters is given in Table C.2. In the different runs the influence of the resolution and the artificial viscosity is studied.

C.2.3 Comparison

Figs. C.7, C.8 and C.9 each show one snapshot of the density and velocity distribution for the LR, HR and NV run (see Table C.2). In Figs. C.10 and C.11 the numerical and the analytical profiles for the density ρ , pressure p and absolute velocity v are compared for the runs ST, HR, HV and LQV (see Table C.2). Fig. C.9 reveals that the code cannot reproduce the analytical result without the artificial viscosity, not even the location of the shock

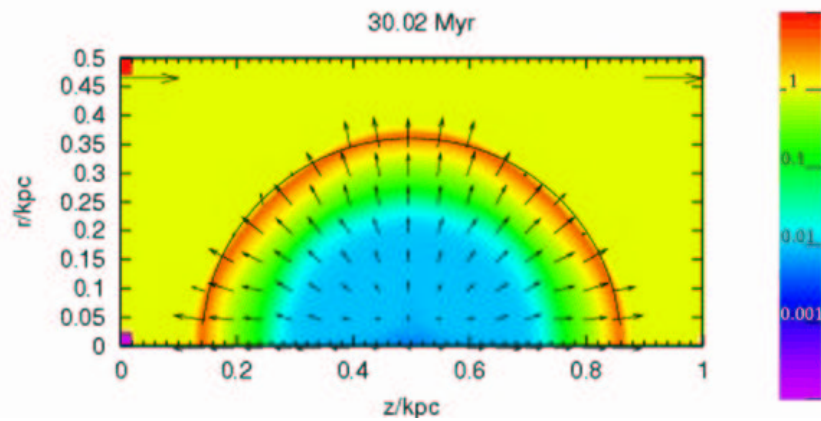


Figure C.7: Sedov test: Snapshot of the low resolution run (LR) showing the colour-coded density distribution (colour scale on the right) and the velocity field (arrows; the standard arrows in the upper corners indicate 10% of the sound speed in the external gas). The black semicircle indicates the analytical position of the shock front.

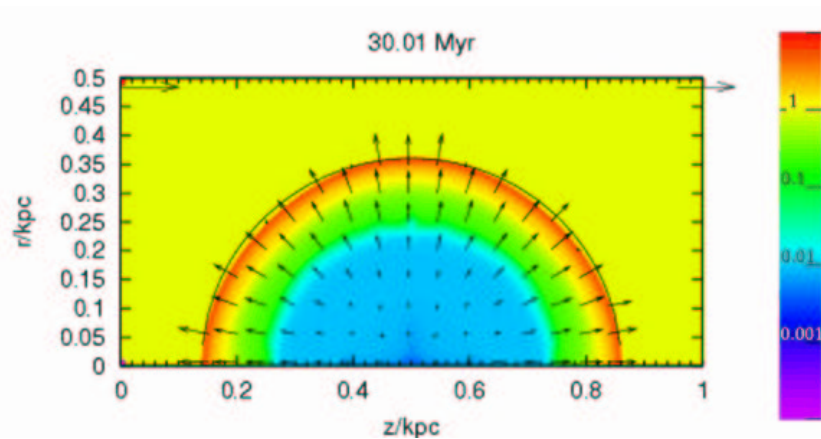


Figure C.8: Same as Fig. C.7, but for the high resolution run (HR).

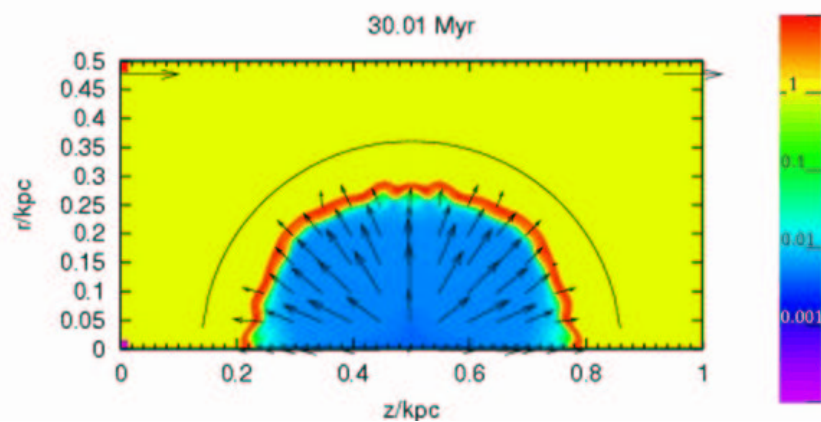
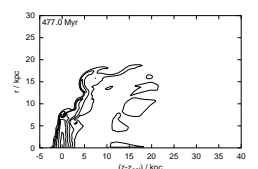


Figure C.9: Same as Fig. C.7, but for the run without viscosity (NV).



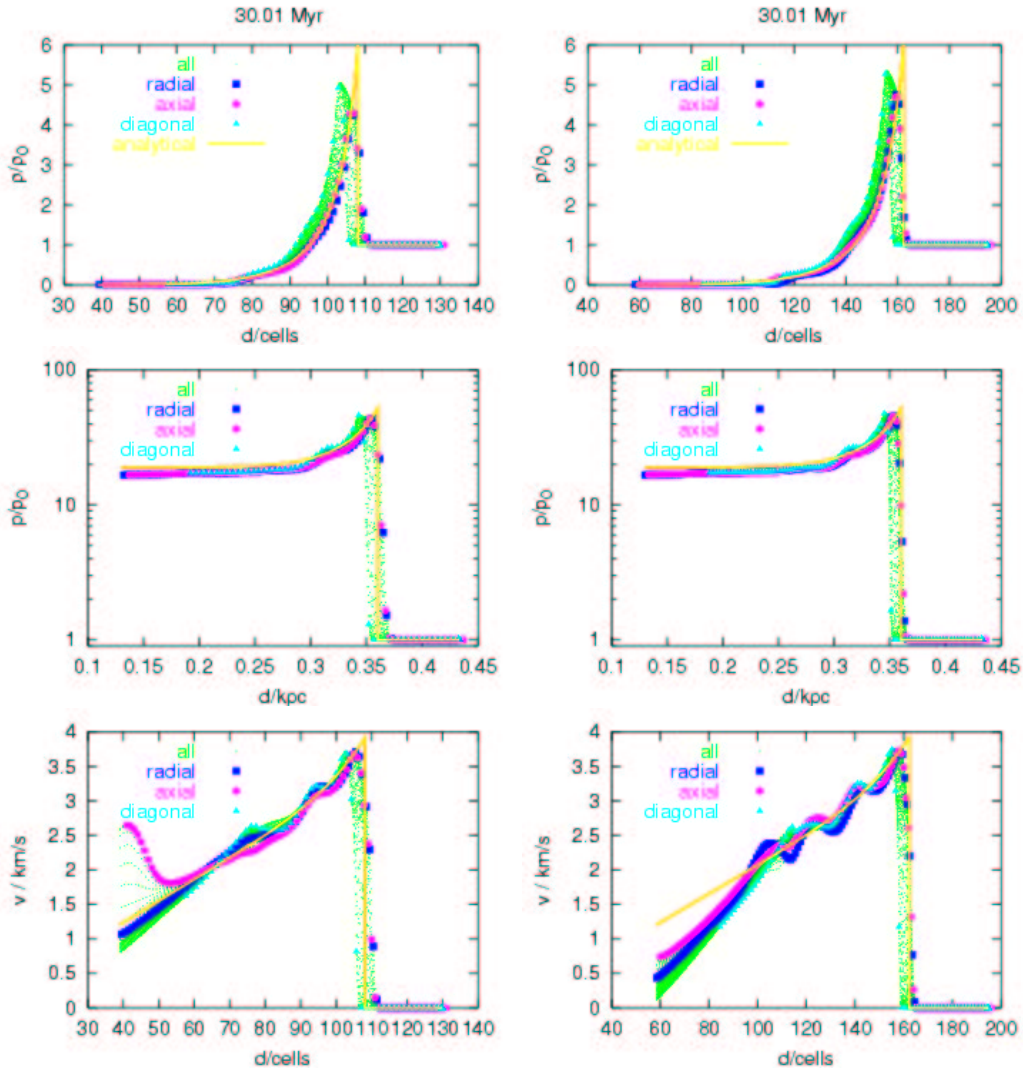


Figure C.10: Sedov test: Comparison of analytical and numerical profiles for density ρ , pressure p and absolute velocity v . For all cells these values are plotted against the radius d (distance from explosion centre), which is given in cells or in kpc as indicated. The cells in radial, axial and diagonal direction from the explosion centre are marked with special symbols, see key in the plots. The solid lines mark the analytical solutions. **Left column:** standard run (ST), **right column:** high resolution run (HR).

front. The same holds for the run with linear viscosity alone (LV). Using the quadratic viscosity term ($C_2 > 0$), the location of the shock front as well as profiles for ρ and p are reproduced sufficiently.

The snapshots in Figs. C.7 and C.8 reveal a slight anisotropy. The advection along the z - and r -direction works correctly, in these directions the position of the numerical and analytical shock front agree very well. However, in diagonal direction the simulated shock front lags slightly behind the

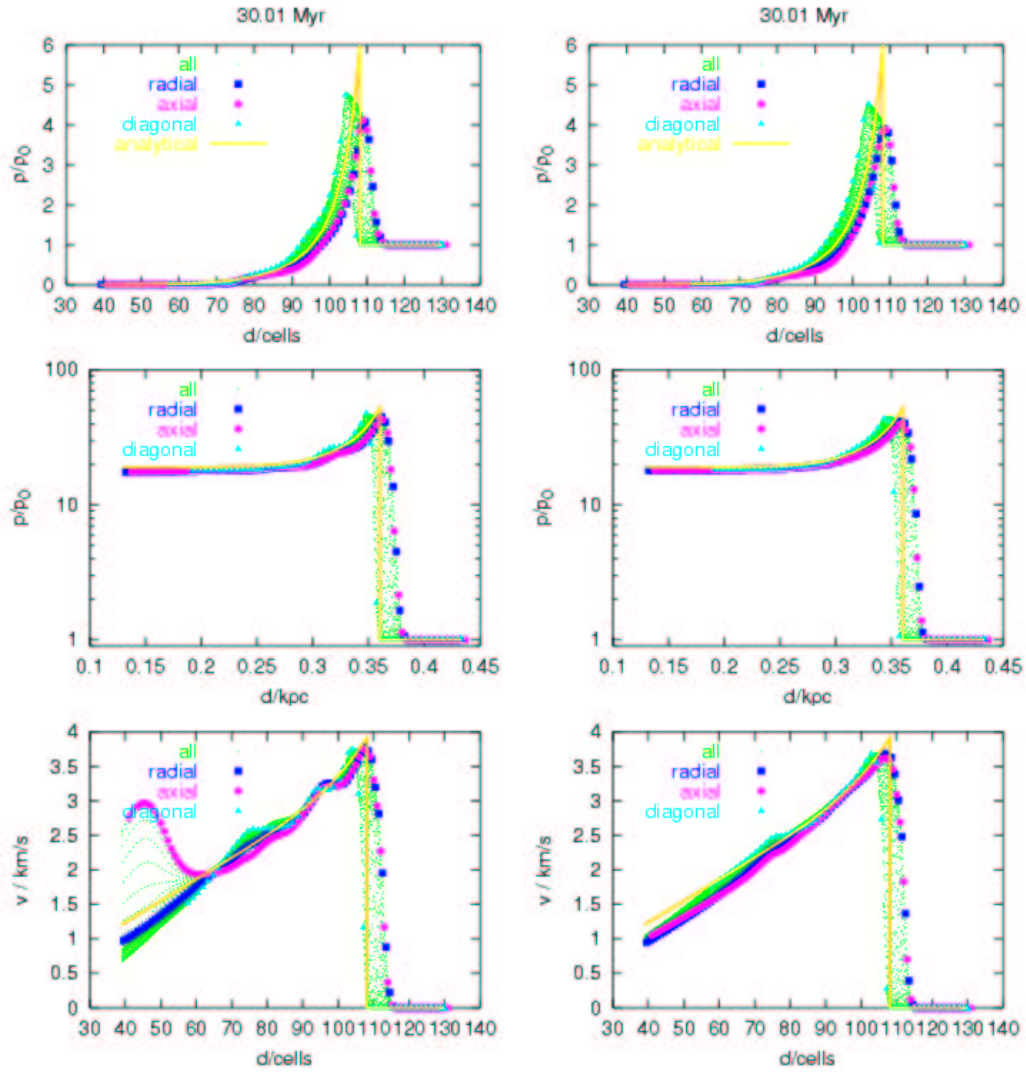
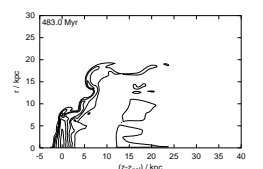


Figure C.11: Same as Fig. C.10. **Left column:** high viscosity run (HV), **right column:** linear and quadratic viscosity run (LQV).

analytical one. The comparison of the standard and the high resolution run shows that this is not a resolution problem but intrinsic to the code. The anisotropy is also evident in the profiles (Figs. C.10 and C.11).

In the runs with quadratic viscosity but without the linear term, the velocity profiles show strong oscillations. Small oscillations can also be seen in the density and pressure profiles. The Sedov test is a case with strong shocks and stagnant regions. The linear viscosity was designed to damp oscillations in such cases. Indeed it improves the profiles significantly (Fig. C.11).

We also compare the analytical and numerical time evolution of the shock front radius $R_{\text{sh}}(t)$. To account for the anisotropy in the code as well as for the spreading of the shock front by the viscosity we use four different versions to determine $R_{\text{sh}}(t)$ in the simulations. R_{sh} is set by either:



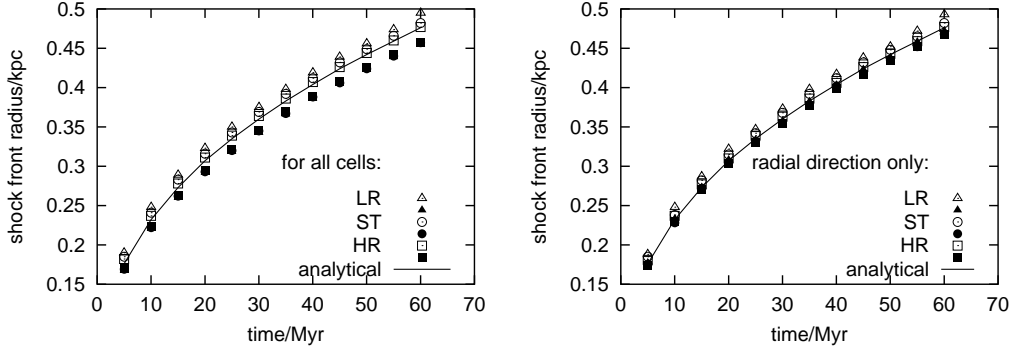


Figure C.12: Influence of the resolution on the shock front radius evolution: The analytical result (solid line) for the shock front radius depending on time (Eq. C.7) is compared with numerical estimates (see text). The **left plot** shows the numerical estimates following methods a) (solid symbols) and b) (open symbols), the **right plot** shows the numerical estimates following methods c) (solid symbols) and d) (open symbols).

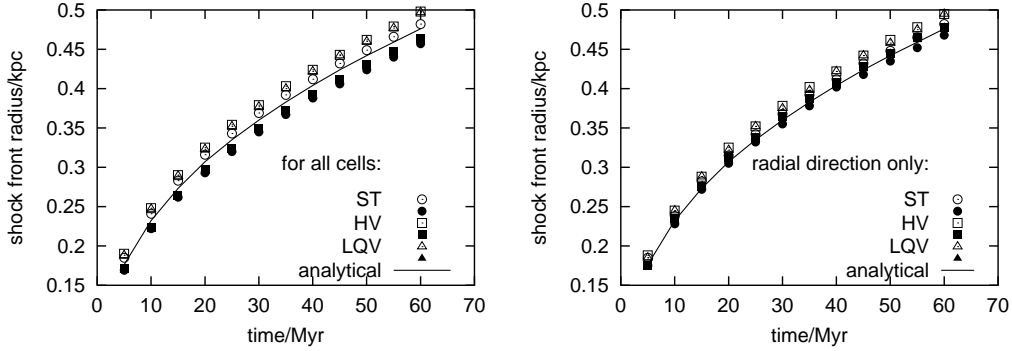


Figure C.13: Influence of the artificial viscosity on the shock front radius evolution. For further explanation see Fig. C.12.

- a) the cell with maximum density of all cells,
- b) the outmost (that is with largest d) cell with $\varrho > 1.1\varrho_0$, of all cells.
- c) the cell with maximum density of profile in radial direction ($z = z_0 = \text{const.}$),
- d) the outmost cell with $\varrho > 1.1\varrho_0$, of profile in radial direction ($z = z_0 = \text{const.}$).

Methods c) and d) are the same as methods a) and b), but restricted to the cells in the radial direction. The comparison of the analytical and the numerical $R_{\text{sh}}(t)$ is shown in Figs. C.12 and C.13, which demonstrate the effect of resolution and viscosity, respectively. The simulations can reproduce the time evolution of R_{sh} . Fig. C.14 completes this test, displaying also the results from the long-time run (LT). In the end of this time range the shock

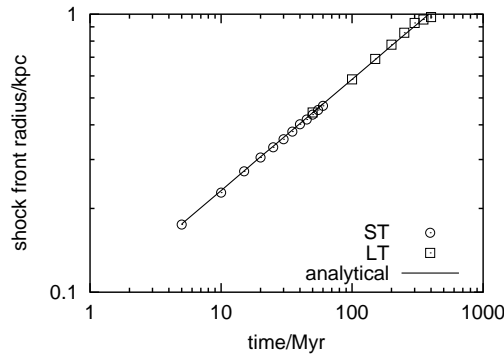


Figure C.14: Shock front radius – long time run (LT) and standard run (ST). Estimates from the simulations with method c) (see text).

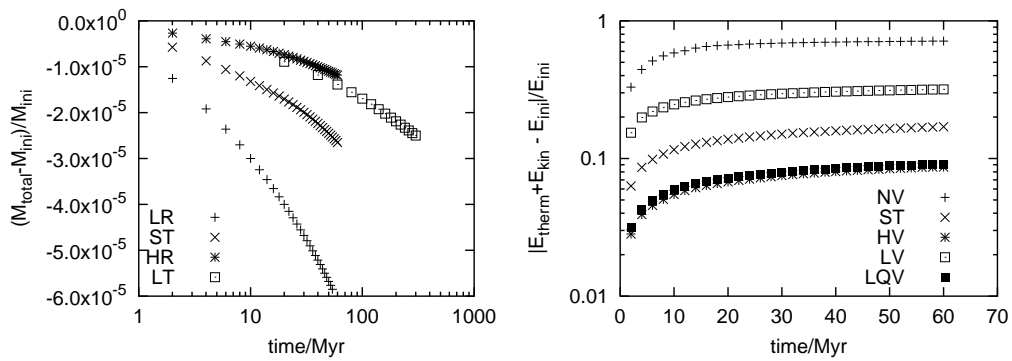


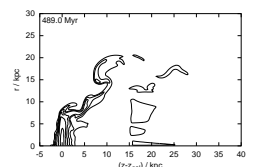
Figure C.15: Conservation of total mass and energy in the Sedov test for different models. **Left:** relative change in total mass. **Right:** relative change in total energy.

front pressure has dropped to about $3p_0$, which is comparable to the external pressure. Here the analytical solution comes to its limit.

As a conclusion, with the correct choice for the viscosity parameters (model LQV) the code can reproduce the analytical result well. It has passed this challenging test successfully.

C.2.4 Conservation of total mass and energy

Also for this test we checked the conservation of total mass and energy. The result is demonstrated in Fig. C.15. The mass conservation works well. It is independent of viscosity, but a better resolution improves the conservation. The ST and the LT run show a similar behaviour because of a comparable relative size of the structure in the grid. The energy conservation does not perform well in this test case. This is a known problem in artificial viscosity codes with strong shocks. According to Fig. C.15, the main problem lies in the first phase of the simulation. However, in the RPS simulations such strong shocks do not occur, so we do not regard this as a problem for our application.



C.2.5 Courant-Friedrich-Levy safety factor

For all tests a Courant-Friedrich-Levy safety factor $S_{\text{CFL}} = 5$ (see Sect. 2.4) was used. The ST run was repeated twice with $S_{\text{CFL}} = 2, 10$. The numerical result was the same for all three cases.

C.3 Flow past a sphere

The test case of a flow past a solid sphere is related closely to the actual application of the code in this work. In contrast to the shock-tube and the Sedov test, here the fluid has to enter and leave the grid. This is a good opportunity to study the behaviour of the boundaries.

C.3.1 Analytical solution

A detailed derivation of the analytical solution can be found e.g. in Landau & Lifschitz (1991). Assuming a stationary flow in an incompressible (i.e. $\varrho = \text{const.}$) ideal (no viscosity, no friction) fluid, the hydrodynamical equations for this problem simplify drastically. The main point is that in an ideal fluid the circulation of the velocity field is conserved along streamlines. At infinite distance to the sphere the flow is homogeneous and therefore irrotational. Consequently, the velocity field is curl free everywhere, which means that it can be written as the gradient of a scalar potential Ψ :

$$\vec{v} = \nabla\Psi \quad (\text{C.12})$$

This is the origin of the name “potential flow”.

If in addition the fluid is incompressible ($\varrho = \text{const.}$), the continuity equation (Eq. 2.2) simplifies to

$$\Delta\Psi = 0 \quad (\text{C.13})$$

plus the boundary conditions. At infinite distance to the body they are density $\varrho = \varrho_0$, pressure $p = p_0$ and velocity $\vec{v} = \vec{v}_0$. Here \vec{v}_0 is parallel to the z -axis. Additionally, the boundary condition at the surface of the sphere is that the gas cannot cross the surface, i.e. at the surface the velocity normal to the surface has to be zero. The resulting potential and velocity field at position \vec{x} are

$$\begin{aligned} \Psi(\vec{x}) &= \frac{R^3}{2d^2} \vec{v}_0 \cdot \vec{n} \\ \vec{v}(\vec{x}) &= \vec{v}_0 + \frac{R^3}{2d^2} [\vec{v}_0 - 3\vec{n}(\vec{v}_0 \cdot \vec{n})], \end{aligned} \quad (\text{C.14})$$

where R is the radius of the sphere and \vec{n} is the normalised vector from the centre of the sphere to the position \vec{x} . Again d is the distance of \vec{x} to the

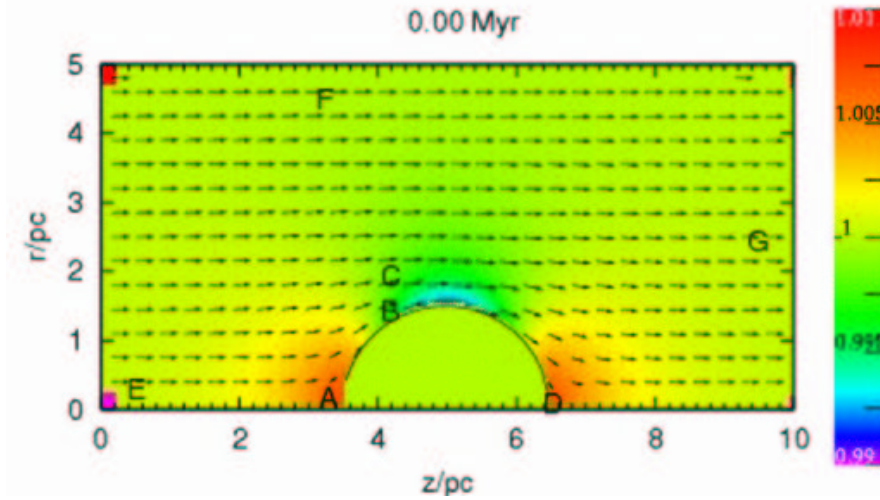


Figure C.16: Analytical solution for the flow past a sphere with Mach number 0.1: velocity field (arrows) and colour-coded pressure distribution. The lhs corners are used to calibrate the colour scale. The colour scale on the right shows the pressure in units of p_0 (pressure at the inflow boundary). The two extra arrows in the top corners indicate the inflow velocity v_0 . The letters A-G mark positions in which some quantities are monitored in the simulations.

centre of the sphere. This result is already transformed from the fluid rest frame to the sphere rest frame. In the stationary case, for an incompressible ideal fluid also the Eulerian equations (Eqs. 2.3 and 2.4) simplify to the general Bernoulli equation

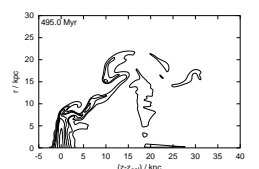
$$p + \frac{1}{2}\rho v^2 = \text{const.}, \quad (\text{C.15})$$

which here is not only constant along a stream line but everywhere. The resulting velocity and pressure distributions are shown in Fig. C.16 for a flow with Mach number 0.1. Please note that the pressure variations are very small.

C.3.2 Applicability of the analytical solution

In reality, potential flows are very rare. The analytical solution is a good approximation if a fluid can be treated as incompressible, i.e. (see Landau & Lifschitz 1991)

$$\begin{aligned} v &< c && \text{and} \\ \tau &< \frac{l}{c}, \end{aligned} \quad (\text{C.16})$$



where c is the sound speed and l, τ are the characteristic length scales and time scales on which the velocity field changes. The second crucial point is that viscosity must be negligible. If it is not, vortices are expected to develop on the downstream side of the sphere. Also in the code the fluid is neither incompressible nor inviscid. Therefore we also expect vortices on the downstream side of the sphere in the simulations. Due to the enforced cylindrical symmetry these vortices cannot take the characteristic form of the von Karman vortex wake known from the real world.

C.3.3 Simulations

This test has two goals: to check the performance of the code and to calibrate and optimise numerical parameters concerning the inflow and outflow.

Preliminary considerations

The simulations shall check to what extent a potential flow is established by the code, therefore it is not reasonable to start with such a potential flow. Moreover, the RPS simulations shall start with the gas at rest. We choose the same initial condition here. All gas is set at rest, then the flow is switched on over a time interval t_{switch} . We test the influence of this parameter.

No matter how slowly the inflow velocity is increased, a shock front crosses the grid in z -direction. In the pre-shock region the fluid of density ϱ_0 is at rest, in the post-shock region the density and velocity will be enhanced. For a very short switching time, especially for $t_{\text{switch}} = 0$, this front is steep, but the longer t_{switch} , the flatter it will be. If nothing else happens, the moment the velocity has reached its final value at some position, also the density will have reached a certain enhanced value, no matter if this took a long or a short time.

Stone & Norman (1992) mentioned that the outflow (and inflow) boundaries are difficult to handle because they are never perfectly transparent to wave energy. This means the shock front resulting from the flow initialisation is reflected repeatedly at both boundaries. If t_{switch} is longer than the time the shock front needs to cross the grid ($t_{\text{gridcross}}$), both the ongoing initialisation process and the reflected wave superimpose. We therefore expect that oscillations caused by the wave reflections at the boundaries are superimposed to the true result.

Considering the boundaries we test different possibilities. The options are explained in Sect. 2.5.

We also vary the viscosity and the spatial resolution.

List of simulations

The strategy of this series of simulations is first to investigate the influence of t_{switch} and find an optimal value. Next, different boundary conditions will be

initial density ρ_0	1 cm^{-3}
initial temperature T_0	100K
sound speed c	0.72 pc/ Myr
grid crossing time $t_{\text{gridcross}}$	14Myr (except model O-far/S)
sphere radius R	1.5 pc
z -position of sphere centre z_0	$z_{\text{max}}/2$

Table C.3: Parameters for all simulation runs for the potential flow test

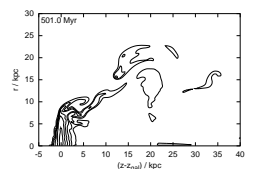
Model	v_0/c	$t_{\text{switch}}/\text{Myr}$	physical grid size (in pc)	number of cells	$\Delta x/\text{pc}$	boundary at z_{max}	boundary at r_{max}	C_1, C_2
SW0	0.1	0	10×5	200×100	1/20	open	open	0,2
SW1.5	·	21	·	·	·	·	·	·
SW2	·	28	·	·	·	·	·	·
SW4	·	56	·	·	·	·	·	·
SW3.85	·	54	·	·	·	·	·	·
SW4.14	·	58	·	·	·	·	·	·
O/S	·	56	·	·	·	open	solid	·
F/O	·	·	·	·	·	outflow	open	·
F/S	·	·	·	·	·	outflow	solid	·
O/O-far	·	·	10×10	200×200	·	open	open	·
O-far/S	·	112	20×5	400×100	·	open	solid	·
HR	·	56	10×5	400×200	1/40	·	·	·
NV	·	·	·	200×100	1/20	·	·	0,0
LV	·	·	·	·	·	·	·	1,0
LQV	·	·	·	·	·	·	·	1,2
HV	·	·	·	·	·	·	·	0,4
FAST	0.2	·	·	·	·	·	·	0,2

Table C.4: Parameters for the simulation runs for the potential flow test: inflow velocity v_0 , initialisation time t_{switch} for the inflow, physical grid size $z_{\text{max}} \times r_{\text{max}}$, number of cells, resolution Δx , choice for boundary conditions at z_{max} and r_{max} , artificial viscosity parameters C_1 and C_2 . The · means the same value as in the previous line.

studied, and after that the distance of the boundaries to the sphere is varied. Then the influence of the resolution and the artificial viscosity is examined. Finally a run with a higher velocity is performed. Table C.3 summarises the parameters that are the same for all simulation runs. Table C.4 gives an overview over the varied parameters.

Presentation of the numerical result

To visualise the results from the simulations we show snapshots (Figs. C.17 to C.19) and monitor the evolution of pressure, density and the velocity com-



ponents at certain positions (A-G) in the grid (Figs. C.20 to C.22). The positions are marked by the appropriate letters in the snapshots and in Fig. C.16. Some of these points were chosen to observe the behaviour near the sphere (the two stagnation points A and D; B and C at the side of the sphere), the others were put near the boundaries. We normalise pressures and densities to the local analytical values p_{an} and ρ_{an} . For the velocity components we show the deviations from the analytical value normalised to the inflow velocity v_0 (i.e. $(U_{\text{num}} - U_{\text{an}})/v_0$ and $(V_{\text{num}} - V_{\text{an}})/v_0$), because the analytic values are zero in some points.

C.3.4 Comparison between analytical and numerical result

Qualitative comparison

Figs. C.17 to C.19 show snapshots of the simulations for the SW0, O-far/S and the F/S runs. For the case with $t_{\text{switch}} = 0$ (SW0) the pressure distribution is dominated by the steep compression front and successive reflections at the sphere and at the boundaries. Nonetheless the velocity field appears approximately correct (see Fig. C.16).

In the cases with longer t_{switch} the pressure distribution in the initial phase is dominated by the initial shock front and the subsequent oscillations. However, the oscillations decay and the true pressure distribution emerges. The velocity distribution is similar to the analytical solution. Soon after the initialisation phase a vortex develops at the downstream side of the sphere. Small vortices separate from the surface of the sphere and feed the big one. The vortex is evident in Figs. C.18 and C.19, which display the snapshots of this stable phase of the two best simulations. The upstream side is similar to the analytical solution. The main difference between Figs. C.18 and C.19 is that in the first one the overall pressure is slightly too high. This is due to the fact that for the chosen boundary conditions in that model (boundary at r_{max} is simply open) the *inflow* into the grid starts earlier than the *outflow*. That's why there is always a bit more matter in the grid than was originally set, and hence the overall density and pressure come out slightly higher than expected from the analytical solution. This is not the case in model F/S (Fig. C.18), because at r_{max} an active outflow balancing the inflow was set.

Calibrating the wind initialisation

The evolution of the pressure at points A-G is shown in Fig. C.20 for runs with different t_{switch} .

In all cases the initial variations due to the initialisation shock front are larger than the spatial variations seen in the analytical solution. Then due to the subsequent reflections of this shock the pressure oscillates around the analytic value. These oscillations decay. The best result was achieved

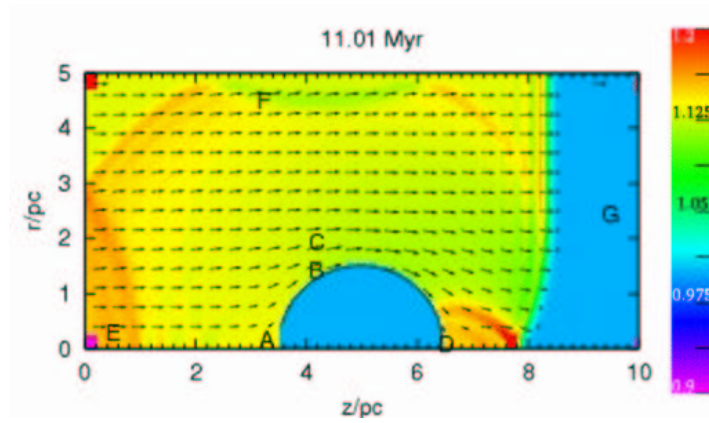


Figure C.17: Test – potential flow past a sphere: Snapshot of model SW0 (time see top of figure), showing the pressure and velocity field. For a further explanations see Fig. C.16.

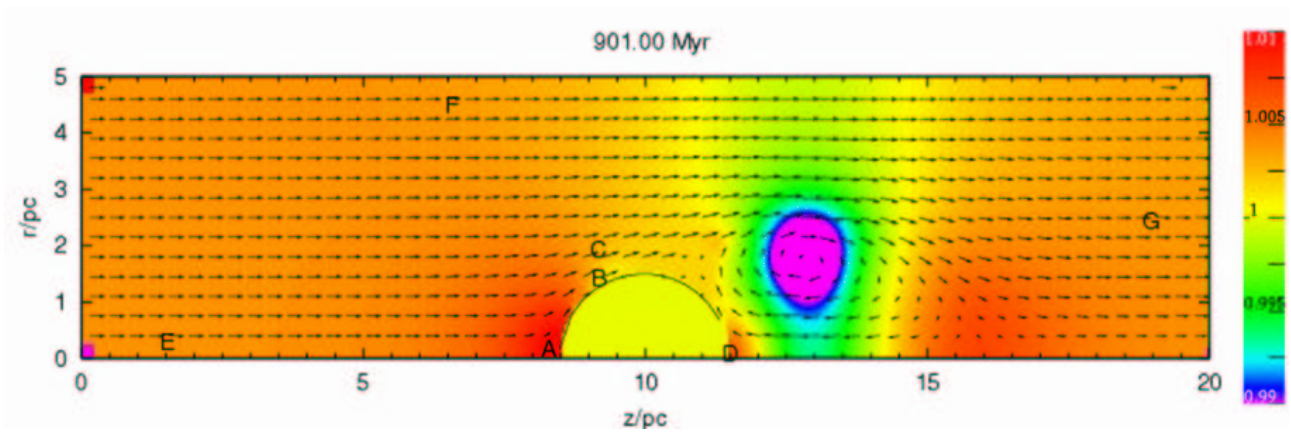


Figure C.18: Same as Fig. C.17, but for model O-far/S.

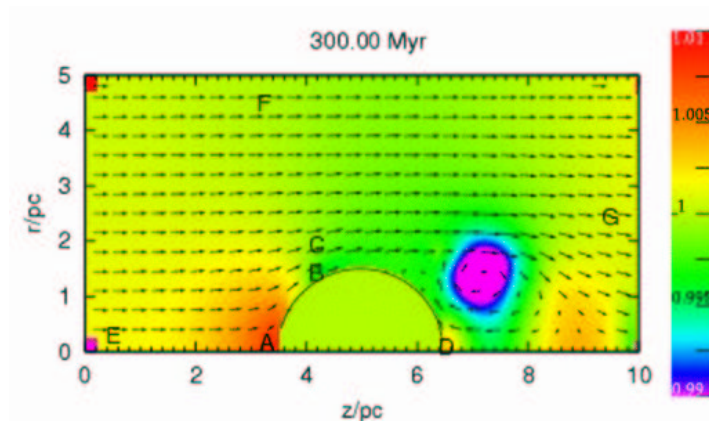
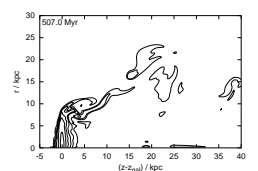


Figure C.19: Same as Fig. C.17, but for model F/S.



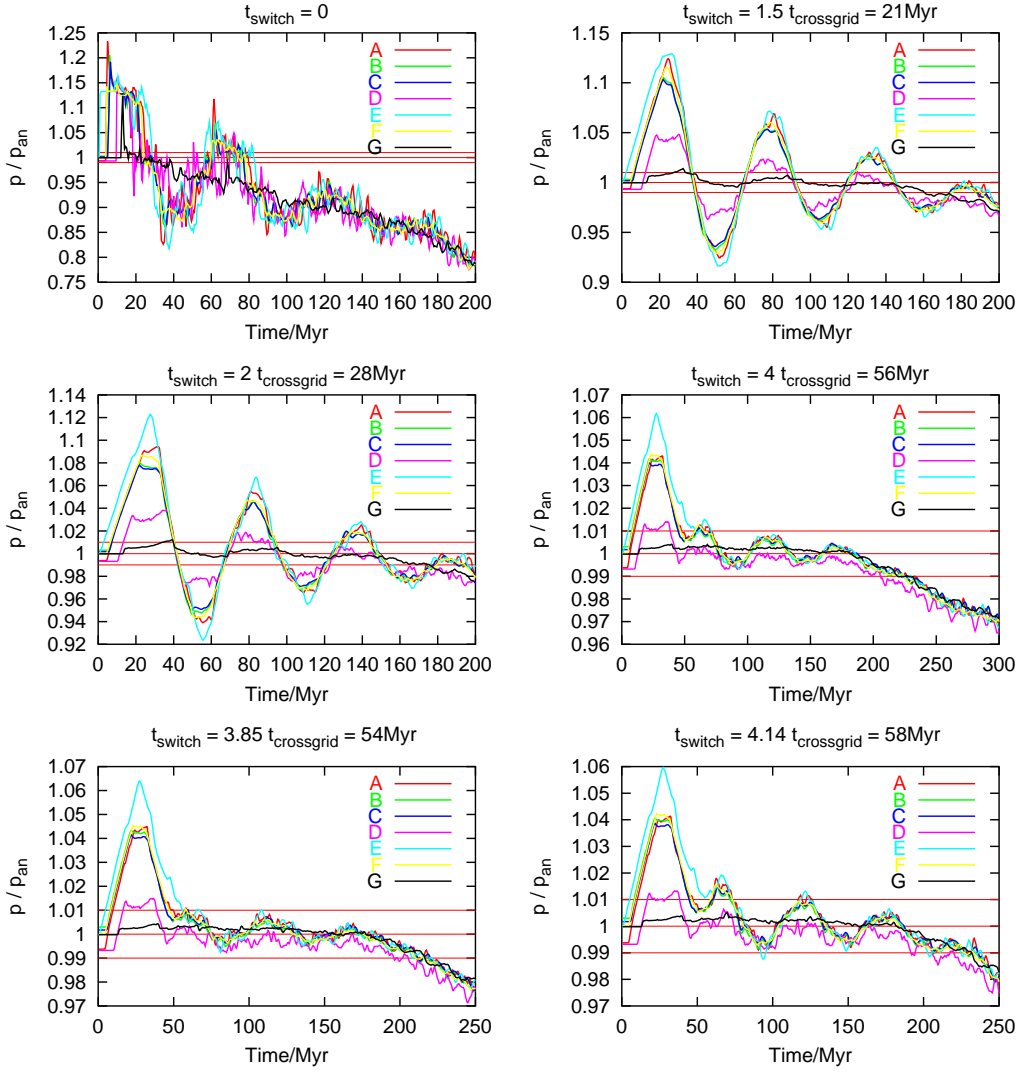


Figure C.20: Influence of initialisation time t_{switch} : pressure evolution for models SW0, SW1.5, SW2, SW4, SW3.85 and SW4.14. t_{switch} is given in the title of the single plots. The pressure is monitored at the positions A-F indicated in Fig. C.16, it is normalised to the local analytical value. The horizontal lines mark the correct analytical solution and $\pm 1\%$. Note the different scales on both axes.

for $t_{switch} = 4t_{gridcross}$. Towards the end, in all cases the pressure starts to decrease suddenly in the whole grid. The density evolution shows a similar behaviour, indicating that material is lost from the computational grid.

Boundaries

We continue the parameter study with $t_{switch} = 4t_{gridcross}$ but varying the boundary conditions. As before the pressure monitoring for different cases is summarised in Fig. C.21. We learn the following:

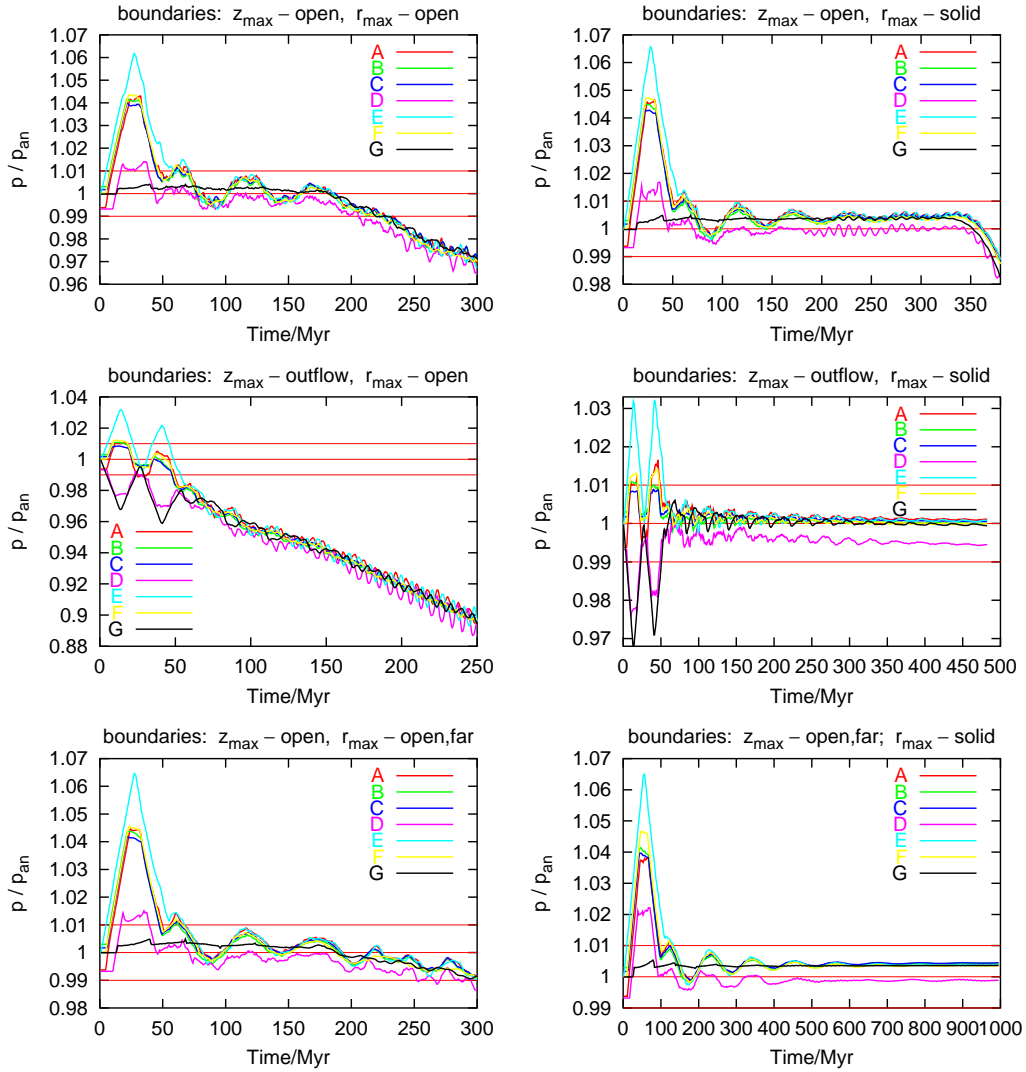
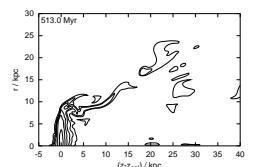


Figure C.21: Influence of the boundaries: pressure evolution for models SW4, O/S, F/O, F/S, O/O-far, O-far/S, the choice of boundaries is given in the title of the single plots. For further explanation see Fig. C.20.

- The problem that gas is lost out of the grid is due to the r_{\max} boundary as described in Sect. 2.5.4. Choosing a solid r_{\max} boundary instead of an open one solves this problem.
- The outflow boundary needs to be far away from the sphere, otherwise the vortex starts to interact with the outflow boundary, which leads to an enhanced outflow as well.
- The simple open condition for the z_{\max} -boundary effects that the inflow starts earlier than the outflow, which results in a slightly enhanced density and pressure level all over the grid. If for the outflow boundary an active outflow is set instead of a simple (passive) open one, the



correct level of p and ρ can be reproduced. Moreover, the active outflow initiates a rarefaction wave moving backwards through the grid in addition to the compression wave starting at the inflow boundary. The superposition of both reduces the characteristic period of the artificial oscillations by a factor of two. Keeping t_{switch} as before, also the amplitude of the oscillations is reduced further.

Detailed comparison of the analytical and numerical result

The monitoring of the density, pressure and velocity components of the two best cases (O-far/S and F/S) is summarised in Fig. C.22. In all quantities the decaying oscillations described above appear. Their period is determined by the grid length and the boundary conditions as was explained before. The values oscillate around the physical value and converge to it. So the *physical* result can be extracted by ignoring the oscillations and considering their central values.

Except in the initialisation phase the numerical value of the pressure agrees with the analytical one in all monitored points except in the downstream stagnation point (D). Neither in reality nor in the simulation the velocity there is zero, so the pressure needs to be a bit smaller than in the analytical solution. Of course this point is also perturbed by the vortex.

The fluid in the simulation is not incompressible, hence a perfect agreement of the density with the analytical result cannot be expected. For a compressible fluid the density should be enhanced in the two stagnation points. In the simulation this is clearly the case for the upstream side stagnation point (A). The density at the downstream side stagnation point (D) is also higher than in the other monitored positions, but –consistent with the pressure behaviour– not as high as at A. The density should be lowest at the side of the sphere (point B, followed by point C), because the pressure is smallest there. This is also the case in the simulation, although the effect is very weak.

Due to the vortex the velocity cannot be correct at the downstream side of the sphere. Especially the downstream side stagnation point (D) is affected by the vortex. In both the O-far/S and the F/S models the deviation of the numerical result for the velocity components from the analytical solution is very similar, indicating that this is the physical solution (as far as the 2D-symmetry could be forced physically).

The deviation of the velocity at point B, that is at the side of the sphere, very close to the surface, is due to a boundary layer at the surface of the sphere. This also explains why the density at B is not as low as expected. Such a boundary layer also develops in real fluids. In addition, both points B and C are influenced by the vortex, it is like a further obstacle for the flow. The difference of the numerical velocity to the analytical solution is only about 10% of v_0 . Because in the F/S model the z_{max} -boundary is quite close to the vortex, also point G is influenced by it. Especially the radial

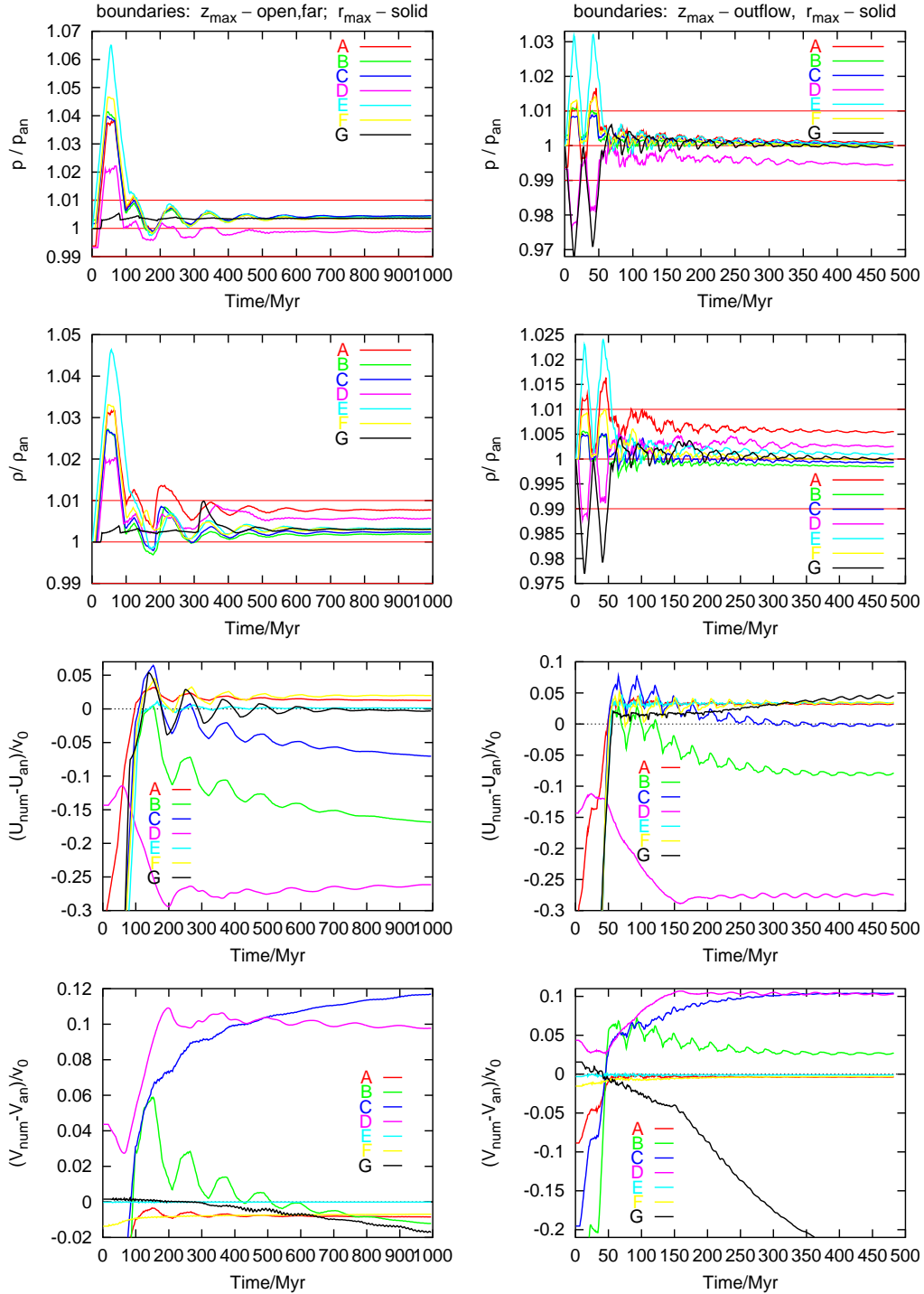
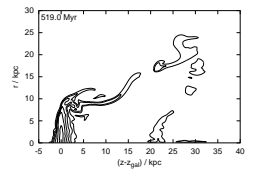


Figure C.22: Detailed result for potential flow for models O-far/S (**left** column) and F/S (**right** column). Time evolution of pressure, density, z - and r -component of velocity at the positions A-F, compared to the local analytical values.



velocity component at G deviates from the analytical value. In the O-far/S model, the z_{\max} -boundary is far away from the sphere. Although the vortex grows, there is enough space on its downstream side for the flow to become regular again. In the O/S model, which is identical to the O-far/S model despite the distance of the z -boundaries to the sphere, at about 350Myr the vortex comes too close to the z_{\max} -boundary and leads to a sudden mass loss out of the computational grid. Before that the results of models O/S and O-far/S are very similar. In model F/S the z_{\max} -boundary is also closer to the sphere, but the fixed outflow velocity stabilises the flow and prevents a growth of the vortex and the “catastrophe”.

The small deviation of about $0.03v_0$ of the velocity at the points A (upstream side stagnation point) and F (near r_{\max} -boundary) is due to the distance of the boundaries to the sphere. For a larger distance of the boundaries to the sphere these deviations nearly vanish. E.g. point E (near the inflow boundary) shows a similar deviation in model O/S, but is nearly perfect in model O-far/S.

Resolution

The difference between the numerical and analytical result is dominated by the deviation from the assumptions for the analytical solution. An improvement of a factor of 2 in the spatial resolution (model HR) does not give any improvement. The numerical result looks the same as for model O/S.

Viscosity

Switching off the viscosity completely (model NV) or using the linear viscosity term (models LV and LQV) gives wrong results. In the first case the jump conditions cannot be reproduced correctly, in the latter the linear viscosity terms damps true features. It was designed for situations with strong shocks to damp oscillations in stagnant regions. As this is not the case here it leads to wrong results.

Using a larger quadratic viscosity parameter (model HV) causes a stronger boundary layer at the surface of the sphere. This makes the velocity at point B slower compared to model O/S and compared to the analytical solution. All other regions are nearly unaffected. Such a behaviour would also be expected for a real fluid with a higher viscosity.

Higher v_0

The higher the inflow velocity, the more the assumption of an incompressible fluid is violated. In the FAST model the result is in principle the same as in the O/S one, but the vortex becomes dominant much earlier and when it comes too close to the boundaries it leads to a mass loss out of the computational grid.

Conclusion

With calibrated boundaries and t_{switch} also this test was passed successfully. The numerical results meet the expectations.

C.4 Potential test

The correctness of the computation of the gravitational potential is tested for the example of a homogeneous sphere. Even more important than to check the potential itself is to check the gravitational force, because it is the relevant quantity. It is derived by differentiating the potential. Therefore the potential has to be very accurate.

C.4.1 Analytical solution

For a homogeneous sphere of mass M and radius R the potential Φ and the gravitational force F are spherically symmetric, they depend only on the distance d of the point (z, r) to the centre of the sphere $(z_0, 0)$. With

$$d = \sqrt{z^2 + r^2}$$

and the gravitational constant G the well known solution is:

$$\Phi(d) = -GM \begin{cases} \frac{1}{d} & \text{if } d > R \\ \frac{1}{2} \left(\frac{3}{R} - \frac{d^2}{R^3} \right) & \text{if } d \leq R \end{cases} \quad (\text{C.17})$$

$$F(d) = -GM \begin{cases} \frac{1}{d^2} & \text{if } d > R \\ \frac{d}{R^3} & \text{if } d \leq R \end{cases} \quad (\text{C.18})$$

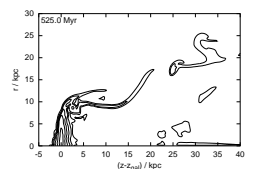
The minimum in the potential is $\Phi_{\min}(d = 0) = -\frac{3}{2}GM\frac{1}{R}$, the extremal force is $F_{\max} = |F(d = R)| = GM\frac{1}{R^2}$. The components F_z and F_r of the gravitational force are (multiplying F with sinus and cosinus)

$$F_z = F \frac{z - z_0}{d} \quad (\text{C.19})$$

$$F_r = F \frac{r}{d}. \quad (\text{C.20})$$

C.4.2 Simulation

A numerical result is obtained for different setups (see Table C.5). The resolution, the physical size of the grid compared to the sphere and the position



Model	physical grid size (in kpc)	number of cells	sphere centre z_0
ST (standard)	2×1	300×150	1 kpc
HR (high resolution)	.	450×225	.
LR (low resolution)	.	200×100	.
OffC+ (off centre positive direction)	.	300×150	1.68 kpc
OffC- (off centre negative direction)	.	.	0.30 kpc
SmGr (small grid)	0.88×0.44	200×100	0.44 kpc

Table C.5: Parameters for the potential tests: physical grid size $z_{\max} \times r_{\max}$, number of cells $NZ \times NR$ and position of the sphere centre z_0 . The \cdot means the same value as in the previous line. The radius of the sphere is 0.3 kpc in all cases.

of the sphere in the grid are varied. Due to the assumed 2D symmetry the sphere can only be shifted along the z -axis. The sphere was set in a homogeneous background medium of density $\varrho_{\text{ICM}} = 1 \text{ cm}^{-3}$, the density inside the sphere was set to $(\varrho_{\text{ICM}} + 1000\varrho_{\text{ICM}})$, so that effectively a sphere with density $1000\varrho_{\text{ICM}}$ was set on top of the background density.

C.4.3 Comparison

The lhs plot in Fig. C.23 shows the numerical and analytical result for the gravitational potential for the low resolution run (LR). They agree very well. The rhs plot of Fig. C.23 gives a quantitative impression of the difference between the analytical and the numerical result for different resolutions. The largest relative errors arise at the surface of the sphere, but even for the low resolution they reach only a few permille. Outside the sphere and at its surface the amplitude of the errors decreases with improving resolution. Inside the sphere the amplitude of the errors does not only depend on the resolution, but also on the exact way how the sphere is approximated by the cells. The errors inside the sphere are of the same order as at the surface or as outside or can even be two orders of magnitude smaller than at the surface. But, as a general trend, also inside the sphere the errors decrease with improving resolution.

The corresponding relative errors in the gravitational force are shown in Fig. C.24 for the low resolution case (LR). Like other vector quantities the gravitational force is not defined in the centre of a cell, but the components are defined on the cell walls. That's why the z - and the r -component are

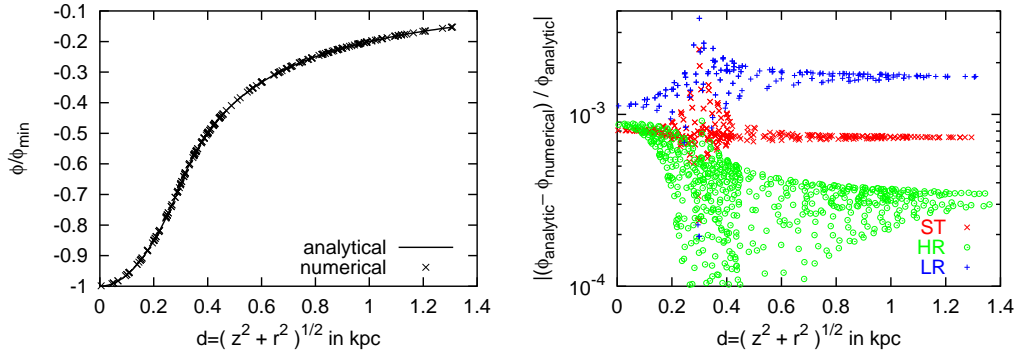


Figure C.23: **Left:** Comparison of analytical (line) and numerical (crosses, for a subset of all cells) normalised potential of a homogeneous sphere, for the low resolution case (LR). **Right:** Relative error of the potential for different resolutions, see key in the plot and Table C.5. Only a subset of the cells was used to maintain clarity.

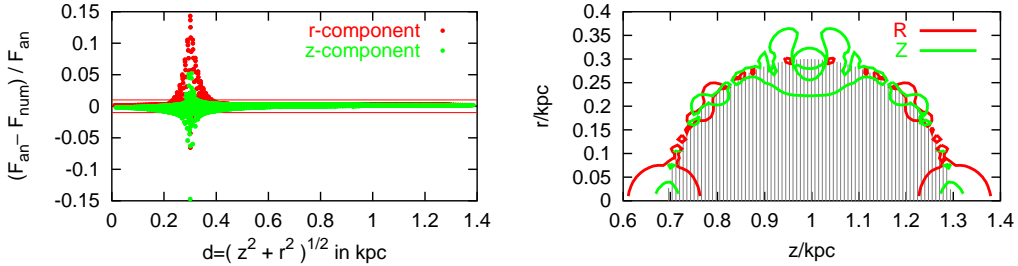
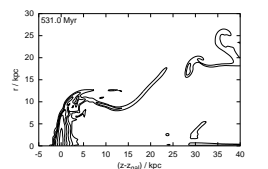


Figure C.24: Relative error in the gravitational force components, for all cells, for the low resolution run (LR). **Left:** Relative error depending on d . The horizontal lines mark $\pm 1\%$. **Right:** Contour plots, contours for relative error $\pm 1\%$ are shown for both components, see key in the plot. The sphere itself is shaded.

treated separately. Again the relative errors are largest near the surface of the sphere, in a handful of cells they reach even 15%. But even for most cells near the sphere surface the relative errors are smaller than 5%, and inside $2/3R$ and outside $4/3R$ the relative errors are far below 1%. The large local relative errors arise at positions where the theoretical result is very small (see rhs plot in Fig. C.24), e.g in the z -component near $z = z_0 = \text{const}$. There, theoretically, F_z should vanish, and a small deviation (small compared to e.g. F_{max}) from that causes a large local relative error. The hole picture looks less dramatic if not the local relative errors but errors normalised to F_{max} are considered. Still the largest errors appear at the sphere surface, but they are smaller than 2-3% of F_{max} . No matter if local relative or normalised errors are used, a better resolution leads to smaller errors.

The influence of shifting the sphere along the z -axis off the axis centre is demonstrated in the lhs plot in Fig. C.25. The sphere can be shifted until it nearly touches the boundary, the result for the potential and naturally for



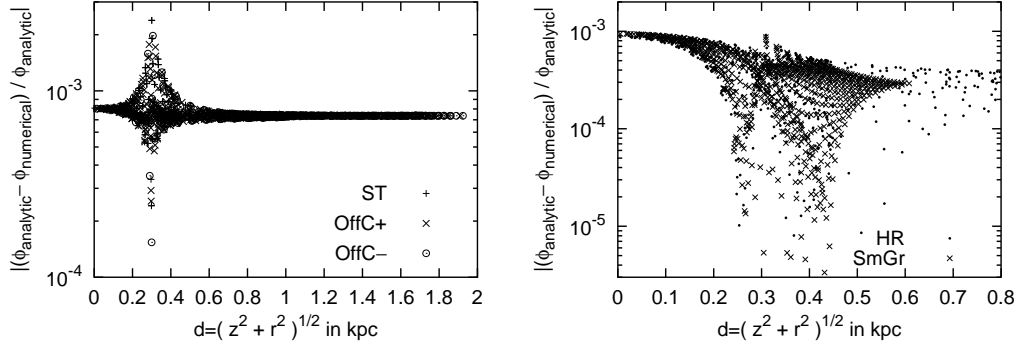


Figure C.25: Like rhs plot in Fig. C.23. **Left:** Influence of sphere position inside the grid. **Right:** Influence of grid size compared to sphere radius

the force is nearly indistinguishable.

The rhs plot in Fig. C.25 compares runs with the same physical resolution, but different physical grid sizes. In the small-grid case (SmGr) the numerical grid is only slightly larger than the sphere itself ($1.5R \times 3R$), whereas the HR run has the same physical resolution ($\Delta r = \Delta z = 4.444444\text{pc}$), but extends further away from the sphere ($3.3 \times 6.6R$). As seen in the rhs plot of C.25, in the range which is covered by both grids, the results are practically identical.

The sphere mass was also varied, but it does not influence the results.

C.5 Implications for further simulations

Artificial viscosity

The code does not work without the quadratic term of the artificial viscosity. Following the suggestions of previous work and of the tests we choose $C_2 = 2$. In general the RPS simulations do not involve strong shocks accompanied by stagnant regions. Therefore we take $C_1 = 0$.

Boundaries

According to the potential flow test we choose the r_{\max} boundary to be solid. The best choice for the z_{\max} boundary would be an active outflow. Unfortunately it does not work in cases where stripped gas clumps leave the grid. This boundary condition causes strange reflections when the gas clumps cross the downstream boundary. Therefore we choose the normal open boundary.

The potential flow test demonstrates that the grid boundaries must have a sufficient distance to the sphere/galaxy. Approximate values are $r_{\max} \geq 2r_{\text{gal}}$, $z_{\max} \geq 4r_{\text{gal}}$, $z_{\text{gal}} \geq r_{\text{gal}}$, $z_{\max} - z_{\text{gal}} \geq 2r_{\text{gal}}$, where z_{gal} is the z coordinate of the galaxy and r_{gal} the galaxy's radius.

Wind initialisation

According to the potential flow test the wind initialisation should be as slow as possible. The choice of t_{switch} is discussed in more detail in Sect. 4.3.2.

Appendix D

Tests for ram pressure stripping simulations

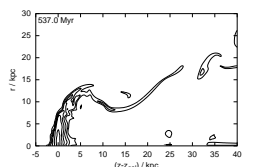
This appendix summarises a few tests performed for RPS simulations. Analysis techniques, general parameter choices and the interpretation of the results are not repeated here, please refer to Chapters 4 and 3.

D.1 Resolution and grid size

Requirements on the numerical parameters grid size and resolution are explained in Sect. 4.3.1. To be appropriate, the grid should be large enough and the resolution small enough so that the results do not depend on them any more. That this is indeed the case for the choices listed in Sect. 4.3.1 is demonstrated here. Table D.1 lists a few test runs in which resolution and grid size are varied. For these models the massive galaxy with a normal exponential disk ($b_{\text{gas}} = 0.4 \text{ kpc}$) was used (see Sect. 3.1.5). Similar runs have been performed for a flared disk. Figure D.1 verifies that indeed the evolution of neither radius nor the mass of the remaining gas disk nor the amount of fallen-back gas depends on grid size and resolution. The small differences

model name	physical grid size (kpc \times kpc)	numerical grid size $NZ \times NR$	resolution (pc)
small grid	100×50	660×330	151.5
standard	100×100	650×650	153.8
low resolution	.	500×500	200
high resolution 1	.	1000×1000	100
high resolution 2	.	2000×2000	50

Table D.1: List of simulations testing the influence of resolution and grid size. Common parameters for all runs are: massive galaxy with standard exponential disk, ICM wind with $\tilde{p}_{\text{ram}} = 1000 \text{ cm}^{-3} \text{ km}^2 \text{ s}^{-2}$, $T_{\text{ICM}1}$, Mach number 0.8, $t_{\text{switch}} = 20 \text{ Myr}$.



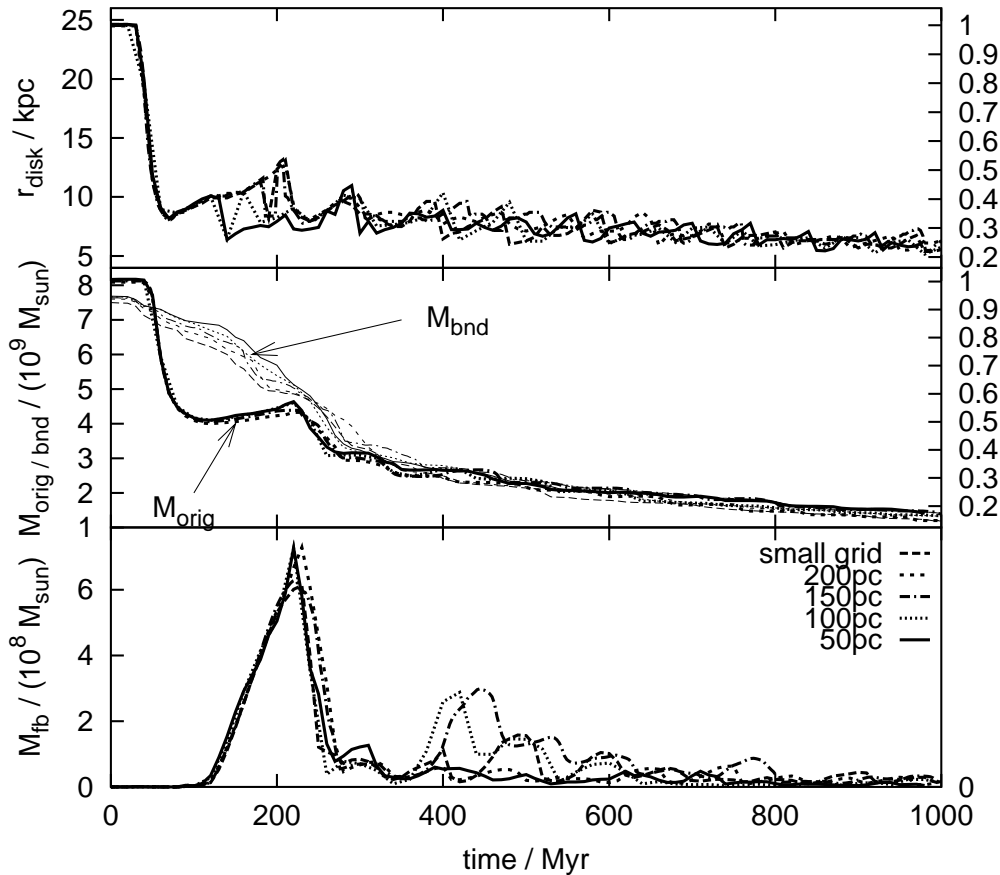


Figure D.1: Influence of grid size and resolution on evolution of gas disk radius, mass and fallen-back mass. See Table D.1 for parameters.

in M_{bnd} arise because in cases with higher resolution the the stripped gas can be compressed into smaller volumes, reaching higher densities locally. Such dense clouds are more likely to be bound than the clouds with lower densities.

In Fig. D.2 we show snapshots at $t = 200$ Myr for the four different resolutions (see Table D.1). The strongest difference occurs for the stripped material. The coarser grids cannot resolve the small-scale fragmentation of the stripped gas evident in the highest resolution. However, we did not attempt to interpret the fate of the stripped material shown in the simulations, as we neglected e.g. thermal conduction, which might be play an important role in the evolution of the stripped gas.

D.2 Wind initialisation

The wind initialisation procedure is described in Sect. 4.3.2. The main point is that the flow is “switched on” during a time t_{switch} . On the one hand, on

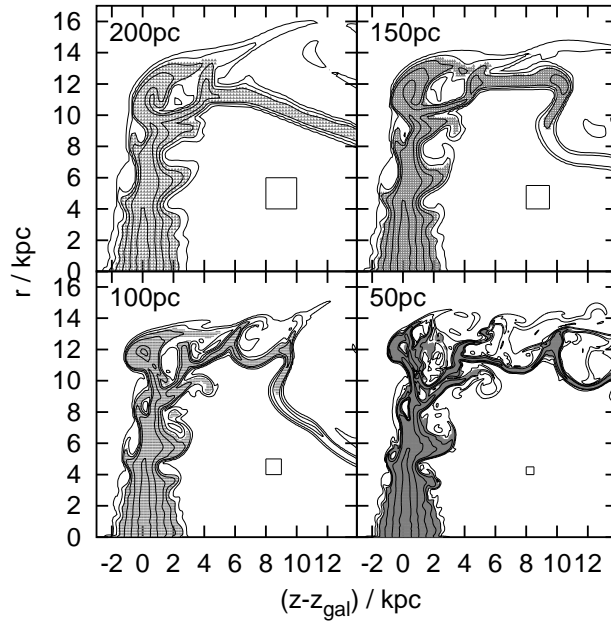
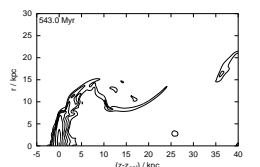


Figure D.2: Influence of resolution: Snapshots at $t = 200$ Myr for four different resolutions as given in the plot, see Table D.1 for parameters. The gas density is shown by logarithmic contours like in Fig. 3.6. The size of 10×10 cells is indicated by the rectangle in each panel. Gas in the shaded areas is gravitationally bound.

behalf of an unperturbed flow, t_{switch} should be rather long, on the other, in order to resolve the involved stripping time scales, it should be rather short. Here we describe tests how the simulation results depend on this numerical parameter.

We ran some representative cases with $t_{\text{switch}} = 20, 70, 150$ Myr. The shortest t_{switch} is chosen to resolve the expected stripping time scale (see Sect. 4.2.1). The longest t_{switch} was chosen to be as long as possible under the condition that the initialisation must be finished before the first stripped material reaches the outflow boundary. Stripped material that would reach the outflow boundary during t_{switch} would cause reflection problems, as during t_{switch} the outflow boundary has a fixed velocity and is not open, as explained in Sect. 2.5. The maximum t_{switch} was found by trial and error. The parameters for these runs are listed in Table D.2. The resulting mass and radius of the gas disk for runs with different t_{switch} are shown in Fig. D.3. Again we smooth the curves for $r_{\text{disk}}(t)$ (see Sect. 4.5.3).

At first glance, the results are independent of t_{switch} . However there are small systematic differences in the initial phase, but these differences were expected. The decrease in mass and radius due to the instantaneous stripping is fastest for the shortest t_{switch} . After that r_{disk} , M_{orig} and M_{bnd} agree well despite the different t_{switch} . The cases with the longest t_{switch} tend to retain a little more mass during the intermediate phase due to an overlap of t_{switch}



\tilde{p}_{ram} ($\text{cm}^{-3} \text{km}^2 \text{s}^{-2}$)	v_{ICM} (km s^{-1})	n_{ICM} (cm^{-3})	t_{switch} (Myr)
1000	800	$1.56 \cdot 10^{-3}$	20, 70, 150
1000	2530	$1.56 \cdot 10^{-4}$	20, 70, 150
100	800	$1.56 \cdot 10^{-4}$	20, 70, 150
100	2530	$1.56 \cdot 10^{-5}$	20, 70, 150

Table D.2: Parameters for the simulations testing influence of t_{switch} . All these runs use the massive galaxy with an exponential disk with $b_{\text{gas}} = 0.4 \text{ kpc}$ and $T_{\text{ICM}1}$, corresponding to a sound speed $c_{\text{ICM}} = 1000 \text{ km s}^{-1}$.

and the beginning of the intermediate phase. For weaker \tilde{p}_{ram} the agreement between cases with different t_{switch} is not as tight as for strong \tilde{p}_{ram} , which is due to the longer dynamical (chaotic) intermediate phase for weaker \tilde{p}_{ram} . The qualitative behaviour of the amount of bound mass outside the disk region and of the fallen back mass is independent of t_{switch} .

We conclude that the influence of different choices of t_{switch} can be neglected.

D.3 Gravitational potential of the gas disk

As the gas distribution changes due to RPS, also the gravitational potential evolves. However, we used a static potential in the simulations. Does this bias our results? We performed a test run that took the contribution of the gas to the potential and its evolution into account. Figure D.4 displays the disk mass and radius for this run ($\tilde{p}_{\text{ram}} = 1000 \text{ cm}^{-3} \text{ km}^2 \text{ s}^{-2}$) as well as the corresponding case with static potential. Clearly, taking into account the gas potential or not makes no difference. Hence we use a static potential.

We want to stress that for a study of the fate of the stripped gas (Does it become gravitationally instable? Are stars formed? ...) the evolution of the gravitational potential must be taken into account along with a multi-phase treatment of the ISM and processes like cooling and thermal conduction.

D.4 Influence of artificial viscosity

In our simulations we observed the long phase of turbulent viscous stripping. The code uses an artificial viscosity mainly to be able to handle shocks. A concern may be that due to this artificial viscosity the code cannot handle the KH-instability correctly and hence biases the results of the viscous stripping phase. We performed test runs (see Table D.3) to investigate the influence of the artificial viscosity by varying the viscosity parameter C_2 (see Sect. 2.3.1). The results for the disk radius, mass and bound mass are compared in Figs. D.5 and D.6. The differences are negligible. Fig. D.7

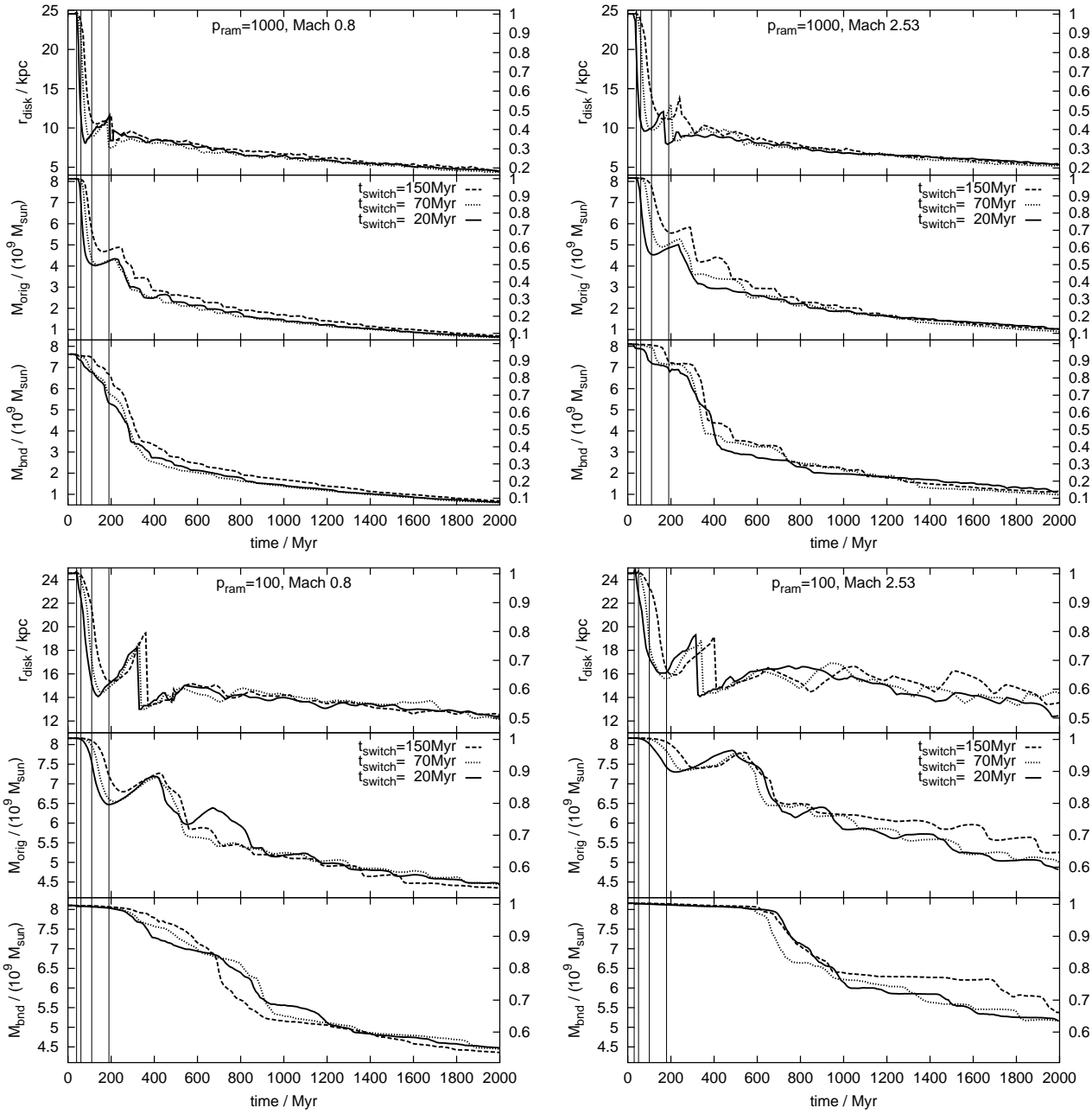
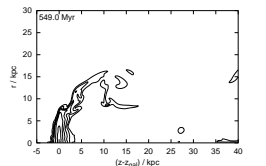


Figure D.3: Comparison of stripping radius $r_{\text{disk}}(t)$, mass in original disk region $M_{\text{orig}}(t)$ and bound mass $M_{\text{bnd}}(t)$ for different t_{switch} , for four representative winds. We mark the moment where a sound wave starting at the inflow boundary reaches galaxy (t_0), and $t_0 + t_{\text{switch}}$ for the three different t_{switch} by the four thin vertical lines. For further explanations see Fig. 4.11.

compares snapshots at $t = 200$ Myr for the test cases with varying viscosity. As expected, for the high viscosity parameter, the surface instabilities are softer, whereas in the low viscosity case ($C_2 = 1$) the features are sharper. However, almost all features can be identified for all viscosities. We conclude



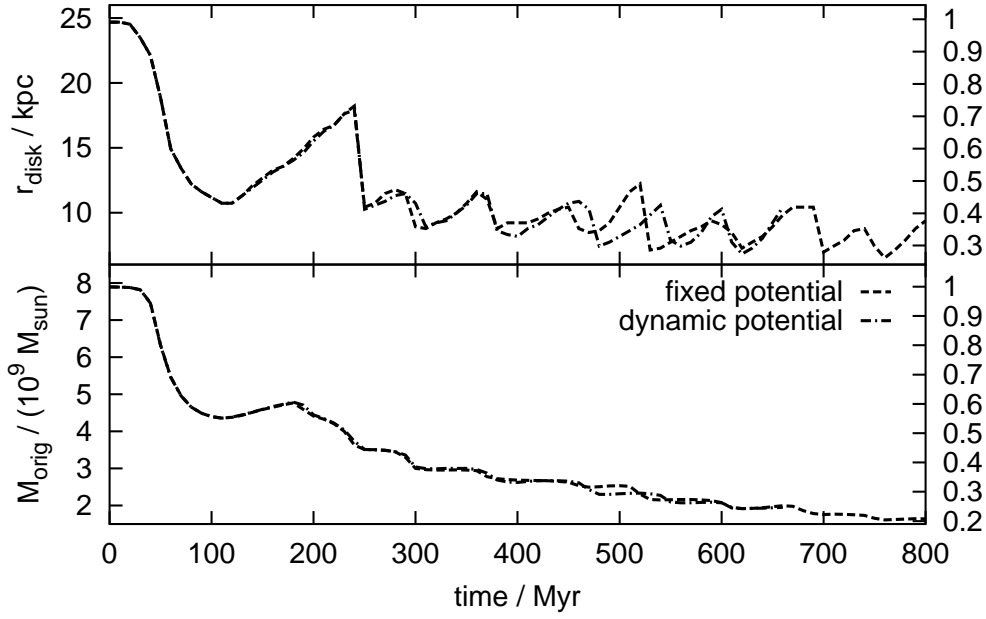


Figure D.4: Comparison of gas disk mass and radius, once with static potential, once with dynamic potential, where evolution of potential due to changing gas distribution is taken into account.

\tilde{p}_{ram} ($\text{cm}^{-3} \text{km}^2 \text{s}^{-2}$)	Mach number	viscosity parameter C_2 (see Sect. 2.3.1)
1000	0.8	1,2,6
.	2.53	.

Table D.3: List of simulations to study the influence of the artificial viscosity. Common parameters for all runs are: massive galaxy with standard exponential disk, ICM wind with T_{ICM1} ($c_{\text{ICM}} = 1000 \text{ km s}^{-1}$).

that the use of the artificial viscosity does not bias our results.

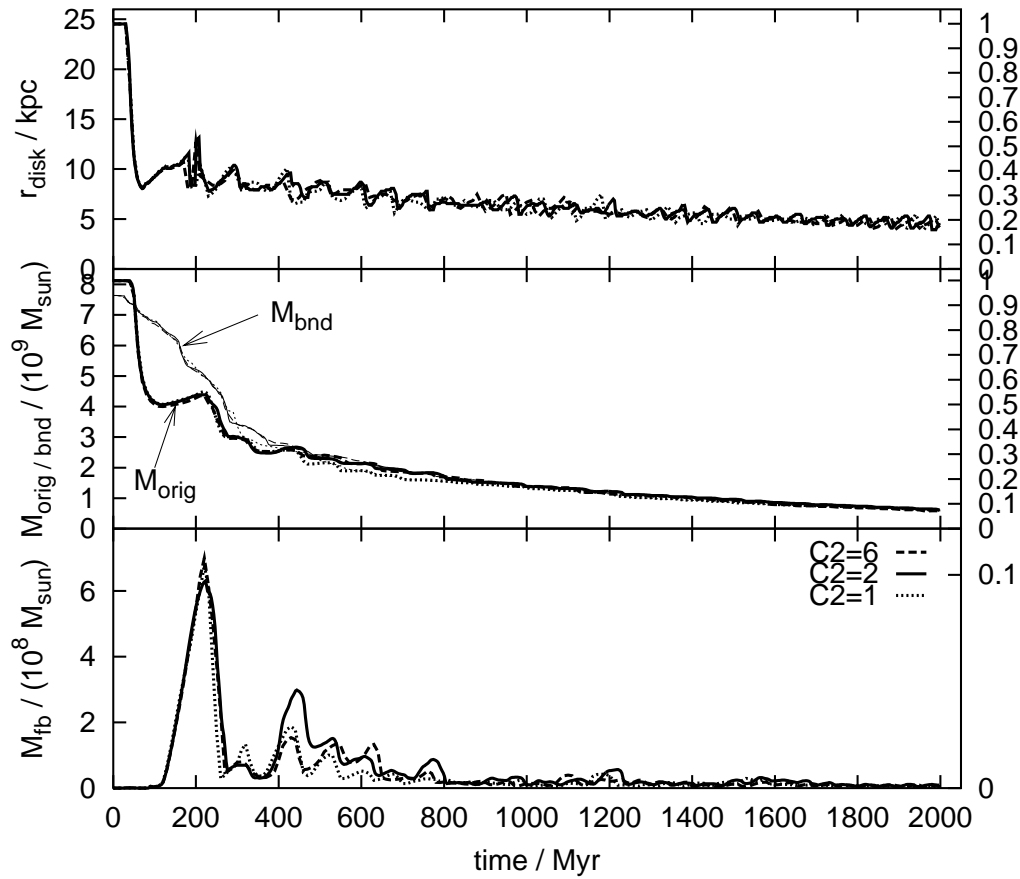
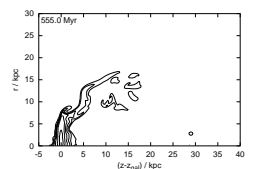


Figure D.5: Influence of the viscosity on the evolution of the gas disk radius, mass and fallen-back mass. The value of the viscosity parameter C_2 (see Sect. 2.3.1) is indicated in the key. For further parameters of these runs see Table D.3. This plot is for the runs with Mach number 0.8.



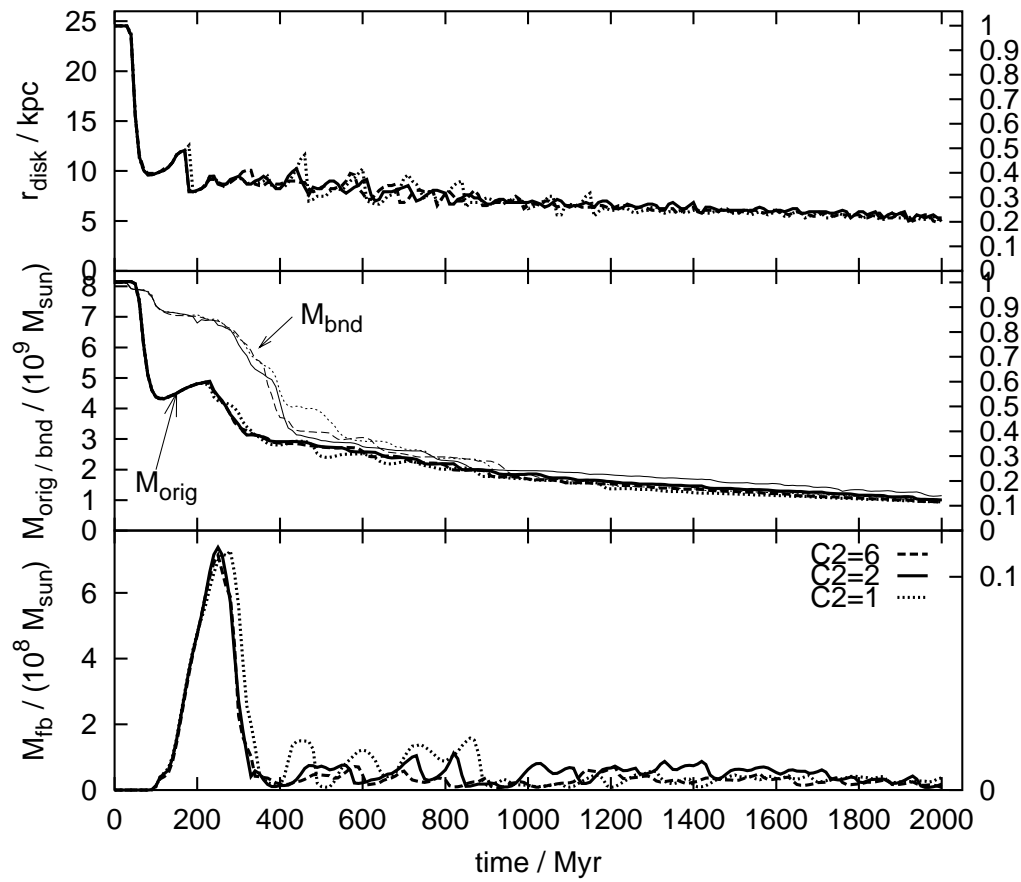


Figure D.6: Like Fig. D.5, but for the runs with Mach number 2.53.

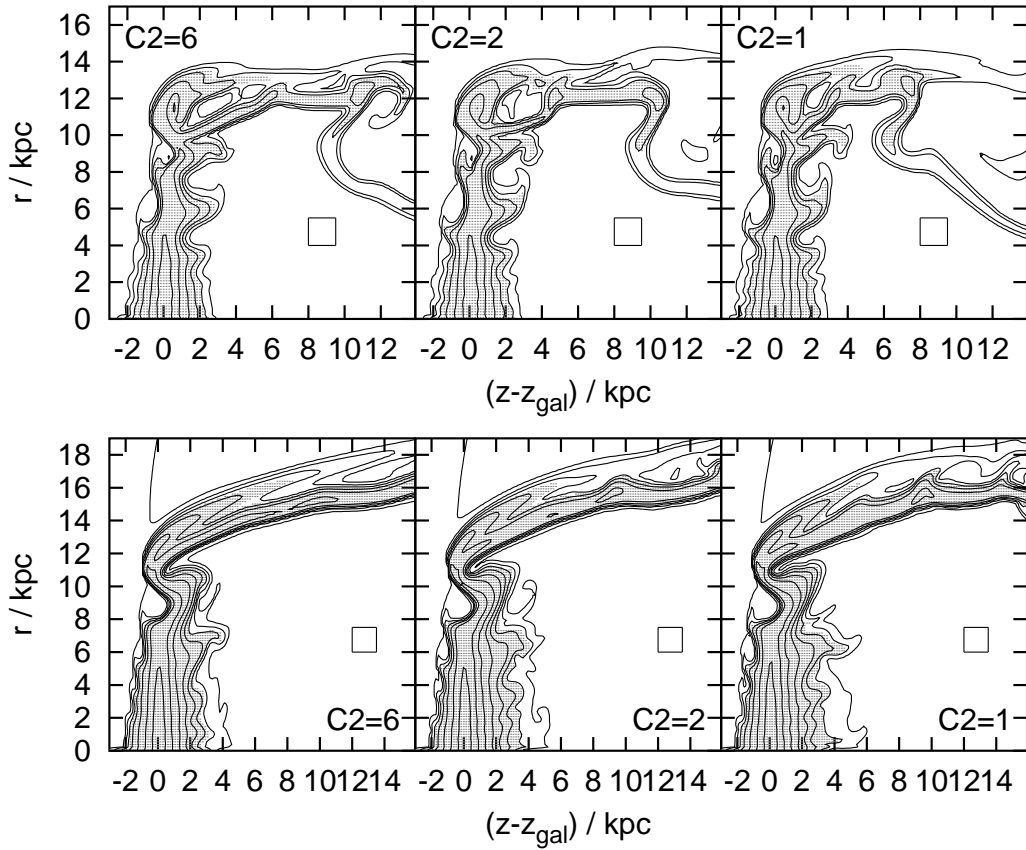
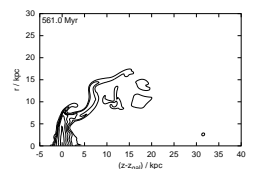
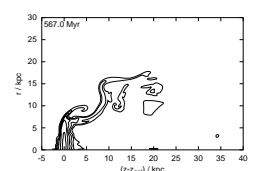


Figure D.7: Comparison of the density distribution (at $t = 200$ Myr) for different viscosities. The gas density is shown by logarithmic contours like in Fig. 3.6. The top panels are for Mach number 0.8, the bottom panels for Mach number 2.53. For further parameters see Table D.3. Each panel is labelled with the appropriate viscosity parameter C_2 (see Sect. 2.3.1). The rectangle corresponds to 10×10 cells.



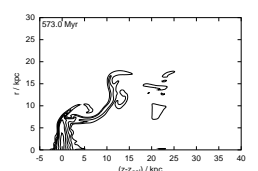
Bibliography

- Abadi, M. G., Moore, B., & Bower, R. G. 1999, MNRAS, 308, 947
- Acreman, D. M., Stevens, I. R., Ponman, T. J., & Sakelliou, I. 2003, MNRAS, 341, 1333
- Aguerri, J. A. L., Iglesias-Paramo, J., Vilchez, J. M., & Muñoz-Tuñón, C. 2004, AJ, 127, 1344
- Ballesteros-Paredes, J. 2004, Ap&SS, 289, 243
- Balogh, M., Eke, V., Miller, C., et al. 2004, MNRAS, 348, 1355
- Balogh, M. L. & Morris, S. L. 2000, MNRAS, 318, 703
- Balogh, M. L., Navarro, J. F., & Morris, S. L. 2000, ApJ, 540, 113
- Bekki, K., Couch, W. J., & Shioya, Y. 2002, ApJ, 577, 651
- Bergmann & Schaefer. 2002, Bergmann Schaefer: Lehrbuch der Experimentalphysik, Vol. 8, Sterne und Weltraum (Berlin New York: de Gruyter)
- Binggeli, B., Tarenghi, M., & Sandage, A. 1990, A&A, 228, 42
- Binney, J. & Merrifield, M. 1998, Galactic Astronomy (Princeton, New Jersey: Princeton University Press)
- Binney, J. & Tremaine, S. 1987, Galactic Dynamics (Princeton, New Jersey: Princeton University Press)
- Black, D. C. & Bodenheimer, P. 1975, ApJ, 199, 619
- Bohringer, H., Briel, U. G., Schwarz, R. A., et al. 1994, Nature, 368, 828
- Böhringer, H. & Hensler, G. 1989, A&A, 215, 147
- Bomans, D. J., Hensler, G., Tschöke, D., Boselli, A., & Napiwotzki, R. 2004, A&A, in press
- Borriello, A. & Salucci, P. 2001, MNRAS, 323, 285
- Boselli, A., Gavazzi, G., Lequeux, J., et al. 1997, A&A, 327, 522



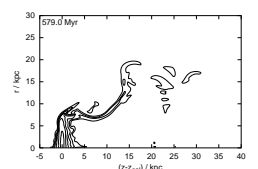
- Boselli, A., Lequeux, J., & Gavazzi, G. 2002, *A&A*, 384, 33
- Bravo-Alfaro, H., Cayatte, V., van Gorkom, J. H., & Balkowski, C. 2000, *AJ*, 119, 580
- Breitschwerdt, D. 2004, *Ap&SS*, 289, 489
- Broeils, A. H. & van Woerden, H. 1994, *A&AS*, 107, 129
- Burkert, A. 1995, *ApJ*, 447, 25L
- Burns, J. O. 1998, *Science*, 280, 400
- Burstein, D. & Blumenthal, G. 2002, *ApJ*, 574, 17L
- Butcher, H. & Oemler, A. 1978a, *ApJ*, 219, 18
- Butcher, H. & Oemler, A. 1978b, *ApJ*, 226, 559
- Butcher, H. & Oemler, A. 1984, *ApJ*, 285, 426
- Butcher, H. & Oemler, A. 1985, *ApJS*, 57, 665
- Butcher, H., Oemler, A., & Wells, D. C. 1983, *ApJS*, 52, 183
- Casoli, F., Dickey, J., Kazes, I., et al. 1996, *A&A*, 309, 43
- Casoli, F., Sauty, S., Gerin, M., et al. 1998, *A&A*, 331, 451
- Cayatte, V., Kontanyi, C., Balkowski, C., & van Gorkom, J. H. 1994, *AJ*, 107, 1003
- Cayatte, V., van Gorkom, J. H., & Kotanyi, C. 1990, *AJ*, 100, 604
- Chandrasekhar, S. 1961, *Hydrodynamic and Hydrostatic Stability* (Oxford University Press)
- Colless et al., M. 2001, *MNRAS*, 328, 1039
- Colless et al., M. 2003, *astro-ph/0306581*
- Combes, F., Boissé, P., Mazure, A., & Blanchard, A. 1995, *Galaxies and Cosmology* (Springer)
- Cowie, L. L. & McKee, C. F. 1977, *ApJ*, 211, 135
- Cowie, L. L. & Songaila, A. 1977, *Nature*, 266, 501
- Crowl, H. H., Kenney, J. D. P., van Gorkom, J. H., & Vollmer, B. 2004, *American Astronomical Society Meeting*, 204
- Dahlem, M. 1997, *PASP*, 109, 1298

- Dalgarno, A. & McCray, R. A. 1972, *ARA&A*, 10, 375
- Davies, J. 2004, in *The environments of galaxies – from kpc to Mpc*, e-proceedings <http://astronomy.swin.edu.au/conferences/crete2004/>
- de Avillez, M. A. & Breitschwerdt, D., eds. 2004, *Ap&SS*, Vol. 289, *From observations to self-consistent modelling of the ISM in galaxies* (Dortrecht: Kluwer Academic Publishers)
- De Propriis, R., Colless, M., Peacock, J. A., et al. 2004, *MNRAS*, 351, 125
- Dickey, J. M. 1997, *AJ*, 113, 1939
- Dickey, J. M. & Lockman, F. J. 1990, *ARA&A*, 28, 215
- Doyon, R. & Joseph, R. D. 1989, *MNRAS*, 239, 347
- Dressler, A. 1980, *ApJ*, 236, 351
- Dressler, A. 1986, *ApJ*, 301, 35
- Falgarone, E. & Puget, J. L. 1985, *A&A*, 142, 157
- Farouki, R. & Shapiro, S. L. 1980, *ApJ*, 241, 928
- Fujita, Y. 1998, *ApJ*, 509, 587
- Fujita, Y. 2001, *ApJ*, 550, 612
- Fujita, Y. 2004, *PASJ*, 56, 29
- Fujita, Y. & Nagashima, M. 1999, *ApJ*, 516, 619
- Gavazzi, G., Boselli, A., Mayer, L., et al. 2001, *ApJ*, 563, 23L
- Gavazzi, G., Boselli, A., Pedotti, P., Gallazzi, A., & Carrasco, L. 2002, *A&A*, 396, 449
- Gavazzi, G., Contursi, A., Carrasco, L., et al. 1995, *A&A*, 304, 325
- Giovanelli, R. & Haynes, M. P. 1985, *ApJ*, 292, 404
- Gisler, G. R. 1976, *A&A*, 51, 137
- Gómez, P. L., Nichol, R. C., Miller, C. J., et al. 2003, *ApJ*, 584, 210
- Goto, T., Okamura, S., Sekiguchi, M., et al. 2003a, *PASJ*, 55, 757
- Goto, T., Okamura, S., Yagi, M., et al. 2003b, *PASJ*, 55, 739
- Goto, T., Yamauchi, C., Fujita, Y., et al. 2003c, *MNRAS*, 346, 601



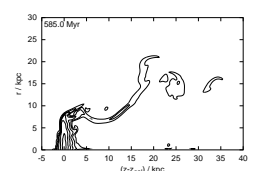
- Goto et al., T. 2004, in *Carnegie Observatories Astrophysics Series, Vol. 3, Clusters of Galaxies: Probes of Cosmological Structure and Galaxy Evolution*, ed. J. S. Mulchaey, A. Dressler, & A. Oemler (Cambridge: Cambridge Univ. Press), 21
- Grebel, E. K. 2001, in *Dwarf galaxies and their environments*, ed. K. S. de Boer, R. Dettmar, & U. Klein (Shaker), 45
- Gunn, J. E. & Gott, J. R. 1972, *ApJ*, 176, 1
- Hartmann, J. 1904, *ApJ*, 19, 268
- Hawley, J. F., Smarr, L. L., & Wilson, J. R. 1984, *ApJS*, 55, 211
- Helsdon, S. F. & Ponman, T. J. 2003, *MNRAS*, 339, 29L
- Hernquist, L. 1993, *ApJS*, 86, 389
- Hubble, E. P. 1926, *ApJ*, 64, 321
- Hubble, E. P. 1936, *The Realm of the Nebulae* (Yale University Press)
- Ikebe, Y., Makishima, K., Fukazawa, Y., et al. 1999, *ApJ*, 525, 58
- Kenney, J. D. & Young, J. S. 1988, *ApJS*, 66, 261
- Kenney, J. D. P. & Koopmann, R. A. 1999, *AJ*, 117, 181
- Kenney, J. D. P., van Gorkom, J. H., & Vollmer, B. 2004, *AJ*, 127, 3361
- Kenney, J. D. P. & Young, J. S. 1989, *ApJ*, 344, 171
- Kilborn, V. A., Koribalski, B. S., Forbes, D. A., Barnes, D. G., & Musgrave, R. C. 2004, *MNRAS*, 581
- Koopmann, R. A. & Kenney, J. D. P. 1998, *ApJ*, 497, 75L
- Koopmann, R. A. & Kenney, J. D. P. 2004a, *ApJ*, in press, astro-ph/0406243
- Koopmann, R. A. & Kenney, J. D. P. 2004b, *ApJ*, in press, astro-ph/0209547
- Koopmann, R. A., Kenney, J. D. P., & Young, J. 2001, *ApJS*, 135, 125
- Landau, L. D. & Lifschitz, F. M. 1991, *Lehrbuch der theoretischen Physik VI: Hydrodynamik* (Berlin: Akademie Verlag)
- Larson, R. B., Tinsley, B. M., & Caldwell, C. N. 1980, *ApJ*, 237, 692
- Lea, S. M. & Young, D. S. D. 1976, *ApJ*, 210, 647
- Lewis, I., Balogh, M., De Propris, R., et al. 2002, *MNRAS*, 334, 673

- Lieu, R. 2000, *A&A*, 364, 497
- Loewenstein, M. 2004, in *Carnegie Observatories Astrophysics Series, Vol. 4, Origin and Evolution of the Elements*, ed. A. McWilliam & M. Rauch (Cambridge: Cambridge University Press), 425
- Lohmann, F. C. 2000, Diploma thesis, University of Kiel
- Magri, C., Haynes, M. P., Forman, W., Jones, C., & Giovanelli, R. 1988, *ApJ*, 333, 136
- Mamon, G. A., Sanchis, T., Salvador-Solé, E., & Solanes, J. M. 2004, *A&A*, 414, 445
- Marcolini, A., Brighenti, F., & A.D'Ercole. 2003, *MNRAS*, 345, 1329
- Margoniner, V. E., de Carvalho, R. R., Gal, R. R., & Djorgovski, S. G. 2001, *ApJ*, 548, L143
- Martínez, H. J., Zandivarez, A., Domínguez, M., Merchán, M. E., & Lambas, D. G. 2002, *MNRAS*, 333, 31L
- Matsumoto, H., Tsuru, T. G., Fukazawa, Y., Hattori, M., & Davis, D. S. 2000, *PASJ*, 52, 153
- McKee, C. F. & Cowie, L. L. 1977, *ApJ*, 215, 213
- McKee, C. F. & Ostriker, J. P. 1977, *ApJ*, 218, 148
- Mihos, J. C. 2004, in *Carnegie Observatories Astrophysics Series, Vol. 3, Clusters of Galaxies: Probes of Cosmological Structure and Galaxy Evolution*, ed. J. S. Mulchaey, A. Dressler, & A. Oemler (Cambridge: Cambridge Univ. Press), 278
- Miyamoto, M. & Nagai, R. 1975, *PASJ*, 27, 533
- Mohr, J. J., Mathiesen, B., & Evrard, A. E. 1999, *ApJ*, 517, 627
- Molendi, S. 2004, in *American Institute of Physics Conference Series, Vol. 703, Plasmas in the laboratory and in the universe*, 345
- Monaco, P. 2004, *MNRAS*, 354, 151
- Moore, B., Katz, N., Lake, G., Dressler, A., & Oemler, A. 1996, *Nature*, 379, 613
- Moore, B., Lake, G., & Katz, N. 1998, *ApJ*, 495, 139
- Moore, B., Lake, G., Quinn, T., & Stadel, J. 1999, *MNRAS*, 304, 465
- Mori, M. & Burkert, A. 2000, *ApJ*, 538, 559



- Mulchaey, J. S. 2000, *ARA&A*, 38, 289
- Mulchaey, J. S. 2004, in *Carnegie Observatories Astrophysics Series, Vol. 3, Clusters of Galaxies: Probes of Cosmological Structure and Galaxy Evolution*, ed. J. S. Mulchaey, A. Dressler, & A. Oemler (Cambridge: Cambridge Univ. Press), 354
- Mulchaey, J. S., Davis, D. S., Mushotzky, R. F., & Burstein, D. 1996a, *ApJ*, 456, 80
- Mulchaey, J. S., Davis, D. S., Mushotzky, R. F., & Burstein, D. 1996b, *ApJ*, 456, 80
- Navarro, J. F., Frenk, C. S., & White, S. D. M. 1996, *ApJ*, 462, 563
- Norman, M. L. & Winkler, K.-H. A. 1986, in *Astrophysical Radiation Hydrodynamics*, ed. K.-H. A. Winkler & M. L. Norman, NATO Advanced Research Workshop (Dordrecht: Reidel), 187
- Nulsen, P. E. J. 1982, *MNRAS*, 198, 1007
- Oetken, L. & Scholz, G. 2004, *SuW*, 43, 40
- Okamoto, T. & Nagashima, M. 2003, *ApJ*, 587, 500
- Omar, A. 2004, *Bull. Astr. Soc. India*, 32, 239
- Otmianowska-Mazur, K. & Vollmer, B. 2003, *A&A*, 402, 879
- Persic, M., Salucci, P., & Stel, F. 1996, *MNRAS*, 281, 27
- Phookun, B. & Mundy, L. G. 1995, *ApJ*, 453, 154
- Pimblet, K. A. 2003, *Publications of the Astronomical Society of Australia*, 20, 294
- Poggianti, B. M. 2003, in *ASP Conf. Proc., Vol. 301, Matter and Energy in Clusters of Galaxies*, ed. S. Bowyer & C. Hwang (San Francisco: Astronomical Society of the Pacific), 245
- Portnoy, D., Pistinner, S., & Shaviv, G. 1993, *ApJS*, 86, 95
- Press, W. H., Teukolsky, S. A., Vetterling, W. T., & Flannery, B. P. 1992, *Numerical Recipes* (Cambridge: Cambridge University Press)
- Quilis, V., Moore, B., & Bower, R. 2000, *Science*, 288, 1617
- Reynolds, R. J. 1989, *ApJ*, 339, L29
- Różyczka, M. 1985, *A&A*, 143, 59

- Salucci, P. & Burkert, A. 2000, *ApJ*, 537, 9L
- Sanchis, T., Mamon, G. A., Salvador-Solé, E., & Solanes, J. M. 2004, *A&A*, 418, 393
- Sanchis, T., Solanes, J. M., Salvador-Solé, E., Fouqué, P., & Manrique, A. 2002, *ApJ*, 580, 164
- Sarazin, C. L. 1988, *X-ray emission from clusters of galaxies* (Cambridge: Cambridge University Press)
- Scheffler, H. & Elsässer, H. 1982, *Bau und Physik der Galaxis* (Bibliographisches Institut Mannheim)
- Schindler, S. 2003, *SuW*, 42, 26
- Schindler, S. 2004, *Ap&SS*, 289, 419
- Schindler, S., Binggeli, B., & Böhringer, H. 1999, *A&A*, 343, 420
- Schröder, A., Drinkwater, M. J., & Richter, O. 2001, *A&A*, 376, 98
- Schulz, S. & Struck, C. 2001, *MNRAS*, 328, 185
- Sedov, L. I. 1959, *Similarity and Dimensional Methods in Mechanics* (London: Infosearch Ltd.)
- Severing, I. 1995, Diploma thesis, University of Kiel
- Shannon, B. 1999, *Catch the Wave*, Photo, www.siskiyous.edu/shasta/map/mp (Mt. Shasta homepage)
- Shu, F. H. 1992, *The physics of astrophysics, Vol. II. Gas dynamics* (Mill Valley, California: University Science Books)
- Sod, G. A. 1978, *J.Comp.Phys.*, 27, 1
- Solanes, J. M., Manrique, A., García-Gómez, C., et al. 2001, *ApJ*, 548, 97
- Spitzer, L. 1956, *Physics of Fully Ionized Gases* (New York: Interscience Publishers)
- Stark, A. A., Knapp, G. R., Bally, J., et al. 1986, *ApJ*, 310, 660
- Stevens, I. R., Acreman, D. M., & Ponman, T. J. 1999, *MNRAS*, 310, 663
- Stone, J. M. & Norman, M. L. 1992, *ApJS*, 80, 753
- Storm, V. 1993, Diploma thesis, University of Kiel
- Takeda, H., Nulsen, P. E. J., & Fabian, A. C. 1984, *MNRAS*, 208, 261



- Toniazzo, T. & Schindler, S. 2001, MNRAS, 325, 509
- Toomre, A. & Toomre, J. 1972, ApJ, 178, 623
- Toro, E. F. 1999, Riemann Solvers and Numerical Methods for Fluid Dynamics (Springer)
- Toyama, K. & Ikeuchi, S. 1980, Prog. Theo. Phys., 64, 831
- Tschöke, D., Bomans, D. J., Hensler, G., & Junkes, N. 2001, A&A, 380, 40
- Turner, B. E. 1989, Space Science Reviews, 51, 235
- Unsöld, A. & Baschek, B. 1999, Der neue Kosmos (Springer)
- Valluri, M. & Jog, C. J. 1991, ApJ, 374, 103
- van Gorkom, J. 1996, in ASP Conf. Ser., Vol. 106, The Minnesota Lectures on Extragalactic Neutral Hydrogen, ed. E. D. Sullivan, 293
- van Leer, B. 1977, Comp. Phys., 23, 276
- Vieser, W. 2001, PhD thesis, University of Kiel
- Vollmer, B. 2003, A&A, 398, 525
- Vollmer, B., Balkowski, C., Cayatte, V., van Driel, W., & Huchtmeier, W. 2004a, A&A, 419, 35
- Vollmer, B., Beck, R., Kenney, J. D. P., & van Gorkom, J. H. 2004b, AJ, 127, 3375
- Vollmer, B., Braine, J., Balkowski, C., Cayatte, V., & Duschl, W. J. 2001a, A&A, 374, 824
- Vollmer, B., Cayatte, V., Balkowski, C., & Duschl, W. J. 2001b, ApJ, 561, 708
- Vollmer, B., Cayatte, V., Boselli, A., Balkowski, C., & Duschl, W. J. 1999, A&A, 349, 411
- Vollmer, B., Cayatte, V., van Driel, W., et al. 2001c, A&A, 369, 432
- Vollmer, B., Marcelin, M., Amram, P., et al. 2000, A&A, 364, 532
- Welch, G. A. & Sage, L. J. 2003, ApJ, 584, 260
- Winkler, K.-H. A. & Norman, M. L. 1986, in Astrophysical Radiation Hydrodynamics, ed. K.-H. A. Winkler & M. L. Norman, NATO Advanced Research Workshop (Dordrecht: Reidel), 71
- Yamauchi, C. & Goto, T. 2004, MNRAS, 352, 815
- York, D. G., Adelman, J., Anderson, J. E., et al. 2000, AJ, 120, 157

An dieser Stelle an alle, die zum Gelingen dieser Arbeit beigetragen haben, ein großes

Dankeschön!

Der erste Dank geht an Gerhard Hensler für die Vergabe des interessanten Themas und seine ansteckende Begeisterung für die Wissenschaft. Die wirkt auch über die Entfernung zwischen Kiel und Wien. Der Galaxien-Arbeitsgruppe möchte ich für die freundliche Aufnahme und die anregenden Diskussionen danken, auch wenn sie sich nach 2 Jahren zerstreut hat. Besonders Christian Theis und Joachim Köppen haben mir beim Lösen des ein oder anderen Knotens in meinem Gehirn geholfen. Detlev Koester möchte ich dafür danken, daß er ganz unkompliziert die offizielle Betreuung dieser Arbeit übernommen hat, nachdem Gerhard Hensler nach Wien gegangen war. Für die freundschaftliche Atmosphäre und das angenehme Arbeitsklima im Institut geht ein großes Dankeschön an alle Mitglieder!

Besonders bedanken möchte ich mich auch bei Sabine Möhler für's Korrekturlesen dieser Arbeit, und für gelegentlich ein offenes Ohr und gute Ratschläge. Also Dolf Michielsen and Sven De Rijcke (both University of Ghent) have done a final check of the thesis, thank you!

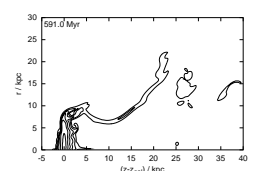
Meinen Zimmerkollegen Andreas Rieschick und Stefan Harfst danke ich für fachliche und auch nichtfachliche Unterhaltungen, ganz besonders Stefan für's Kontrollieren des Galaxien-Abschnitts und für's gemeinsame Aufrechterhalten des (Galgen)Humors während der letzten Wochen und Monate.

Ein riesengroßes Dankeschön geht an meinen Mann Carsten Rödiger für seine Unterstützung und unendliche Geduld und Aufmerksamkeit während langer Diskussionen über die Freuden und Tücken dieses Projektes.

Zum Gelingen dieser Arbeit haben auch einige Leute indirekt oder auch schon lange vorher beigetragen. Hier möchte ich zuerst meinen Eltern und meiner Schwester danken für ihre moralische Unterstützung und ihren Glauben an mich. Ein Dankeschön geht auch an Ragnar Nevries für's Einrichten des CD-Brenners unter Linux, was die Datensicherung immens vereinfacht hat. Ich habe gemerkt, daß ich einen Teil der Fähigkeiten, die mir jetzt zugute gekommen sind, schon in der Schule gelernt habe. Dafür möchte ich mich bei meinen Lehrern von damals bedanken.

Frühere Simulationsrechnungen für dieses Projekt wurden auf der Cray (crashi) des Rechenzentrums der Uni Kiel gemacht. Die in dieser Arbeit verwendeten Rechnungen stammen vom Vektorrechner NEC-SX5 (nesh) des Rechenzentrums.

Finanziert wurde dieses Projekt und die meisten Tagungsbesuche durch die DFG unter dem Kennzeichen He-1487/30. Von der IAU erhielt ich eine Unterstützung für die Reise zur General Assembly im Juli 2003.



Lebenslauf

Elke Rödiger (geb. Schumacher),
geboren am 7. Februar 1978
in Neubrandenburg.
Staatsangehörigkeit: deutsch

Schulausbildung:

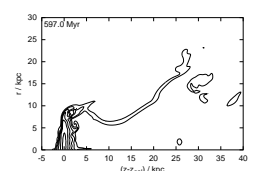
- 5.POS Neubrandenburg Sept 1984 - Juli 1991
- Curie-Gymnasium in Neubrandenburg Aug 1991 - Juni 1996
- Abitur Juni 1996

Studium:

- Grundstudium und Beginn des Hauptstudiums and der Christian-Albrechts-Universität zu Kiel (CAU) Okt 1996 - Sept 1999
- Auslandsstudienjahr an der Universität Glasgow, Schottland, Großbritannien. Anfertigung einer Masterarbeit bei Dr. Martin Hendry zum Thema *Optimal representation of the density field from redshift surveys* Okt 1999 - Sept 2000
- Verleihung des Abschlusses "Master of Science in Physics and Astronomy" von der Universität Glasgow July 2001
- Fortsetzung des Physikstudiums an der CAU, Diplom-Hauptprüfungen Okt 2000 - Okt 2001
- Überarbeitung der Masterarbeit aus Glasgow zur Diplomarbeit bei Prof. Dr. Gerhard Hensler Okt 2001 - Nov 2001
- Diplomzeugnis der CAU im Fach Physik, Gesamturteil: "mit Auszeichnung" Jan 2002
- Promotion zum Thema *Ram pressure stripping of disk galaxies* an der CAU bei Prof. Dr. Gerhard Hensler seit Nov 2001

Stipendien:

- Stipendiatin der Studienstiftung des deutschen Volkes Feb 1999 - Sept 2001
- Stipendiatin des DAAD während des Auslandsjahres in Glasgow Okt 1999 - Sept 2000



Erklärung

Diese Dissertationschrift wurde von mir in Form und Inhalt unter Anleitung von Prof. Dr. G. Hensler und nur unter Zuhilfenahme der angegebenen Hilfsmittel angefertigt. Sie wurde noch nicht an anderer Stelle ganz oder zum Teil im Rahmen eines Prüfungsverfahrens vorgelegt.

Teile dieser Arbeit wurden bei der Zeitschrift *Astronomy & Astrophysics* eingereicht und zur Veröffentlichung akzeptiert.

Kiel, den 16. Dezember 2004

Elke Rödiger

